



Investigation of pore closure during polar firn densification

Alexis Burr

► To cite this version:

Alexis Burr. Investigation of pore closure during polar firn densification. Earth Sciences. Université Grenoble Alpes, 2017. English. NNT : 2017GREAI089 . tel-01725405

HAL Id: tel-01725405

<https://theses.hal.science/tel-01725405>

Submitted on 7 Mar 2018

HAL is a multi-disciplinary open access archive for the deposit and dissemination of scientific research documents, whether they are published or not. The documents may come from teaching and research institutions in France or abroad, or from public or private research centers.

L'archive ouverte pluridisciplinaire **HAL**, est destinée au dépôt et à la diffusion de documents scientifiques de niveau recherche, publiés ou non, émanant des établissements d'enseignement et de recherche français ou étrangers, des laboratoires publics ou privés.

THÈSE

Pour obtenir le grade de

DOCTEUR DE LA COMMUNAUTE UNIVERSITE GRENOBLE ALPES

Spécialité : **2MGE : Matériaux, Mécanique, Génie civil,
Électrochimie**

Arrêté ministériel : 25 mai 2016

Présentée par

Alexis BURR

Thèse dirigée par **Armelle PHILIP**
codirigée par **Christophe MARTIN**

préparée au sein de l'**IGE** et du **laboratoire SIMaP**
dans l'**École Doctorale I-MEP2**

Investigation of pore closure during polar firn densification

Étude de la fermeture des pores lors
de la densification du névé polaire

Thèse soutenue publiquement le **29 novembre 2017**,
devant le jury composé de :

M. Christian GEINDREAU

Professeur, 3SR, Université Grenoble Alpes, Président

Mme, Dominique POQUILLON

Professeure, CIRIMAT, ENSIACET - INP Toulouse, Rapporteure

M. Martin SCHNEEBELI

Directeur de recherche, WSL/SLF, Davos, Suisse, Rapporteur

M. Samuel FOREST

Directeur de recherche CNRS, Centre des Matériaux, Mines Paristech,
Evry, Examineur

M. Johannes FREITAG

Chargé de recherche, AWI, Bremerhaven, Examineur

Mme, Amaëlle LANDAIS

Directrice de recherche CNRS, LSCE, Gif-sur-Yvette, Examinatrice

M. Christophe MARTIN

Directeur de recherche CNRS, SIMaP, Université Grenoble Alpes,
Co-directeur de thèse

Mme Armelle PHILIP

Maître de conférences, IGE, Université Grenoble Alpes, Directrice de thèse



Abstract

Densification from firn to ice is an essential phenomenon for the interpretation of the climate record. A good knowledge of this mechanism is necessary for the precise dating of the air embedded in the ice. Pore closure (or close-off) is the stage at which air becomes entrapped in the ice. Typically, the close-off arises approximately 50-120 m under the ice sheet surface. Because of gas flow in the firn column above close-off, the ice is older than the entrapped air. The difference between ice and gas is defined as Δage and may reach several millennia in certain sites. The precise determination of the Δage is mandatory to link temperature changes (recorded in the ice) and greenhouse gas concentrations (recorded in the gas phase). This issue may be addressed through the modeling of the firn densification processes that lead to pore-closure.

Firn densification consists of grain rearrangements, sintering and viscoplastic deformation. Although the viscoplastic behavior of the ice crystal is strongly anisotropic, densification models do not take into account this anisotropy. Firn also bears some granular characteristics that may affect its densification. The interactions between pore closure and microstructural mechanisms in the firn are still misunderstood. The aim of this PhD thesis is to incorporate both the granular aspect of firn and its anisotropy into an innovating approach of firn densification modeling. The mutual indentation of viscoplastic monocrystalline ice cylinders was experimentally carried out to propose a contact law that is based on indentation theory and that takes into account the preferential viscoplastic deformation on the basal plane. We have integrated this contact law into a DEM (Discrete Element Method) code for the prediction of firn densification. 3D X-ray micro-tomography was performed on polar firn at different stages of the densification ($\rho = 0.55 - 0.88 \text{ g.cm}^{-3}$) and depths ($\approx 23 \text{ m} - 130 \text{ m}$). A thorough investigation of pore closure and of different morphological and physical parameters was achieved for the Dome C and the newly drilled Lock In polar sites. In addition to these ex situ analyses, in situ X-ray micro-mechanical experiments were carried out on firn extracted from Dome C in order to model its densification. Ex situ and in situ microstructural observations indicate significant differences that can be explained by the relatively large strain rates imposed to the firn during in situ tests. These large strain rates allow for a decoupling of the effects of diffusion kinetics and of viscoplastic deformation. Their relative weights on the morphology of pores and on their closure are discussed. To measure pore closure, we propose a connectivity index, which is the ratio of the largest pore volume over the total pore volume. We show that this index is better suited for X-ray tomography analysis than the classical closed porosity ratio to predict the close-off density.

Key words : firn, densification, pore closure, anisotropy, X-ray tomography, discrete simulations

Résumé

Il est essentiel de comprendre le processus de densification du névé en glace afin d'interpréter les enregistrements climatiques. Une bonne connaissance des mécanismes permet une datation précise de l'air capturé dans la glace lors de la fermeture des pores. La glace est plus vieille que l'air capturé car le transport des gaz dans la colonne de névé est plus rapide que la densification de celui-ci. Cette différence d'âge entre la glace et le gaz est généralement appelée le Δ age. La densification de la neige est un processus complexe de réarrangement de grains, de frittage et de déformation viscoplastique. Bien que le comportement viscoplastique du cristal de glace soit fortement anisotrope, les modèles de densification actuels ne tiennent pas compte de cette anisotropie. De plus, le caractère granulaire du névé affecte aussi sa densification. La relation entre la fermeture des pores et les mécanismes microstructuraux sous-jacents est encore méconnue. Le but de cette thèse est d'incorporer à la fois l'aspect granulaire et l'anisotropie du cristal de glace dans une approche de modélisation innovante de la densification. Des expériences sur l'indentation viscoplastique de cylindres monocristallins de glace ont été réalisées pour proposer une loi de contact basée sur la théorie de l'indentation, et prenant en compte la déformation préférentielle du cristal de glace sur les plans basaux. Cette loi de contact a été implémentée dans un code utilisant la méthode des éléments discrets pour prédire la densification du névé.

La micro-tomographie aux rayons X a été utilisée pour caractériser ex situ le névé polaire en trois dimensions à différentes étapes de la densification ($\rho = 0.55 - 0.88 \text{ g.cm}^{-3}$), i.e. pour différentes profondeurs ($\approx 23 \text{ m} - 130 \text{ m}$). Une étude fine de la fermeture des pores et de différentes caractéristiques morphologiques et physiques a été réalisée pour les sites polaires Dome C et Lock In. Des essais mécaniques ont aussi été réalisés in situ sur du névé extrait de Dome C dans le but de modéliser la densification du névé. Les observations microstructurales des expériences ex situ et in situ révèlent d'importantes différences dues aux vitesses relativement importantes utilisées lors des essais mécaniques. Ces vitesses élevées permettent de découpler la contribution des cinétiques de diffusion de la contribution viscoplastique de la déformation. Les effets de ces contributions sur la morphologie des pores et leur fermeture sont discutés. Pour caractériser la fermeture des pores, cette thèse propose un indice de connectivité défini par le ratio entre le volume du plus gros pore sur la porosité totale. En effet, cet indice est plus approprié lors de l'utilisation de la tomographie aux rayons X que le ratio de pores fermés pour prédire la densité au close-off.

Mots clés : névé, densification, fermeture des pores, anisotropie, tomographie X, simulations discrètes

Le vent, pareil à l'enfance, se joue de l'arbre moqueur ...

Kaamelott, Alexandre Astier

Remerciements - Acknowledgements

Ces trois années de thèse ont été longues et riches en émotions : de la joie, de l'envie, de la motivation, mais aussi de la tristesse et du désespoir. Non, je n'essaie pas de démotiver un nouveau thésard avide de découvrir le contenu de ce manuscrit de 300 pages ! Je mets juste des mots sur mon ressenti. Je vais d'ailleurs m'autoriser dans ces remerciements un peu plus de fantaisie et d'opinions personnelles que je ne le fais dans le corps du manuscrit. En effet, les six prochains chapitres visent à donner un aperçu rigoureux du travail effectué pendant ces 36,25 mois, à destination de la communauté scientifique mais aussi de toute personne s'intéressant au sujet. Dans ces quelques pages plus personnelles, je vais donc un peu plus me lâcher.

La thèse, c'est une vraie rentrée définitive dans le monde du travail, tout en ayant à prouver qu'on peut obtenir un diplôme supplémentaire (encore un ! Si tu es jeune thésard, il est encore temps de t'arrêter !). Il y a de la joie d'aller faire ce que l'on aime, i.e. faire presque uniquement de la science (il y a toujours une partie administrative et humaine contraignante mais bon...). Il y a de l'envie d'aller plus loin, de repousser les limites de la recherche, là où personne n'a exploré avant ("*where no man has gone before*" - Star Trek), un peu à la manière d'un James T. Kirk de la recherche. Pour cela, il faut de la motivation, qui se doit de rester intacte tout au long de la thèse. Cependant, ce n'est pas si évident. De petits accrocs nous ramènent à la réalité, comme un Mr Spock qui serait sur notre route et nous stopperait dans notre élan. Ces petits accrocs ce sont les aléas de toute thèse : des problèmes expérimentaux et numériques (car aucun domaine n'est épargné !), qu'on ne sait pas trop comment résoudre. C'est aussi éventuellement des problèmes humains à gérer au mieux.

De temps en temps, tout se produit en même temps, si bien qu'on peut penser être le thésard le plus génial de tous les temps et sortir un *Nature* dans les prochains mois, ou à l'inverse vouloir tout claquer car on se sent mauvais, le monde de la recherche n'étant définitivement pas notre truc.

Heureusement, pour résoudre ces problèmes, et nous faire avancer quand on est bloqué, il y a d'autres personnes. Non, je n'ai pas été tout seul pendant ces trois ans derrière mon ordinateur ... Le manuscrit présenté n'est pas que le fruit de mon seul travail. D'autres personnes y ont contribué de manières plus ou moins lointaines, et ce sont ces personnes que j'aimerais remercier.

Il s'agira donc ici comme dans tous remerciements de lire entre les lignes pour savoir qui est particulièrement bien remercié, et qui ne fait ici que de la figuration. Je vous laisse gentiment démêler tout ça. J'ai décidé de faire des remerciements assez longs, pas du tout formels, et totalement avec mes mots. Ne vous étonnez pas si cela paraît décousu, d'ailleurs, cela le sera.

Je remercie d'abord mes directeurs pour m'avoir fait confiance lors du choix de cette

thèse après un seul entretien Skype. Soit j'ai fait très forte impression à ce moment-là, soit il n'y avait pas d'autre candidat, soit ils ont choisi le premier venu. J'opte pour la première possibilité qui est bien plus gratifiante, et leur suis extrêmement reconnaissant de la confiance qu'ils m'ont accordée.

Je remercie en premier ma directrice de thèse, Armelle Philip (et pas que par galanterie !), qui m'a très bien encadré durant ces trois ans. Avec Armelle, on a beaucoup discuté, on a bien réfléchi, beaucoup potassé sur le sujet, on s'est même énervé, bref on a mené un débat long de trois ans, ce qui a permis de choisir les bonnes directions et de valoriser ce travail. J'ai beaucoup appris avec Armelle, sur la glace, la mécanique, et beaucoup d'autres choses que je pensais connaître à ma manière un peu prétentieuse. Elle m'a laissé beaucoup de liberté dans mon travail, tout en venant voir ou j'en étais, si elle pouvait m'aider, me décoincer sur des sujets et me réorienter. Son implication dans les manips et surtout sa contribution à la rédaction du manuscrit sont plus que considérables. J'insiste sur ce dernier point. Je n'étais pas du tout serein à l'idée de rédiger ma thèse. À ma grande surprise, cela a été relativement agréable au niveau des corrections qui étaient toujours bien justifiées. Tu as toujours été très réactive et à l'écoute, et pas que pendant les derniers mois, mais tout au long de la thèse, tu ne m'as pas abandonné. Merci. J'aurai plaisir à revenir manger chez toi, et j'espère vraiment que tu continueras à travailler sur ce sujet passionnant.

Petit interlude...

Je tiens aussi particulièrement à remercier Christophe Martin, mon directeur de thèse. Je ne peux pas mettre co-directeur tellement Christophe a été impliqué dans un sujet qui était plus qu'éloigné de son domaine de compétences scientifiques. Cependant, il s'est fortement engagé dans la thèse, il a lu de la biblio sur le névé, analysé et interprété les résultats avec toujours un grand recul. J'aurais voulu faire plus d'éléments discrets dans cette thèse, ce qui m'aurait permis de plus travailler avec Christophe sur la simulation numérique (mais on ne peut pas tout faire !). Cependant, tu t'es impliqué dans tous les aspects de cette thèse, malgré le fort côté expérimental de mon travail, ce dont je te remercie. Je tiens aussi à saluer ton incroyable calme, ta capacité à réfléchir de manière très posée et tes prédispositions remarquables pour valoriser le travail en particulier par ta motivation pour écrire des publications. Christophe a eu le don de sortir les grands résultats qui intéressent la communauté, donnant vraiment une dimension impressionnante à mes résultats que je n'avais pas vue.

En résumé, mes directeurs de thèse ont été à la fois Kirk et Spock. Ils ont toujours été motivés pour faire plusieurs choses à la fois, mais m'ont retenu lorsque je voulais aller trop loin. Le mot direction prend donc ici tout son sens puisqu'on a choisi ensemble les routes à suivre sur toutes celles qui s'offraient à nous pendant cette thèse.

Je continue dans le bon ordre des remerciements avec Pierre Lhuissier. Incroyable homme à tout faire, véritable génie vivant de la manip' qui marche, de l'analyse d'images, du développement algorithmique... Peu de laboratoires ont un Pierre Lhuissier, qui sait tout faire et aide tout le monde. Sauf qu'en fait il m'a un peu plus aidé moi qu'il n'aurait peut-être dû. Pierre donne les bonnes pistes, pose les bonnes questions, résout tous les problèmes. Je pense qu'il a comblé les quelques "lacunes" de mes directeurs de thèse, et que le manuscrit s'est écrit par la combinaison de ces trois personnes Armelle-Christophe-Pierre. Face à leur investissement, j'ai l'impression de n'être qu'un exécutant. Un grand merci.

Voilà une partie un peu formelle mais qui était vraiment sincère.

Ensuite, je tiens à remercier Mathieu Bourcier qui m'a aussi considérablement aidé. Je ne sais pas s'il existe quelque chose que Mathieu ne sait pas faire expérimentalement. Il fait mieux les mouchetis que moi sur la glace alors que c'est moi qui lui ai montré. Il a été le soutien logistique et technique indispensable sur la tomographie. Plus qu'une aide en chambre froide, un véritable soutien psychologique pendant ces trois années, et en particulier pendant mes sessions à -10°C . J'aurai grand plaisir à revenir dans ton chalet jouer à Abyss, profiter de la vue ou manger un bon petit plat (ou les trois en même temps). Merci beaucoup.

Vient maintenant le tour d'autres personnes qui ont contribué de près ou de loin à la réalisation de cette thèse. Pour être un peu original, je tiens à remercier l'organisme financeur de cette thèse, c'est-à-dire le Ministère de l'enseignement supérieur et de la recherche qui, par un financement con-si-dé-rab-le de la recherche scientifique, m'a permis de subvenir royalement à mes besoins pendant trois ans. J'espère que les futurs thésards auront droit à ces bourses ministérielles d'exception qui font passer le financement CIFRE pour un canular.

J'aimerais remercier les membres du jury qui ont été choisis pour leur expertise reconnue dans les différents domaines que ma thèse a traités, et qui ont gentiment accepté d'examiner ce travail. Je remercie particulièrement les rapporteurs de ce manuscrit, Dominique Poquillon et Martin Schneebeli, ainsi que les examinateurs : Johannes Freitag, Samuel Forest et Amaëlle Landais. Merci à Christian Geindreau, avec qui on a pu bien travailler sur mes images tomos dans le cadre d'un stage, et qui a accepté de présider le jury. Merci à toi, j'espère qu'on va rapidement concrétiser le travail déjà effectué. J'en profite pour remercier le membre complémentaire de mon comité de thèse qui m'a suivi pendant trois ans : Wolfgang Ludwig, avec qui j'ai eu le plaisir de travailler plusieurs semaines sur de la reconstruction d'images scannées par tomographie à contraste de diffraction. À ce titre, Amaëlle Landais et Pierre Lhuissier sont remerciés une nouvelle fois pour leur participation à ce comité, qui je pense a été très bénéfique dans l'avancement de ma thèse.

J'aimerais remercier Elsa Gauthier et Nicolas Caillon pour leur proposition bienvenue de récupération de carottes de névé de Dome C. La thèse aurait pris une toute autre tournure sans ses carottes. Merci à Xavier Faïn, Maurine Montagnat, Anaïs Orsi. Je remercie aussi chaleureusement Patricia Martinerie dont l'aide dans l'interprétation des résultats et les explications scientifiques sur le névé ont été tout à fait limpides.

Je tiens à remercier Frédéric Flin qui nous a bien aidés pour faire évoluer des images binaires par une méthode à champs de phase, mais aussi le pro des éléments finis avec Elmer/Ice, i.e. Fabien Gillet-Chaulet qui a travaillé avec nous sur les cylindres de glace. On ne savait plus trop où aller avec ces monocristaux, la simulation était une solution bienvenue pour sortir de vrais résultats. Merci à Edward Ando pour les scans tomographiques à 3SR qui nous ont sauvé la vie !

Merci à Greg, Jean-François et Christophe Frau pour les aides techniques et de fabrication. De manière générale, merci à l'atelier qui a débordé de motivation et d'efficacité pour réaliser les différentes pièces...

Un grand merci à Camille qui a travaillé sur le même sujet que moi pendant cette thèse mais d'un point de vue climatique. On s'est mutuellement aidé et soutenu, je te souhaite bon vent dans ta vie de docteur !

De manière générale, j'aimerais remercier l'équipe permanente GPM2 pour m'avoir

bien intégré, et en particulier de m'avoir invité sur plusieurs sessions de nuit à l'ESRF que j'ai particulièrement appréciées ! J'en profite pour remercier Didier Bouvard, mon directeur de stage de deuxième année d'école, et qui, je pense, m'a bien vendu auprès de mes directeurs de thèse lors de leur choix. Je remercie aussi Rémy Dendievel, qui nous a soufflé l'idée de l'indice de connectivité (le lecteur découvrira vite que ce paramètre nous a bien été utile), et avec qui je vais travailler pendant un an et demi en post-doc !

De manière plus sobre, je tiens à remercier les membres et financeurs des projets Volsol, Lock In et DC12.

J'aimerais aussi remercier toute l'équipe enseignante de l'IUT 1 en génie mécanique et productique, qui m'a accueilli pendant deux ans. Je remercie particulièrement Mohammed Mhamdi-Alaoui et Franck Plunian pour leur aide durant mon monitorat.

Je continue dans la lignée des remerciements pour dire un grand merci aux trois stagiaires qui ont travaillé sur mon sujet de thèse : Wendy, Clément et Lucas. C'est aussi grâce à eux qu'on a pu explorer d'autres pistes et traiter beaucoup de données. Leur travail a été excellent !

Toi futur doctorant je te remercie de lire ce manuscrit. J'espère qu'il éclairera ton chemin vers l'illumination. Tu noteras dans ces premiers remerciements que pour avancer dans une thèse, il ne faut pas hésiter à aller toquer aux portes des gens.

Ensuite, je continue par les nombreux thésards ! Ça a été un grand plaisir de venir travailler dans les deux laboratoires IGE et SIMaP-GPM2 dont les doctorants sont plus que géniaux. On s'est bien amusé tous ensemble, on a fait des week-ends ski de folie, bu des coups, fait des soirées plus tranquilles, avec des croziflettes ou des tartes flambées, etc. J'aimerais remercier les doctorants qui ont commencé en même temps que moi d'abord, car on a tous souffert en même temps durant ces trois ans, on s'est tous plaint d'une thèse qui n'avancait pas, d'une période de rush intenable, d'une rédaction d'article interminable ! Merci à Ilann, Etienne, Olivier, Julien, Camille, Gabi, Marina du côté glacio, et Edouard, Paul, Alex et Robin côté SIMaP. Vous êtes des personnes formidables, on s'est vraiment bien entendu, et je pense m'être fait de bons amis durant ces trois années avec vous. Parmi les autres thésards, je tiens à remercier Cédric pour la solidarité en chambre froide ainsi que Thomas qui m'a montré comment faire de la corrélation d'images sur la glace ! Ça m'a fait du bien de voir d'autres personnes souffrir dans le froid en même temps que moi ! Je remercie plus que chaleureusement Thibaut, qui en plus d'être un type bien, a gardé mes chats plus d'une fois. J'aimerais remercier Pauline qui passe sa vie à étudier des pores en salle informatique, et c'est bien agréable d'avoir quelqu'un à qui parler pendant qu'on fait de la reconstruction d'images 3D. Je remercie les autres thésards de salle bleue, i.e. mes co-bureaux. Il y a beaucoup de thésards que j'aimerais remercier, des anciens comme Xavier qui m'a laissé LE meilleur bureau du GPM2, Mathieu qui m'a accompagné en conf à Madrid et qui a fait la discussion à ma place, Jérémy qui m'a accompagné pendant mon stage d'application au GPM2 et qui est vraiment cool, Sébastien, qui est la classe incarnée, Charles qui m'a emmené skier, Chloé qui était tout le temps déprimée mais bien marrante, Hélène qui me fait penser à un bouddha, mais aussi les nouveaux thésards qui sont tellement nombreux que je ne vais pas les nommer sinon je vais en oublier. Idem pour les stagiaires qui ne sont que de passage, mais qui sont souvent forts intéressants et attachants. Bref à vous tous je dis merci et bon courage pour les années qui viennent. Ne vous inquiétez pas, on en voit le bout un jour !

Je tiens à saluer la loi d'Hofstadter pour sa vision si juste de la vie d'un thésard : "Il

faut toujours plus de temps que prévu, même en tenant compte de la Loi de Hofstadter". Si j'ai bien un conseil d'expérimentateur à donner aux prochains doctorants pour leur éviter de perdre du temps, c'est de se rappeler que "le mieux est l'ennemi du bien" comme disait Voltaire, et de ne jamais commencer une manip' le vendredi après-midi, ça ne fonctionnera pas.

Enfin, je remercie mes parents qui m'ont soutenu pendant toutes mes études, et qui ont préparé un pot de thèse choucroute-knack qui restera dans les annales ! J'en profite pour remercier mon parrain et ma cousine qui ont fait le déplacement, ainsi que toute ma famille pour son soutien. J'espère qu'ils ont enfin compris le sujet de ma thèse... Je remercie aussi la famille d'Adeline pour son aide, pour la quiche réalisée pour mon pot de thèse et pour les trois semaines où j'ai pu rédiger ma thèse au bord de la piscine.

Merci aussi à mes deux chats, Berlioz et Prunelle, pour leurs ronronnements et leurs câlins à 5h du matin lorsque je manquais de sommeil...

Voilà voilà...

Meuh non voyons, évidemment je finis par LA personne qui m'a accompagné pendant toute cette thèse, et surtout qui m'a supporté toutes ces années, je parle bien sûr d'Adeline, incroyable jeune femme dont les qualificatifs manquent pour la décrire. En plus, elle nous a organisé une fondue au chocolat du tonnerre pour le pot.

Bref, sur ce, mettez vos combinaisons polaires, les boots, les gants, le bonnet, je vous souhaite une bonne lecture bien froide !

Table of Contents

1	Introduction	1
1.1	Ice cores and their secrets.	3
1.1.1	Entrapped air in ice cores	3
1.1.2	Parameterizations of entrapped air	7
1.2	Firn : a mixture of ice and air	12
1.2.1	The single crystal of ice	12
1.2.1.1	Crystallography	12
1.2.1.2	Elasticity and brittle behavior	15
1.2.1.3	Dislocation creep	15
1.2.1.4	Viscoplastic law for a single crystal of ice	19
1.2.2	Polycrystalline ice	21
1.2.3	Evolution of texture in ice cores	23
1.2.4	Recrystallization	25
1.3	Literature review on firn densification	26
1.3.1	Densification mechanisms	26
1.3.2	Current models of densification	28
1.3.3	Stratification of firn and impurities effect	30
1.3.4	Pressure-sintering diagrams	32
1.4	Outcomes and outlines	34
2	Modeling of the contact between ice grains	37
2.1	Introduction	39
2.2	Contact model	40
2.3	Methods	45
2.3.1	Single crystal machining and set up	45
2.3.2	The Digital Image Correlation on ice	47
2.3.2.1	Principles of the Digital Image Correlation	47
2.3.2.2	Computation of strains	48
2.3.2.3	Computation of strain rates	51
2.3.2.4	Correlation criterion	52
2.3.2.5	Use, accuracy and interests	52
2.4	Experimental indentation of ice cylinders	54
2.4.1	Diametrical loading on a single cylinder	54
2.4.2	Diametrical loading on two cylinders	59
2.4.3	Neck size effect	60
2.5	Comparison between 2D FEM simulations and experiments	62

2.6	Concluding remarks	65
3	Microstructure of polar firn	67
3.1	Tomography on ice cores	69
3.1.1	Up to date knowledge on ice core tomography	69
3.1.2	State of the art	71
3.2	Polar sites characteristics	73
3.3	Methods	75
3.3.1	Cold cell	77
3.3.2	Image Analysis	79
3.3.3	Control of sublimation	82
3.4	Representativeness of morphological parameters	84
3.4.1	Density	84
3.4.2	Closed porosity	86
3.4.3	Connectivity Index	88
3.4.4	Specific surface area	90
3.4.5	Key results on error estimations	91
3.5	Representative Volume Element in ice	91
3.5.1	Determination methods	92
3.5.2	Formal description of statistical RVEs	93
3.5.3	Representativeness of closed-porosity and connectivity indexes	98
3.5.4	Discussion	100
3.6	Multi-site comparisons	102
3.7	Refined geometrical parameters for Dome C and Lock In sites	105
3.8	Corrected data of Dome C	109
3.9	Pore size	112
3.10	Characterization of the ice phase	115
3.10.1	Crystallographic orientation	115
3.10.2	Grain size	118
3.11	Concluding remarks	122
4	In situ compression of natural firn	125
4.1	Review of in situ compression on snow and firn	127
4.2	Methods	129
4.2.1	Cold cell for oedometric test	129
4.2.2	Tested samples	131
4.2.3	Digital Volume Correlation	133
4.3	Mechanical behavior	136
4.3.1	Evolution of stresses	136
4.3.2	Pore pressure	138
4.3.3	Specific surface area	141
4.3.4	Grain size and anisotropy	142
4.4	Evolution of pores with artificial densification	144
4.4.1	Effects of densification on pore closure and morphologies	144
4.4.2	Curvatures	144
4.4.3	Discussion	150
4.5	Modeling thermally activated processes	152

4.5.1	Heat treatment	152
4.5.2	Effect of heat treatment on pore closure and morphologies	152
4.5.3	Grain size and texture after heat treatment	159
4.5.4	Curvature minimization modeling	161
4.6	Conclusion	165
5	Discrete Element modeling	167
5.1	Principles of the Discrete Element Method	169
5.1.1	Basis of DEM	169
5.1.2	Algorithm	170
5.1.3	Boundary conditions and stress calculation	173
5.1.4	Example of a contact law: elasticity	174
5.1.5	Generating numerical microstructure	176
5.2	Contact law for ice particles	177
5.2.1	Isotropic viscoplastic contact law	179
5.2.1.1	Normal force	179
5.2.1.2	Tangential force	180
5.2.2	Viscoplastic anisotropic contact law for ice	180
5.2.2.1	Normal force	180
5.2.2.2	Tangential force	181
5.2.2.3	Comparison of the normal and tangential viscoplastic anisotropic contact laws	182
5.3	Image voxelization	184
5.4	Results of discrete simulations with the anisotropic model	185
5.5	Using binary images from in situ X-ray tomography : an attempt	194
5.5.1	Methods	194
5.5.2	Results	196
5.6	Conclusion	199
6	Conclusion and future work	201
6.1	Conclusion	203
6.2	Future work	205
	Numerical simulations on digitized images from X-ray tomography	205
	Extending X-ray characterization to other sites	207
	Coupling Digital Volume Correlation and Diffraction Contrast Tomography	207
	Towards a firm layer modelling	209
	Implementation of the anisotropic model in the IGE firm densification model	211
	Bibliography	213
	Appendices	245
A	The transverse isotropic viscoplastic law	247
A.1	Analytical description for the behaviour of ice single crystal	247
A.2	Case 1 : Simplifications for an applied uniaxial stress	249
A.3	Case 2 : Simplifications for an applied shear stress	252

B	Errors on macroscopic strain calculation	255
B.1	Choice of the macroscopic strain calculation	255
B.2	Methods for errors calculation	256
C	Creep test on monocrystalline cylinders	259
D	Evolution of firm microstructure at Dome C and Lock In	265
D.1	Frame of reference	265
D.2	Dome C	266
D.3	Lock In	270
D.4	Microstructure of in situ samples before and after the compression tests.	273
D.5	Microstructure of in situ samples after Heat Treatment.	276
D.6	Evolution of eigenvalues and vectors with depth	279
E	Correction of the closed porosity ratio at Dome C	283
E.1	Parameterizations of the closed porosity ratio	283
E.1.1	Parameterization of Schaller et al. [2017]	283
E.1.2	Parameterization of Goujon et al. [2003]	283
E.1.3	Parameterization of Mitchell et al. [2015]	283
E.2	Correction of closed porosities	284
F	Dimension and calibration of the in situ cold cell	287
F.1	Micro-compression cold cell	287
F.2	Oedometric test	291

Chapter 1

Introduction

Contents

1.1	Ice cores and their secrets...	3
1.1.1	Entrapped air in ice cores	3
1.1.2	Parameterizations of entrapped air	7
1.2	Firn : a mixture of ice and air	12
1.2.1	The single crystal of ice	12
1.2.2	Polycrystalline ice	21
1.2.3	Evolution of texture in ice cores	23
1.2.4	Recrystallization	25
1.3	Literature review on firn densification	26
1.3.1	Densification mechanisms	26
1.3.2	Current models of densification	28
1.3.3	Stratification of firn and impurities effect	30
1.3.4	Pressure-sintering diagrams	32
1.4	Outcomes and outlines	34

1.1 Ice cores and their secrets...

1.1.1 Entrapped air in ice cores

Air content of past climate is embedded in polar ice caps, making them a major source of data for the interpretation of the climate record. Depending on the drilling site, the climate can be reconstructed to different periods of the planet life. For example, the EPICA community traced climate back to 800 ky [Augustin et al., 2004] from an ice core drilled at Dome Concordia. This ice core is still the oldest one recovered. However, current studies aim to find even older ice approximately 1.5 million years old [Fischer et al., 2013; Passalacqua, 2017]. Greenhouse gases are typical examples of what can be tracked with time in ice cores. For instance, CO_2 and CH_4 received much interest with studies using newly drilled ice cores that continue to enrich past measurements and improve data precision [e.g., Barnola et al., 1991; Battle et al., 1996; Petit et al., 1999; Louergue et al., 2008; Lüthi et al., 2008; Landais et al., 2013; Rubino et al., 2013]. Temperature evolution across time is also crucial in order to evaluate the implications of orbital and anthropogenic forcings on future climate [Masson-Delmotte et al., 2006; Jouzel et al., 2007]. In any case, results obtained by the scientific community from different sites, all exhibit the same trend for CO_2 concentration in air for instance. Figure 1.1 is a composite data of several ice cores and illustrates the current increase in CO_2 content in the atmosphere. It comes from Bereiter et al. [2015] whose data are available on the National Oceanic and Atmospheric Administration website¹.

The natural variability of greenhouse gases in the past (e.g., CO_2 in Fig. 1.1) contributed to about half of the temperature change during glacial and interglacial periods [Petit et al., 1999]. Therefore the current climate change is the result of the striking rise of greenhouse gases combined with sulphate aerosols in the atmosphere [Hegerl et al., 1997] because of anthropogenic forcings (i.e. human activities), while other forcings such as solar radiation or volcanic influences can not explain climate evolution since 1950 [Tett et al., 1999; Ammann et al., 2007]. Still, the relative weights of the different forcings have to be understood at different scale of the planet in separating natural contributions to anthropogenic ones [Ahmed et al., 2013], so that the future climate and its regional impact can be predicted.

The importance of the firn core (about the 50 to 100 first meters of the ice core) is paramount in tackling the problem of dating when reconstructing and simulating past climate. Indeed it is the gradual densification of snow to ice that captures the air. This densification (also named firnification) can last from a few centuries to a few thousands

¹ <http://ncdc.noaa.gov/paleo/study/17975>

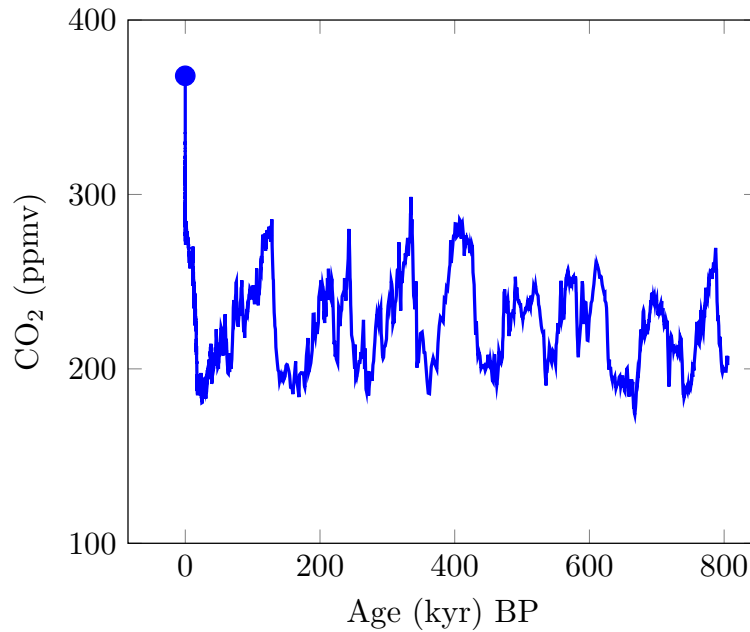


Figure 1.1: Reconstruction of the CO₂ content in the atmosphere for the past 800 kilo years from different Antarctica ice cores [Bereiter et al., 2015] (BP = Before Present). The blue dot corresponds to the CO₂ concentration in the year 2000.

years before pore occlusion. An important consequence is that the entrapped air is younger than the ice at a given depth [Schwander & Stauffer, 1984; Schwander et al., 1988]. This difference of age is called $\Delta\text{age}_{\text{gas-ice}}$. Linking unambiguously gas content (from the air) and temperature evolution (from the ice) of the past climate is challenging. In addition, the progressive closure of pores usually leads to a broad distribution of the gas age [Schwander et al., 1993]. In other words, the precise evaluation of the $\Delta\text{age}_{\text{gas-ice}}$ requires a full understanding of the densification and gas trapping mechanisms. This is hindered by the differences that polar sites exhibit, in terms of local temperatures, accumulation rates, impurity contents and topographies. Moreover, evolution of climate proxies, and air dating depend on the polar sites studied, but they should come together when compiling data. Therefore, ice cores are extensively compared in the literature and are synchronized in time using stratigraphic markers such as volcanic dust in ice, and methane or $\delta^{18}\text{O}$ (isotopic fraction of O) in entrapped bubbles for instance [e.g., Veres et al., 2013; Bazin et al., 2013]. In fact, although the most straightforward technique is to count annual layers, dating the ice is rather performed by inverse methods [Parrenin et al., 2007] that rely on ice flow modeling and different age markers from different time scales. This is required in particular when ice thinning is important (with depths) or at low accumulation sites. Some markers such as $\delta^{18}\text{O}$ and deuterium also enable to reconstruct the surface temperature at the time of snow deposition, thus the temperature of the past

atmosphere (known as the isotopic thermometer).

The firn column is classically divided into three distinct zones [Sowers et al., 1992]. When considering air circulation, a convective zone is first encountered, where gases are mixed with the atmosphere in the top surface due to the high permeability of snow and/or the effect of wind. The main part of the firn consists of a diffusive zone where molecular diffusion is dominant in the pore network and where isotopic fractionation occurs². At the Lock-in Depth (LID), air does not flow anymore, and gravitational enrichment stops³. This starts a non-diffusive zone (in open pores), defined as the Lock-in Zone (LIZ). Typically, isotopes of nitrogen ($\delta^{15}\text{N}$) and of argon ($\delta^{40}\text{Ar}$) are good indicators of this zone. In brief, the concentration of a heavy isotope of an element (for instance $\delta^{15}\text{N}$ compared to $\delta^{14}\text{N}$) tends to be more accentuated deep in the firn than on the top of the diffusive zone. This increase is linear with depth (following the barometric equation of [Sowers et al., 1992]), and stagnates when the LID is reached. It is essential to determine this depth as this is where molecular diffusion stops, i.e. where the Δage is defined. At the bottom of this zone, the close-off depth (COD) is the depth at which pores are fully isolated from the surface and where air cannot be pumped out of the firn anymore.

Successive densification mechanisms appear along the firn column. From a microstructural point of view, the top is chaotic (the first two meters). Snowflakes are already rounded because of the wind when they reach the ground in dry polar sites. These rounded particles undergo complex metamorphism because of the thermal gradient at shallow depths, wind and sublimation-deposition [Colbeck, 1983]. Then snow experiences grain rearrangement and sintering until 0.55 g.cm^{-3} [Anderson & Benson, 1963; Alley, 1987]. This density⁴ corresponds to an approximate porosity of 40%, close to the porosity that characterizes a Random Close Pack of spheres [Scott & Kilgour, 1969]. As for many other granular materials, further densification requires the plastic deformation of the grains themselves. Above this threshold density, dislocation creep⁵ becomes the dominant mechanism [Maeno & Ebinuma, 1983] accompanied by pressure sintering. Maeno & Ebinuma [1983] proposed a second critical density at 0.73 g.cm^{-3} because of maximum contact between ice particles, but as shown by Hörhold et al. [2012] on 16 ice cores, there is no evidence of an alteration in the densification rate at this density. The last stage of densification is traditionally porosity-related. When the density exceeds 0.84 g.cm^{-3} ,

² Different isotopes of an atom exist with different relative abundances. For instance for nitrogen, the abundance of $\delta^{14}\text{N}$ is 99.64 % while for $\delta^{15}\text{N}$ it is 0.36 % [Lide et al., 1947]. When one isotope is favored by a chemical reaction or a change of state rather than other isotopes, such phenomenon is called isotope fractionation.

³ Thermal fractionation also occurs more preferentially in the diffusive zone and gives information on abrupt temperature transition.

⁴ In this work, density is expressed in g.cm^{-3} instead of the standard international unit kg.m^{-3} .

⁵ Creep is a thermally activated mechanism for deformation under an applied stress. More information on dislocation creep is given in section 1.2.1.3

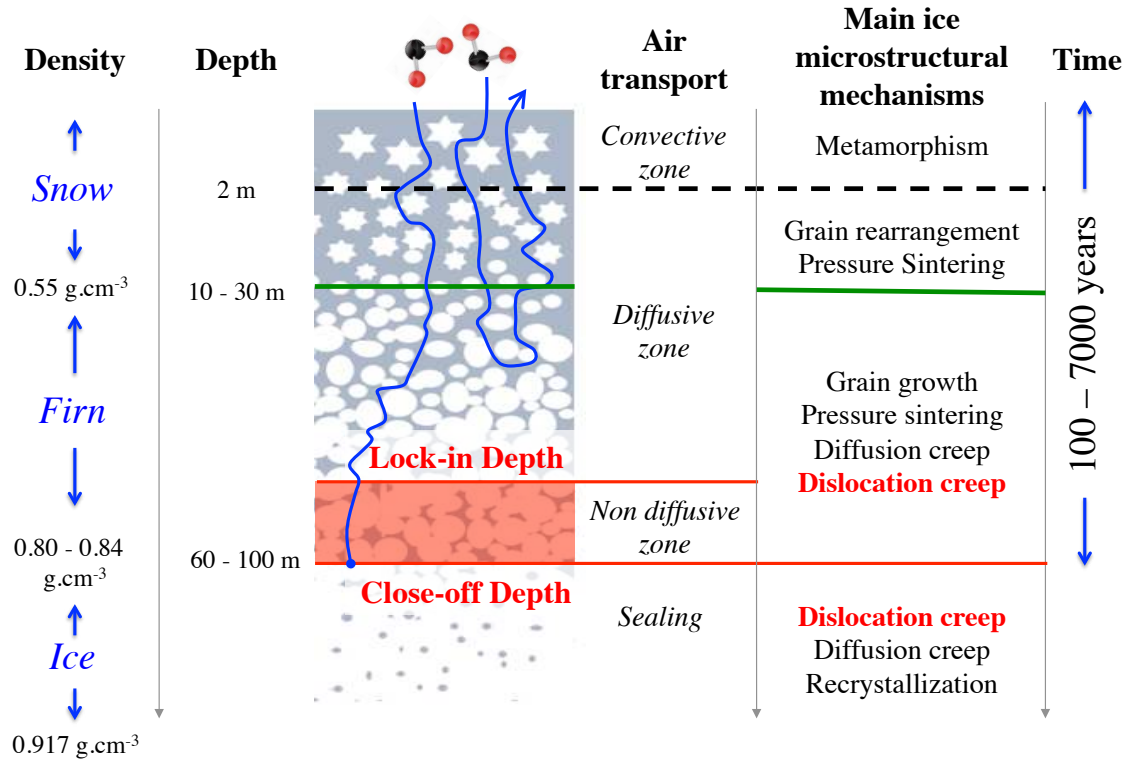


Figure 1.2: Diagram of snow densification separating the three sections of a firn column (adapted from Bréant et al. [2017]): snow, firn and ice. Values for depths, densities and times are indicative. The diagram summarizes the major phenomena of air transport and microstructural mechanisms. Note that below 500 m deep, ice forms clathrates, i.e. air molecules are entrapped within ice crystallographic structures [Lüthi et al., 2010].

pores are closed and further shrinking is driven by the fact that their internal pressure is smaller than the surrounding stress. The aforementioned mechanisms are used in some extent in firn densification models, in order to estimate precisely the Δ_{age} gas-ice, so that a correct reconstruction of the past atmospheric signal can be made. Further details of these models are given in section 1.3.2. Figure 1.2 summarizes these different stages of firn densification.

Some definitions : For an easier understanding of the following chapters, some definitions and acronyms are introduced below :

- **Accumulation rate** : it is the amount of ice that is deposited during one year, usually expressed in centimeter water equivalent per year (cm.w.eq.yr⁻¹). It can be obtained by identification of successive layers or by measurements of the ¹⁰Be isotope.

- **Lock-in Depth (LID)** : the depth where the gravitational fractionation of $\delta^{15}\text{N}$ stops and where a plateau starts.
- **Lock-in Zone (LIZ)** : the depth or density range for which the concentration of $\delta^{15}\text{N}$ is constant. It is represented by the non-diffusive zone in Fig. 1.2.
- **Close-off Depth (COD)** : in this work it is the last depth possible for air pumping (or ultimate depth). The determination of the COD relies on on-site air pumping measurements. ρ_{COD} is the density associated to this depth.

Other definitions for these words are specified when used.

In practice, once the firn is drilled, the air contained in open pores is extracted on-site (see Fig. 1.3). An inflatable rubber bladder is entered into the hole, down to the drill depth, and air is pumped along a sampling line and collected into flasks [Schwander et al., 1993]. The bladder is supposed to seal off the firn air from the atmosphere, avoiding contaminations. Note that air sampling is performed on the same ice core that is retrieved. Various depths are selected for air pumping, and when it is not possible anymore, the close-off is considered reached. This method comes with serious issues. The COD depends on the pump capacity. The method does not differentiate the air pumped from downward from the air pumped from lateral sides. Thus, the pump can still work while the close-off is reached, which means that the COD could be overestimated (deeper than the correct COD). Moreover, air pumping may break some tenuous bonds between grains and thus open some pores, but this is hardly quantifiable. Despite these flaws, sampling air on-site is a necessary precaution to avoid analysing air contaminated by present atmosphere in the open pores, when the ice core is removed from the drill hole.

1.1.2 Parameterizations of entrapped air

As described in the previous section, the gas diffusion within the firn and the progressive closure of pores dictate the composition and age of trapped gases in ice. However this is totally dependent on the site characteristics (accumulation rate, temperature, altitude, history, ...). Therefore, modeling the transport of air inside the firn is not an easy task, but it is crucial to reconstruct the past climate, or estimate the evolution of the future climate. Several models exist for air transport in firn such as those developed by Trudinger et al. [1997], Severinghaus & Battle [2006] or Witrant et al. [2012] for instance. They all rely on a diffusion coefficient linked to the evolution of the open porosity with depth. Thus, these models are strongly dependent on a correct parameterization of the closed porosity ratio (volume of closed pores divided by the total volume of pores) to work out the diffusivity in

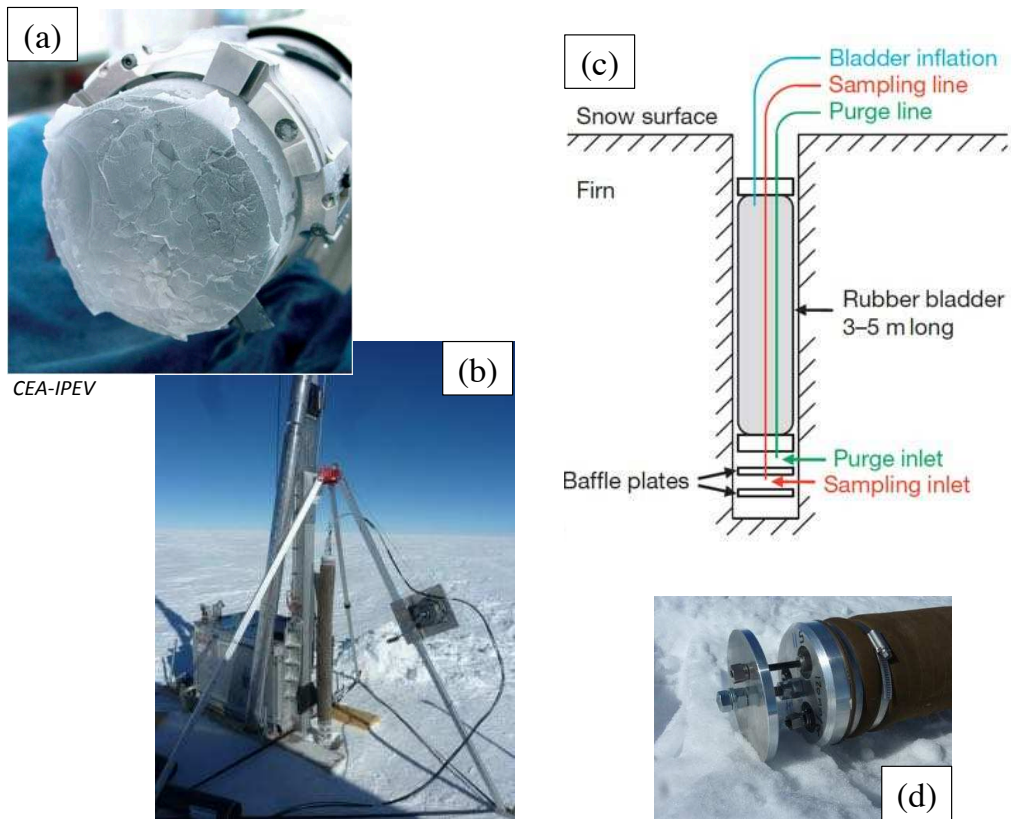


Figure 1.3: (a) Picture of a freshly drilled ice core. (b) Positioning of the rubber bladder above the drill hole at Dome Concordia. (c) Diagram of the rubber bladder inside the hole. (d) The nosepiece of the pump apparatus with the baffle plates (courtesies of Xavier Faïn).

firm. However there is no consensus on these parameterizations. Indeed, [Schwander \[1989\]](#) and then [Severinghaus & Battle \[2006\]](#) proposed parameterizations dependent only on the density and with particular values of close-off density. [Goujon et al. \[2003\]](#) developed a multi-site parameterization that relies on an empirical relationship between the enclosed volume of air into bubbles V_c and the mean annual surface temperature T_s (in Kelvin) of the studied sites [Eq. (3), [Goujon et al., 2003](#)]:

$$V_c = 6.95 \cdot 10^{-4} T_s - 0.043 \quad (1.1)$$

This linear formulation of V_c comes from measurements [[Martinerie et al., 1992, 1994](#)] performed below the COD (several meters), and which are corrected to account for the cut-bubble⁶ effect of the samples [[Martinerie et al., 1990](#)]. Note that the technique used consisted in melting and refreezing samples, giving the air content data (content in the pores) and not the closed porosity data (the pores). Using the Boyle-Mariotte law enables [Martinerie et al. \[1992, 1994\]](#) to work out the air volume at the depth where isolation of pores is triggered in terms of pressure (not the atmospheric pressure anymore). In other words this gives a density at which close-off occurs assuming the process is instantaneous⁷.

A new close-off density ρ_{Gc} is thus derived a posteriori [Eq. (1), [Goujon et al., 2003](#)] :

$$\frac{1}{\rho_{Gc}} = V_c + \frac{1}{\rho_{Gice}} \quad (1.2)$$

where ρ_{Gice} is the density of pure ice (in g.cm^{-3}) as proposed by [Eq. (7), [Goujon et al., 2003](#)] :

$$\rho_{Gice} = 0.9165(1 - 1.53 \cdot 10^{-4}(273.15 - T_s)) \quad (1.3)$$

In the following ρ_{Gice} will refer to Eq. (1.3), while $\rho_{ice} \approx 0.917 \text{ g.cm}^{-3}$ is defined at $T = 0 \text{ }^\circ\text{C}$ [[Bader, 1964](#)]⁸.

Then, the ratio of the closed porosity over the total porosity is :

$$r_{cp} = \frac{\phi_{cp}}{\phi} = 0.37 * \left(\frac{\phi}{\phi_{Gc}} \right)^{-7.6} \quad (1.4)$$

with ϕ_{cp} the closed-porosity ($0 < \phi_{cp} < 1$), ϕ the porosity ($0 < \phi < 1$) and ϕ_{Gc} its value at the close-off density ρ_{Gc} , hence $\phi_{Gc} = \rho_{Gc} V_c$. This formulation of the closed porosity is related to air content and pressure increase at isolation depth. Equation (1.4) means that

⁶ Pores that touches the borders of the sample.

⁷ Such measurements do not take into account the progressive closure of pores neither discriminate a pressure increase due to a firm layer that would seal above an open firm layer.

⁸ The polar sites studied in this work have close mean annual temperature, and experiments are carried out at $-10 \text{ }^\circ\text{C}$. For simplicity, ρ_{ice} is considered independent of T_s and equal to 0.917 g.cm^{-3} in this work unless stated otherwise.

at the COD as defined by ρ_{Gc} there are only 37 % of closed pores in the volume assuming a virtual instant close-off, and not 100 % as we could expect. This parameterization was since used to reconstruct several trace gases in various polar sites [Buizert et al., 2012; Witrant et al., 2012]. Other relation between air content and close-off temperature of the site can be found in the literature and could have been used for this parameterization, but they are also linear and based on measurements [Raynaud & Lebel, 1979; Higashi et al., 1983].

Recently, Mitchell et al. [2015] proposed a stochastic description of the pore closure in layered polar firn. The formulation is less straightforward than Eq. (1.4). Using the local density of samples, instead of the bulk density, it writes [Mitchell et al., 2015] :

$$r_{cp} = 1 - f(u, 0, v) + \exp\left(-u + \frac{v^2}{2} + \ln(f(u, v^2, v))\right) \quad (1.5)$$

with

$$\begin{aligned} f(x, y, z) &= \frac{1}{2} + \frac{1}{2} \operatorname{erf}\left(\frac{x - y}{\sqrt{2z^2}}\right) \\ u &= \frac{75}{\rho_{Mc}}(\rho_{Mc} - \rho) \\ v &= \frac{75}{\rho_{Mc}}\sigma_{Mc} \end{aligned} \quad (1.6)$$

The model also involves a different definition of the close-off and pure ice densities than Goujon et al. [2003] with :

$$\rho_{Mc} = \frac{1}{1 - \frac{1}{75}} \left(\frac{1}{\rho_{Mice}} + 7.02 \cdot 10^{-4}T - 4.5 \cdot 10^{-2} \right)^{-1} \quad (1.7)$$

and with $\rho_{Mice} = 0.917 \text{ g.cm}^{-3}$. The formulation of Mitchell et al. [2015] introduces the parameter σ_{Mc} representing the smoothness of the closure, which essentially governs the slope on Fig. 1.4 (using $\sigma_{Mc} = 0.007 \text{ g.cm}^{-3}$).

All the aforementioned parameterizations were based on experimental data obtained with the melting-refreezing technique [Raynaud & Lebel, 1979; Raynaud et al., 1982] or with an air expansion method close to gas pycnometry [Schwander & Stauffer, 1984; Stauffer et al., 1985]. Very recently, Schaller et al. [2017] uses X-ray tomography first to obtain the evolution of the close porosity ratio along the firn core, and second to propose a new parameterization ruled by a critical porosity at which all sites are supposed to have reached the close-off density, independently of the site temperature. This technique gives this time the air container, i.e. the closed pores, and not the air content. Therefore, it gives no information on the entrapped volume of air. The following equation uses

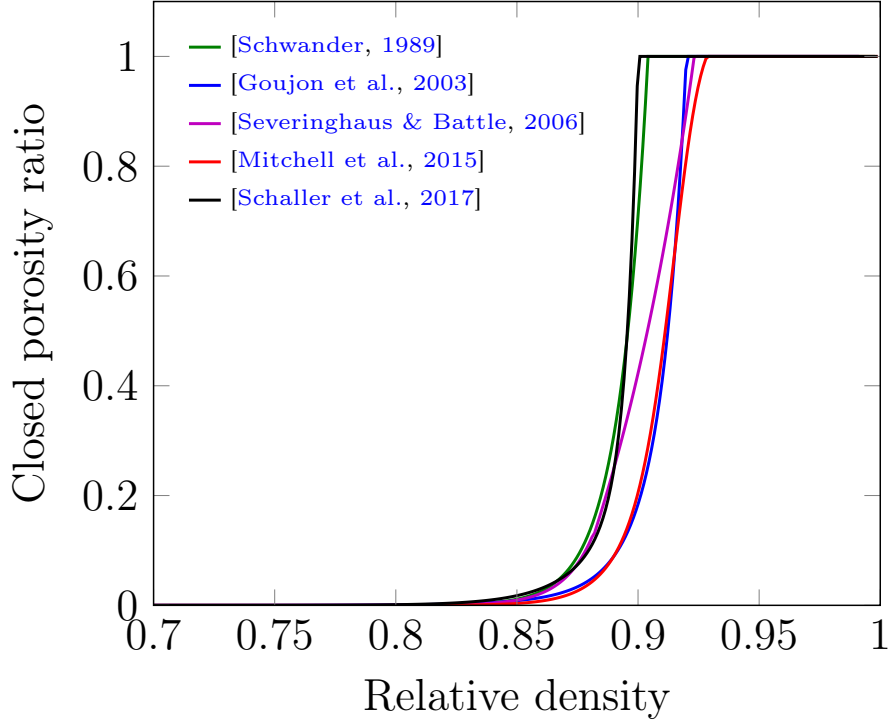


Figure 1.4: Comparison of closed porosity parameterization for the same temperature $T = -55^\circ\text{C}$.

parameters b , λ_1 and λ_2 that are fitted on three different ice cores :

$$\begin{aligned} \text{if } \phi > \phi_{crit} &\rightarrow r_{cp} = \frac{\phi_{crit}}{\phi} \left(b e^{-\lambda_1(\phi - \phi_{crit})} + (1 - b) e^{-\lambda_2(\phi - \phi_{crit})} \right) \\ \text{if } \phi \leq \phi_{crit} &\rightarrow r_{cp} = 1 \end{aligned} \quad (1.8)$$

The five parameterizations discussed are shown in Fig. 1.4, for a temperature of -55°C . All equations used are related to the publications therein and to equations (1.1)-(1.8). This means the parameterization from Schwander [1989] is directly used without changing the threshold density. Therefore is it certainly wrong in Fig. 1.4, as authors prescribed to use it between -20 and -30°C . The density of pure ice and close-off are calculated for each method as the different authors specified them. However to avoid issues related to the different ρ_{ice} for the same temperature, the Fig. 1.4 is plotted with the relative density. The parameterization of Schaller et al. [2017] is plotted using the parameters these authors proposed for the B53 core (Dome Fuji, Antarctica), whose mean annual temperature is -55°C .

There are clear discrepancies between the proposed parameterizations that lead to different results in terms of diffusivity. Moreover, from these curves, finding the close-off density seems inappropriate. These were all based and fitted on experiments, however a

percolation theory does exist, and proposes a critical point at which occlusion of gases occurs as [Schaller et al. \[2017\]](#) proposed. It consists in calculating the closed porosity ratio with the probability of the closure. This theory is found to be very dependent on small fluctuations, especially in the critical zone of percolation. It was also shown to depend in a less extent on the sample-to-sample variability (as the trapping process is erratic) and on the sample size [[Enting, 1993](#)].

Finally, the diffusion coefficient of air within firn also requires the knowledge of a tortuosity factor, which is strongly related to the microstructure. While [Schwander et al. \[1988\]](#) calculated it thanks to the measurements of diffusion coefficients, it is clear that it depends on the studied site, and that X-ray tomography should be THE appropriate tool to obtain both the closed porosity ratio and the tortuosity factor from the same experiment. However, of these two parameters, only the closed porosity ratio is thoroughly studied in our work. Following chapters do not attempt to quantify the tortuosity factor.

To have a complete knowledge of the progressive closure of pores and entrapment of gases, the densification of firn with temperature, time, accumulation, and stress state have to be better understood.

1.2 Firn : a mixture of ice and air

Firn is a material made of air and ice particles. Firn exhibits some granular behavior as ice particles may rearrange under external load. Previous sections focused on the circulation of air and its entrapment in the pores. This section focuses on some physical properties of ice and their implications for the firn.

1.2.1 The single crystal of ice

1.2.1.1 Crystallography

In this work, a grain of ice will refer to a crystal of ice unless stated otherwise. In terms of crystallography, a crystal of ice is defined by an atomic unit cell, which can be repeated periodically by translation. When a new orientation of molecule arrangement appears a new grain is formed. The frontier between the two different stacks is named a grain boundary.

Under terrestrial temperature and pressure conditions, the crystallographic structure of ice is hexagonal and denominated ice I_h . Its structure is close to the hexagonal compact ($c/a = \sqrt{8/3} = 1.63299$) with a ratio $c/a = 1.628168$ at -8°C [chap. 2, [Petrenko & Whitworth, 1999](#)] ($a = 4.5214\text{\AA}$ and $c = 7.3616\text{\AA}$ at -8°C). \mathbf{c} is the vector perpendicular to the basal plane (and to vectors \mathbf{a}). This ratio is almost independent of temperature.

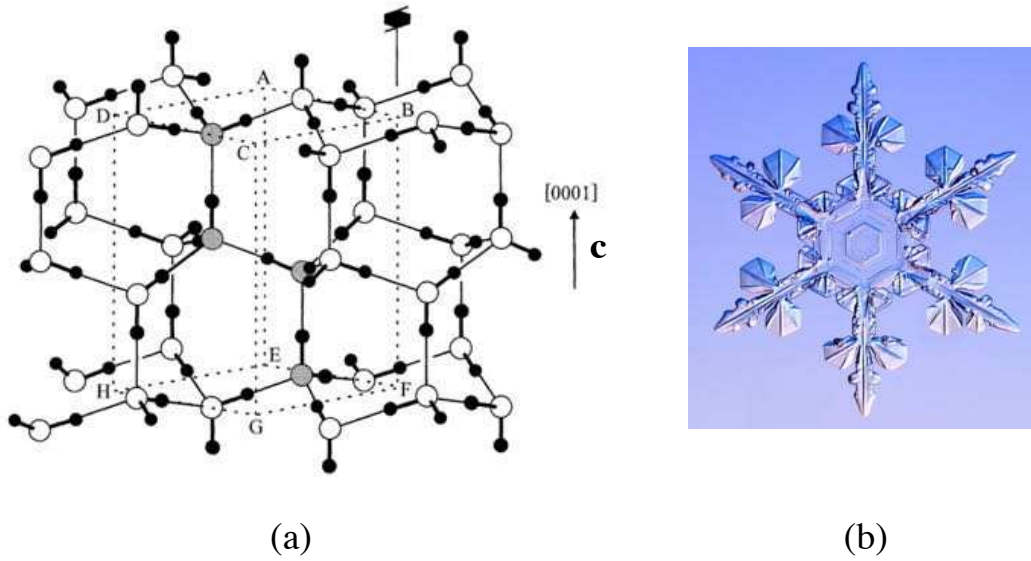


Figure 1.5: (a) Structure I_h of an ice crystal [chap. 2, [Petrenko & Whitworth, 1999](#)] in 3D. White circles represent atoms of oxygen, while hydrogen atoms are small black circles. The prism ABCDEFGH displays the unit cell, and the four atoms of oxygen describing it are in light grey. The space group of this structure is $P6_3/mmc$ whose 6_3 symmetry axis is displayed above the dashed line [FB]. (b) A typical snowflake exhibiting a symmetry 6 [<http://www.snowcrystals.com>].

The unit cell of ice is shown in Fig. 1.5a and also displays the symmetry 6 that can be observed on snowflakes such as the one shown on Fig. 1.5b. Moreover there is only one atom of hydrogen between two atoms of oxygen, but hydrogen atoms are disordered in the structure (no preferential orientation of the H_2O molecule). Only oxygen atoms are ordered.

The I_h hexagonal structure induces some peculiar features such as interesting optical properties. Indeed, ice is transparent for visible and ultraviolet light. The hexagonal symmetry also causes the ice to be birefringent [chap. 9, [Petrenko & Whitworth, 1999](#)]: depending of the propagation of the light with respect to the \mathbf{c} axis, the refractive index of ice is not the same.

Crossed polarizers are used to determine orientations of ice grains. The polarizer enables to align the electromagnetic field in one direction, while the analyzer lets only one wavelength pass for each grain. When polarizers are crossed, this means an extinction of the light without ice between them. When ice is inserted, one grain appears bright or dark depending on the orientation of the \mathbf{c} axis. For instance, if the light propagation is parallel to the \mathbf{c} axis, the grain appears black (extinct). To determine correctly the \mathbf{c} axis

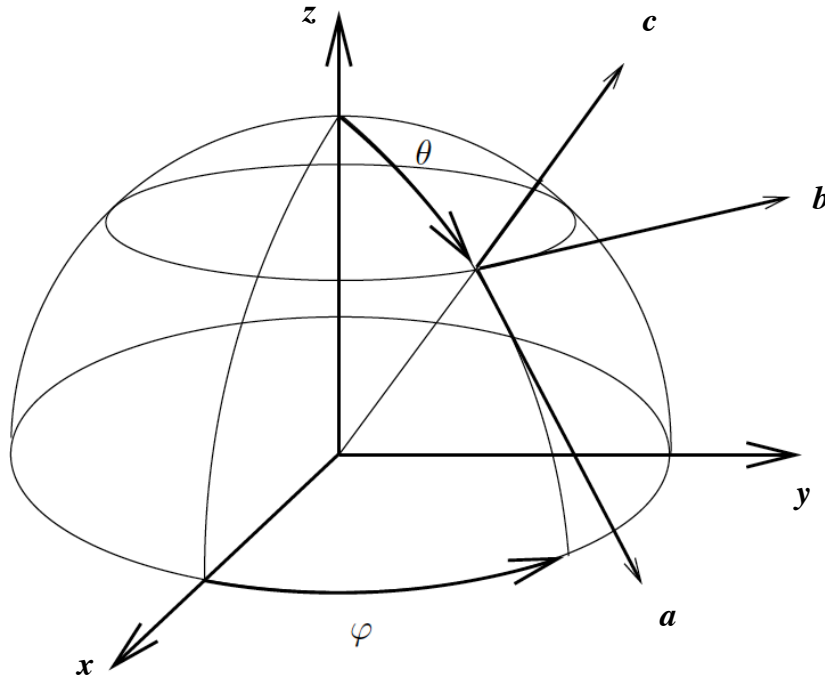


Figure 1.6: Reference frame of the crystal with respect to the laboratory frame. Adapted from [Meyssonier & Philip \[1996\]](#).

orientation, one should find the extinction positions of the grain.

In the case of polycrystalline ice, grains are not all oriented in the same direction. As the polarizer lets pass different wavelengths with the same polarization, grains exhibit different colors meaning different refractive indices.

The orientation of a crystal **c** axis can be determined from the hemisphere Fig. 1.6. The colatitude $\theta \in [0, \pi/2]$ and the longitude (or azimuth) $\varphi \in [0, 2\pi]$ are the angles describing the orientation in 3D, and are obtained thanks to a three-axis universal stage or to an automated texture analyzer. Note that the orientation of the **a** axes are not known with this technique. However, this is not detrimental for mechanical properties as these are transverse isotropic (detailed in section 1.2.1.4).

Finally, as for other crystalline materials, defects are numerous in ice. They can be punctual (vacancies, interstitials, solutes, ...), linear (dislocations), planar (grain boundaries, free surface, ...), and volumetric (pores, some rare inclusions such as brines in sea ice) [chap. 2, [Schulson et al., 2009](#)]. The pores will be extensively studied in this work but not as defects. The dislocation motion drives the crystalline plasticity and is developed in section 1.2.1.3.

1.2.1.2 Elasticity and brittle behavior

The ice single crystal exhibits a transversely isotropic elastic behavior (i.e. symmetric about the **c** axis which is normal to a plane of isotropy). It is difficult to determine elastic properties from mechanical tests, as creep⁹ inevitably contributes to the deformation leading to some underestimation of the stiffness. This is why [Gammon et al. \[1983\]](#) applied Brillouin spectroscopy on single crystals of ice to determine the tensor components of elastic stiffness -16°C, which was found to be anisotropic. [Fletcher \[1970\]](#) worked out the Young's modulus at the same temperature. It ranges from 8.42 GPa to 11.8 GPa when the **c** axis is oriented between $\theta = 50^\circ$ and $\theta = 0^\circ$ with respect to the tensile direction. It is equal to 9.71 GPa when $\theta = 90^\circ$. The anisotropy exists but may be considered moderate compared to plasticity (see section 1.2.1.3), as differences are within 30 %.

The ductile-brittle transition of monocrystalline ice occurs for strain rates above 10^{-3} s^{-1} under tension and compression. Tensile and compressive strength are also dependent of the **c** axis orientation. The lowest strength was found with a disorientation of 45° with respect to the loading direction. The tensile strength is 2.5 MPa and the compressive strength is 12 MPa for this orientation (at -10°C and under $7 \cdot 10^{-3} \text{ s}^{-1}$) [chap. 11, [Schulson et al., 2009](#)].

For firn, compiled data from [Shapiro et al. \[1997\]](#) show large differences of the Young's modulus depending on the experiments. Overall, the Young's modulus increases from 0.3 MPa at 0.55 g.cm^{-3} to 8 MPa at pure ice density. However, ice single crystals undergo plastic deformation when a shear stress as low as 0.02 MPa is imposed on the basal plane [chap. 5, [Schulson et al., 2009](#)]. The next section explains this plasticity.

1.2.1.3 Dislocation creep

Irreversible strain process can occur thanks to viscoplastic diffusion (motion of atoms) or by dislocation glide. However in laboratory conditions (for ice it corresponds to stresses of approximately 1 MPa, strain rates $> 10^{-7} \text{ s}^{-1}$ and typical temperature of -10°C), dislocation glide is the dominant mechanism for plasticity.

A dislocation line is a crystal defect. It consists of an extra half plane of atoms inserted in the crystal. This results in a distortion inside the crystal around the dislocation. Figure 1.7 illustrates the two types of dislocations that can exist. Points ABCD display a loop around the defect. When trying to close this loop, a final vector is needed to complete this circuit : it is named the Burgers vector **b**. Screw dislocations are lines parallel to **b**, while edge dislocations are lines perpendicular to **b**. In general, dislocations are a mix of these two types (see Fig. 1.7).

⁹ See section 1.2.1.3

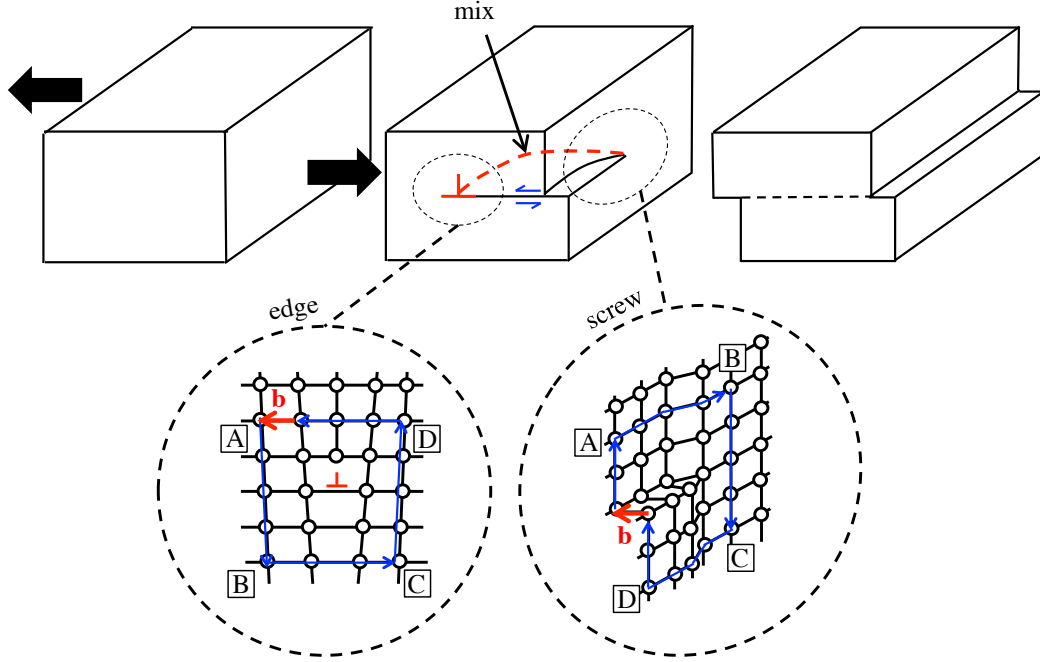


Figure 1.7: Edge and screw dislocations (red line), with associated Burgers circuit ABCD in blue. The glide of dislocation leads to a permanent step on the crystal face.

A slip plane along with a Burgers vector defines a glide system. A slip plane is usually a dense plane, as the dislocation motion should be facilitated. [Hondoh \[2000\]](#) proposed five glide planes of dislocations for ice which are shown in Fig. 1.8. Plasticity occurs mainly by dislocation glide in the (0001) plane and with $\mathbf{b} = (\mathbf{a}/3) < 11\bar{2}0 >$ as these are the least energetic lines. However, these can dissociate in two partials (Shockley) $\mathbf{p} = (\mathbf{a}/3) < 10\bar{1}0 >$.

Intersection of two dislocations can lead to the formation of a jog (or kink). The multiplication of dislocations occurs then by climb of basal dislocations thanks to punctual defects or jogs, but also by cross-slip of basal screw dislocations to prismatic slip plane. A double-cross slip mechanism was also proposed by [Chevy et al. \[2012\]](#) in the case of torsion experiments, and its use in a dislocation dynamic code reproduced well the experiment. Multiplication of dislocations can also come from Frank Read sources (observed in ice with X-ray topography [[Ahmad et al., 1992](#)]). In any case, the accumulation of dislocations reduces their mobility and usually leads to work hardening. However in the case of ice, work hardening is hardly observable [[Higashi et al., 1964](#)].

Ice is a viscoplastic material. Depending on temperature and applied stress, it will deform at different strain rates. Moreover, creep experiments on single crystals of ice revealed that deformation mainly occurs from gliding in the basal planes [[Nakaya, 1958](#)].

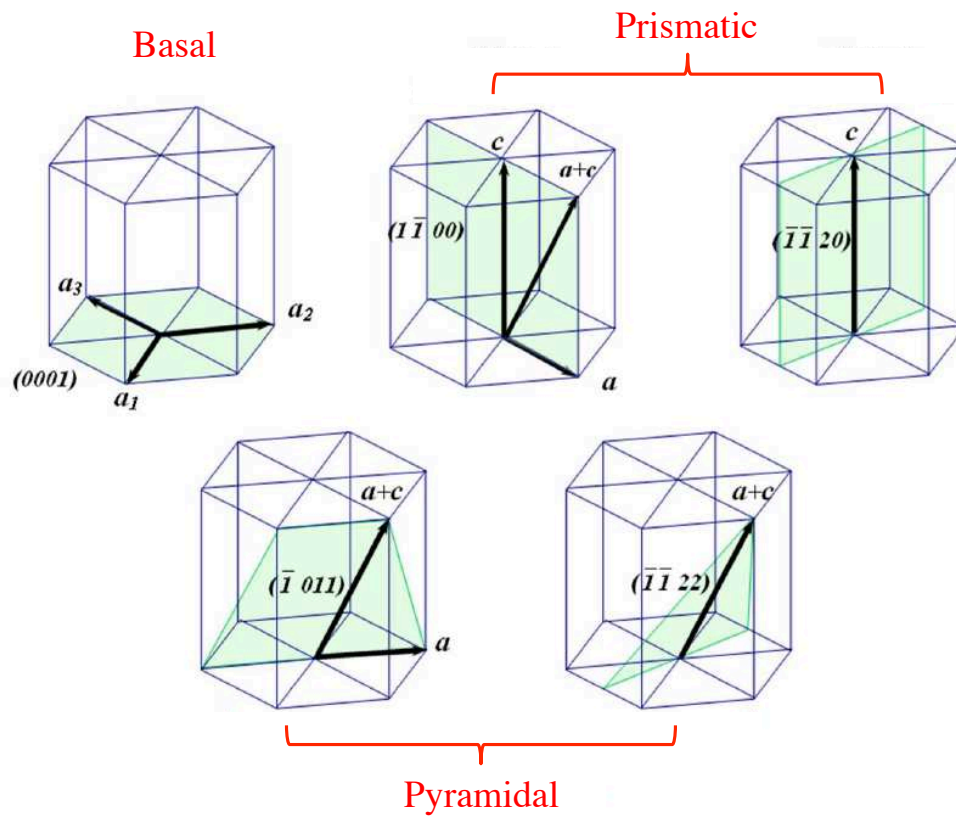


Figure 1.8: Possible slip planes in ice according to [Hondoh \[2000\]](#) with their associated Burgers vectors.

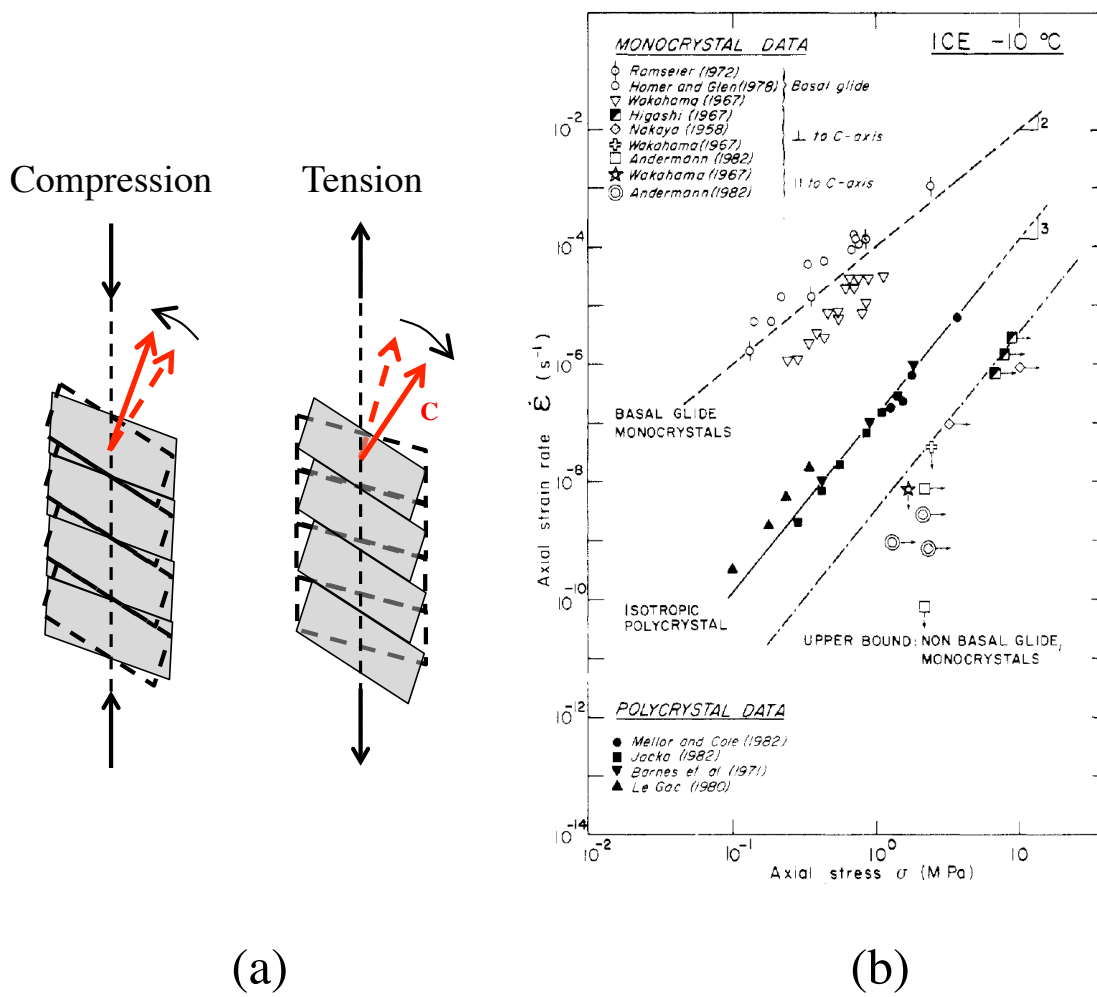


Figure 1.9: (a) Diagram of a tensile and compression test on ice. (b) Stress-strain rate relationship for monocrystalline and polycrystalline ice. All data for basal slip were obtained before steady-state [Duval et al., 1983].

This leads to strong anisotropy of the plastic deformation. Indeed, bending tests even showed that with the c axis parallel to the loading direction, basal slips still appears. Implications of this anisotropy is shown in Fig. 1.9a. Ice is like a pile of cards. When a compressive test is performed, the c axes tend to align with the loading direction, whereas a tensile test leads to an alignment perpendicular to the loading direction. Thus, during mechanical tests, rotation of the ice crystal occurs. Tensile creep tests of Jones & Glen [1969] revealed that steady state is never reached as the strain rate continuously increases. Duval et al. [1983] compiled data of creep tests on monocrystals and polycrystals of ice (Fig. 1.9b). The trends are striking. For the same strain rate, basal slip will occur for a stress 60 times smaller than non-basal glide. A slight misorientation of the c axis or a small perturbation will lead to basal slip.

Non-basal glide is very difficult to observe. The very recent work of [Chauve et al. \[2017b\]](#) offers new insights on that scope. They used EBSD to study torsion tests on polycrystalline ice and showed that 13 % to 35 % of the dislocations had a $\langle c \rangle$ component of the Burgers vector. Thus pyramidal or prismatic slip planes could be activated. Such dislocations were also noticed by X-ray topography when deforming single crystals of ice [[Philip et al., 2015](#); [Capolo, 2007](#)].

The flow law for viscoplasticity and especially for basal slip is classically written as:

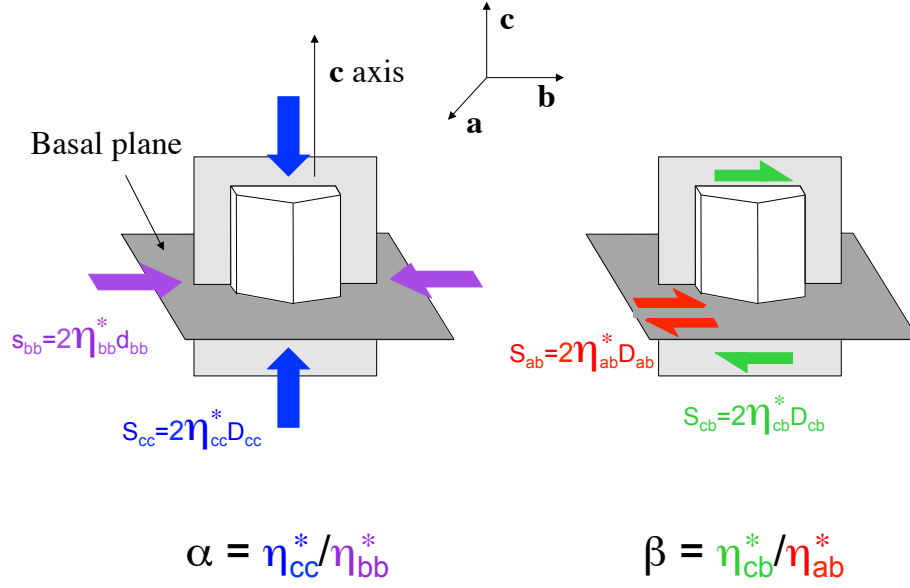
$$\dot{\epsilon} \propto \sigma^n \exp\left(\frac{-Q}{RT}\right) \quad (1.9)$$

with $\dot{\epsilon}$ the strain rate, σ the stress, Q the activation energy, T the temperature, R the ideal gas constant and n the stress exponent. From [chap. 5, [Schulson et al., 2009](#)], [chap. 8, [Petrenko & Whitworth, 1999](#)] and references therein, the stress exponent ranges from 1.5 to 2.5 for most authors, while the activation energy for basal glide should be close to 65 kJ.mol^{-1} . Note that authors proposed a stress exponent while it is unsure if the steady state was reached.

1.2.1.4 Viscoplastic law for a single crystal of ice

Two approaches are used in the literature to describe the viscoplastic behavior of a single crystal of ice. One can describe the single crystal by its different glide systems (not well known), thus linking the resolved shear stress and deviatoric stress with the Schmid factor in a self-consistent model [e.g., [Castelnau et al., 1997](#)]. An alternative is to use a continuous transversely isotropic law for the crystal [e.g., [Meyssonier & Philip, 1996](#)]. This is the approach used in this work. It assumes that the basal plane is isotropic, with easy shear parallel to it. This is in good agreement with [Kamb \[1961\]](#) who showed a zero deviation between the resolved shear direction and the gliding direction for a stress exponent of $n = 1$ or 3 for an hexagonal crystal. In the Newtonian case, the two approaches gave similar results [[Gillet-Chaulet, 2006](#)]. However in the non-linear case, the approach of [[Castelnau, 1996](#)] is not orthotropic. A non-linear formulation of the continuous law of the crystal is given by [Meyssonier & Philip \[1999\]](#), [Mansuy \[2001\]](#) and [Mansuy et al. \[2002\]](#). Its derivation for the linear case is given in chapter 2, and its application to a uniaxial stress state case and a shearing stress state case is given in appendix A.

In the local crystal frame $\mathcal{R}_i = (\mathbf{a}, \mathbf{b}, \mathbf{c})$ illustrated in Fig. 1.6, the transverse isotropic law for an incompressible medium with rotational symmetry axis along the \mathbf{c} direction,


 Figure 1.10: Illustration for the α and β parameters.

expresses the deviatoric stress tensor \mathbf{S} in terms of the strain rate tensor \mathbf{D} :

$$\begin{aligned}
 S_{aa} - S_{bb} &= 2\eta_{ab}^* (D_{aa} - D_{bb}) \\
 S_{cc} &= 2\eta_{ab}^* \left(\frac{4\alpha - 1}{3} \right) D_{cc} \\
 S_{bc} &= 2\eta_{ab}^* \beta D_{bc} \\
 S_{ca} &= 2\eta_{ab}^* \beta D_{ca} \\
 S_{ab} &= 2\eta_{ab}^* D_{ab}
 \end{aligned} \tag{1.10}$$

where η_{ab}^* is the apparent viscosity for shear in the basal plane (\mathbf{a}, \mathbf{b}). α is the ratio of the axial viscosity along the \mathbf{c} axis to the axial viscosity normal to the \mathbf{c} axis and β the ratio of the shear viscosity parallel to the basal plane over the shear viscosity in the basal plane η_{ab}^* . These parameters are illustrated in Fig. 1.10.

The apparent viscosity is written as :

$$\eta_{ab}^* = A_n^{-1/n} \dot{\gamma}_{\diamond}^{(1/n)-1} = A_n^{-1} \tau_{\diamond}^{1-n} \tag{1.11}$$

A_n is a temperature dependent fluidity parameter. τ_{\diamond}^2 and $\dot{\gamma}_{\diamond}^2$ are two invariants by rotation around the \mathbf{c} axis (but they are not invariant in an other reference frame). From Eq. (1.11), $\tau_{\diamond} = \eta_{ab}^* \dot{\gamma}_{\diamond}$ and $\dot{\gamma}_{\diamond} = A_n \tau_{\diamond}^n$. If ice is chosen isotropic, then $\alpha = \beta = 1$ and equations (1.10) reduces to the Glen's law equation (1.17) (described in section 1.2.2).

τ_{\diamond}^2 and $\dot{\gamma}_{\diamond}^2$ are defined by :

$$\begin{aligned}\tau_{\diamond}^2 &= \frac{3}{4\alpha - 1} \tau_{axial}^2 + \tau_{\perp}^2 + \frac{\tau_{\parallel}^2}{\beta} \\ \dot{\gamma}_{\diamond}^2 &= \frac{4\alpha - 1}{3} \dot{\gamma}_{axial}^2 + \dot{\gamma}_{\perp}^2 + \beta \dot{\gamma}_{\parallel}^2\end{aligned}\tag{1.12}$$

with :

$$\begin{aligned}\tau_{axial}^2 &= \frac{3}{4} S_{cc}^2 \\ \tau_{\perp}^2 &= \frac{(S_{aa} - S_{bb})^2}{4} + S_{ab}^2 \\ \tau_{\parallel}^2 &= S_{bc}^2 + S_{ca}^2 \\ \dot{\gamma}_{axial}^2 &= 3D_{cc}^2 \\ \dot{\gamma}_{\perp}^2 &= (D_{aa} - D_{bb})^2 + 4D_{ab}^2 \\ \dot{\gamma}_{\parallel}^2 &= 4(D_{bc}^2 + D_{ca}^2)\end{aligned}\tag{1.13}$$

This leads to :

$$\eta_{ab}^* = A_n^{-1} \left(\frac{9S_{cc}^2}{4(4\alpha - 1)} + \frac{(S_{aa} - S_{bb})^2}{4} + S_{ab}^2 + \frac{S_{bc}^2 + S_{ca}^2}{\beta} \right)^{\frac{1-n}{2}}\tag{1.14}$$

Inspection of this formulation shows that the stress exponent only appears in η_{ab}^* . This eases the simplification towards a Newtonian formulation that is proposed in chapter 2.

The use of a structural tensor \mathbf{M} linked to the crystal reference enables a formulation of the law that is independent of the reference system. \mathbf{M} is related to the \mathbf{c} axis by [Gagliardini, 1999] :

$$\mathbf{M} = \mathbf{c} \otimes \mathbf{c}\tag{1.15}$$

The deviatoric stress tensor can be written in the way of Mansuy et al. [2001] :

$$\mathbf{S} = 2\eta_{ab}^* \left[\mathbf{D} + \left(2(\alpha - \beta)\mathbf{M} - \frac{2}{3}(\alpha - 1)\mathbf{I} \right) tr(\mathbf{MD}) + (\beta - 1)(\mathbf{MD} + \mathbf{DM}) \right]\tag{1.16}$$

The two formulations (1.16) and (1.10) correspond to the same viscoplastic law.

1.2.2 Polycrystalline ice

In the case of an isotropic polycrystalline ice (isotropy of grain morphologies and orientations), creep can be separated in three stages [chap. 6, Schulson et al., 2009]:

- The primary/transient creep : after an immediate elastic strain, the strain rate de-

creases progressively as dislocations are accumulating near grain boundaries (leading to a hardening of the ice)

- The secondary creep : it is reached after 1 % of strain and exhibits a minimum creep rate around 2 %. The Norton-Hoff law which is named the Glen’s law in glaciology, describes the minimum creep rate as :

$$\mathbf{D} = \frac{1}{2} B_n(T) \tau^{n-1} \mathbf{S} \quad (1.17)$$

with \mathbf{D} the strain rate tensor, \mathbf{S} the deviatoric stress tensor and τ^2 the second invariant of \mathbf{S} . $B_n(T)$ is a fluidity dependent of an Arrhenius law, whose reference value $B_n(T_0)$ was found around $18.6 \text{ MPa}^{-3} \text{y}^{-1}$ in average for $n = 3$ at -10°C [Mansuy, 2001] and equal to $0.16 \pm 0.07 \text{ MPa}^{-1} \text{y}^{-1}$ for $n = 1$ at -10°C [Lipenkov et al., 1997]. Values for the stress exponents n for polar ice modeling is usually 3, as also observed on Fig. 1.9. But a value of $n = 1$ was proposed by Doake & Wolff [1985], and Pimienta & Duval [1987] obtained $n < 2$ for low stresses laboratory experiments and inclinometer survey on a bore hole. These low values are specific to ice. Indeed, results from Brown & Ashby [1980] for hexagonal metals lead to a stress exponent n between 4 and 6.1. For instance, magnesium yields a stress exponent of 5, while it exhibits strong similarities with ice. Significant strain heterogeneities arise when deforming polycrystals [Martin et al., 2014; Orozco-Caballero et al., 2017] and development of texture is also similar. It also deforms mainly by basal slip (at room temperature [Barnett, 2003]). However twinning frequently occurs in magnesium whereas this mechanism has never been observed in ice.

- The tertiary creep : the strain rate increases again and then stabilizes if fracture does not arise. Recrystallization typically occurs if enough strain is accumulated.

However the isotropic Glen’s law (Eq. (1.17)) is not suited for columnar ice for instance. The solidification of lakes from the surface induces elongated grains with \mathbf{c} axes in a plane perpendicular to the ice columns. It is also not adapted for firn and ice from polar caps that exhibit strong textures. The creep stages are similar but deformations are anisotropic. Thus, modeling such behavior is very challenging but necessary to simulate correctly the flow of polar ice. The use of a viscoplastic self-consistent model for anisotropic materials [Lebensohn & Tomé, 1993] proved to be suitable for simulating the development of ice texture [Castelnau, 1996]. However these mean-field approaches need homogenization assumptions and give average quantities. The use of full-field models such as FFT [Montagnat, 2001; Lebensohn et al., 2009] or the finite element method [Mansuy, 2001], enable to estimate the strain heterogeneities inside a polycrystal due to contact

between grains, but these are limited to a microscopic scale. Thus, [Gillet-Chaulet et al. \[2005\]](#) derived a general orthotropic linear flow law for ice, with the texture described by an oriented distribution function set into a micro-macroscopic model. This enables glacier and ice cap flow to be simulated at large scales.

1.2.3 Evolution of texture in ice cores

Because of the strong anisotropy of ice crystal, the progressive flow of firn and ice down to the bedrock involves an important evolution of the crystallographic texture. In fact, the fabric (texture + ice grain size and shape) is the witness of the ice behavior, i.e. of the evolving stress state of glaciers or ice caps across the ages.

Let us consider the reference frame shown in Fig. 1.6. The \mathbf{c} axis of a crystal is defined in the reference frame (global frame, $\mathcal{R}_g = (\mathbf{x}, \mathbf{y}, \mathbf{z})$) by :

$$\mathbf{c} = \begin{pmatrix} \sin(\theta) \cos(\varphi) \\ \sin(\theta) \sin(\varphi) \\ \cos(\theta) \end{pmatrix} \quad (1.18)$$

When analyzing thin sections with an Automatic Ice Texture Analyzer (AITA) for instance, the \mathbf{c} axes of a large number of pixels inside the grains are retrieved. The fabric can then be quantified with the help of the second order orientation tensor \mathbf{a} :

$$\mathbf{a} = \frac{1}{N_p} \sum_{i=1}^{N_p} \mathbf{c}^i \otimes \mathbf{c}^i \quad (1.19)$$

with N_p the number of pixels used by the analysis. This accounts for volume fraction of grains. This tensor can be diagonalized and eigenvalues and vectors give the degree of anisotropy of the texture. If a_i are the eigenvalues they verify :

$$0 \leq a_3 \leq a_2 \leq a_1 \leq 1 \quad (1.20)$$

and

$$a_1 + a_2 + a_3 = 1 \quad (1.21)$$

Their values can be a good indicator of a tendency for the fabric. For instance :

- $a_2 \approx a_3 < 1/3$ indicates a single-maximum fabric
- $a_1 \approx a_2 > 1/3$ indicates a girdle fabric
- $a_1 = a_2 = a_3 = 1/3$ indicates an isotropic fabric

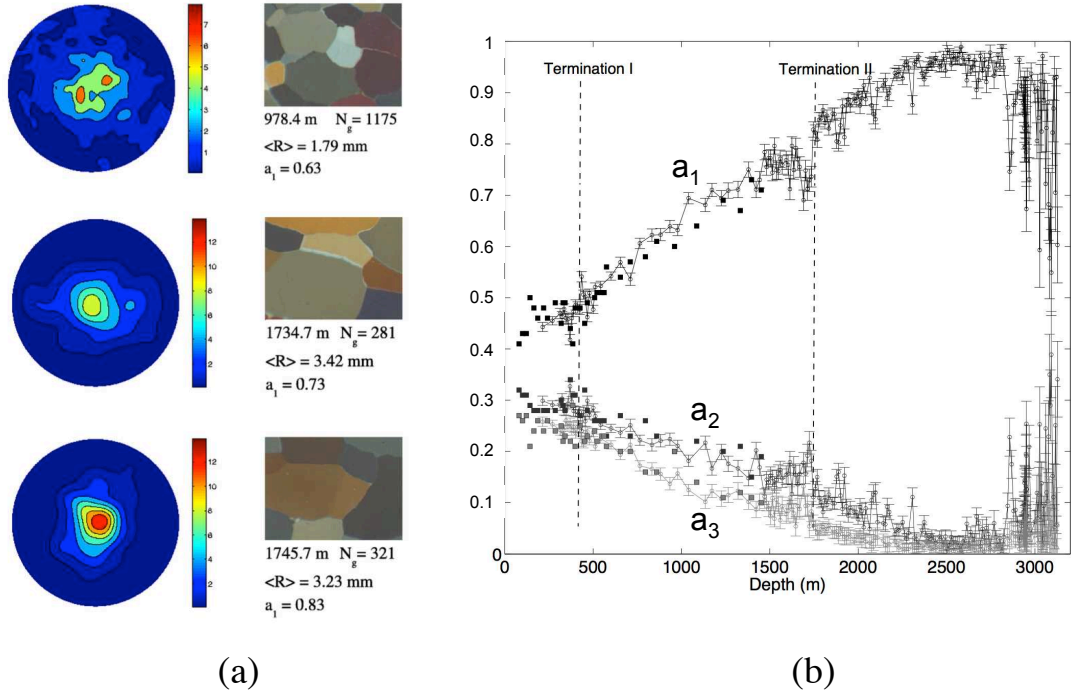


Figure 1.11: Fabric of Dome C from [Durand et al. \[2009\]](#). (a) Pole figure evolution with depth. The core axis is perpendicular to the view. (b) Evolution of eigenvalues for the ice core between 80 m and 3250 m.

Stereographic projections are usually performed on the \mathbf{c} axis, making Pole figures only on one crystallographic direction. Indeed, \mathbf{a} axes are not obtained with polarized light.

The fabric evolution of polar ice with depth has received much attention. For instance, [Durand et al. \[2009\]](#) continued the work of [Wang et al. \[2003\]](#) and [Durand et al. \[2007\]](#) at Dome C and proposed the full evolution of the fabric along the dome (see Fig. 1.11b). As expected, the \mathbf{c} axes tend to align to the loading direction since a dome is in uniaxial compression (single-maximum fabric). However, some features can appear, such as a strengthening of the fabric after around 1750 m that [Durand et al. \[2007\]](#) explained by an horizontal shear at this depth, and a decrease of the shear viscosity. Such a local strengthening was also observed in the NEEM ice core (Greenland) by [Montagnat et al. \[2014\]](#) who also associated it to a climatic transition, and a reduced shear viscosity. Fabric analyses were performed on various polar sites such as Summit (Greenland) [[Thorsteinsson et al., 1997](#)], which also exhibited a single-maximum fabric, or at the Vostok station (Antarctica), which displayed a girdle fabric, thus characterising an ice under uniaxial tension.

Texture was proved to already exist in shallow depths of the firn column. [Diprinzio](#)

et al. [2005] observed that **c** axes aligned to the vertical direction at only 22 m deep at Siple Dome (Antarctica). Montagnat et al. [2012, 2014] showed from Talos Dome (A) and NEEM (G) ice cores that fabric was not isotropic below 18 and 33 m, respectively (which were the shallowest analyzed samples). Results from Durand et al. [2009] also illustrated a single maximum fabric at Dome C but only below 80 m (already deep firn). According to Montagnat et al. [2012], the relation between the densification mechanisms and the resulting early apparition of the fabric is not completely understood. In any case, the fabric being not isotropic, the densification of firn should be affected, as the dominant mechanism at high density is dislocation creep. However, to date, models of firn densification do not take into account the ice anisotropy.

1.2.4 Recrystallization

Recrystallization is a thermally activated process that occurs in crystalline materials when they are subjected to stress. The recrystallization can be static, when it happens after a mechanical test, in the case of an annealing for instance. But it can also be dynamic as in the case of polar ice, because it occurs during deformation. In such conditions, rotation recrystallization is characterized by division in subgrains because of local stresses inducing local misorientations (intragranular polygonization) and is supposed to be responsible of the stop in grain growth of polar ice [Alley, 1992]. Thorsteinsson et al. [1997] showed polygonization occurred below 700 m deep at Summit. Moreover, accumulation of dislocations at grain boundaries for instance, leads to high stored energy, thus to strain-induced recrystallization. To reduce the stored energy, grain boundaries are migrating to free-dislocation grains or nuclei. In that case, a new grain appears and its orientation can be linked to the parent grain (influencing the texture strength). Thorsteinsson et al. [1997] attributed this rapid grain growth in the deep part of the ice core to this process.

In the NorthGRIP core, Durand et al. [2008] observed rotation recrystallization in the upper part (from 115 m deep). Fractionation of grains occurred but was not as pronounced as the grain growth rate, thus leading to a net increasing mean grain size. Subgrains were also found at very shallow depths (50 m) in the firn [Spaulding et al., 2011] in East Antarctica ice cores. High resolution images enabled Kipfstuhl et al. [2009] to observe all types of dynamic recrystallization, especially for firn with $\rho > 0.73 \text{ g.cm}^{-3}$. These authors concluded that the stored strain energy was not negligible compared to grain boundary energy as commonly believed, and that the important number of new grains counteracted normal grain growth.

The effects of recrystallization on ice flow seem clear even in firn. However, this process is not taken into account in ice sheet modeling or firn densification. In fact, implementing it or estimating its impact on the results is challenging. A more complete

review on recrystallization processes as well as their implications on texture development in laboratory conditions can be found in [Chauve \[2017b\]](#).

1.3 Literature review on firn densification

1.3.1 Densification mechanisms

The mechanisms of densification from snow to ice vary with depth as illustrated by Fig. 1.2. In the firn, at large enough density, plastic flow governs the densification and is the dominant mechanism of the sintering between two particles [[Maeno & Ebinuma, 1983](#)]. Sintering is a thermally activated mechanism, which consists in the growth of a neck between two particles to form a coherent structure. Its driving force is the reduction in the surface free energy of a porous material via mass transport at the atomic scale. Figure 1.12a clarifies the various solid state sintering mechanisms that allow the neck to grow independently of the material (these processes can occur for metals, ceramics or ice particles for instance). Transporting mass from different sources to concave regions, i.e. regions between the two particles, carries out the reduction of surface energy. The different mechanisms do not all involve a gain of density for the material. Indeed, sublimation-deposition (vapor transport) and surface diffusion do not lead to densification. To that end, sintering should occur by volume diffusion from grain boundaries, surfaces or volume through lattices (Nabarro-Herring creep), by diffusion along grain boundaries (Coble creep) or by plastic flow. Depending on the temperature, the grain size, the material and the presence of an applied external stress, mechanisms and therefore activation energies differ.

The high vapor pressure of ice leads to sintering dominated by vapor transport followed by surface diffusion for dry snow without external pressure [[Maeno & Ebinuma, 1983](#)]. Various mechanisms are concurrent. As shown by [Hobbs & Radke \[1967\]](#), volume diffusion should not be excluded for metamorphism of dry snow even if its contribution to neck growth was measured to be one order of magnitude less than evaporation-condensation. Still, modeling evaporation-condensation proved to be appropriate to simulate dry snow metamorphism [[Flin et al., 2003, 2004](#)]. Liquid sintering is also possible for freshly fallen snow depending on the climatic conditions. A full review of ice sintering mechanisms, experiments and modeling is available from [Blackford \[2007\]](#) who provided the solid-state sintering illustration on Fig. 1.12b. In practice, sintering of snow and firn is not only driven by the surface energy minimization but also by an external load, i.e. the weight of the above layers. The following sections concentrate on mechanisms of densification in the case of pressure sintering for firn.

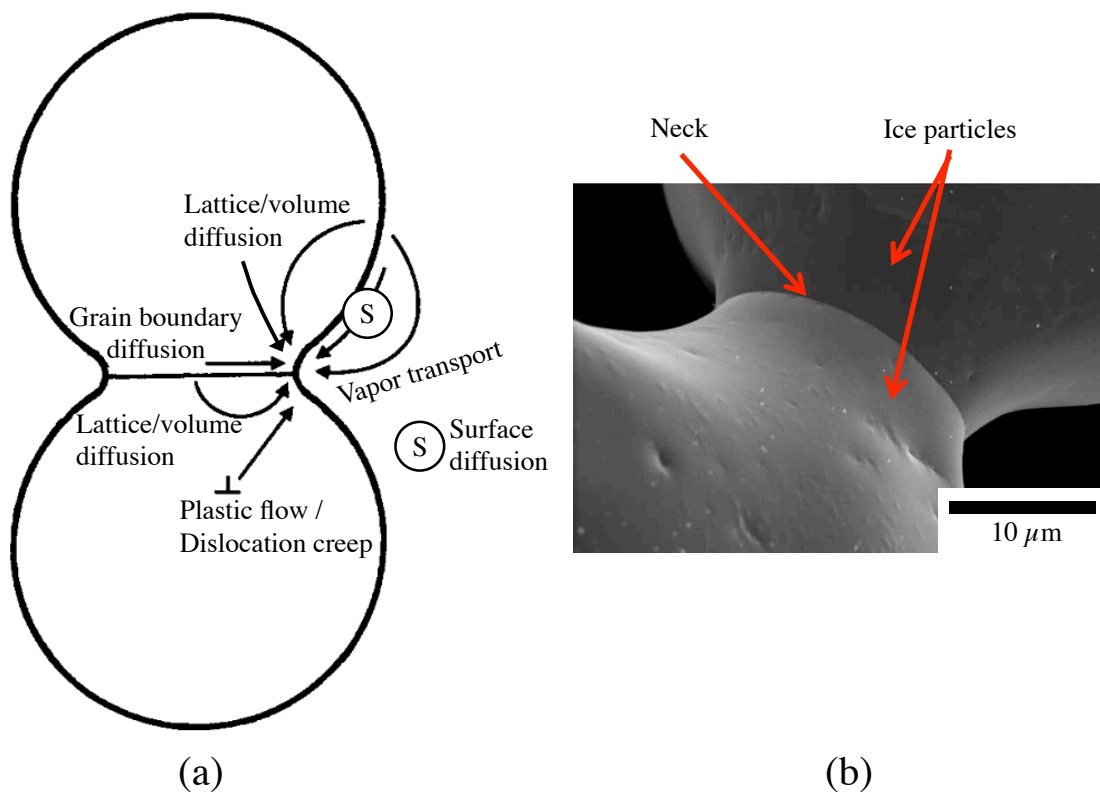


Figure 1.12: (a) Diagram of solid-state sintering mechanism between two particles. (b) From [Blackford \[2007\]](#) : low temperature SEM image of two ice particles after sintering at -25°C for 216 hours. Particles were obtained by spraying water into liquid nitrogen.

1.3.2 Current models of densification

The densification of polar firn is dependent on many parameters such as the temperature gradient, the site temperature, the accumulation rate and also the stress state. It induces various microstructural mechanisms such as sintering, grain growth, recrystallization and dislocation creep.

Herron & Langway [1980] used a simple empirical model of densification in which the density ρ and the densification rate $\frac{d\rho}{dt} = \dot{\rho}$ were proportional. The model was fitted on data assuming that only the accumulation rate, the temperature and the initial density played a role in the process. Despite these simplifying assumptions it could predict rather well (within five years) the age of the firn with depth for five different ice cores. Focusing on the compaction of spherical particles in the case of powder metallurgy, Arzt [1982] proposed a law for a densification rate caused by power-law creep under hot isostatic pressing. These authors emphasized the importance of the coordination number when compacting particles. Wilkinson & Ashby [1975] also worked on pressure sintering by power-law creep but looked at the contribution of cylindrical and then spherical holes (final stage of the densification) to the densification rate. A semi-empirical approach for firn densification was performed by Barnola et al. [1991], which related the densification rate with an effective pressure and a function derived from Wilkinson & Ashby [1975] to account for the compression of pores. It led to similar results to the Herron & Langway [1980] model, and improved the simulated density profile for high accumulation rates sites. Both models are also successful in calculating a Δage or the CO_2 evolution but their parameters are strongly tuned for the model to work. Finally, Alley [1987] described successfully the densification of firn by grain boundary sliding, however this is true only for coordination numbers below 6, and can not represent the mechanisms above 0.55 g.cm^{-3} .

Using initially only the geometrical model of Arzt [1982] and then carrying on with the models of Alley [1987] and Wilkinson & Ashby [1975], [Arnaud et al., 1998] and Arnaud et al. [2000] proposed the basis for a complete densification model for firn that is dedicated to paleoclimatic studies. Despite a few changes, the densification process is still separated in three parts in the model. This model is used by scientists from the IGE and is thus described in the following :

1. **First stage** $\rho_r < 0.6$ ($\approx 0.55 \text{ g.cm}^{-3}$)¹⁰ : The first part of the firn column being ruled by grain rearrangement, the model of densification for grain boundary sliding from Alley [1987] is used.
2. **Second stage** $0.6 < \rho_r < 0.9$ ($0.55 \text{ g.cm}^{-3} < \rho < 0.83 \text{ g.cm}^{-3}$) : Densification of the firn is ruled by power-law creep, thus the work of Arzt [1982] is used with the

¹⁰ ρ_r is the relative density defined by $\rho = \rho_r \rho_{ice}$

addition of an Arrhenius term to take into account temperature. The relative rate of densification writes :

$$\frac{d\rho_r}{dt} = A_0 \exp\left(\frac{-Q}{RT}\right) k(\rho_r, \rho_0, a) P_{eff}^n \quad (1.22)$$

With A_0 a fitted constant, Q the activation energy of the mechanism (usually 60 kJ.mol^{-1} for power-law creep [Pimienta & Duval, 1987]), $R = 8.314 \text{ J.mol}^{-1}.\text{K}^{-1}$ and T the temperature in Kelvin. k is a function of the relative density ρ_r , the initial density ρ_0 (from the surface) and the average contact area a between particles. P_{eff} is an effective pressure applied on a . For this depth range, it is a function of the "overburden" pressure of ice and atmosphere minus the pressure inside the closed pores. In the firn core, it corresponds to the weight of the firn at a particular depth as there is few enclosed pores. This stress is only function of the density ρ , the gravity g and the height of the overlaying firn z :

$$\sigma_{zz} = P_{eff} = \int \rho(z) g dz \quad (1.23)$$

The stress exponent n is usually chosen to 3 for this part of the densification as $\sigma_{zz} > 0.1 \text{ MPa}$ on bonds between ice particles [Barnola et al., 1991; Arnaud et al., 2000]. The evolution of this stress as well as the density for the polar site Dome C is shown in Fig. 1.13.

3. **Final stage** $\rho_r > 0.9$ ($\approx 0.83 \text{ g.cm}^{-3}$) : It mainly consists of the size reduction of bubbles (or spherical pores) because the equivalent stress in ice is larger than internal pressure of pores. The work of Wilkinson & Ashby [1975] is used as it is appropriate for spherical pores such as in deep firn. The formulation also relates the densification rate to the effective pressure (on the contact particle area), which is supposed to decrease with depth as the internal pressure of bubble increases.

Some additional physics to this model were implemented. Indeed, temperature dependence of these different mechanisms is essential. Thus, Goujon et al. [2003] proposed a coupling between heat diffusion and mechanical densification. To consider heat transported by vertical advection, the vertical velocity of the firn is also calculated in one dimension. Finally, a gas-age module was implemented to estimate the gas trapping depth and Δage gas-ice. Note that the accumulation rate is not explicitly used in the model, and is supposed to be part of the effective pressure.

Recent adjustments of this model were proposed by Bréant et al. [2017] to model continuously the snow-firn transition. These authors also tuned the sensitivity of the

model with temperature by varying the activation energy (meaning different underlying sintering mechanisms), but foremost in applying the parameterization of Freitag et al. [2013b] to account for impurity effects.

Other densification models are noteworthy to cite but are not detailed here. For instance Zwally & Jun [2002] and Li & Zwally [2011] coupled the Herron & Langway [1980] model with grain growth and vertical velocity. They used activation energies that can vary without discussing the underlying changes of densification mechanisms. Arthern et al. [2010] and Cummings et al. [2013] also proposed alternative models.

None of these models consider the effect of anisotropy of the ice crystal (see section 1.2.1.4), while ice cores revealed a texture development during densification and further ice burying (see section 1.2.3). Such texture and anisotropy of the ice crystal should have an effect on the densification.

The densification profile of the polar site Dome C (Antarctica) is given in Fig. 1.13. The polar site Dome C is extensively studied in this work and is presented in chapter 3. Figure 1.13 is accompanied by the corresponding ice age and stress evolution due to the weight of firn (without the contribution of the atmosphere pressure) for the first hundred meters. The density data come from Bréant et al. [2017], and the age evolution from Veres et al. [2013] and Bazin et al. [2013], while the vertical component of the stress is calculated with Eq. (1.23).

1.3.3 Stratification of firn and impurities effect

On several polar sites, usually those with high accumulation rates and large seasonal variability, the density evolution is not monotonic and shows winter and summer layers, depicted by the appearance of local minima and maxima for the density with depth (NorthGRIP, Greenland for instance) [Landais et al., 2006]. Densification models do not take into account such layering, while they seem important as air can be sealed off before close-off. On low accumulation sites with very low mean annual temperature, such layering is barely visible (at Dome C for instance), although Fourteau et al. [2017] observed evidences of gas trapping layering at the centimeter scale for such sites. Hörhold et al. [2012] showed that soluble impurities such as Ca^{2+} decrease the firn viscosity and were distinctly correlated to layering. This led Freitag et al. [2013b] to model stratification of polar firn including this impurities by adjusting the model of Herron & Langway [1980]. Similarly, accounting for impurities in ice through an activation energy, led to a reduction of the $\delta^{15}\text{N}$ model–data mismatch over the last deglaciation at the coldest sites in East Antarctica [Bréant et al., 2017] .

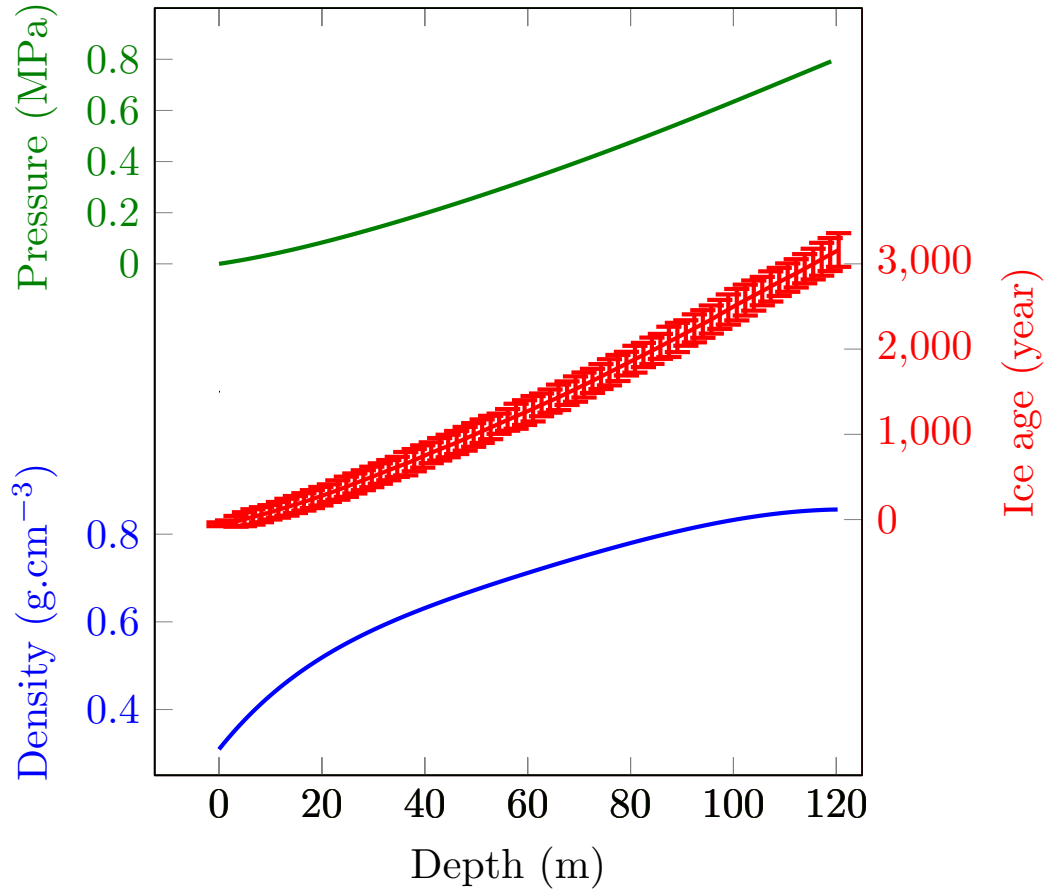


Figure 1.13: Evolution of density [Bréant et al., 2017], age [Veres et al., 2013; Bazin et al., 2013] and hydrostatic pressure (Eq. (1.23)) with depth at Dome C.

A few definition :

- **Summer layers** : usually described as low density layers because of high accumulation [Landais et al., 2006]. They often exhibit large (or coarse) grain size [Hörhold, 2010] because of temperature increase in summer. These layers are thicker than the winter layers.
- **Winter layers** : usually described as high density layers formed by low accumulation in winter. They are thinner than summer layers and exhibit fine grain size. The porous network is more tortuous than coarse grain size layers [Gregory et al., 2014]. At a given depth, they are also more homogeneous laterally than summer layers [Lomonaco et al., 2011]. The fine grain size layers usually seal at shallower depths than coarse grain size layers.
- **Crossover** : From the two definitions above, a winter layer should seal first. However it could happen that a crossover occurs when initially higher-density layers consisting of fine-grained firn are less dense than corresponding initially lower-density layers consisting of coarse-grained firn [Hörhold et al., 2011]. Such phenomenon was observed on the firn core B25 from Berkner Island [Gerland et al., 1999] or B26 from Greenland [Freitag et al., 2004] for instance.

Soluble impurities were also found to reduce the rate of grain growth [Alley & Woods, 1996]. Results with X-ray tomography on deep ice suggested that insoluble impurities such as dust particles (about 1 μm in diameter) are located on 2D structures or planes (therefore in grain boundaries) and act against grain growth [Durand et al., 2006b].

1.3.4 Pressure-sintering diagrams

Interestingly, Maeno & Ebinuma [1983] and Wilkinson [1988] used a pressure sintering model to plot pressure-sintering mechanisms maps, very similar to Ashby maps but showing the effect of relative density. The interested readers can refer to the maps presented by Duval et al. [1983] or Frost & Ashby [1982] for ice and different grain size ranging from 0.1 mm to 10 mm. However, these maps do not represent the mechanisms in the firn. Figure 1.14 depicts pressure sintering maps from equations (17) to (24) proposed by Maeno & Ebinuma [1983] in the case of firn at -55°C and at -10°C which correspond to the temperature of Dome C and to the temperature used to perform mechanical tests in this work, respectively. To compute these diagrams, the same parameters from Maeno & Ebinuma [1983] are utilized except for the creep stress which is approximated to 3. A few parameters from Maeno & Ebinuma [1983] are defined only down to -45°C but are used regardless.

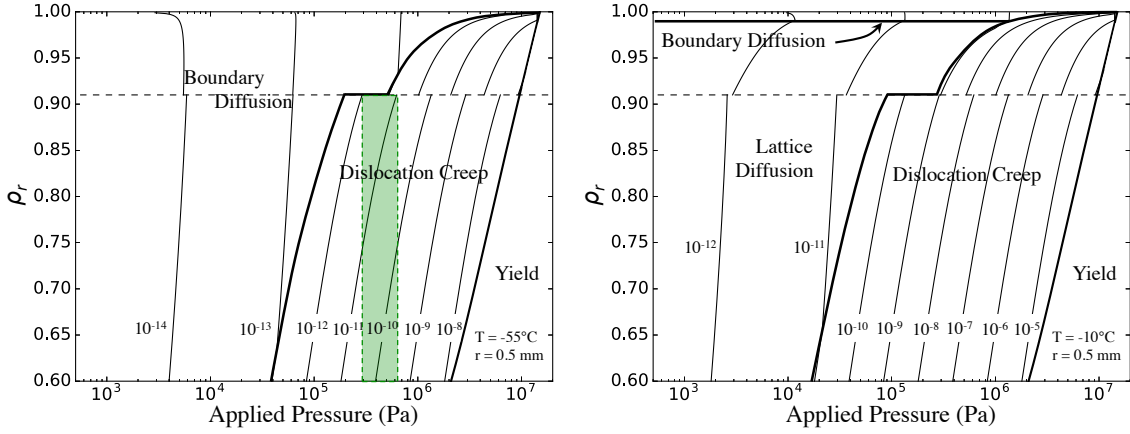


Figure 1.14: Pressure-sintering maps following equations from [Maeno & Ebinuma \[1983\]](#), for (a) $T = -55^\circ\text{C}$ (mean annual temperature of the polar site Dome C), and (b) at $T = -10^\circ\text{C}$. The grain radius used is $r = 0.5$ mm. Strain rates $\dot{\epsilon}_{zz} = -\frac{\dot{\rho}}{\rho}$ are annotated in powers of 10 and are in s $^{-1}$. Bold black lines represent the frontiers between the dominant mechanisms, and the dashed line separates two stages of the densification at $\rho_r = 0.91$ corresponding to the close-off density chosen by [Maeno & Ebinuma \[1983\]](#) ($\rho = 0.834$ g.cm $^{-3}$). Changing this density does not affect the overall results. The "Yield" region corresponds to firn breakage. The green shaded rectangle on (a) is the range of σ_{zz} values for firn with $0.6 < \rho_r < 0.91$ (see Fig. 1.13).

Figure 1.14a displays that the dominant mechanisms are dislocation creep and grain boundary diffusion, while for a warmer temperature (such as in cold rooms) boundary diffusion is replaced by lattice diffusion (Fig. 1.14b). Although multiple mechanisms are concurrently occurring, the diagrams show the regions where one dominates the others. Calculating densification rates from Fig. 1.13 at Dome C, one can note that the strain rate $\dot{\epsilon}_{zz} = -\frac{\dot{\rho}}{\rho}$ ranges from 10^{-13} to 10^{-11} s $^{-1}$, meaning a creep ruled by dislocation glide and by grain boundary diffusion. The green shaded area on Fig. 1.14 represents the component σ_{zz} of the stress from Fig. 1.13 for this range of density at Dome C, and exhibits larger strain rates than obtained by the density curve. Note that increasing the grain size, as it happens in polar ice, broadens only the region of the dislocation creep without changing the strain rate curves positioning. It is also worth mentioning that for the last stage of densification ($\rho_r > 0.91$), [Maeno & Ebinuma \[1983\]](#) predicts that grain boundary and lattice diffusion should play a more significant role.

In conclusions these maps give correctly the dominant mechanisms but they only propose a rough estimation of the densification rate with the applied stress (σ_{zz} equal here to the effective pressure). Indeed, these pressure-sintering diagrams are calculated using spheres to model ice grains, which is an important approximation. Moreover, depending of the stress exponent chosen, the results are completely different. [Pimienta & Duval](#)

[1987] and Arnaud et al. [2000] used $n = 1$ when the effective pressure was below 0.3 MPa which in terms of applied stress, is true above ≈ 60 m at Dome C (i.e. when $\rho_r < 0.79$). Maeno & Ebinuma [1983] used $n = 3.08$ at low temperature and $n = 3.16$ above -8°C which divides the stress by two on the diagrams. Finally, as for the densification model, these diagrams completely neglect the effects of the anisotropic viscoplasticity of the ice crystal described in section 1.2.1.3.

1.4 Outcomes and outlines

Firn is a porous material made of ice and air. Ice was shown to be a very anisotropic material because of its hexagonal crystallographic structure. For the considered temperature and strain rate ranges ($\approx 10^{-12} \text{ s}^{-1}$ at -55°C for the polar site Dome C, and 10^{-6} - 10^{-5} s^{-1} at -10°C for usual laboratory experiments), dislocation creep is supposed to be the dominant deformation mechanism, which occurs mainly on basal slip plane.

Air content in polar firn is of primary interest to reconstruct correctly the past climate and predict the future one. However its capture in the firn is still under discussion, whether it be from the microstructure evolution or from the underlying physical process points of view. Also, the current densification models completely neglect the anisotropy of ice viscoplasticity, and the transport model of air in the firn does not take into account the microstructure of ice skeleton.

In this work we propose an original approach to model in three dimensions the densification and which accounts for the anisotropy of ice as well as the microstructure of firn. The firn is a granular material that consists of grains of ice. Therefore, the Discrete Element Method (DEM) is used in this work to simulate the compaction of firn at the grain scale, in contrast with phenomenological models presented in section 1.3.2. This method uses spherical particles to represent each grain of ice, and work out the behavior of the packing of particles from the interactions between only two grains. This work concentrates on feeding the DEM code with experimental results. The Fig. 1.15 is a diagram of the organization of this manuscript. The different chapters are linked together as they produce results to be compared or used as input for a new chapter. Chapter 2 couples laboratory experiments on the creep of single crystals of ice with a simplified model of contact between those crystals. Chapters 3-4 move to the multiple contact situation by studying with X-ray micro-computed tomography the firn densification **ex situ** with samples from polar sites, and **in situ** with laboratory experiments on polar firn. These chapters focus on the microstructure evolution with special attention for the texture anisotropy and air entrapment from comparison of two polar sites (Dome C and Lock In, Antarctica), and from mechanical tests. An anisotropic contact law for viscoplastic monocrystalline ice

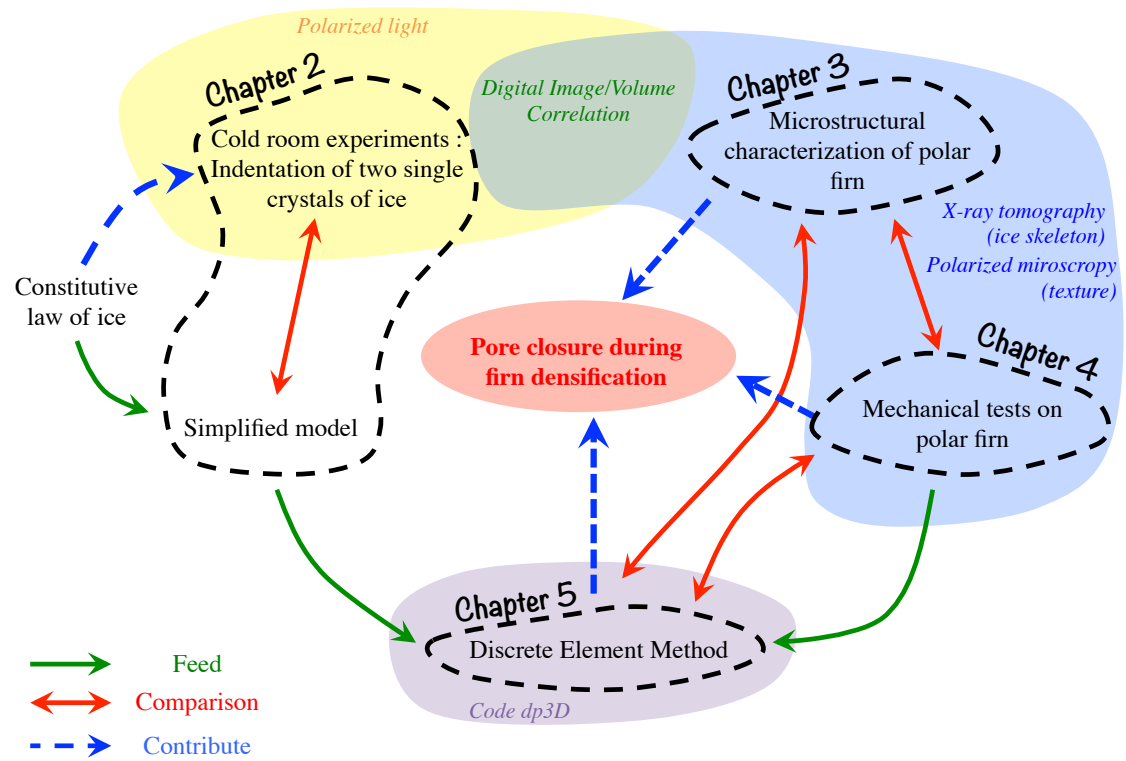


Figure 1.15: Organization of the manuscript along with chapters associated tools.

particles is derived in chapter 2 and implemented in the DEM code, which chapter 5 details. Results from the DEM are compared as feedback of experiments carried out in chapters 3-4. Some specific literature is proposed at the beginning of each chapter.

Chapter 2

Modeling of the contact between ice grains

This chapter is based on the following publication [Burr et al., 2017] : Burr, A., Noël, W., Trecourt, P., Bourcier, M., Gillet-Chaulet, F., Philip, A. and Martin, C. L. (2017). The anisotropic contact response of viscoplastic monocrystalline ice particles. *Acta Materialia*.

Contents

2.1	Introduction	39
2.2	Contact model	40
2.3	Methods	45
2.3.1	Single crystal machining and set up	45
2.3.2	The Digital Image Correlation on ice	47
2.4	Experimental indentation of ice cylinders	54
2.4.1	Diametrical loading on a single cylinder	54
2.4.2	Diametrical loading on two cylinders	59
2.4.3	Neck size effect	60
2.5	Comparison between 2D FEM simulations and experiments	62
2.6	Concluding remarks	65

2.1 Introduction

It has been suggested that dislocation creep is the main deformation mechanism responsible for the densification of firn at low strain rates ($<10^{-5} \text{ s}^{-1}$) [Salm, 1982; Ebinuma & Maeno, 1985]. It is taken into account in densification models of firn for which density is in the range $0.55\text{--}0.84 \text{ gcm}^{-3}$ (relative density in the range $0.60\text{--}0.92$, $\rho_{ice} = 0.917 \text{ gcm}^{-3}$) [Arzt, 1982; Arnaud et al., 1998]. However, some other mechanisms have been also proposed for firn densification. These mechanisms are grain rearrangement, grain-boundary sliding, sublimation, recrystallization, volume and surface diffusion [Herron & Langway, 1980; Alley, 1987; Theile et al., 2011].

The relative importance of these mechanisms is still an open question and depends on the densification stage considered. A common feature of these proposed mechanisms is that they do not take into account the anisotropic viscoplastic behavior of an ice crystal. However, Rolland Du Roscoat et al. [2011], using Diffraction Contrast Tomography on in-situ compression experiments, have demonstrated its importance on the intragranular deformation of large-grained samples during densification of snow. The hexagonal structure of ice induces dislocation slip mainly on basal planes. This leads to a strong viscoplastic anisotropy: for a given applied stress, a crystal of ice deforms approximately 10^3 times faster in the basal plane than in any other planes [Duval et al., 1983; Petrenko & Whitworth, 1999].

Additionally, in the low range of density, the granular nature of snow was recognized very early on by analytical models that represented snow as a collection of grains bonded by solid necks [Brown, 1980]. More recently, Theile et al. [2011] coupled tomography with Finite Element Modeling, meshing each grain of ice by a beam element. Ice anisotropy was taken into account by the use of orientation-dependent material parameters in the flow law. The use of beams was justified by the density range (0.20 to 0.35 gcm^{-3}) studied by the authors, which qualifies the material as low-density snow. In this range of densities, the Discrete Element Method (DEM) is also a tool of choice since it allows the discrete nature of snow to be accounted for. Hagenmuller et al. [2015], also proposed to couple tomography reconstructed volumes of snow with simulations. Representing ice particles as rigid clumps of spheres, they showed that the actual relative density mainly controls the compression behavior of snow. Snow densification may also be tackled using homogenization techniques as in Wautier et al. [2017], where again X-ray tomography images were used as initial microstructures.

At the other extreme of density, for deep dense ice core, the coupling between anisotropy (fabrics) and the state of stress, and their strong impact on ice flow has received much attention (see for example Durand et al. [2007]; Martín et al. [2009]; Montagnat et al.

[2011]). In particular, the effect of dynamic recrystallization that accommodates deformation is well documented [Montagnat & Duval, 2000].

In between these two extremes, in the intermediate range of relative density (0.60-0.90), the effect of ice anisotropy on the densification of firn has received much less attention. In that density range, firn may be considered as a material that consists of crystallites of ice in contact with each other. Firn bears some important granular characteristics such as grain rearrangement, grain rotation and macroscopic densification under compressive stresses. It may be advantageously modeled as a set of discrete grains that interact with each other through their contacts. The modeling of such granular packing requires a good understanding of the contact forces that arise upon densification. However, a reliable contact law is still in need to account for the mutual indentation of ice particles. The main ingredients of such a contact law should incorporate viscoplasticity, ice anisotropy, and size effects. Ideally, the contact law should be simple enough to allow for its implementation into an analytical model or a DEM code. Thus, the improvement of current models for firn densification requires the contact mechanics between two grains of ice to be considered in more details, with special attention to anisotropy.

The aim of this chapter is to provide a firm experimental basis for the derivation of a simple contact model for ice particles. The sections in this chapter are organized as follows. In section 2.2, we present a contact model based on indentation theory that incorporates explicitly the viscoplastic anisotropy of an ice crystal. Section 2.3 develops the methods used in this chapter, which are the manufacturing of monocrystalline ice cylinders and the use of the Digital Image Correlation. In section 2.4, the diametrical loading of one or two monocrystalline ice cylinders provides the necessary data to understand the phenomenology of ice particle indentation with particular consideration for anisotropy. This section also presents a partial validation of the model proposed in section 2.2. Section 2.5 uses a 2D FEM simulation in which a transverse isotropic law is used to finalize the validation of the analytical model.

2.2 Contact model

In this chapter, we report on experiments focusing on the indentation of monocrystalline ice cylinders and in particular on their anisotropic response. The \mathbf{c} axis, which defines the cristallographic orientation of an ice crystallite, is perpendicular to the basal plane of the ice hexagonal structure. The elastic behavior of ice is itself anisotropic. The effective Young's modulus varies when it is evaluated about axes that are rotated away from the \mathbf{c} axis direction. Still, the maximum value (along the \mathbf{c} axis) is only 30% larger than the minimum [Fletcher, 1970]. At the rather high temperatures considered here, elasticity

may be neglected. Indeed, ice monocrystals undergo plastic deformation when a shear stress as low as 0.02 MPa is imposed on the basal plane [Schulson et al., 2009; Chevy et al., 2012]. Easy basal slip can occur in the three potential glide directions on the basal plane. Thus the analysis of experimental results uses a constitutive equation that accounts only for the viscoplastic anisotropy of ice crystals [Meyssonier & Philip, 1996] by modeling ice as a transversely isotropic medium. It has been shown that this simple model captures the essential features of deforming ice single crystals [Mansuy et al., 2002]. Further simplification is achieved in this model by assuming a Newtonian behavior for the ice crystallite. The literature indicates power-law exponents less than 2.5 for single crystals [Duval et al., 1983; Petrenko & Whitworth, 1999; Chevy et al., 2012; Higashi et al., 1964].

Let us consider the reference frame of the ice crystal i ($\mathbf{a}_i, \mathbf{b}_i, \mathbf{c}_i$) from Fig. 2.1a. In this work, the constitutive law of an ice crystal is defined by the transverse isotropic law of the ice single crystal as formulated by Eq. (1.10) in chapter 1. The apparent viscosity for shear in the basal plane η_{ab}^* defined by Eq. (1.11), can also be expressed in terms of the deviatoric stress as proposed in Eq. (A.13) from section A.1 :

$$\eta_{ab}^* = A_n^{-1} \tau_{\diamond}^{1-n} = A_n^{-1} \left(\frac{9S_{cc}^2}{4(4\alpha - 1)} + \frac{(S_{aa} - S_{bb})^2}{4} + S_{ab}^2 + \frac{S_{bc}^2 + S_{ca}^2}{\beta} \right)^{\frac{1-n}{2}} \quad (2.1)$$

where S_{kl} are components of the deviatoric stress tensor \mathbf{S} . n is the stress exponent and A_n is a fluidity parameter. For a uniaxial stress test, with normal stress σ_{zz} , Eq. (2.1) becomes (appendix A):

$$\eta_{ab}^* = A_n^{-1} \left(\frac{9\sigma_{zz}^2}{4(4\alpha - 1)} \left(\frac{2}{3} \cos^2(\theta) - \frac{1}{3} \sin^2(\theta) \right)^2 + \sigma_{zz}^2 \frac{\sin^4(\theta)}{4} + \sigma_{zz}^2 \frac{\cos^2(\theta) \sin^2(\theta)}{\beta} \right)^{\frac{1-n}{2}} \quad (2.2)$$

where θ is the angle between the \mathbf{c} axis and the loading axis (Fig. 2.1). Introducing:

$$K = \left(\frac{9}{4(4\alpha - 1)} \left(\frac{2}{3} \cos^2(\theta) - \frac{1}{3} \sin^2(\theta) \right)^2 + \frac{\sin^4(\theta)}{4} + \frac{\cos^2(\theta) \sin^2(\theta)}{\beta} \right)^{\frac{1-n}{2}} \quad (2.3)$$

Equation (2.2) simplifies to:

$$\eta_{ab}^* = A_n^{-1} K^{\frac{1-n}{2}} \sigma_{zz}^{1-n} = \mu_{basal}^* \sigma_{zz}^{1-n} \quad (2.4)$$

with μ_{basal}^* a material apparent viscosity parameter for shear in the basal plane [Mansuy et al., 2002].

The complete strain rate tensors is detailed in appendix A. Here, only the axial strain

rate along the \mathbf{z} axis is selected for the contact law :

$$D_{zz} = \frac{\sigma_{zz}^n}{2\mu_{basal}^*(4\alpha - 1)} f(\theta) \quad (2.5)$$

where $f(\theta)$ is a $\frac{\pi}{2}$ periodic function derived in appendix A.2 :

$$f(\theta) = 3\cos^4\theta + 2\alpha\sin^4\theta + \frac{2(4\alpha - 1) - \beta}{\beta} \sin^2\theta \cos^2\theta - \cos^2\theta \quad (2.6)$$

with α the ratio of the axial viscosity along the \mathbf{c} axis to the axial viscosity normal to the \mathbf{c} axis and β the ratio of the shear viscosity parallel to the basal plane to the shear viscosity in the basal plane (μ_{basal}^*). Axial viscosities are similar along the \mathbf{c} axis and the basal plane [Mansuy et al., 2002], thus α is approximated in the remaining to unity leading to a simpler expression for $f(\theta)$:

$$f(\theta) = 2 \left(1 + 3 \frac{1 - \beta}{\beta} \sin^2\theta \cos^2\theta \right) \quad (2.7)$$

In the case of a normal contact as represented in Fig. 2.1a, we simply denote in the following $\sigma_{zz} = \sigma$ and $D_{zz} = \dot{\epsilon}$. Equation (2.5) writes:

$$\sigma^n = 2\mu_{basal}^*(4\alpha - 1) f(\theta)^{-1} \dot{\epsilon} \quad (2.8)$$

The viscoplastic response of the crystal submitted to a uniaxial stress state with axial stress σ and axial strain-rate $\dot{\epsilon}$ thus writes:

$$\sigma = (2\mu_{basal}^*(4\alpha - 1))^{\frac{1}{n}} f(\theta)^{-\frac{1}{n}} \dot{\epsilon}^{\frac{1}{n}} \quad (2.9)$$

A value $\beta = 0.01$ was proposed in Mansuy et al. [2002] to fit, within the approximation of a Newtonian behavior ($n = 1$), the experimental data obtained on a monocrystalline inclusion embedded in a fine-grained isotropic ice matrix. Whatever its initial crystallographic orientation, the shape of the initially circular inclusion, became ellipsoidal as axial strain increased. The $\beta = 0.01$ value allowed for a reasonable agreement between observed and computed evolutions of the deformed ellipse aspect ratio and of the crystallographic orientation.

Figure 2.1b shows that the minima of $f(\theta)$ are located at $\theta = 0$ and $\theta = \pi/2$ while the maximum arises for $\theta = \pi/4$. In other words, the creep rate is maximum when the \mathbf{c} axis is oriented at $\theta = \pi/4$ with the axial loading axis. For a given applied stress, Eq. (2.7) shows that the maximum creep rate is $\frac{3 + \beta}{4\beta}$ times the creep rate of the least favourable \mathbf{c} orientation ($\theta = 0, \pi/2$). For $\beta = 0.01$, this ratio is approximately 75, indicating the

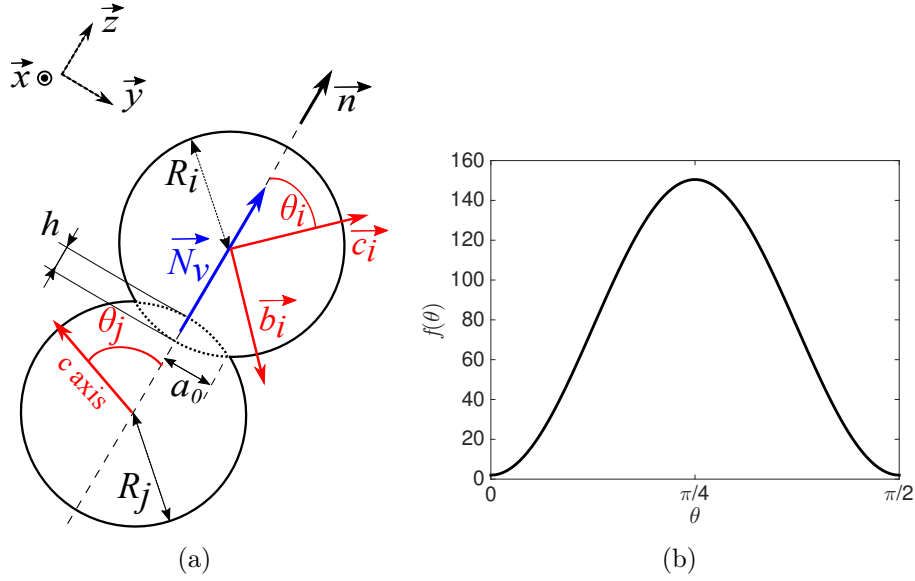


Figure 2.1: (a) Schematic representation of the anisotropic contact law between two indented spheres. $(\mathbf{x} = \mathbf{a}_i, \mathbf{b}_i, \mathbf{c}_i)$ is the local reference of the ice crystal i . a_0 is the initial contact radius (Eq. 2.13) (b) Evolution with the angle θ of orientation function f given by Eq. (2.6) for $\alpha = 1$ and $\beta = 0.01$.

large anisotropy experienced by ice crystallites.

Indentation laws are generally written for spherical particles, taking advantage of spherical symmetries for the derivation. For viscoplastic isotropic materials, [Storåkers et al. \[1999\]](#) have for example proposed analytical contact laws that give the indentation load on a spherical body as a function of the viscoplastic material properties. More importantly for the problem treated here, these authors have resolved the contact problem between two dissimilar viscoplastic bodies i and j with constitutive equations of the form:

$$\sigma = \sigma_i \dot{\epsilon}^{\frac{1}{n}} \quad (2.10)$$

where the material parameter σ_i pertains to material i but the stress exponent n is identical for the two materials. Based on indentation theory and on von Mises isotropic flow theory, the indentation load, N_v , writes for two spherical particles of radius R_i and R_j ($R^* = R_i R_j / (R_i + R_j)$) [[Storåkers et al., 1999, 1997](#)]:

$$N_v = \chi (\sigma_i^{-n} + \sigma_j^{-n})^{-\frac{1}{n}} (2R^*)^{(1-\frac{1}{2n})} h^{(1-\frac{1}{2n})} \dot{h}^{\frac{1}{n}} \quad (2.11)$$

where h is the indentation (Fig. 2.1) and \dot{h} is the normal rate of approach of the two particles and χ is a geometric factor with no unit. N_v is positive in compression ($\dot{h} > 0$). For two particles i and j , which \mathbf{c} axis make angles θ_i and θ_j with the contact normal,

the formulation of Storåkers et al. applied to Eq. (2.9) leads to:

$$N_v = \chi (2\mu_{basal}^* (4\alpha - 1))^{\frac{1}{n}} (f(\theta_i) + f(\theta_j))^{-\frac{1}{n}} (2R^*)^{(1-\frac{1}{2n})} h^{(1-\frac{1}{2n})} \dot{h}^{\frac{1}{n}} \quad (2.12)$$

Equation (2.12) is the general contact law of two particles which anisotropic behavior is given by Eq. (2.9). Now specializing the problem to a Newtonian material and for two particles of identical radius R and a small indentation ($h \ll R$), the contact radius, a (Fig. 2.1), may be approximated by:

$$a^2 = Rh \quad (2.13)$$

with $n = 1$, μ_{basal}^* becomes linear and equal to $\mu_{basal}^* = A_1 = \mu_{basal}$. Introducing the area of contact, $A = \pi a^2$, Eq. (2.12) rewrites ($\alpha = 1$), :

$$N_v = 6\chi\mu_{basal} (f(\theta_i) + f(\theta_j))^{-1} \left(\frac{A}{\pi}\right)^{1/2} \dot{h} \quad (2.14)$$

The aim of this chapter is to analyze the applicability of Eqs. (2.7) and (2.14) to the indentation problem of two ice particles having arbitrary \mathbf{c} orientations. The general formulation of Storåkers et al. [1997] applies to an indenter of arbitrary profile. However, Eq. (2.12) has only been derived for axisymmetric contact conditions (typically spheres or flat punches). From an experimental point of view, it is too complex a task to machine or form spherical monocrystalline ice particles. Instead, for practical reasons, we opt for cylindrical geometry. The full derivation of Storåkers et al. formulation for the problem of two indenting cylinders is beyond the scope of this work (see Johnson [1987] for the elastic problem of two identical indenting cylinders). Still, we aim at evaluating the suitability of Eq. (2.14) to the 2-dimensional problem of two cylinders indenting each other and forming a contact of radius a and area of contact $A = 2aL$ with L the cylinder length. The rationale for cylinders also rests on the pluses of a 2D configuration, which allows the propagation of basal slips to be visualized by polarized light (section 2.4.1), and strains to be quantified by Digital Image Correlation (section 2.4.2). These observations would be much more difficult with spheres. Finite Element simulations using the open source code Elmer/Ice (<http://elmerice.elmerfem.org/>) complement the experimental investigation and allow for a direct comparison with Eq. (2.14). These simulations are carried out on a cylindrical geometry (section 2.5).

2.3 Methods

2.3.1 Single crystal machining and set up

Diametrical loading tests were carried out either on a single cylinder or on two cylinders (Fig. 2.3). To that end, single crystals of ice were slowly grown in a crystallizer in cold room [Baruchel et al., 2013]. The process is the following :

1. A monocrystal of ice whose \mathbf{c} axis is parallel to the planar faces is deposited at the bottom of a crystallizer. The crystallizer is a tube of glass which height is about 50 cm and with a 8 cm diameter. Its bottom is metallic (stainless steel) ensuring thermal conduction with a cooling device (Peltier). The whole set up is put in a cold room at 0 °C. The single crystal acts as a nucleus for the crystal growth.
2. Snow is deposited on the sides to adjust more tightly the single crystal within the tube.
3. The crystallizer is filled with pure water between 0 and 3 °C, in order to avoid any thermal shock, but still enabling some melting of the rough surface of the monocrystal (a smoothed surface is necessary to avoid defects initiation in the crystal). The water is deionized and demineralized using a commercial system named Milli-Q.
4. The Peltier device is set to -3 °C to make the crystal grow slowly. Slow growth ensures that no impurities or bubbles are trapped inside the ice. Thus, although laborious, adjusting temperature to control the crystal growth in the first days is essential.
5. The single crystal typically grows between 0.5 and 1 mm per day to avoid aforementioned issues. Water must be changed daily to remove gas and possibly dust.
6. When the single crystal reaches the required height (typically 20 cm after at least 20 days of growth), water is removed and the temperature of the ice crystal is slowly increased above 0 °C, avoiding the occurrence of thermal shocks. Finally, the ice glides along the tube thanks to gravity and temperature.

This large monocrystal of ice is then split into bars, which are machined into cylindrical rods. Slices of 8 mm are then cut out with a slotting machine as illustrated in Fig. 2.2, leading to monocrystalline cylinders (diameter: $20 \text{ mm} \pm 0.05 \text{ mm}$, height: $8 \text{ mm} \pm 0.05 \text{ mm}$). The out-of-plane scatter of the \mathbf{c} axis is then verified to be less than $\pm 2^\circ$ to ensure plane strain conditions in the experimental set up. All the manufacturing procedure is carried out in a cold room at -10 °C.

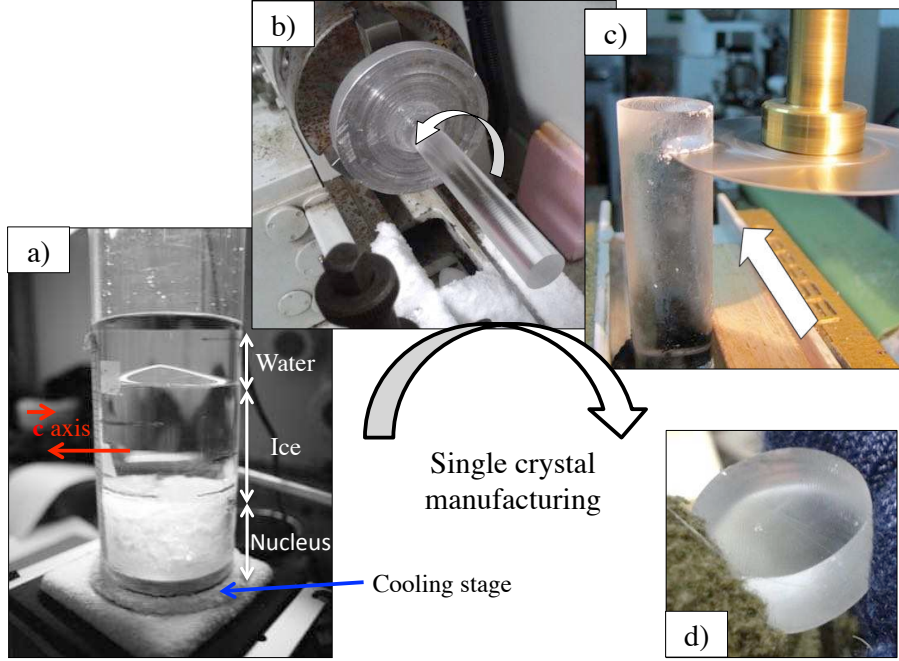


Figure 2.2: Snapshots of the different steps of single crystal manufacturing : a) growth in crystallizer, b) rods machining with a lathe, c) cylinders slicing with a slotting saw d) one typical monocrystalline ice cylinder. Final dimensions of cylinders are $20 \text{ mm} \pm 0.05 \text{ mm}$ in diameter, for slices of $8 \text{ mm} \pm 0.05 \text{ mm}$ in height.

The creep test set up is detailed in Mansuy et al. [Mansuy et al., 1999; Mansuy, 2001] and is sketched in Fig. 2.3. A constant load was applied on the diameter of the cylinders and the maximum applied load ($109 \text{ N} \pm 1 \text{ N}$) was small enough to avoid fracture. Various θ angles were selected to investigate the effect of the crystal orientation on the viscoplastic contact behavior. Tests lasting typically five hours were carried out in a cold room at -10°C ($\pm 1^\circ\text{C}$).

Ice samples are placed between two plates of glass to avoid sublimation and to ensure the plane strain conditions. The c axis being parallel to the cylinder plane ($\pm 2^\circ$), the out-of-plane strain (ε_{xx}) is negligible. Horizontal black marks allow the samples to be correctly positioned during the tests. Polarized light was used to follow the evolution of basal slips. Images were recorded and analyzed by Fiji [Schindelin et al., 2013] to compute logarithmic strains and rotations. For some tests with two cylinders, both cylinders were truncated to mimic indented particles and to limit rotation of the c axis during loading. The initial configuration is characterized by the ratio $\frac{a_0}{R}$, where $2a_0$ is the initial length of the truncated contact (Fig. 2.3b). Some of the two-cylinders configuration experiments were analyzed by Digital Image Correlation (DIC) to quantify the strain field. The principles as well as its use on ice is detailed in the following section (2.3.2).

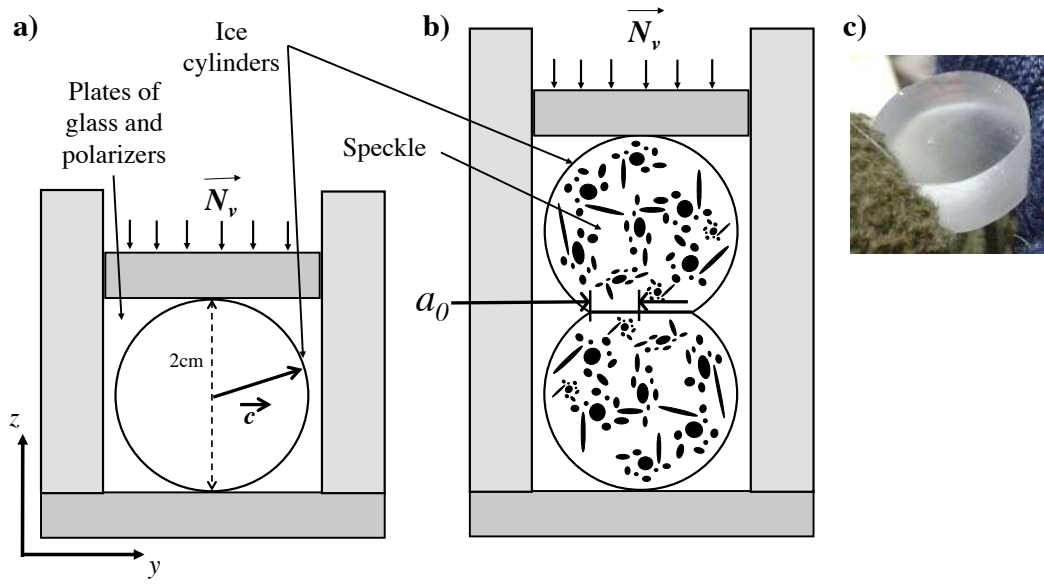


Figure 2.3: Experimental diametrical loading set-ups with \mathbf{c} axis parallel to the planar surface of cylinders. Crossed polarizers may be placed in front and behind the set-up. a) Single cylinder configuration. b) Double cylinder configuration with initial contact length $2a_0$. c) Photo of a typical monocrystalline ice cylinder.

2.3.2 The Digital Image Correlation on ice

2.3.2.1 Principles of the Digital Image Correlation

The Digital Image Correlation (DIC) is used in solid mechanics since the early 80's with the work of [Peters & Ranson \[1982\]](#) and [Chu et al. \[1985\]](#) who assessed the applicability of the theory to experimental mechanics. [Sutton et al. \[1983\]](#) proposed the first numerical algorithm of the correlation. Since then, the technique was considerably developed and became common for quantification of strain fields. New technological advances enabled [Allais et al. \[1994\]](#) to perform digital image correlation on tensile tests in a scanning electron microscope [[Doumalin, 2000](#)]. Similar tools along with 3D imaging were used in the recent work of [Bourcier \[2012\]](#) and [Gaye \[2015\]](#) on strain heterogeneities in halite. Besides geomaterials, metals were also extensively studied, for instance in magnesium alloys [[Martin et al., 2013, 2014](#)]. Those recent works focused on uncovering mechanisms at the scales of grains. For example, small features inside grains (such as plane slipping or twinning) were studied, the amount of grain boundary sliding compared to intragranular strain was quantified and the relation between the macroscale and the microscale was investigated. They also aimed to relate local crystallographic orientations (usually thanks to electron backscatter diffraction) with local strains.

Figure 2.4 sketches the principles of the DIC. It is based on the resemblance between

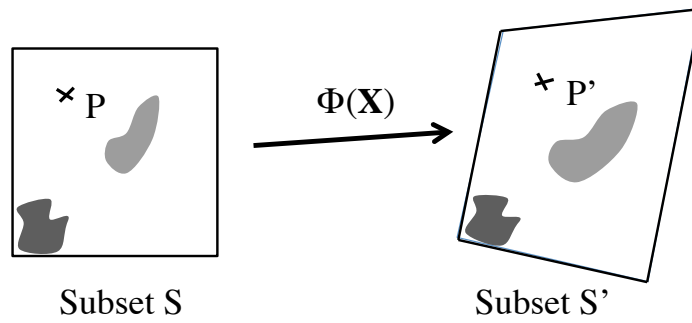


Figure 2.4: Principle of Digital Image Correlation. The subset S becomes S' after the transformation Φ that modifies the grey level distribution. The user selects the size of subsets according to the image quality in DIC softwares (resolution, speckle pattern and thickness). It is about 20 pixels in the different experiments presented section 2.4.2.

two images. The similarities are evaluated using a correlation criterion (named C) between the reference image or the undeformed state, and the other (the deformed state). Correlation domain or "subsets" are set in the reference state, and are part of a correlation grid. A DIC software finds the best match for each subset of the grid in the deformed state. This matching relies on the grey level of the image and especially on the local preservation of the contrast inside the subset. When subsets are matching, the displacement field can then be computed.

2.3.2.2 Computation of strains

Basic concepts of strain calculations and of correlation processing are detailed in the following. However, note that the calculations of strains and of the correlation function is partly dependent of the software used. In this work, image correlation is performed with CMV [Allais et al., 1994].

Let us take the material point P from Fig. 2.4 whose position in the undeformed state of a medium is \mathbf{X} in an orthonormal coordinate system, and that moves to P' whose position is \mathbf{x} in the same reference system when a displacement vector \mathbf{u} is applied :

$$\mathbf{u} = \mathbf{x} - \mathbf{X} \quad (2.15)$$

Considering an infinitesimal element $d\mathbf{X}$ in the undeformed configuration, and introducing the deformation gradient \mathbf{F} , one obtains the infinitesimal element in the deformed state:

$$d\mathbf{x} = \mathbf{F}d\mathbf{X} \quad (2.16)$$

Φ is a shape function that is either a translation (order 0) or an affine transformation (order 1) such that :

$$\mathbf{x} = \Phi(\mathbf{X}) \quad (2.17)$$

Thus, replacing Eq. 2.17 in (2.15), one obtains the definition of \mathbf{F} :

$$\mathbf{F} = \frac{\partial \mathbf{x}}{\partial \mathbf{X}} = \frac{\partial \Phi}{\partial \mathbf{X}} = \mathbf{I} + \frac{\partial \mathbf{u}}{\partial \mathbf{X}} \quad (2.18)$$

where \mathbf{I} is the identity tensor. A possible measure of strain which in CMV is the Green-Lagrange tensor defined by :

$$\mathbf{E} = \frac{1}{2}(\mathbf{F}^t \mathbf{F} - \mathbf{I}) \quad (2.19)$$

where \mathbf{F}^t is the transpose of \mathbf{F} . In practice, the section 2.4.2 shows very large strains during the experiments, thus the logarithmic strain or "true strain" tensor is adopted instead. It is defined using the Cauchy Green tensor :

$$\mathbf{B}^{-1} = (\mathbf{F}^{-1})^t \mathbf{F}^{-1} \quad (2.20)$$

Thus leading to the true strain tensor :

$$\boldsymbol{\varepsilon} = -\frac{1}{2} \ln(\mathbf{B}^{-1}) \quad (2.21)$$

As detailed in Bourcier et al. [2013], the discrete nature of the displacement field and the dependence of \mathbf{F} with \mathbf{dX} makes it difficult to be computed. Hence finite difference is used to work out the strain. This needs a domain of integration which is defined in CMV by the different schemes proposed in Fig. 2.5. The gage length represented accounts for the resolution of the strain, as it is included in the strain computation. Even if gage length and subset size are independent from one another, the choice of the subset will strongly affect the gage length. Indeed one should choose the subset in a way that they are close to one another without overlapping, so that sufficient grey level is contained in the subset, and uncertainties are not introduced. Indeed, an overlapping may bias the displacement search, as the same information would be used several times. Therefore, for a given integration scheme, increasing the subset size will increase the gage length (if overlapping is avoided).

Once the domain of integration is chosen, the deformation gradient tensor may be expressed in terms of coordinates of the neighbor and measurement points. Its full formulation can be found in Allais et al. [1994] and is not discussed here for sake of conciseness. However, it is noteworthy to recall that only the in-plane components of the linearized strain tensor \mathbf{e} can be worked out from these derivations (namely e_{xx} , e_{xy} and e_{zz}). The

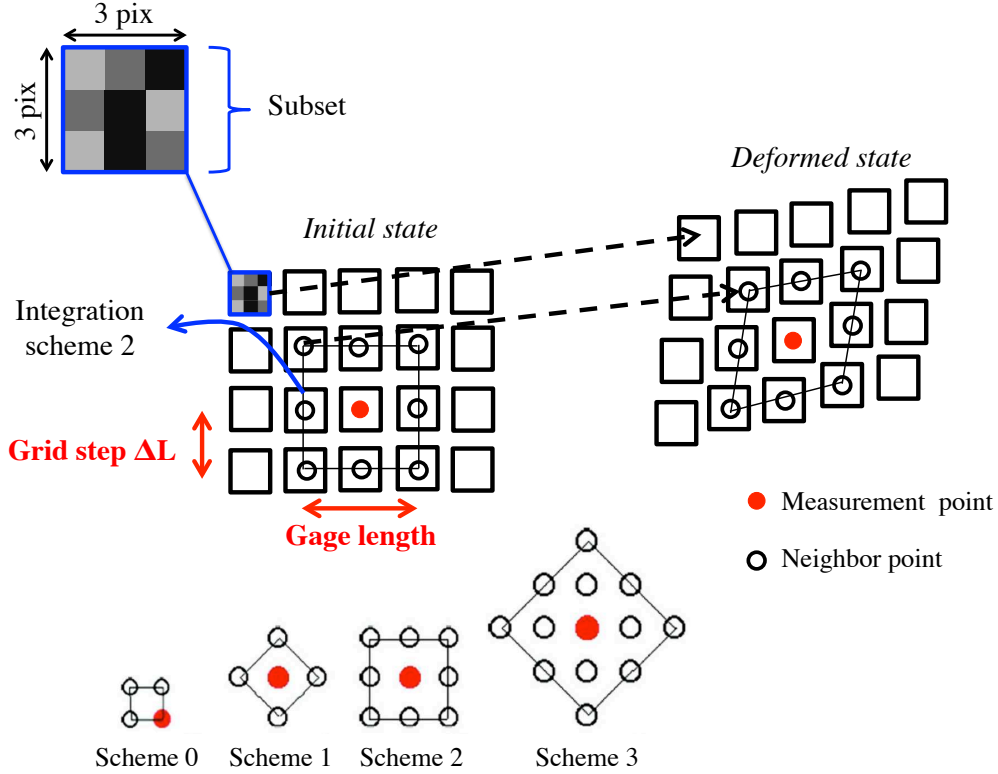


Figure 2.5: Principle of the strain computation in DIC. A correlation grid represented by squares is created on an image. A subset size, containing pixels, is chosen (here the side length of the subset is 3 pixels for the example). Correlation enables to find the corresponding subsets in the deformed state, and the displacement field can be computed. The strain field is worked out depending on the integration scheme chosen. Different integration schemes are available in CMV. Scheme 0 will yield very local strain but with large errors, while scheme 3 will yield accurate but less local strains (from Bourcier et al. [2013]). Gage length is calculated thanks to the grid step ΔL (length between two measurement points) of the scheme. The gage length is thus $p * \Delta L * pix_{size}$ with p depending of the integration scheme. In fact p is 1 for scheme 0, $\sqrt{2}$ for scheme 1, 2 for scheme 2 and $2\sqrt{2}$ for scheme 3.

Green-Lagrange components however are only determined if E_{xx} is known. To solve this issue, CMV assumes that the normal axis to the plane (\mathbf{y}, \mathbf{z}) is a principal axis for strain, and it also neglects out-of-plane rotations. Other assumptions are selected by the user to work out E_{xx} : plane strain conditions ($E_{xx} = 0$), isochoric strain ($E_{xx} = -(E_{yy} + E_{zz})$) and axisymmetric strain. The logarithmic strain tensor, ε which is calculated in the following, uses the same assumption than the Green-Lagrange tensor. In the experiments detailed in section 2.4.2, plane strain is selected and justified, but isochoric strain was also computed and showed very little differences.

Finally, the deformation gradient decomposes in a rigid-body rotation tensor \mathbf{R} and a stretch tensor \mathbf{U} that contains the distortion in the principal axis direction :

$$\mathbf{F} = \mathbf{R}\mathbf{U} \quad (2.22)$$

In CMV the orientation of the principal axes directions is thus known.

2.3.2.3 Computation of strain rates

In the case of experiments performed in this chapter (section 2.4.2), images were taken at regular intervals of time. The strain fields were obtained using the first image as a reference, during the whole experiment. Regarding strain rates, CMV does not offer the possibility of computing directly these fields. However, these are computed using incremental calculation of a strain map over time. This means that at each time step, the reference image is changed to the previous step, and the strain field is recomputed. To justify this method, the velocity tensor \mathbf{L} should be worked out in terms of the deformation gradient. Between the steps t and $t + dt$, it can be approximated by :

$$\mathbf{L} = \dot{\mathbf{F}}\mathbf{F}^{-1} \approx \frac{1}{dt}(\mathbf{F} - \mathbf{I}) \quad (2.23)$$

The strain rate tensor \mathbf{D} is the symmetric part of the velocity tensor \mathbf{L} , leading to :

$$\mathbf{D} = \frac{1}{dt} \left(\frac{1}{2}(\mathbf{F} + \mathbf{F}^t) - \mathbf{I} \right) \quad (2.24)$$

Multiplying Eq. (2.24) by dt makes it coincide with the linear formulation of the Green-Lagrange tensor in the case of an infinitesimal transformation between t and $t + dt$. This suggests that one can use an Eulerian description to calculate the strain rate field.

2.3.2.4 Correlation criterion

As for the correlation itself, as aforementioned in section 2.3.2.1 it totally relies on the grey level of the considered subset and its correspondence in the deformed state. When searching in the deformed state image, the software can find multiple solutions for a given local contrast. To avoid this as well as long computation, CMV proposes a "research domain" around the subset. Typically, in this work it is set to be half the size of the subset size and never more. The correlation is controlled by a criterion $C(\Phi)$ that minimizes the error between the discrete grey level f from the reference and the grey level g from the deformed state :

$$g(\mathbf{x}_i) - f(\mathbf{X}_i) \rightarrow 0 \quad (2.25)$$

where \mathbf{X}_i and \mathbf{x}_i are respectively the coordinates of the points in the reference and deformed state (with $\mathbf{x}_i = \Phi(\mathbf{X}_i)$). In a three dimension coordinate system, $\mathbf{X}_i = (X_i, Y_i, Z_i)$ and $\mathbf{x}_i = (x_i, y_i, z_i)$. Doumalin [2000] derived a correlation criterion implemented in CMV, that is independent of the contrast and of the brightness, thanks to the use of the mean grey level f_S and g_S of the subset S considered in the undeformed and deformed configuration. This criterion writes:

$$C(\Phi) = 1 - \frac{\sum_{i \in S} (f(\mathbf{X}_i) - f_S) (g(\Phi(\mathbf{X}_i)) - g_S)}{\sqrt{\sum_{i \in S} (f(\mathbf{X}_i) - f_S)^2} \sqrt{\sum_{i \in S} (g(\Phi(\mathbf{X}_i)) - g_S)^2}} \quad (2.26)$$

The correlation criterion $C(\Phi)$ ranges from 0 - perfect correlation - to 1 - total mismatch - and is set by default to 0.3 in CMV. This means that when correlation of a particular subset exceeds this value, it is not taken into account in the strain calculations. In this work it is usually less than 0.6 for the whole correlation grid. However biquintic subpixel optimization is always performed enabling a continuous function of the grey level (while it was discrete before), and improving the final correlation output as it retrieves some badly correlated points.

2.3.2.5 Use, accuracy and interests

Ice does not have a natural grey level that could be used for DIC. Thus the surface of ice samples was slightly scratched with glass paper and a speckle (shoe polish) was applied to obtain a proper grey level and a sufficient contrast for the DIC analysis. A correct light level was obtained by using two LED lamps with the advantage of limiting brilliance, enabling sufficient contrast and avoiding shadows. This method was already successfully used on polycrystalline ice by Grennerat et al. [2012] and recently by Chauve et al. [2015, 2017a]. Potential issues are the potential melting of the ice during scratching, but also the tendency of the speckle to crumble after a few hours. In a configuration similar to the

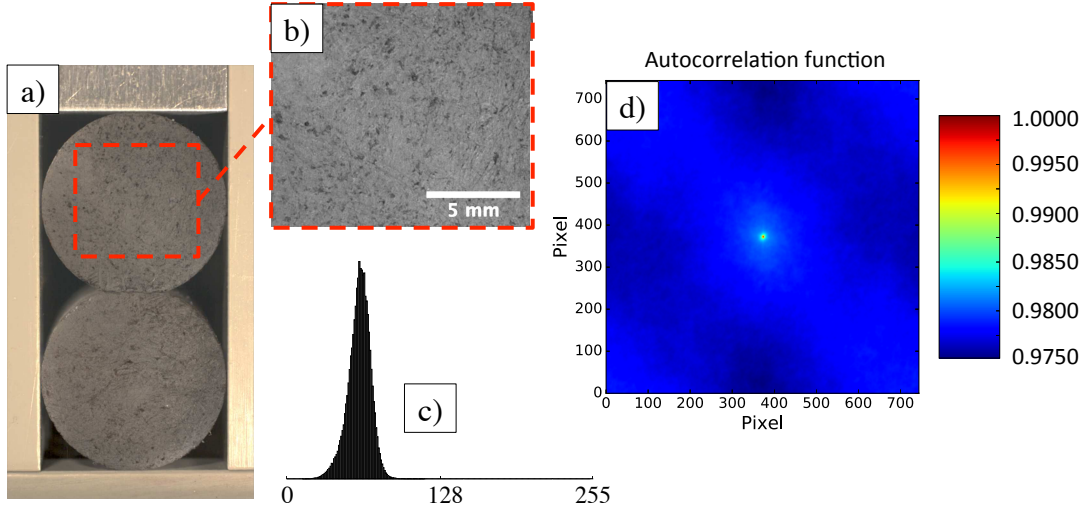


Figure 2.6: a) A diametrical loading on two cylinders with $\frac{a_0}{R} = 0.32$. Pixel size is $16 \mu\text{m}$ b) A zoom on the speckle in 8 bits. c) The grey levels of b). d) The autocorrelation function of b).

experiments presented below, [Chauve \[2017b\]](#) studied the effect on the macroscopic strain of the drying of the speckle as well as of the noise from the cold room (vibrations). He also tested the effect of the resolution on the macroscopic strain, while [Grennerat \[2011\]](#) measured the out-of-plane strain by stereo-correlation. Still, the contribution of the added noise is about 0.3 % for the errors on strain field components, which is one or two orders of magnitude below what is obtained by experiments (see section 2.4.2). Experiments presented in section 2.4.2 lasted about 3 to 4 hours, so the crumbling of the speckle was very limited. Besides, as discussed in section 2.3, the out-of plane scatter is negligible because **c** axes are in the plane of the cylinders. Subset sizes were chosen so that they are touching one another without overlapping. Finally, strain fields were extracted using a plane strain hypothesis, with a gage length that is exactly twice or $2\sqrt{2}$ the size of the grid step times the pixel size (in the case of the integration scheme 2 or 3).

Figure 2.6 exemplifies the speckle methodology on an experiment. The grey level shown in Fig. 2.6c is similar for all tested samples. In theory, the contrast should extend from 0 to 255 to perform a good image correlation. This is not the case, as also shown by the autocorrelation function in Fig. 2.6d which does not span from 0 to 1. Despite this poor contrast, the correlation works well. Besides, the autocorrelation radius at half-height is about $52 \mu\text{m} = 3.25$ pixels, while [Bornert et al. \[2009\]](#) claims that a medium pattern for a speckle should give a half-height radius at 2.2 pixels. The knowledge of this radius is an interesting approach to define the subset size as explained by [Triconnet et al. \[2009\]](#). Its size should be more than four times the autocorrelation radius, which gives in

our case a subset size larger than 13 pixels of width. All the experiments presented here used a subset size around 20 pixels (the pixel size ranging from 12 to 16 $\mu\text{m}/\text{pixel}$).

Regarding errors originating from the correlation itself, this work does not attempt to quantify them accurately. However [Bornert et al. \[2009\]](#) assessed them by varying several parameters such as the shape function of the displacement, the speckle quality (fine, medium or coarse), its period, or the subset sizes. What comes out from this study is that in the case of large subsets, large strains and low order shape function, the error is mainly controlled by the difference between the true displacement and the assumed shape function. Thus, in the present work, using a biquintic subpixel optimization after the first correlation does reduce errors.

For macroscopic strain calculation, we chose to follow the motion of the piston on all images. For the logarithmic macroscopic strain $\varepsilon_{zz} = \ln(1 + \frac{h}{2R})$, the error was evaluated to be of the order of 0.3% for the single cylinder configuration, and less than 0.1% for the two-cylinders configuration. Appendix B compares this choice to the use of DIC ([B.1](#)), and gives further details on the associated errors ([B.2](#)).

In conclusion, this section focused on explaining briefly the basic concepts of the DIC as well as the possible errors made with this tool. The next sections will focus on the actual experiments, first with the indentation of one monocrystalline of ice and then on the mutual indentation of two truncated cylinders.

2.4 Experimental indentation of ice cylinders

2.4.1 Diametrical loading on a single cylinder

Polarized light allows for the observation and the identification of the deformation by basal slips. A color evolution near the contact is detected when deformation initiates in the sample ([Fig. 2.7](#)). The deformation is strongly heterogeneous. However, because test conditions are symmetric, heterogeneities are also symmetric with respect to the cylinder center. The strain is localized in slip bands along basal planes. Two perpendicular lines appear for each contact point in red, contrasting with the undeformed green color. Slip lines are propagating through the crystal perpendicularly to the \mathbf{c} axis direction ([Fig. 2.7](#)). The bottom contact in images (A2) and (A3) could indicate an additional slip line parallel to the \mathbf{c} axis direction. However, a closer examination reveals that these patterns are in fact short slip lines that develop perpendicular to the \mathbf{c} axis. These lines fully develop in images (A4) and (A5).

Since the basal plane provides only two independent systems, additional degrees of freedom are necessary to accommodate arbitrary loading. In ice, non-basal planes are

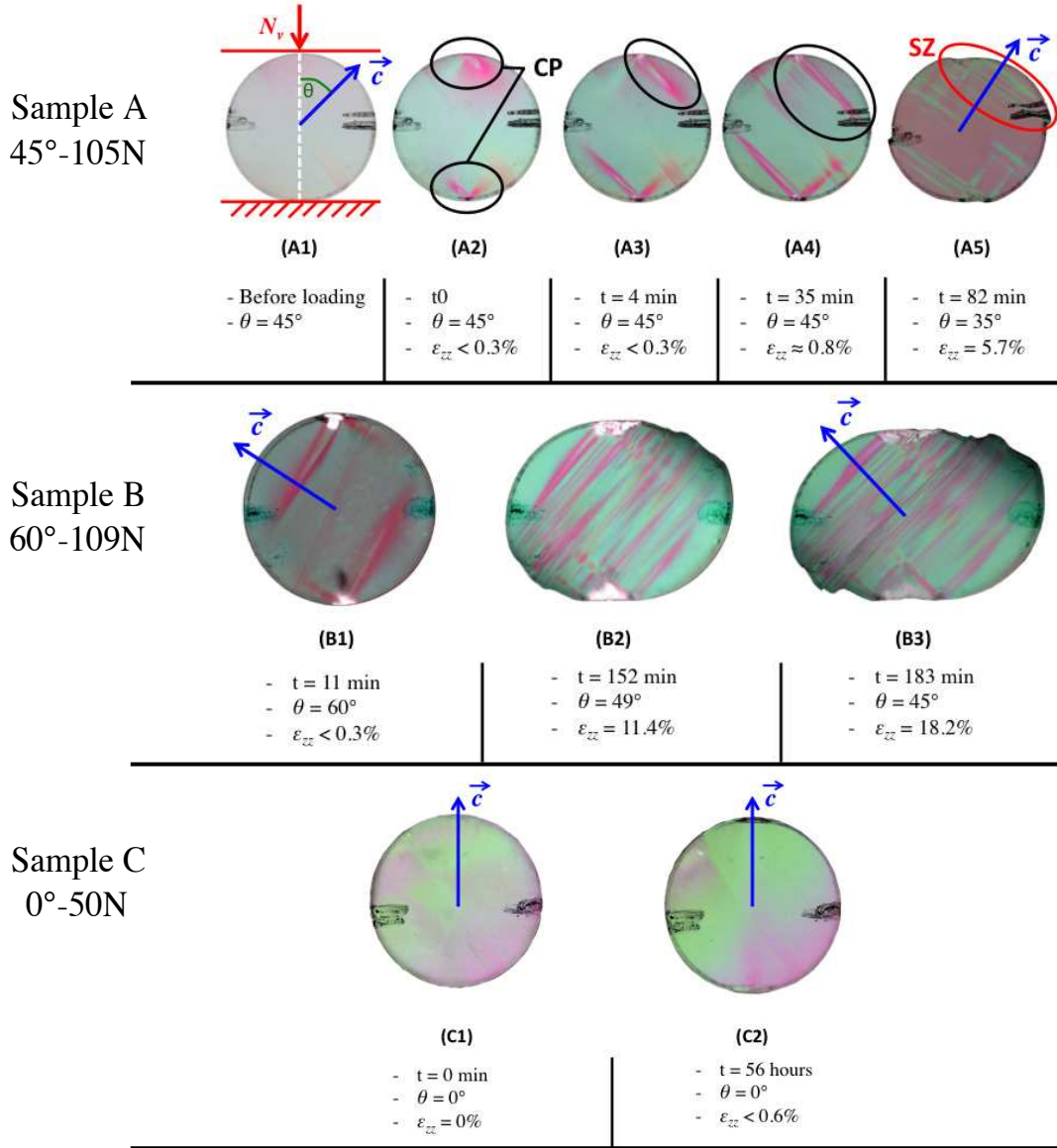


Figure 2.7: Evolution of the propagation of basal slips under polarized light for three different initial orientations (A: $45^\circ \pm 2^\circ$, B: $60^\circ \pm 2^\circ$, C: $0^\circ \pm 2^\circ$) and various applied loads. Cylinder (A1) is the crystal just before loading. The dashed line indicates the loading direction. Strain localization is shown at Contact Points (CP) on (A2). (A3) and (A4) illustrate the propagation of slips through the crystal with the red areas spreading perpendicular to the \vec{c} axis. (A4) shows the activation of multiple basal slip planes. (A5) shows an entire cap sliding (area SZ, Shearing Zone). Cylinder (B) exemplifies a condition for which the rotation is significant. Cylinder (C) exhibits negligible strain and rotation of the \vec{c} axis even for very long times.

seldom activated, thus requiring other mechanisms [Schulson et al., 2009]. For example, recent studies [Chauve et al., 2015, 2017a] emphasized that recrystallization could occur even at low strain (less than 1 %) or low stress (0.5 MPa) at grain boundaries and triple junctions of polycrystalline ice. Moreover, despite being commonly observed in hexagonal metals, twinning is excluded in ice. Kink and bending bands on the other hand can appear and were observed on polycrystalline ice deformed with our experimental set up [Mansuy, 2001; Lebensohn et al., 2009]. In our loading conditions, the cylinder has few constraints and can deform easily by shear on basal planes except for specific values of θ (0° and 90°). This peculiar condition is well illustrated by sample C in Fig. 2.7. For all other θ values the cylinder can deform freely. Melting is another candidate for strain accommodation. It may have occurred as large stress concentration may develop below the contact points. The melting point temperature decreases by about 0.1° C for every 1 MPa [Petrenko & Whitworth, 1999]. A 100 MPa stress would thus be necessary to trigger melting under contacts at -10° C.

In any case, all these mechanisms (recrystallization, kink and bending bands, and melting) would have left a clear signature that was not observed with polarized light. Note that bright spots at contact points on sample B are linked to an image contrast enhancement processing. Hence, dislocation motion on $\{0001\}$ planes should be the main strain accommodation mechanism in our experiment. This should mainly occur by screw dislocations with Burgers vector $(\frac{a}{3}) < 11\bar{2}0 >$ as these are the least energetic dislocation lines [Schulson et al., 2009].

We observed a clear evolution of the orientation of the \mathbf{c} axis during the test (Fig. 2.7). Whatever the θ value, the \mathbf{c} axis rotates towards the loading direction in agreement with the compression of a single crystal [Honeycombe, 1975]. For example, crystal (A) has rotated by approximately 10° between its initial state (A1) and its (A5) state. In accordance with crystal anisotropy, strain is primarily limited when the \mathbf{c} axis is perpendicular or parallel to the loading direction as shown by sample (C).

Figure 2.8a quantitatively confirms the qualitative observations of Fig. 2.7. Figure 2.8a plots the rotation $\Delta\theta$ of the \mathbf{c} axis angle against time for all tested samples in the single-cylinder configuration. Relative uncertainties are shown only for the 60° curves but are representative of the other curves (typically $\Delta(\Delta\theta) < 4^\circ$). Significant rotation is observed for samples with loads of the order of 100 N as demonstrated by Fig. 2.7. For these samples, basal glide propagates from the contact point (CP) through the whole cylinder. This is due to the heterogeneous stress field around CP and to the strong ice crystal anisotropy. Note that the two samples corresponding to $\theta = 0^\circ$ and $\theta = 90^\circ$ lead to $\Delta\theta = 0^\circ$ even for very long times (Fig. 2.7) .

Figure 2.9 sketches the proposed main deformation mechanisms encountered for small

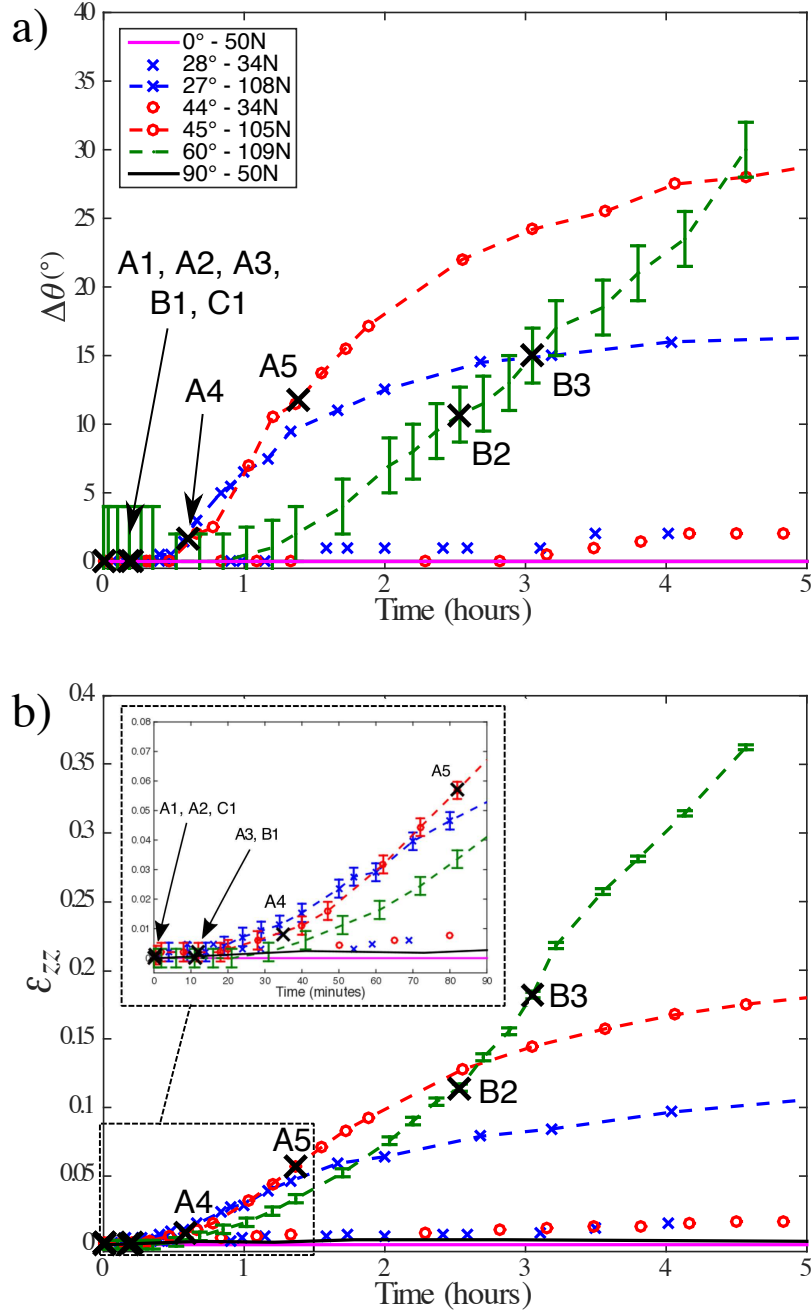


Figure 2.8: Evolution of the (a) rotation angle $\Delta\theta$ and (b) strain ε_{zz} against time for monocrystalline cylinders of ice (single cylinder configuration). Samples are submitted to various loads and different initial angles of the \mathbf{c} axis with respect to the load direction are tested. Strain is positive in compression. Error bars are shown only for sample B for clarity. Black markers A, B, C relate to observations in Fig. 2.7. Sample C2 is outside the time scale (56 h). The two samples corresponding to $\theta = 0^\circ$ and $\theta = 90^\circ$ lead to $\Delta\theta = 0^\circ$. All strain-time curves and orientation evolution obtained on a single cylinder configuration are given in appendix C.

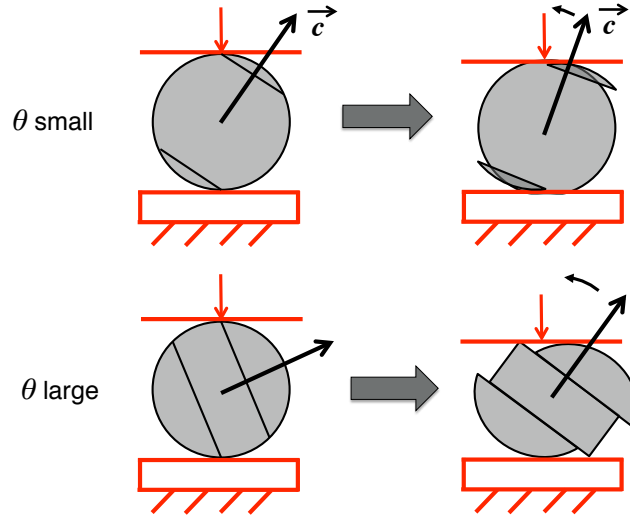


Figure 2.9: Schematics of the deformation process for the cylinders with a (a) small θ and a (b) large θ .

and large initial θ angles. Cylinders are sheared by two localized bands to form three different fragments. The central fragment is contained between the contact points and the first basal planes that shear (Fig. 2.7). The three fragments differ in size depending on initial θ angle. The central fragment contains all the planes that are gliding during the deformation. The other two fragments are simply pushed away by the rigid planes. For small θ values, two small caps quickly form. This is illustrative of sample (A) in Fig. 2.7. In that case, the rotation initiates early (Fig. 2.8a) but saturates further on since the small cap hinders rotation. For large θ values, two large caps gradually form. This is illustrative of sample (B) in Fig. 2.7. The rotation takes more time to initiate since dislocations need to propagate on a larger distance along the large cap. Once initiated, the rotation is facilitated by the geometry of the two large caps. Thus, the \vec{c} axis rotates towards the loading direction. In that final configuration, the fragments get stuck and there is no more driving force for rotation. Therefore, the rotation reaches its maximum and stays constant with time.

Figure 2.8b shows the strain evolution in the loading direction z . It follows a pattern which is very similar to the pattern of Fig. 2.8a. It indicates that for a \vec{c} axis oriented parallel ($\theta = 0^\circ$) or normal ($\theta = 90^\circ$) to the loading axis, no strain is observed although a non-negligible load (50 N) is applied. We observed that those samples exhibited less than 1 % of axial strain even after more than 17 hours. Similarly, those sample exhibited negligible rotation. Figures 2.8a and 2.8b also demonstrate the effect of the applied load intensity with increasing rotation and strain for increasing loads for a given θ value.

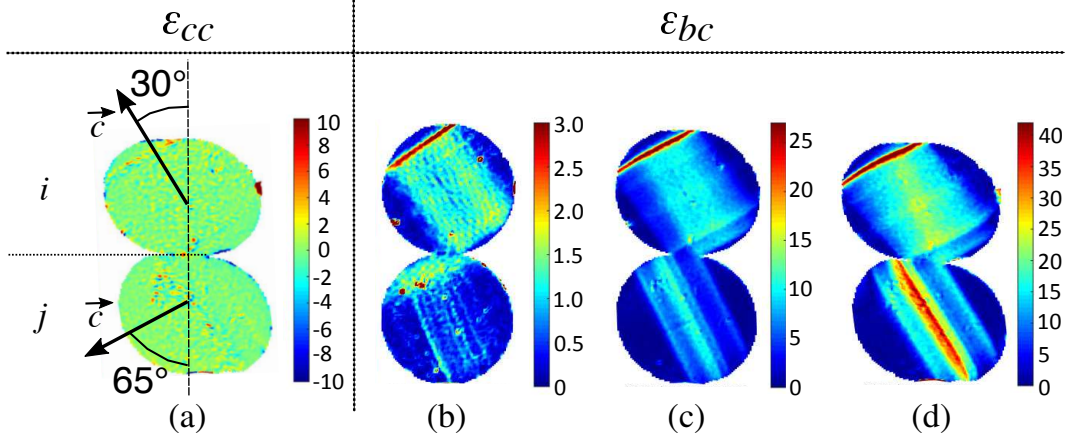


Figure 2.10: Strain maps (in %) in the local reference (**b, c**) obtained by DIC analysis (see Fig. 2.1a), considering that basal planes are parallel to the maximum shearing. Applied load: 53 N, initial orientations: $\theta_i = 30^\circ$, $\theta_j = 65^\circ$. Initial contact size: $\frac{a_0}{R} = 0.20$. (a): strain ε_{cc} at 200 min. (b-d): shear strain in the basal plane ε_{bc} at different times: (b) 20 min, (c) 120 min and (d) 200 min. The gage length for this test is $504 \mu\text{m} \pm 2 \mu\text{m}$ and the pixel size is $12.60 \mu\text{m}/\text{pixel} \pm 0.05 \mu\text{m}/\text{pixel}$ (integration scheme 2 [Bourcier et al., 2013]). All strain-time curves and orientation evolution obtained on the two cylinders configuration are given in appendix C.

2.4.2 Diametrical loading on two cylinders

Tests carried out with the two-cylinders configuration are in qualitative agreement with the observations gathered on the single cylinder configuration. For this configuration, we were able to evaluate the full strain field by DIC on the face of the two cylinders (Fig. 2.10). In particular, it is possible to obtain the shear strain in the basal plane (ε_{bc}). The θ values of each sample were selected using polarized light outside the set-up. Once installed in the set-up, these values were confirmed by the observation of the basal plane angles, which are assumed to correspond to the maximum shearing. This hypothesis is validated by the very small values of the diagonal components of the strain tensor in the crystallographic axes reference (**b, c**), such as ε_{cc} as illustrated in Fig. 2.10a. These low eigenvalues of strain obtained by DIC are associated to the resolved shear stress needed to activate non-basal glide, which is 60 times greater than for the basal plane activation for the same strain rate [Duval et al., 1983; Petrenko & Whitworth, 1999].

As already observed in the single-cylinder configuration, Figs. 2.10b-d show strong heterogeneities in shear strain. These figures illustrate that shearing in localized bands becomes very large with increasing strain. For example, Fig. 2.10d shows that the maximum value of the shear strain in the basal plane ε_{bc} at 200 min is more than 40%, while the macroscopic strain ε_{zz} is only 10%.

We observed that for small strains the cylinder with the most disorientated **c** axis

(j cylinder) consistently exhibits localized shear strain around its contact with the other cylinder (Fig. 2.10b). For larger strains, heterogeneities that start from loaded contact points or from the extremities of the neck rapidly overthrow any other heterogeneities (Figs. 2.10c-d).

For the top cylinder (i), which exhibits a small θ angle, we observed that a strong shear band always develops from the contact with the rigid plane. The maximum shear strain is consistently larger in the small θ angle cylinder as compared to the maximum shear strain in the large θ angle cylinder. The width of the shear band in cylinder i is clearly larger than the one of the bottom cylinder j . This is in agreement with experiments involving only one cylinder where we observed large peripheral fragments for large θ angles. This confirms that the size of the shear bands depends primarily on the \mathbf{c} axis orientation, whatever the configuration.

Figure 2.11 groups the rotation $\Delta\theta$ of the \mathbf{c} axis angle against time for samples tested either with point contact between the two cylinders ($\frac{a_0}{R} = 0$) or with finite contact size ($\frac{a_0}{R} = 0.2, 0.32, 0.35$). The imposed load for all samples is 54 N. Figure 2.11 only plots $\Delta\theta$ for the cylinder that experiences maximum rotation but the same qualitative conclusions can be drawn for others. Although error bars on $\Delta\theta$ are rather large (Fig. 2.8a), machining an initial finite neck size tends to decrease the ability of cylinders to rotate. This may reflect a more realistic state for which multiple contacts between ice crystals exist in the firm. Such contacts would have enlarged over time through sintering mechanisms and viscoplastic deformation to form necks with finite size.

2.4.3 Neck size effect

When rotation is hindered by an initially large neck size, Eq. (2.14) should allow for a simple relation between strain and load for a given set of angles θ_i and θ_j . In this section, we show that experimental data on truncated cylinders support such a relation. For small axial strain ε_{zz} , the initial area of contact $A_0 = 2a_0L$ is assumed to remain constant and the ratio of actual to initial indentation is:

$$\frac{h}{h_0} = 1 + 2\frac{R}{h_0}\varepsilon_{zz} \quad (2.27)$$

with ε_{zz} positive in compression. Integrating between times 0 and t for a constant load test (creep), Eq. (2.14) leads to:

$$\varepsilon_{zz} \left(\frac{a_0}{R}\right)^{1/2} = \frac{(f(\theta_i) + f(\theta_j)) \left(\frac{\pi}{2}\right)^{1/2}}{12\chi\mu_{basal}R^{3/2}L^{1/2}}N_v t \quad (2.28)$$

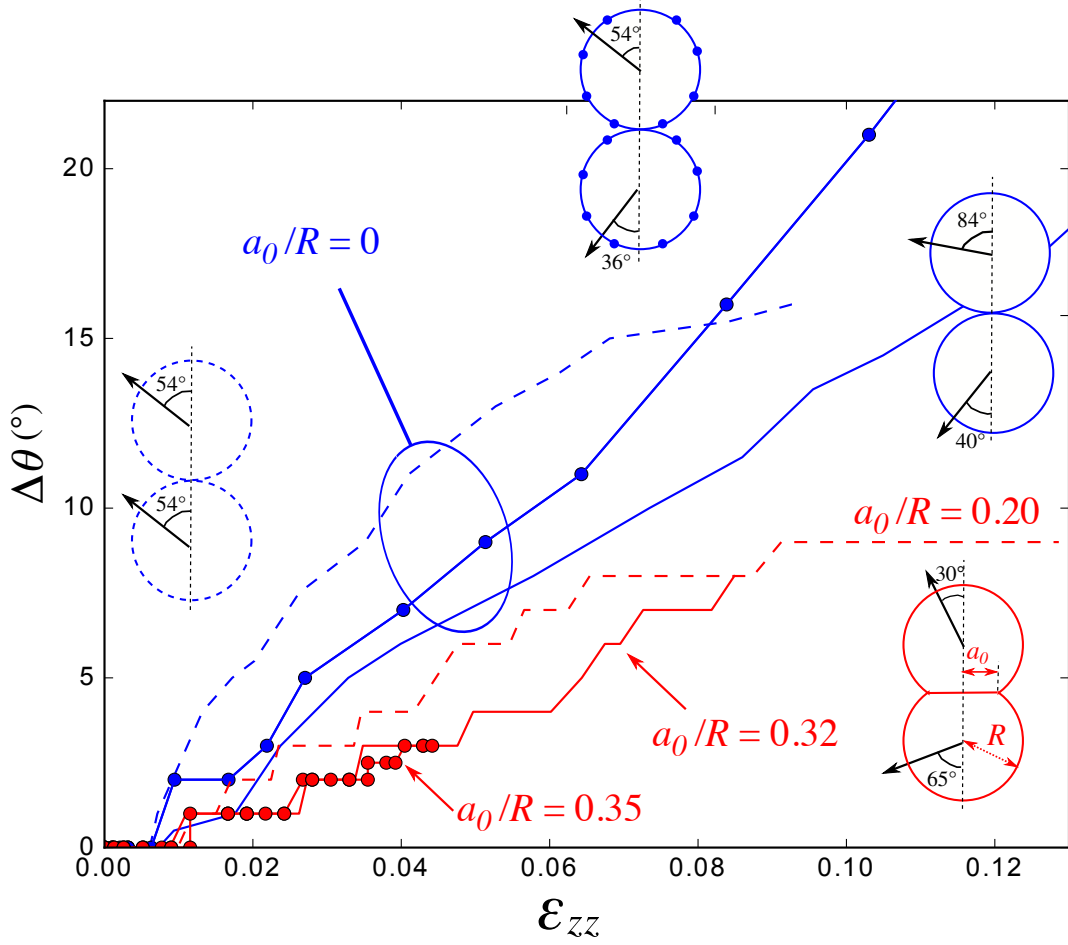


Figure 2.11: Evolution of the disorientation of θ with the indentation for the cylinder that turns the most in two-cylinders configuration experiments (load 54 N). One can notice that maximum rotations for cylinders with initial neck size are lower than without neck. In other terms, the blue lines come from experiments in which cylinders rotate independently of one another in point contact configurations, while the red lines show that rotation is hindered because of the contact plane.

Figure 2.12 plots the product $\varepsilon_{zz} \left(\frac{a_0}{R}\right)^{1/2}$ against time for three tests with $\frac{a_0}{R} = 0.2, 0.32, 0.35$ for a given load (53 N) and a given set of angles θ_i ($\theta_i = 30^\circ, \theta_j = 65^\circ$). Figure 2.12 shows that the three tests fall on a master curve for small strains (or times). For times smaller than 80 min, the master curve exhibits a linear portion. Using the slope of this linear portion, Eq. (2.28), which is only valid for small strains, allows for an estimation of the product $\chi\mu_{basal}$. Experimental data points lead to $\chi\mu_{basal} \approx 4 \cdot 10^{12}$ Pas. Although the exact value of the geometric parameter χ is difficult to ascertain for two cylinders, we note that for two indenting Newtonian spheres, $\chi \approx 2$ [Storåkers et al., 1999]. The viscosity μ_{basal} at -10°C may be estimated from the literature for the stress range of interest here at the contact (0.1 - 10 MPa). It is of the order of $0.5 \cdot 10^{12}$ to

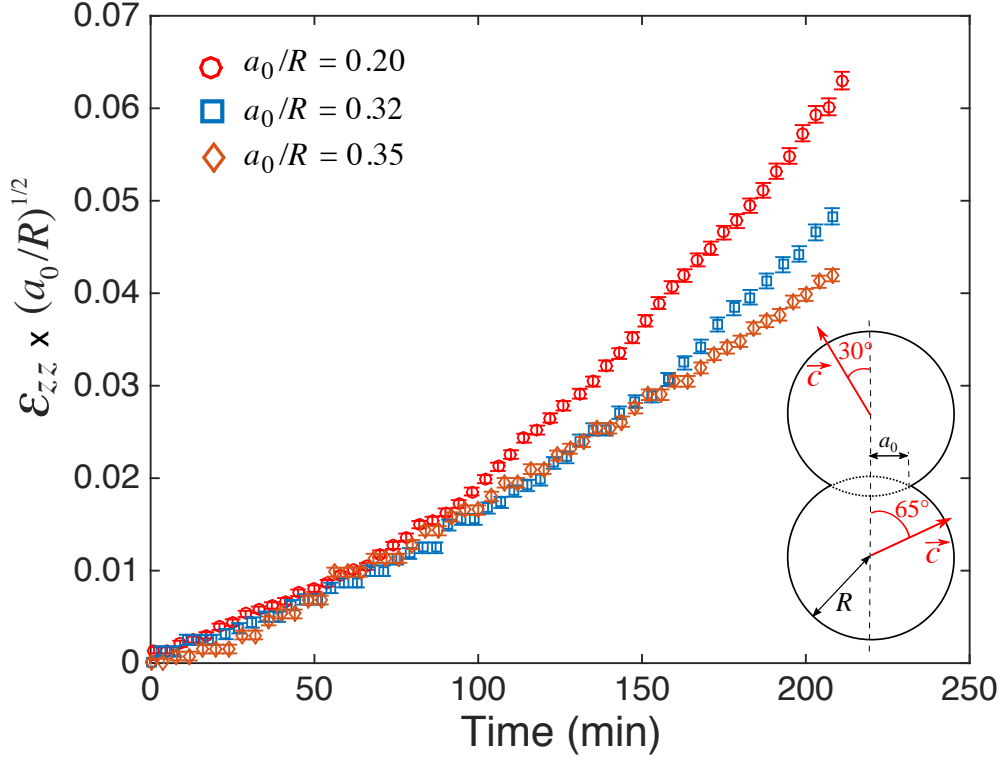


Figure 2.12: Evolution of the product $\varepsilon_{zz} \left(\frac{a_0}{R} \right)^{1/2}$ (with associated error bars) against time for a creep load of 53 N. Tests are carried out for a given set of (θ_i, θ_j) angles (see inset) for three different values of $\frac{a_0}{R}$. Maximum macroscopic strains represented here are $\varepsilon_{zz} = 0.141, 0.084$ and 0.073 for $\frac{a_0}{R} = 0.20, 0.32$ and 0.35 , respectively.

$5.0 \cdot 10^{12}$ Pa.s [Duval et al., 1983; Mansuy et al., 2002], and thus in good accordance with the value of the product $\chi \mu_{basal}$ found here. In the following an approximate basal viscosity $\mu_{basal} = 1 \cdot 10^{12}$ Pas is chosen.

2.5 Comparison between 2D FEM simulations and experiments

The aim of this section is to complement the experimental validation of Eq. (2.14) by specifically investigating the effect of the θ angle on the normal force at the contact. The Finite Element Method (FEM) with the Elmer/Ice open-source code was used to simulate some of the experiments with two truncated cylinders. The model implemented in Elmer/Ice solves the Stokes equations, i.e. neglecting inertial terms, with the full transverse isotropic law of an ice crystal as proposed by Meyssonier & Philip [1996]. It simplifies to Eq. (2.9) for a uniaxial stress state of compression. In accordance with the

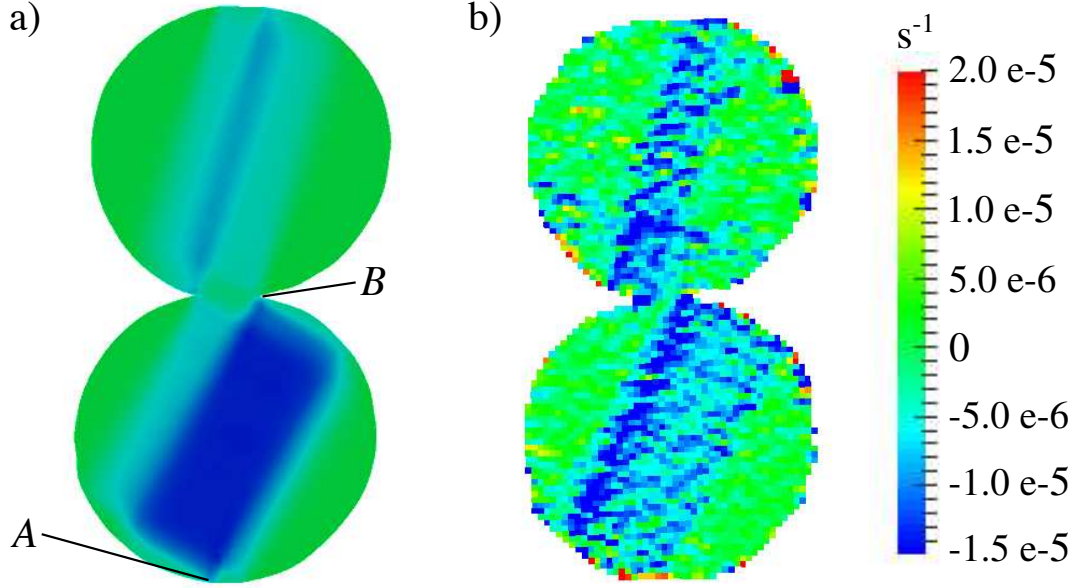


Figure 2.13: Strain rate field $\dot{\epsilon}_{zz}$ (s^{-1}) at 80 minutes under 54 N for $\theta_{initial}(i) = 75^\circ$ and $\theta_{initial}(j) = 63^\circ$. a) Finite Element simulation results with $\mu_{basal} = 1 \cdot 10^{12}$ Pas and b) DIC results $\dot{\epsilon}_{zz}$. The gage length for this test is $864 \mu m \pm 2 \mu m$ and the pixel size is $21.60 \mu m/pixel \pm 0.05 \mu m/pixel$ (integration scheme 2 [Bourcier et al., 2013]).

analytical model, the values of parameters α and β are set to 1 and 0.01, respectively. Gillet-Chaulet et al. [2005] have studied the effect of those parameters on the flow response of ice. Details on the model and on the numerical methods can be found in Gillet-Chaulet [2006] and Gagliardini et al. [2013].

Here, we use the initial angle orientation of the two \mathbf{c} vectors defining the contacting cylinders as input, together with the geometry of the truncated contact. Cylinders were meshed using triangular elements with approximate size of 0.5 mm. No specific mesh refinement was used close to the contact zone. A displacement is imposed on the upper boundary to obtain a compressive force (54 N) with no lateral constraint. Note that neither the cylinder geometry nor the crystallographic orientation evolve for a given simulation.

Figure 2.13 shows the comparison between the FEM simulated and the DIC computed strain-rate fields. Since \mathbf{c} vectors are given as input to the Elmer/Ice code, the orientation of the shear bands coincides with the experimental ones, as it should. More interestingly, FEM simulations predict satisfactorily the position and the width of the shear bands as compared to the DIC results. In particular, the FEM simulations reproduce the significant effect of the contact on the spreading of the shear band. For example, considering the bottom cylinder, the shear band starts from point A and develops leftward until it encounters contact point B. This shear band is relatively thick due to the combination of

geometrical and orientation constraints. In contrast, the shear band on the top cylinder is much thinner due to the \mathbf{c} axis being nearly perpendicular to the load axis. Note that for the two bands, the strain-rate value becomes null at the extremities of the contact.

Since DIC strain rates are calculated using incremental calculation of a strain map over time, they are far less resolved than strain maps which are calculated from the initial configuration (Fig. 2.10). Thus, the comparison between FEM simulations and experimental strain rate is merely qualitative. However, the strain-rate magnitudes of FEM and DIC are in reasonable agreement for the chosen value $\mu_{basal} = 1 \cdot 10^{12}$ Pas .

A second set of FEM simulations was carried out to confirm the validity of the analytical formulation proposed in Eq. (2.14). FEM calculations were performed for two truncated cylinders with various pairs of (θ_i, θ_j) angles for four values of $\frac{a_0}{R}$ (0.141, 0.2, 0.3, 0.4). Figure 2.14 plots the adimensional rate of approach of the two cylinders obtained by FEM simulations:

$$\tilde{h} = \frac{A_0^{1/2} \mu_{basal} \dot{h}}{N_v} \quad (2.29)$$

Using Eq. (2.14), the analytical expression of \tilde{h} rewrites:

$$\tilde{h} = \frac{f(\theta_i) + f(\theta_j)}{6\chi} \pi^{1/2} \quad (2.30)$$

Figure 2.14 compares the analytical expression to the FEM simulations. In this figure, the angle θ_j of the vector \mathbf{c} that characterizes the bottom cylinder is set to 0 and $\pi/4$ while the angle θ_i is varied between 0 and $\pi/2$ by $\pi/20$ steps, taking advantage of the $\pi/2$ periodicity of the $f(\theta)$ function. Note that χ was used as a fitting parameter to minimize by a least square method the error between Eqs. (2.29) and (2.30) ($\mu_{basal} = 1 \cdot 10^{12}$ Pas). A value $\chi \approx 16$ was found to minimize the error. Even though Fig. 2.14 only shows the comparison for $\theta_j = 0$ and $\theta_j = \pi/4$, the fit has been conducted on a much larger set of θ_j values ($11 \theta_i \times 11 \theta_j = 121$ pairs) for the four a_0/R values studied here.

The match between Eqs. (2.29) and (2.30) is far from perfect with maximum error for the smallest a_0/R value and $\theta_j = \pi/4$ of the order of 20% and negligible errors for $\theta_j = 0$. Still the comparison is satisfactory in that the general shape of the $f(\theta)$ function is well retrieved.

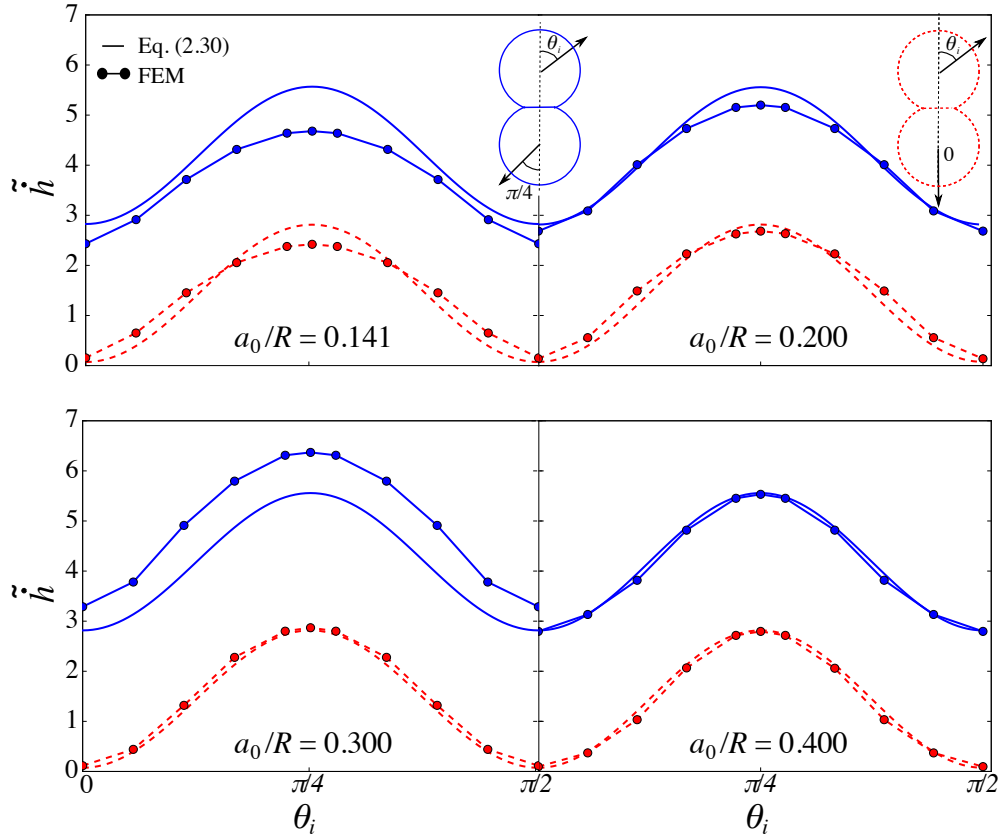


Figure 2.14: Evolution of the adimensional indentation rate \ddot{h} against θ_i for four values of a_0/R . Comparison of \ddot{h} given by finite elements simulations (Eq. (2.29)) and by the anisotropic contact model (Eq. (2.30)) for $\theta_j = 0$ (red dotted curves) and $\theta_j = \pi/4$ (blue plain curves). All curves are $\pi/2$ periodic.

2.6 Concluding remarks

We have shown that the viscoplastic contact response between monocrystalline ice particles exhibits strong anisotropy. This anisotropy directly originates from the hexagonal structure of ice. When rotation is not hindered, the phenomenology of the indentation is rather complex, involving the propagation of basal slips and the formation of ice “fragments” within the particle during loading. Localization of shear bands is the major strain mechanism. Light polarization and DIC are well suited to capture these strong heterogeneities that arise mainly parallel to the basal planes. These strain heterogeneities are coupled with a rotation of the \mathbf{c} axis towards the loading axis.

When rotation is limited by a large contact area, the indentation evolution of two particles with arbitrary \mathbf{c} axis orientation is more tractable. In that case, the simple analytical model presented here provides a means of extrapolating the contact response

of strongly anisotropic ice particles. The simple forms of Eq. (2.7) and Eq. (2.14) have been partially validated by a combination of experiments on truncated cylinders and by 2D FEM calculations. In particular, the role of contact size and of the crystallographic disorientation between the particles are correctly rendered.

It should be clear that the Newtonian law used here for single ice crystals is only a simplifying assumption, which may not reflect the correct strain-rate dependency. Power-law exponent of 1.5 to 2.5 are typically mentioned in the literature [Duval et al., 1983; Chevy et al., 2012]. For polycrystalline ice, both Newtonian and non-Newtonian behaviors have been observed [Doake & Wolff, 1985; Gillet-Chaulet et al., 2011]. In any case, it would be interesting to generalize this study to non-Newtonian behavior and investigate the effect of $n > 1$ in Eq. (2.11) on the shape of the \tilde{h} versus θ_i curves (Fig. 2.14).

As stated above, the proposed analytical model is only valid when rotation may be neglected. Fortunately, this assumption is appropriate in many cases that are relevant for firn at intermediate relative density (above 0.60). In that density range, the firn still exhibits a particulate structure with ice particles contacting each other. During firnification, a representative ice particle is in contact with an increasing number of neighboring particles. Assuming a spherical shape, the coordination number should be larger than five for a relative density larger than 0.6. This should safely ensure a limited amount of rotation at the contact scale. Thus, we believe that the simple equations proposed here should be useful for applications where the viscoplastic anisotropy of the mutual indentation of ice particles needs to be taken into account. Such equations may be used in analytical models or in Discrete Element Method simulations that could predict firn densification with the anisotropy of ice crystals taken into account (see chapter 5). Such models or numerical simulations should shed new light on the problem of pore closure and thus should improve understanding of ice core records of past atmospheric composition. In particular, we have demonstrated here that contacts between ice particles in the firn behave very differently depending on the orientation of particles. The firn microstructure, in the intermediate relative density range, should reflect somehow this contact network, with some contacts experiencing large deformation while others nearly none.

More generally, the methodology described here can be applied to other strongly anisotropic particulate materials such as magnesium, zinc, or titanium powders. The macroscopic behavior of those important engineering materials is well described by a transverse isotropic law. The form proposed in Eqs. (2.9) and (2.6) remains valid. Depending on the relative weight of basal, prismatic or pyramidal gliding mechanisms, the values of the μ_{basal} and of the α and β parameters in Eq. (2.6) may differ. Still, Eq. (2.12) offers a useful tool to model the collective behavior of strongly anisotropic powders.

Chapter 3

Microstructure of polar firn

Contents

3.1	Tomography on ice cores	69
3.1.1	Up to date knowledge on ice core tomography	69
3.1.2	State of the art	71
3.2	Polar sites characteristics	73
3.3	Methods	75
3.3.1	Cold cell	77
3.3.2	Image Analysis	79
3.3.3	Control of sublimation	82
3.4	Representativeness of morphological parameters	84
3.4.1	Density	84
3.4.2	Closed porosity	86
3.4.3	Connectivity Index	88
3.4.4	Specific surface area	90
3.4.5	Key results on error estimations	91
3.5	Representative Volume Element in ice	91
3.5.1	Determination methods	92
3.5.2	Formal description of statistical RVEs	93
3.5.3	Representativeness of closed-porosity and connectivity indexes	98
3.5.4	Discussion	100
3.6	Multi-site comparisons	102
3.7	Refined geometrical parameters for Dome C and Lock In sites	105

3.8	Corrected data of Dome C	109
3.9	Pore size	112
3.10	Characterization of the ice phase	115
3.10.1	Crystallographic orientation	115
3.10.2	Grain size	118
3.11	Concluding remarks	122

The microstructure of polar firn is the witness of the densification process. Chapter 2 concentrated on a very simple case of two ice particles in contact. It is now necessary to understand the behavior of multiple ice grains that were slowly fused together. In this chapter, this behavior is investigated from the point of view of pores, and their progressive closure, but also from the point of view of grains and their crystallographic orientations. Indeed, studying two polar sites, this chapter attempts to confirm and continue what previous work concluded on pore closure and texture in firn (see chapter 1).

3.1 Tomography on ice cores

3.1.1 Up to date knowledge on ice core tomography

For dense firn, the mechanisms of gradual pore closure are of interest in order to interpret the processes that affect the atmospheric signals. Models on air transport in the firn such as [Trudinger et al. \[1997\]](#); [Rommelaere et al. \[1997\]](#); [Severinghaus & Battle \[2006\]](#); [Witrant et al. \[2012\]](#); [Buizert et al. \[2012\]](#) rely on a diffusion coefficient that requires the knowledge of the evolution of the closed porosity with depth and/or density and only limited parameterizations are available [[Schwander, 1989](#); [Goujon et al., 2003](#); [Severinghaus & Battle, 2006](#); [Mitchell et al., 2015](#); [Schaller et al., 2017](#)]. Based on data collected by the melting-refreezing method [e.g., [Raynaud et al., 1982](#)], [Mitchell et al. \[2015\]](#) derived a parameterization taking into account layering for closed porosity. They compared their parameterization to previous ones [[Schwander, 1989](#); [Goujon et al., 2003](#); [Severinghaus & Battle, 2006](#)] and to measurements [[Schwander et al., 1993](#); [Trudinger et al., 1997](#)], showing a general improvement of the fit to the closed porosity ratio for the Summit (Greenland) and Law Dome (Antarctica) polar sites.

The ratio of closed porosity along with air content in closed pores may be obtained by three different techniques: pycnometry (air content) [e.g., [Schwander & Stauffer, 1984](#)], melting-refreezing (air content) [e.g., [Martinerie et al., 1992, 1994](#)] and X-ray computed tomography (closed pores) [e.g., [Barnola et al., 2004](#)]. Each technique comes with its own issues. Pycnometry measurements may open artificially some closed pores that are weakly sealed [[Schwander & Stauffer, 1984](#)]. Melting-refreezing is a destructive technique that forbids any further microstructural investigation [[Raynaud et al., 1982](#)]. X-ray tomography scans a rather small volume of firn, thus questioning the representativeness of measured properties [[Coléou et al., 2001](#)]. These three techniques have all in common the issue of borders effect. In particular, one has to make assumptions on the closed or open status of cut-bubbles.

The X-ray tomography technique has received increasing interest in the last 20 years

for investigating snow and firn microstructure [Flin et al., 2003; Barnola et al., 2004; Schneebeli & Sokratov, 2004; Freitag et al., 2004; Fujita et al., 2009; Lomonaco et al., 2011; Gregory et al., 2014]. Focusing on the microstructural evolution that accompanies the closure process, Barnola et al. [2004] demonstrated the potential of the method by investigating the density and closed porosity evolution along the firn core of Vostok. They uncovered significant discrepancies between the ratio of closed porosity calculated from absorption images and measured by pycnometry. They attributed these differences to the small scanned volumes compared to the ones used when performing pycnometry measurements. Fujita et al. [2009] reported that the stratification of firn had an effect on several properties such as structural anisotropy, crystal orientated fabric or the total air content at Dome Fuji. They also exhibited the importance of studying the capture of air at the micro scale. Other Antarctic sites (WAIS Divide and the Megadunes region in East Antarctica) were also investigated. WAIS Divide exhibits high accumulation rate and relatively warm temperature, whereas Megadunes is very cold with very low accumulation. Gregory et al. [2014] performed X-ray tomography and permeability measurements on these firn cores. They concluded that the coldest site is characterized by a less tortuous pore morphology. WAIS Divide exhibiting strong layering, Gregory et al. [2014] also demonstrated that the air flow in polar firn was mainly controlled by the pore structure and not density variability. Focusing on the Summit site in Greenland, Lomonaco et al. [2011] studied closely fine-grained layers in the firn. Their results displayed that the ratio of the number of closed pores over the pore volume was marked by a sharp increase that correlated well with the LID. Similarly Gregory et al. [2014] also used such parameter but the correlation with the LID seems much less obvious while it is satisfactory for the closed porosity ratio (defined by the ratio of the volume of closed pores over total pore volume). Overall, the literature on firn tomography concentrates on studying parameters evolution and their relation to gas transport within the firn such as permeability. It also focuses on differentiating polar sites, or relating microstructures to deformation mechanisms. However, despite giving useful information for densification modeling, these X-ray tomography studies do not provide an unambiguous prediction of LIZ and COD as gas measurements do.

Other contributions to the microstructure study of firn focus on the layering of firn. Freitag et al. [2004] and Hörhold et al. [2011] used gamma ray absorption techniques to investigate the layering of different polar sites and compared their results with X-ray microtomography. Hörhold et al. [2011] indicated that at high accumulation sites and higher mean annual temperatures, the variability of the density during pore closure is also larger, leading to a broader LIZ. While densification models generally use a mean density profile [Herron & Langway, 1980; Barnola et al., 1991; Arnaud et al., 2000], this density

variability should be taken into account, as high density layers may seal the underneath low density layers from the surface (see [e.g., [Landaïs et al., 2006](#)] for more details). In that sense, the stochastic description of the pore closure from [Mitchell et al. \[2015\]](#) is an improvement as it involves a parameterization of the closed porosity ratio accounting for the layering of firn.

All the above-cited studies on X-ray tomography do not critically discuss the errors related to acquisition (voxel size or resolution), image analysis (image thresholding, labeling of pores) and sample variability (size and spatial heterogeneities). For the X-ray tomography to become a reliable reference technique for firn investigation, these errors and their impact on the microstructural properties should be thoroughly studied. This effort has already started for modeling based on X-ray tomography images, whether for physical effective properties [[Freitag et al., 2002](#); [Courville et al., 2010](#)] or for snow mechanics [[Wautier et al., 2015](#); [Rolland du Roscoat et al., 2007](#)]. For example, [Freitag et al. \[2002\]](#) and [Courville et al. \[2010\]](#) modeled the firn permeability by a lattice Boltzmann technique on a layered firn column using X-ray images. These authors worked out a representative volume element for permeability, going beyond the sole density as done for instance by [Coléou et al. \[2001\]](#) on snow.

In this context, here we investigate in detail the error sources that come with the whole process of X-ray tomography imaging on two East Antarctica polar firn cores originating from Lock In and Dome C. We gather microstructural parameters, going further than the classic closed porosity ratio, to study the closure of pores. We are able to discriminate which parameters correlate to the COD. Taking into account the evaluated errors, we propose a new parameter, the connectivity index which is simply defined by the ratio between the volume of the largest pore and the total porosity, and which is much less plagued by sample size and voxel size.

3.1.2 State of the art

Tomography on snow, firn or ice is quite challenging from a methodology point of view. All research teams on the subject use different set-ups. A possible technique is to use an X-ray scanner inside a cold room. Examples for this approach are from teams from Hanover, USA, which use a Skyscan micro-CT 1172 [e.g., [Lomonaco et al., 2011](#); [Wang & Baker, 2013](#); [Hammonds et al., 2014](#)], from the Alfred Wegener Institute in Germany which use a portable device (Skyscan 1074SR) [e.g., [Freitag et al., 2004, 2008](#); [Hörhold et al., 2009](#); [Linow et al., 2012](#)], or from Davos (Switzerland) which use a SCANCO μ CT80 mainly to study snow metamorphism or deformation [e.g., [Schneebeli & Sokratov, 2004](#); [Löwe et al., 2011](#); [Theile et al., 2011](#); [Schleef & Löwe, 2013](#)]. Despite the clear benefits of having a micro-computed tomograph inside a cold room (very practical, portable device),

issues of this technique are foremost the very limiting size of the holding sample box, as well as small X-ray detectors, leading to small reconstructed samples (less than 1 cm^3). Possible damage of electronic devices is also inherent to cold temperature. One other important known issue of such devices is the relatively long scanning time. For instance, measurements in [Schleef & Löwe \[2013\]](#) lasted two hours. This implied local heating that perturbed the measurements, hence the use of a fan.

The second technique is to use a cold cell inside a common X-ray tomograph. This is the technique used by teams in Grenoble [e.g., [Flin et al., 2003](#)]. For instance, taking advantage of the European Synchrotron Research Facility, [Barnola et al. \[2004\]](#) studied firn from the Vostok ice core, [Coléou et al. \[2001\]](#) exhibited the differences of four types of snow, and [Rolland Du Roscoat et al. \[2011\]](#) succeeded in reconstructing grains of snow with their associated crystallographic orientations. The obvious advantage is the speed of tomographic scans in such a facility (less than a minute) as the energy is specifically selected. However, such a set-up is not handy at all, as one must develop a cooling system that does not hinder the scanning process.

Designing specific cells enables to control much better what happens to the sample. In her thesis, [Calonne \[2014\]](#) developed a cryogenic cell name CellIVM that couples two Peltier devices to impose an accurate temperature gradient to a snow sample, the borders being completely isolated from ambient air by a vacuum chamber. While using a cold room, [Ebner et al. \[2014, 2015\]](#) created a sample holder made of thermistors and microporous foam, which enables the temperature and the velocity of an airflow coming through the snow to be controlled. This set-up was used to study the effect of different Peclet numbers on isothermal metamorphism.

The Alfred Wegener Institute recently acquired a cold lab tomograph named ICE-CT, specifically designed to perform X-ray tomography on entire ice cores of 1 m. Inside the room, air is kept at -14°C . [Freitag et al. \[2013a\]](#) used it for 2D X-ray scanning, and measured the density variability all along the one meter core for a pixel size of $120\text{ }\mu\text{m}$ and a scanning time of approximately 3 min. Higher resolution for 3D volumes of the ice core diameter was reported with a voxel side length down to $25\text{ }\mu\text{m}$ [[Schaller et al., 2017](#)]. It is obvious that this new technology should enable a full description analysis of the ice core and of its heterogeneities. In our study, we took advantage of the tomographs from Université Grenoble Alpes (UGA) to perform X-ray scans of firn, for which cold cells and a cooling system were developed.

After introducing the polar sites studied in this work (section 3.2), we detail the methods developed for scanning firn in section 3.3. In section 3.4, we investigate the scale effect and determine the errors engendered on the main physical properties studied when decreasing the resolution in the tomographic scans. We then performed a thorough analysis

of the representative volume element in section 3.5. Section 3.6 focuses on the comparison between four different sites, with particular interest on the two sites studied in this work (namely Dome C and Lock-In), along with the polar sites detailed in Gregory et al. [2014]. Section 3.7 takes advantage of modern image analysis tools to compute refined microstructural parameters that characterize the pore network throughout densification. A correction of the data obtained for Dome C is suggested in section 3.8 in order to remove cut-pore effects. Finally, section 3.9 concentrates on the pore size distribution. However, tomography alone does not give any information on grain size and crystal orientation. To that end, 2D image analyses were carried out on thin sections of firn and are presented in section 3.10. The cylinders of firn extracted from the stored ice cores are henceforth defined as **ex situ** samples.

3.2 Polar sites characteristics

Two sites in Antarctica are studied, Dome C and Lock In¹. Dome C, near Concordia station, exhibits one of the lowest mean annual temperature (-55°C) and snow accumulation rate ($25\text{ kg m}^{-2}\text{ yr}^{-1} \approx 2.5\text{ cm water equivalent per year, w.eq.yr}^{-1}$). Moreover, Dome C is at 3233 m above sea level, with a thickness of nearly 3300 m of ice. These different characteristics make it an interesting site for drilling, as it shelters old ice [Augustin et al., 2004]. Another distinctive feature of this site is the very small non-diffusive zone (lock-in zone, LIZ) (about 3 m [Landaï et al., 2006]). The ultimate depth attainable to sample air was reached at 99.5 m [Landaï et al., 2006]. The ice core studied comes from the Volsol project carried out in 2010/2011 [Gautier et al., 2016]. Samples originate from a unique ice core, except for three deep samples (115.05, 123.34 and 132.07 m) that come from the DC12 (2012) ice core.

The Lock-In site is 136 km away from the Concordia station towards the French base Dumont d’Urville. This site was drilled during the austral summer 2015-2016, and is characterized by an intermediate snow accumulation rate of $4.5\text{ cm w.eq.yr}^{-1}$ (first guess from Verfaillie et al. [2012]). The mean annual temperature is not yet known but the borehole temperature is -53.15°C at 20 m depth. The LID is certainly between 96-100 m, and air could not be pumped below approximately 108 m indicating that the COD is slightly deeper than for Dome C [Orsi, 2017].

A summary of the different sites characteristics is given in Table 3.1 and their location in Antarctica are shown Fig. 3.1. These sites were all analyzed with X-ray micro-computed tomography (XCT). The majority of them are cold sites, with low accumulation rate, however only the Lock In site exhibits a rather large LIZ compared to other cold sites.

¹ Note that Lock In is a polar site and does not refer to the lock-in phenomenon.

This last feature makes the comparison between no-LIZ sites (such as Dome C) and LIZ sites (such as Lock In) even more interesting, as the porous network should be different. Hopefully the structure should exhibit features explaining the earlier capture of gases.

To our knowledge, apart from the deep sample scanned by [Durand et al. \[2006b\]](#), no sample from Dome C firn core were previously analyzed by XCT. Regarding the Lock In site, the project is still on going. Collaboration between the IGE and the Alfred Wegener Institute is running in the frame of Kevin Fourteau PhD thesis [[Fourteau, 2019](#)]. It is planned that the first 130 m of the ice core should be scanned (a quarter core), with special care to the lock-in and close-off zones. Thus in this work, samples of the same size than for Dome C were extracted in July 2016, before dissemination of the ice cores between the different partners. Samples from Lock In offer here the possibility to directly compare the two sites with the same analysis methods.

Site	Location	Acc. r. (w.eq.yr ⁻¹)	$\langle T \rangle$ (°C)	LIZ (m)	COD (m)
Dome C ^a	75°6'S, 123°21'E	2.5 cm	-55	3	99.5 ^b
Lock In	74°8.310'S, 126°9.510'E	≈ 4.5 cm ^c	-53.15 ^c	8 – 12 ^d	108.3 ^d
Dome Fuji ^{b,e}	77°19'S, 39°40'E	2.1 cm	-57	0	104
Vostok ^{a,f}	77°28'S, 106°48'E	2.2 cm	-57	2	100
WAIS Divide ^{g,h}	79°46.300'S, 112°12.317'W	21 cm	-31	≈ 10	76.5
Megadunes ^{g,i}	80°77.914'S, 124°48.796'E	< 4 cm	-49	≈ 4	68.5
B26 ^j	77°15'N, 49°13'W	18 cm	-30.6	5 – 11(B29) ^b	69 ^k
Summit ^l	72°N, 38°W	21 cm	-31	10	80 ^m

Table 3.1: Characteristics of different polar sites that were studied by X-ray tomography. COD values are taken directly from the literature and may not be exactly defined identically. For the Dome C and Lock In sites studied in this work, the close-off depth is defined as the ultimate depth at which air could be sampled. The temperature is the mean annual temperature.

^a [Bréant et al. \[2017\]](#)

^b [Landais et al. \[2006\]](#)

^c [Martinerie \[2017\]](#)

^d [Orsi \[2017\]](#)

^e [Fujita et al. \[2009\]](#)

^f [Barnola et al. \[2004\]](#)

^g [Gregory et al. \[2014\]](#)

^h [Battle et al. \[2011\]](#)

ⁱ [Severinghaus et al. \[2010\]](#)

^j [Freitag et al. \[2004\]](#)

^k [Hörhold et al. \[2011\]](#)

^l [Lomonaco et al. \[2011\]](#)

^m [Witrant et al. \[2012\]](#)

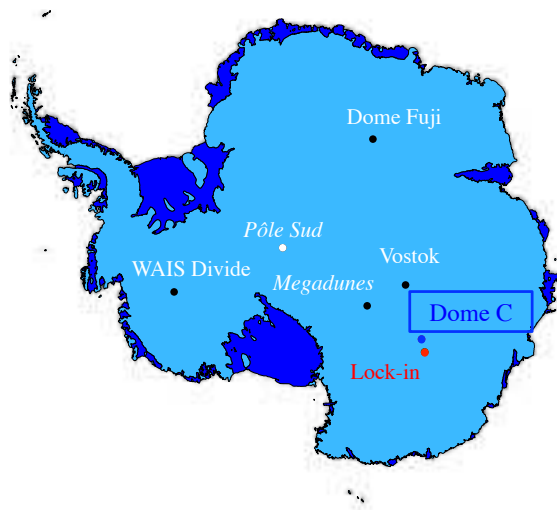


Figure 3.1: The samples used in this work.

3.3 Methods

X-ray micro-computed tomography is a widely used technique of 3D characterization in multiple fields of research (biology, physics, materials science, ...), as it gives the full skeleton for each phase of a multi-phase material. It consists of emission of X-rays that are partly absorbed by the sample. The transmitted X-rays are then captured by a detector and give radiographs or projections of the sample in 2D images. The rotation of the sample (or the source in medical application), allows for a 3D reconstruction of the set of projections. This is summarized in Fig. 3.2. A single set of projections is named a scan.

More than a hundred scans were performed in this work. For sake of time and to avoid sublimation of samples, the time of each scan is a compromise between speed and noise, and depends largely on the detector used. Hence Table 3.2 gives the acquisition parameters used in this work. To sum up, for typical size of samples of 12 mm in diameter, continuous helical scans were performed in the CMTC-UGA laboratory tomograph (an Easytom XL 150-160 developed by Rx Solution). This configuration was chosen to image large samples (from 20 mm to 30 mm) with a volume more than twice the value typically studied by Barnola et al. [2004] and Gregory et al. [2014]. Scans lasted 25 min for a cubic voxel side length of 12 μm . These parameters already lead to well contrasted images in terms of grey level (see Fig. 3.6). The 3SR tomograph proposes different acquisition parameters that were useful for scans of larger samples, which could not fit in the CMTC-UGA tomograph. These scans were longer and needed a much larger flux of photons to image a 10 cm diameter firn (see Table 3.2).

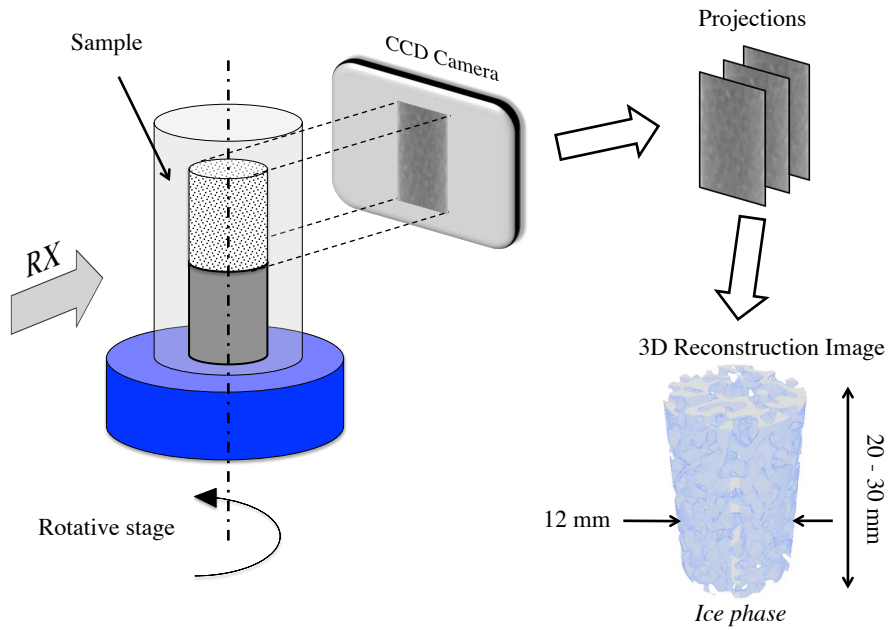


Figure 3.2: Principle of X-ray tomography.

Lab tomograph	CMTC-UGA		3SR	
Detector	CCD		Flat Panel	
Mode	Tomography	Helical	Tomography	
Tube voltage (kV)	60		60	80
Target current (μA)	166		375	500
Exposure time (s)	0.7			
Framerate (s^{-1})			2	3
Voxel size (μm)	12		30	60
Number of projections	150	800	1440	
Number of turns	1	4	1	
Scanning time (min)	4.66	25	48	32

Table 3.2: X-ray tomography acquisition and reconstruction parameters used in this study for the CMTC-UGA (located at SIMaP) and 3SR tomographs

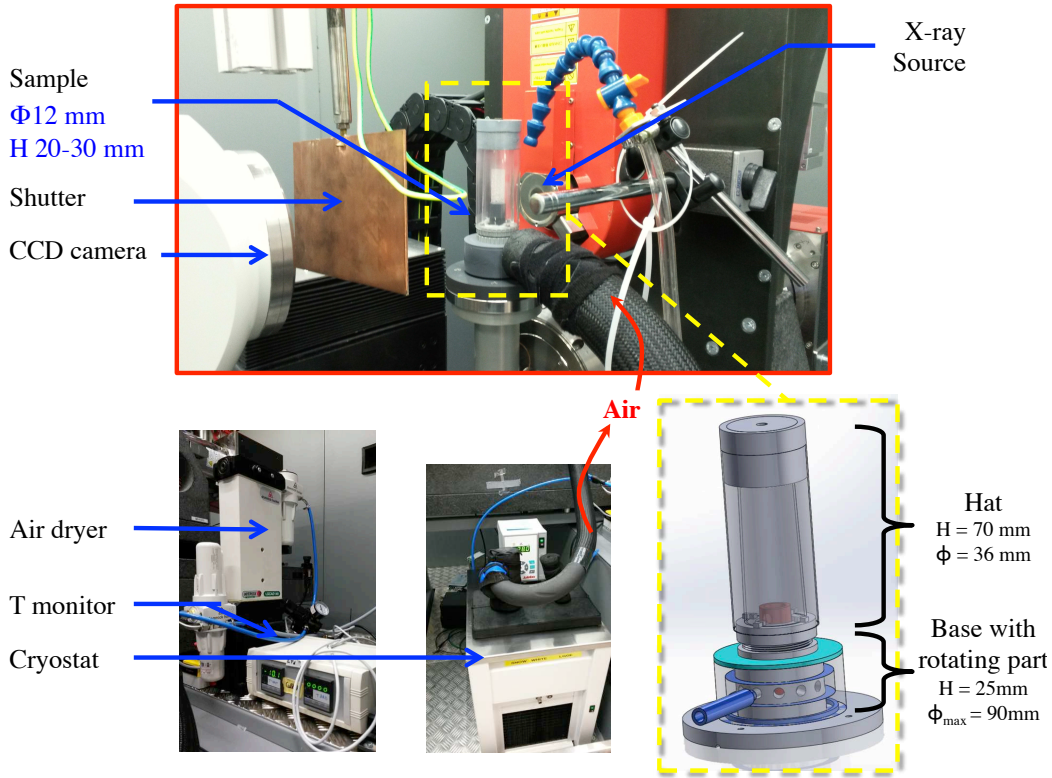


Figure 3.3: Set up in the laboratory tomograph of SIMaP. A snapshot of the cold cell designed with the CAD software SolidWorks [Solidworks, 2013].

3.3.1 Cold cell

A cold cell was developed to scan firm samples with constant negative temperature (see Fig. 3.3). It is divided in two parts. The base is fixed to the stage. The hat consists of a first tube containing the sample, and a larger second one, that mimics double-glazing. The flow of cold air is directed into the cell from the base, using a rotating part that is added to the apparatus. This allows the cell to turn with the stage, while the flow of air is fixed. A tiny hole on top of the hat enables air to escape from the cell. A thermocouple inside the cell measures the temperature which is maintained at $-10^{\circ}\text{C} \pm 2^{\circ}\text{C}$.

Holding such a temperature needs special devices. First, compressed air flows at 5 bar inside an air dryer Thermo Fischer LGCD140. It removes oils and dust, and reduces moisture of air. Thanks to this apparatus the relative humidity of the compressed air from the lab was measured down to 0.5 % in a closed box but was mostly around 1.4 %. Then the air flows into a cryostat (Julabo) set to cool it at -27°C . The output of air is thus connected to the cell. The large difference between the temperature set point and the actual temperature comes from losses and velocity of the flow that does not have enough time to be more cooled. In practice, the flow and the temperature set point are

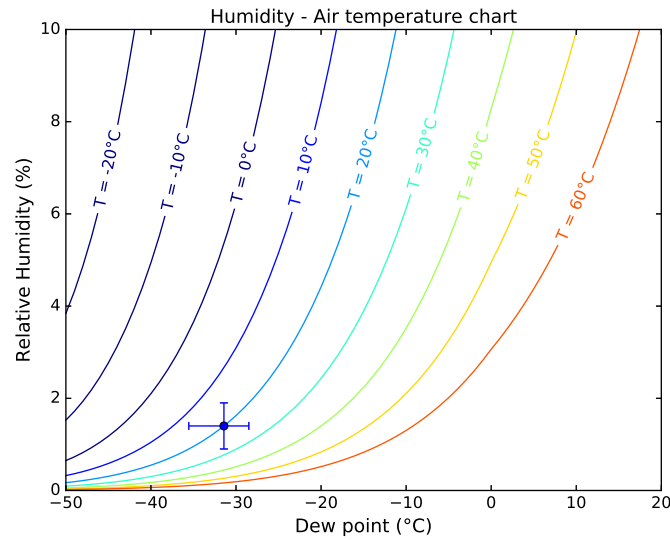


Figure 3.4: Humidity - Air temperature chart (using equations from [Lowe & Ficke \[1974\]](#)). Color lines are air temperatures. The blue point with error bars gives the humidity and temperature of the air before entering the cryostat. For such air, the dew point is $\approx -31^\circ\text{C}$ but it is preferable to set the temperature of the cryostat above -28°C .

manually selected to get a temperature of -10°C in the cell.

This configuration has several benefits. It is more convenient to set up in a laboratory tomograph than Peltier-devices such as in [Hammonds et al. \[2014\]](#) or [Calonne et al. \[2014\]](#). It does not need liquid nitrogen to work, and it does not need to roll up tubes around the stage.

There are only three issues to such a set up. Firstly, the humidity of the air must be carefully controlled. To that aim, a humidity chart Fig. 3.4 gives the window of the dew point of such dry air. It means that one should avoid to cool the air below the tip of the errorbar that is $\approx -28^\circ\text{C}$. Indeed, below this point, the air is likely to contain nucleus of ice that could get stuck inside the cryostat, preventing further air to flow, and finally increasing the temperature in the cell. Secondly, the set up is not handy, and it takes between two to three hours before the first scan. Finally, the sample may be subjected to sublimation. However section 3.3.3 proves this effect can be neglected.

X-ray micro-computed tomography was performed on samples (named **ex situ** samples) coming from a large range of depths with a refined characterization close to the depth at which closure of pores initiates. The majority of the sampling consists in samples labeled S (for small) from Dome C (DC) and Lock In (LI), named DC-S12 and LI-S12 (see Table 3.3. S12 refers to small samples with voxel side length of $12\mu\text{m}$). These were drilled with a milling machine in slices of ice core such that the cylinder axis is along the core axis (vertical axis). The uncertainty of depth after drilling in slices is estimated to

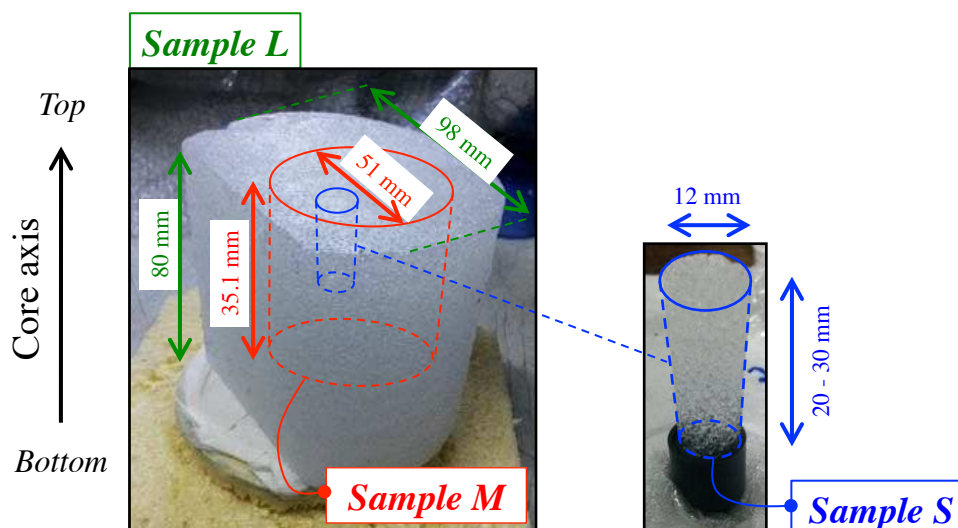


Figure 3.5: Schematic of the different sample sizes used in this work. Sample characteristics are listed in Table 3.3. In green, large samples L of the firn core were characterized by X-ray tomography for a voxel side length of $60\text{ }\mu\text{m}$. Zooming inside the L samples enables to obtain medium sized samples (typical of the size used in pycnometric measurements) named M and shown in red. These were scanned at $30\text{ }\mu\text{m}$ (DC-M30). More than 40 samples (shown in blue) of size S were machined separately and scanned at $12\text{ }\mu\text{m}$ for both sites (samples DC-S12 and LI-S12). The number at the end of names refers to the voxel size in microns.

$\pm 0.05\text{ m}$ for all Lock In samples and most of Dome C samples. A few sample depths are known at $\pm 0.5\text{ m}$. Samples were machined down to a diameter of 12 mm with a lathe. This operation was performed in a cold room at $-10\text{ }^\circ\text{C}$, usually the day before scanning.

Three samples labeled L (for large) were also characterized to investigate the scale effect. They were placed in polystyrene boxes with a eutectic cold pack inside. Samples and cold pack inertia kept the temperature below $0\text{ }^\circ\text{C}$, ranging from $-18\text{ }^\circ\text{C}$ to an observed maximum at $-3\text{ }^\circ\text{C}$ after 1.5 hours (corresponding to two scans)². Volumes M (for medium) were also locally scanned inside the L samples, i.e. a second scan is performed at higher resolution (moving from a voxel size of $60\text{ }\mu\text{m}$ to $30\text{ }\mu\text{m}$). Samples characteristics are detailed in Table 3.3 and the extracted volumes are illustrated in Fig. 3.5.

3.3.2 Image Analysis

Reconstruction is carried out with a filtered-back projection algorithm while image processing uses the free software Fiji [Schindelin et al., 2013]. Figure 3.6 illustrates the

² According to [Kaempfer & Schneebeli, 2007], section 4.5 and considering such massive sample inertia, it seems very unlikely that the microstructure evolved during the 1.5 hours of scan.

Origin	Name	Diameter / Side (mm) of ROI	ROI volume (cm ³)	Voxel size (μm)	Number of samples	Depth (m)	Remarks
DC	DC-L60		> 400	60	3	87.34; 94.5; 100.33	Slice of ice core from Dome C
DC	DC-M60	51	≈ 72	60	3	"	Zoom within the DC-L60 samples
DC	DC-M30	51	≈ 72	30	3	"	Zoom within the DC-L60 samples
DC	DC-S30	9.6	1.305	30	39	"	Sub-volumes from the DC-M30 samples
DC	DC-S12	9.6	0.782 - 1.781	12	29	22.33 - 100.38	Cylinders taken from ice core slices
DC	DC-C12	6.72	0.303	12	29	"	Cubic sub-volumes from the DC-S12 samples
LI	LI-S12	9.6	1.303 - 1.738	12	13	66 - 120	Cylinders taken from ice core slices
LI	LI-C12	6.72	0.303	12	13	"	Cubic sub-volumes from the LI-S12 samples

Table 3.3: Sample characteristics from Dome C (DC) and Lock In (LI). All samples are scanned with an acceleration voltage of 60 kV except for DC-M30 and DC-S30 samples, scanned under 80 kV. DC-L60 samples have polyhedron geometry. M and S samples are cylindrical. DC-C12 and LI-C12 are cubic (C) subvolumes of DC-S12 and LI-S12, respectively. For samples from DC-L60 to DC-S30, the Region Of Interest (ROI) comes from the same 3 samples L. DC-S12 and DC-C12 come from the same 29 samples S. LI-S12 and LI-C12 come from the same 13 samples S.

ensuing image processing. First a 3D median filter of size 3 is applied [Boulos et al., 2013] meaning that the median value of a 3 voxels side cube is chosen. This tends to reduce drastically the noise and to separate a Gaussian-type distribution of the grey level (histogram Fig. 3.6a) to two peaks on the grey level histogram (see contrast enhancement in Fig. 3.6b). The high contrast between air and ice ensures a straightforward thresholding of binary stacks of images (reconstructed set of transverse slices constituting the digitized sample).

Depending on the median type used and the numbers of outliers removed, differences could be observed on the results. Thus, various sizes of median filters were tested in this work on a sample of density $\rho = 0.786 \text{ g.cm}^{-3}$. For this sample, presented on Fig. 3.6, the standard deviation in terms of density after the thresholding of five types of median filter is less than 0.05 %. Using the same type of filter (size 3), thresholding was performed by two different scientists on three samples (the other one being Clément Ballot, [Ballot, 2016]). In any case the difference in density is less than 0.02 %.

Outliers³ of 2 or 3 voxels were removed, leading to the loss of some micro-pores of less than 36 μm in diameter. This represents less than 0.7% of the total porosity and leads to

³ Small artefacts from noise that persist after thresholding.

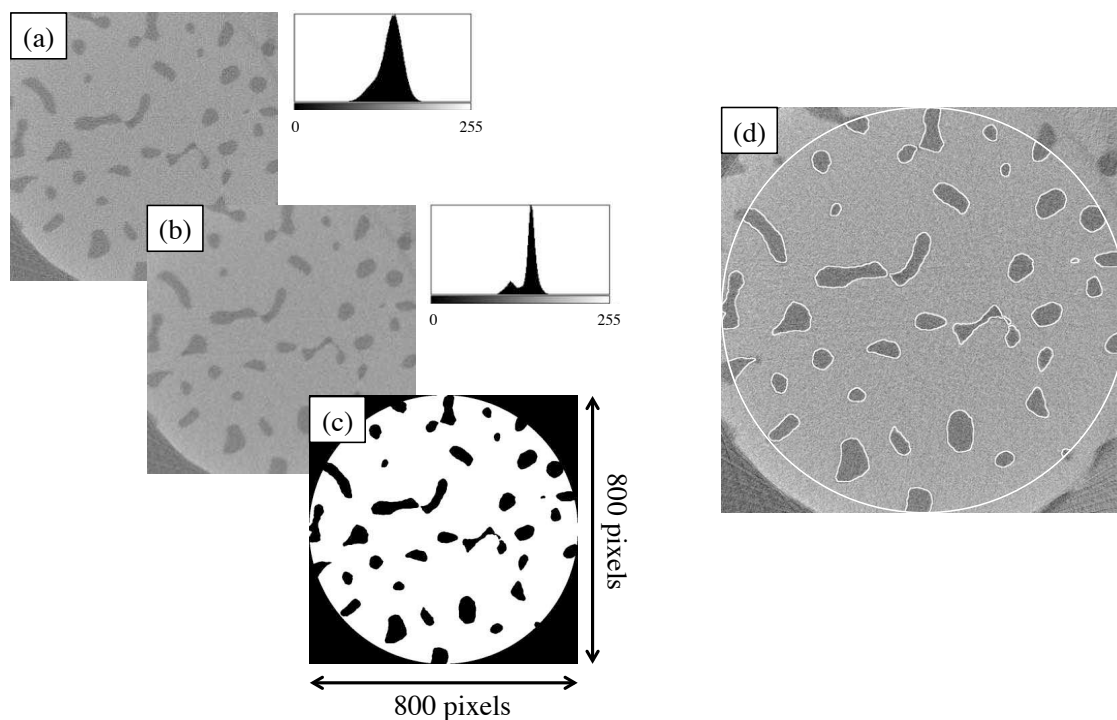


Figure 3.6: Algorithm of the image analysis process for a 79.87 m deep sample from Dome C. A slice of (a) the 8 bits stack, (b) the stack after a 3D median filter of size 3 [Boulos et al., 2013], (c) the stack after thresholding and (d) superimposed with the reconstructed binary stack. On the right side to (a) and (b), their associated grey level histogram is shown. On figure (d), the outward white contour represents the binarised extracted sub-volume (ROI).

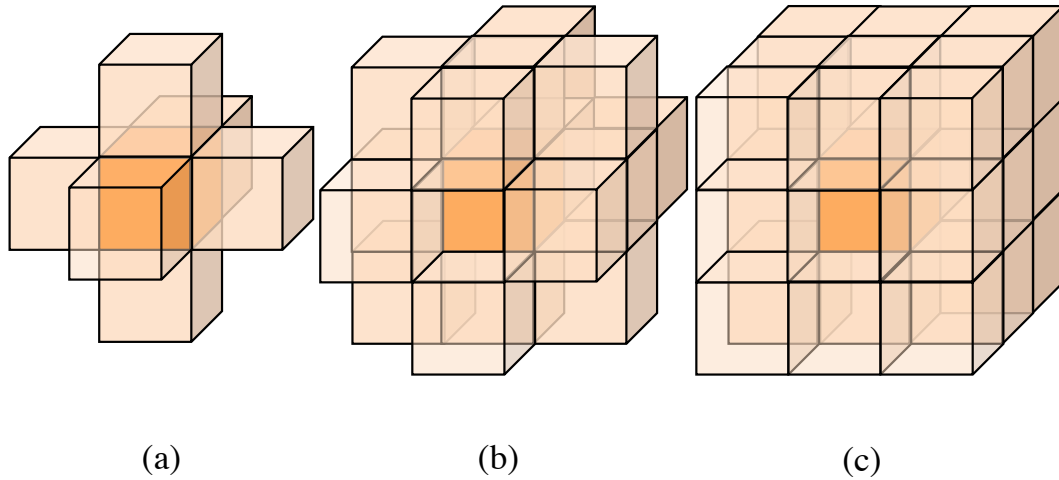


Figure 3.7: Representation of connectivities in 3D for a voxel (the orange voxel in the center) : (a) 6-connectivity (faces are connected), (b) 18-connectivity (faces and edges are connected), (c) 26-connectivity (faces, edges and nodes are connected).

an estimated 0.1% error on density. A cylindrical region of interest (ROI) is systematically extracted from the stack, to ensure that ice fragments localized on the border does not perturb the analysis (typically originating from machining).

Pore labeling is also performed on this ROI by the Analysis 3D plugin [Boulos et al., 2013]. To separate objects from one another, one can choose between the 6-connectivity (6 connected voxels), the 18-connectivity (18 connected voxels) or the 26-connectivity (26 connected voxels) as illustrated Fig. 3.7. For a voxel size of $12\mu\text{m}$, the pore surface is very well represented, thus changing the connectivity type does not alter results. The effect being negligible, the 6-connectivity was chosen in this chapter when using S12 or C12 samples. All extracted ROI's are detailed in Table 3.3.

3.3.3 Control of sublimation

To determine the errors originating from the sublimation of matter inside the cell during scanning time, from the reconstruction, and from the image processing (filtering and thresholding), tomographic scans of 5 minutes were repeated during three hours on a 86 m deep sample, first, every five minutes, then with increasing intervals of time. Figure 3.8a shows that the whole volume of snow does decrease with time and Fig. 3.8b illustrates this

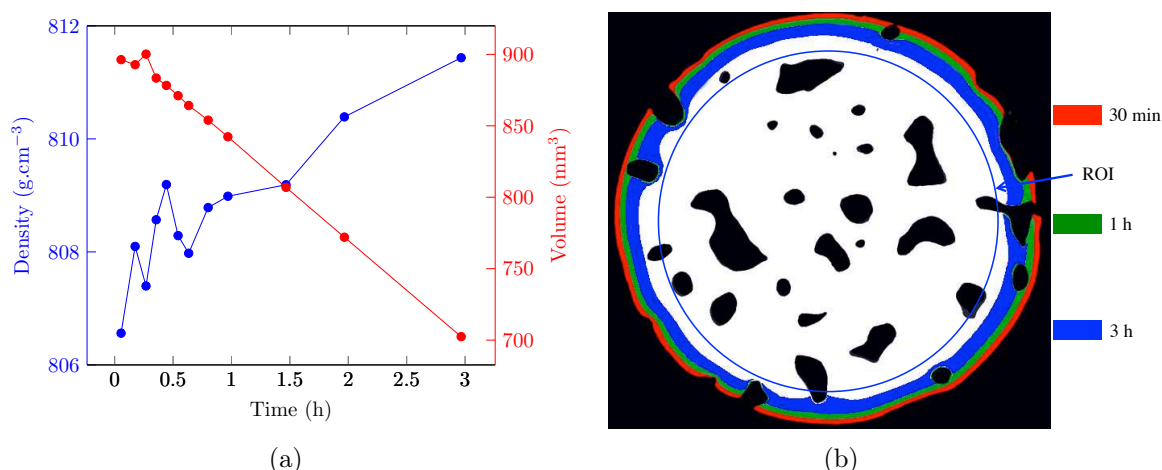


Figure 3.8: (a) Evolution of density (in blue) of the ROI for a 86 m deep sample subjected to an air flow and of the total sample volume (in red) with time. (b) 2D slices of the firn sample and the corresponding loss of matter with time [Ballot, 2016].

loss of matter on a 2D slice for different time. However the density, calculated from an extracted volume of 9.6 cm in diameter, stays about the same, ranging from 0.806 g.cm^{-3} to 0.812 g.cm^{-3} . The results on the 12 scans have shown that sublimation was limited to the outward 0.2 mm of the cylindrical sample after 30 minutes, even for samples for which percolation is significant. As borders are eliminated after extraction of the ROI (diameter 9.6 mm for samples S of diameter 12 mm), there is no influence on the pores of the dry air circulation around the firn in the cold cell (no closed pores are opening). The multiple acquisition of the same sample gives the opportunity to compute the errors combining acquisition, reconstruction and Fiji processing (median filter + thresholding + outliers removal) for such a scan.

Several properties are determined in this work such as the density, the specific surface area (SSA) or other pore related parameters. The SSA is defined as the surface of the pores over the total sample volume. The surface is computed with the marching cube algorithm [Lorensen & Cline, 1987], and the SSA assesses the air-ice interactions (e.g., the SSA is used to compute the snow-to-atmosphere flux of adsorbed molecules on snow [Domine et al., 2008] or even to work out the grain size of firn cores⁴ [Linow et al., 2012]). The volume used to compute porosity is calculated by counting voxels. The closed porosity ratio and the connectivity index (the ratio of the volume of the largest pore with the total pore volume) are also systematically calculated. We define a closed pore as a pore that does not touch the border of the ROI at the sample resolution. Its pore volume fraction is named the closed porosity ratio (in per cent). Results for these parameters are discussed

⁴ In Linow et al. [2012], grain size refers to snow grains, containing multiple crystals of ice. In our work, grain size is associated to the size of one ice crystal

in section 3.4

The 12 successive scans of the same sample are used to compute standard deviations. At 86 m depth, absolute errors are 0.0012 g.cm^{-3} on density, 0.008 mm^{-1} on the specific surface area (SSA), 0.068 % for the connectivity index and 0.25 % on the closed porosity ratio, while relative standard errors are respectively 0.15 %, 0.81 %, 0.11 % and 3.1 %. Since this procedure was performed on only one sample, we assume that the relative errors associated to each microstructural parameter are the same for all depths. In other words, we assume that the precision (from X-ray scans and image processing) on a given property is independent of depth for all samples S12.

3.4 Representativeness of morphological parameters

Conducting a refined X-ray characterization and comparison of polar sites requires a correct estimation of possible errors. Several sources of errors exist which do not have the same influence on the results. Errors can come from spatial heterogeneity, size of the ROI, image resolution, image processing and labeling assumptions.

This section focuses on giving estimates of these errors on the important parameters studied: the density, the closed porosity ratio, the connectivity index and the specific surface area. These errors depend on depth, except for the processing ones for which we assume an independent relative value. Results are discussed and some advices are given for future tomographic-based studies that should include error and variability evaluation.

3.4.1 Density

Densities were determined directly from binary images using $\rho_{ice} = 0.917 \text{ g.cm}^{-3}$ and are shown against depth for both sites in Fig. 3.9a. We also attempted to measure density by weighting samples as done in Gregory et al. [2014]. However, we observed that this method led to very large dispersion, which may be linked to a too small sample volume. In any case, we chose to link the density measurement directly to the local scanned volume. We believe that this is preferable than to give a density originating from a much larger volume as carried out by Gregory et al. [2014], which may not be representative of the scanned sample.

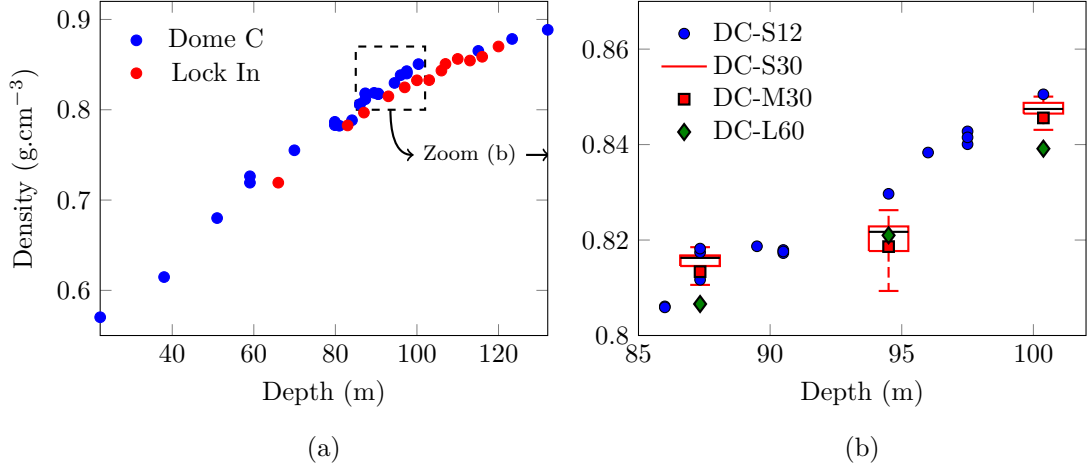


Figure 3.9: (a) Evolution of density with depth for Dome C and Lock In. (b) Zoom-in from (a) focused on Dome C with different sample sizes. Boxplots contains data from DC-S30 samples. Hereafter, boxes represent lower and upper quartiles, the black lines inside being the median values. The confidence interval is set to account for all the data (no outlier data).

Fig. 3.9a illustrates the increase in density with depth. It also shows that for given depth, the density at Dome C is larger than at Lock In. As stated above, the relative error in measuring density is less than 0.15 % and thus is not shown here. For approximately the same depth, differences between the density of Dome C and Lock In are between 1.8 and 2.6 % (in the range of depths studied).

Densification of firn to ice leads to a transition where a pore that was open and that enabled air to flow, start to separate in different pores. This closure of pores occurs all along the firn core, but is more pronounced around the close-off, typically when density ranges between 0.80 and 0.84 g.cm^{-3} where we gathered more data points. Fig. 3.9b is a zoom-in on this region for Dome C. Three DC-S12 samples were extracted from the same slice of ice core at 86 m, 91 m and 98 m depths. These triplets of points are barely distinguishable. The red boxplots shown in this figure represent the extrema on 13 sub-volume measurements (small DC-S30 samples) originating from a medium-size DC-M30 sample. These boxplots show dispersion inside medium-sized samples (volumes of 1.3 cm^3 inside 72 cm^3). The difference between the maximal and minimal values for samples from the same depth is less than 2.5 % (maximum variability is obtained at 94.5 m). Thus, the effects of spatial heterogeneities and of the size of the ROI are limited but are the main contributions for the errors on density. Indeed, three additional samples were scanned at a voxel side length of 12 and 30 μm and exhibited differences of less than 0.1 % for density. Similarly, the difference for densities of the samples DC-M30 and DC-M60 is less than 1 % (from Table 3.4). In conclusion, the density is known quite precisely, and DC-S12 samples are large enough to be considered representative of the density.

3.4.2 Closed porosity

The closed porosity ratio (CP) is obtained by dividing the total volume of closed pores in the ROI by the total volume of pores. Separation of pores arises by pinching of the channel linking two larger globular portions of the pore. Fig. 3.10 shows the evolution of closed pores (in red) within the firn open pore network for Dome C and Lock In. The number of closed-pores increases with depth, as separation persists even for pores already closed.

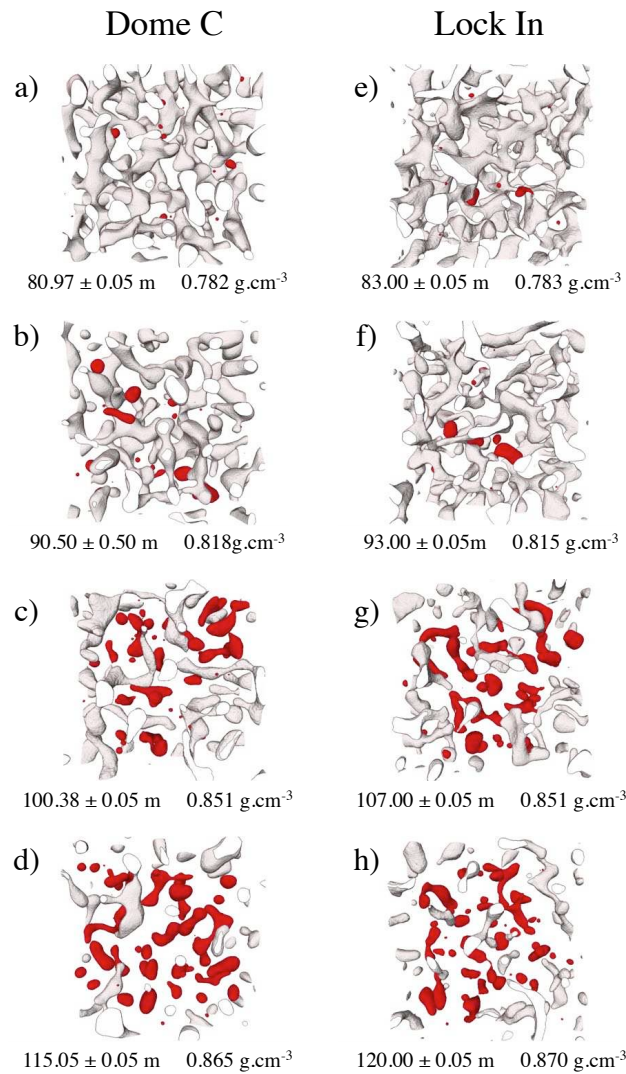


Figure 3.10: Evolution of closed pores (red) within the firn porosity network (white) for different depths at Dome C and Lock In sites for DC-C12 and LI-C12 samples (cross-section dimension is 6.72x6.72 mm²). Note that (a-e), (b-f), (c-g) and (d-h) have approximately the same density. From these views, there is no clear microstructural difference between Dome C and Lock In for those samples with the same density.

The closed porosity percentage (of pore volume) for DC-S12 samples on Fig. 3.11a exhibits a steep increase starting from 80 m depth (about 0.78 g.cm^{-3}). As in Fig. 3.9b, at 86 m, 91 m and 98 m depths, three DC-S12 samples were extracted from the same slice of ice core to evaluate dispersion (area A in Fig. 3.11a). The DC-S30 samples are represented by boxplots which are also large (especially at 94.5 m depth). Boxes represent lower and upper quartile of the distribution of the closed porosity ratio, with median value in black. The proposed confidence intervals take into account all data points. Spatial heterogeneities on the closed porosity ratio strongly depend on depth. This variability is particularly pronounced at 95 and 98 m, but not that much when closed pores are few (at 87.34 m) or after the COD as defined by the last sampling depth (sample from 100.33 m and COD at 99.5 m [Landais et al., 2006; Witrant et al., 2012]). This leaves two possibilities. Either the firm is very heterogeneous horizontally, meaning that a single DC-S12 sample is not representative enough for the closed porosity ratio of the firm for this particular depth, either our definition of a closed pore is not appropriate, because of the sample boundary conditions. Note that for such depths (95 and 98 m), the mean size of a closed pore is still certainly too large to hold inside the DC-S12 samples.

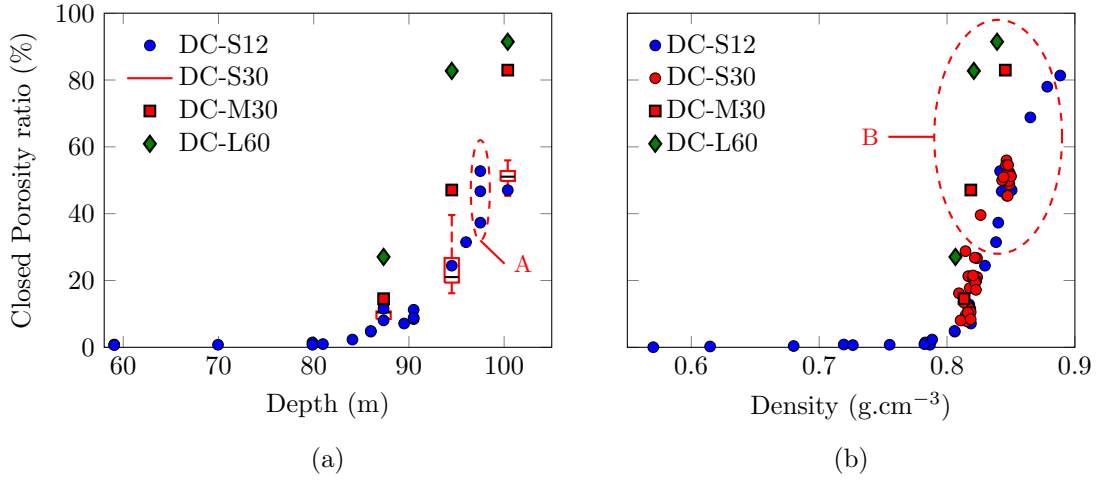


Figure 3.11: Evolution of the closed porosity in percentage of total porosity with (a) depth and (b) density. The effect of sample size is striking as the larger the size the higher the closed porosity ratio. The variability of the closed porosity of various samples from the same depth are represented by red boxplots on (a) and red dots on (b) as the densities are not exactly identical.

ROI size also has a strong influence on the estimation of the closed porosity ratio. Indeed, the larger the volume, the larger the closed porosity ratio (Fig. 3.11). Note that this effect is more pronounced at 100.33 m (when comparing samples DC-M30 and DC-S12 samples) than at 87.34 m depth. Errors due to the coarsening in resolution are summarized in Table 3.4 and reveal a large effect on the results between the DC-M30

and DC-M60 samples⁵. The closed porosity ratio is always larger when increasing the voxel size, but this rise is not as marked as the one implied by the volume of the ROI. For labelling, the type of connectivity (6 or 26) is also investigated, and its influence on the results is limited (for all resolution considered). Using 26 connected voxels does enhance the possibility for different pores to be more connected than it is with only 6 connected voxels. It is especially true at the depths 87.34 m and 94.5 m as this is where pinching is very pronounced and on the verge to cut pore channels (the COD being almost reached). Thus a change in the definition of the pores as implied by the use of 26 connected voxels might connect some closed pores together or to the surface. Similarly, downgrading the resolution means a different threshold value, thus a possible separation of pores or channels. This seems to be especially true for low resolution, e.g. here for a voxel size of 60 μm . Indeed, differences related to voxel size between the same samples DC-S12 and DC-S30 are small, as the relative error for the closed porosity ratio is less than 7 % with respect to the 12 μm voxel side length. This is relatively low compared to the extent of the box plot represented Fig. 3.11a, which spans from 16 % to 40 % at 94.5 m depth. All the samples and the sub-volumes extracted were compiled with density on Fig. 3.11b. While the smallest volumes seem to follow a trend, the larger still spread (area B in Fig. 3.11b). From this plot it is impossible to determine at which density or closed porosity ratio, the close-off could be defined. Considering air content in firn, the model from Goujon et al. [2003] assumes the volume fraction of closed pores is about 37 % at close-off depth (defined as an instantaneous close-off from measurements [Martinerie et al., 1992, 1994], and referred later by COD_G), while DC-L60 samples showed that 82 % of pores are closed at 95 m depth for example. Such a high value could suggest that the close-off is at lower depth than commonly accepted. However the density of this sample ($\rho = 0.821 \text{ g.cm}^{-3}$) is below the close-off density obtained by Martinerie et al. [1992] ($\rho = 0.840 \text{ g.cm}^{-3}$), and air was pumped down to 99.5 m [Landais et al., 2006], which is five meters below. Additionally, the rather large voxel size leads to separation of pores that are linked by channels whose diameter are below the image resolution, increasing artificially the closed porosity ratio. Therefore, the rather large errors on the closed porosity ratio of DC-L60 calls for caution in interpreting results (see Table 3.4). In short, the appropriate use of the closed porosity ratio requires large volumes associated with high resolutions.

3.4.3 Connectivity Index

In this section, we propose an other indicator of the pore closure, which is much less sensitive to the source of errors, especially from the volume size. The connectivity index

⁵ DC-M60 and DC-M30 have the same ROI, but are scanned for a voxel side length of 30 μm and 60 μm respectively (see Table 3.3)

(CI) - volume of the largest pore divided by the total volume of pores - was introduced by Babin et al. [2006] to depict the void coalescence in bread. It proved to be useful (under the name of "interlinkage parameter") to quantify the coalescence of cavities during superplastic deformation of an aluminum alloy [Martin et al., 2000], or to be used as a criterion to optimize box sizes when smoothing density maps of graphite with inclusions [Babout et al., 2006]. This index essentially describes, as the closed porosity ratio does, the evolution of closed pores. However, it is not dependent on sample boundary conditions, since all pores are considered. This is critical for small volumes as the ratio of surface over volume becomes significant. One major setback is that it is very dependent of the statistical size of the pores in terms of volume.

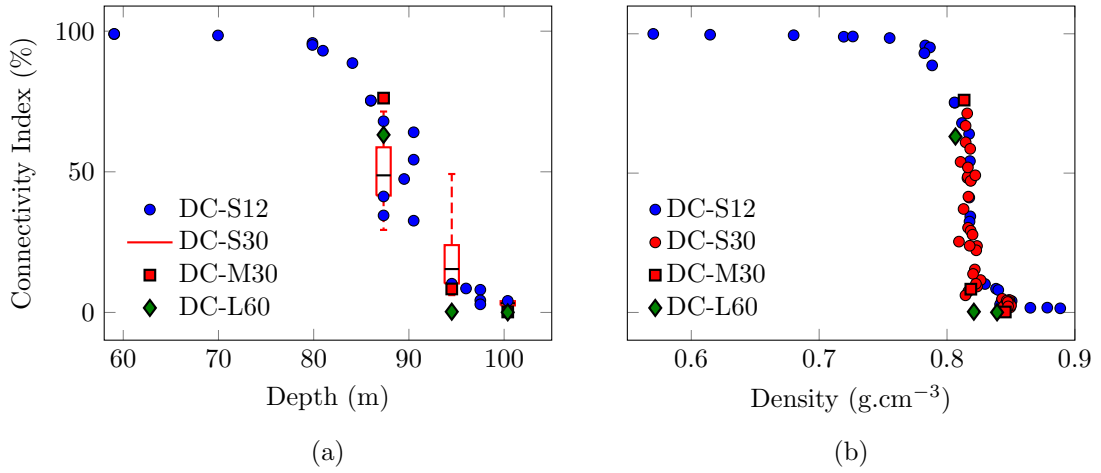


Figure 3.12: Evolution of the connectivity index with (a) depth and (b) density. When it drops, the variability between samples is important, but declines when the connectivity index tends to 0 %. (b) All points are aligning on a master curve. The variability of the connectivity index of various samples from the same depth are represented by red boxplots on (a) and red dots on (b) as the densities are not exactly identical.

As shown in Fig. 3.12, the connectivity index is maximum and equal to 100 % when the porosity is totally open (one large pore overcomes all others), while it is 0 % when all the pores are closed. The curve drops around 0.78 g.cm^{-3} ($\approx 80 \text{ m}$), and stagnates from 0.85 g.cm^{-3} (100 m). Sub-sampling leads to large boxplots thus large variability at 87.34 and 94.5 m, while it is much smaller at 100.33 m. Thus spatial heterogeneity is pronounced during the fall of the connectivity index. DC-M30 or DC-L60 samples are inside or close to the boxplot, while they were much more remote in Fig. 3.11. This means that the effect of ROI volume is strongly reduced with the connectivity index. Comparing resolution and type of connectivity of the DC-S12 and DC-S30 samples, results for the connectivity index are similar to the closed porosity ratio (low errors). Table 3.4 also lists errors between the DC-M30 and DC-M60 samples for the connectivity index. Overall,

these ROI's fall in the box plots of the DC-S30 samples.

In conclusion, variability of the connectivity index mostly comes from the spatial heterogeneity and in a less extent from the voxel size. It is however much less sensitive to the volume of the samples, the resolution or the type of connected voxels than the closed porosity ratio. Interestingly, Fig. 3.12b indicates that the connectivity index points fall on a master curve when plotted against the density. In particular, a clear drop of the connectivity index is observed at a density of about 0.83 g.cm^{-3} . Above this density, samples DC-L60 and DC-M30 exhibit no large pores anymore. At Dome C, Landais et al. [2006] measured the COD at 99.5 m and Goujon et al. [2003] predicts its density $\rho_{Gc} = 0.840 \text{ g.cm}^{-3}$ (at -55°C from Eq. (1.2)) consistently with the data used to parameterize the air isolation depth in Martinerie et al. [1992]. Thus, according to Fig. 3.12, the connectivity index is a good predictor of the close-off.

3.4.4 Specific surface area

The SSA involves a measurement of the surface of pores. This measurement is voxel size dependent as it depends on surface roughness. However, as shown by tables 3.4-3.5, differences of voxel size do not lead to great errors. Changes due to ROI volume and connectivities are also not significant for the SSA. Results are very similar to the density, however the spatial heterogeneity is more marked. Indeed, in the worst case scenario, relative differences for the same depth can reach 20 %. All the other sources of errors give results in the variability of the spatial heterogeneities. Finally, all points are known very precisely as the pores are defined by a tremendous amount of voxels. In the following, the surface-area-to-volume ratio is used instead of the SSA for comparison with Gregory et al. [2014], but is worked out the same way, however the volume considered is the porous phase instead of the whole volume of the ROI. The relative standard error of surface-area-to-volume ratio (S/V) is 0.47 % (less than for the SSA). Similarly, the SMI (described in section 3.6) is computed using the pore surface area. Consequently, errors on each point are negligible and not shown.

Depth (m) Vox. size (μm)	87.34			94.50			100.33		
	30	60	Abs. Err.	30	60	Abs. Err.	30	60	Abs. Err.
$\rho \text{ (g.cm}^{-3}\text{)}$	0.8134	0.8076	-0.0058	0.8186	0.8188	+0.0002	0.8456	0.8397	-0.0059
SSA (mm^{-1})	0.970	0.954	-0.016	1.015	0.973	-0.042	0.711	0.713	-0.002
CP (%) : co-6	14.55	23.23	+8.68	47.08	69.06	+21.98	82.96	83.62	+0.66
CP (%) : co-26	14.41	21.65	+7.24	46.58	65.67	+19.09	82.87	83.22	+0.35
IC (%) : co-6	76.20	60.37	-15.83	8.35	1.46	-6.89	0.16	0.17	+0.01
IC (%) : co-26	76.60	62.82	-13.78	14.74	2.08	-12.66	0.16	0.17	+0.01

Table 3.4: Results and absolute errors between DC-M30 and M60 samples. Results with 6 and 26 connected voxels are shown.

Depth (m)	84.07	Abs. Err.	97.5	Abs. Err.	Rel. Err.
ρ (g.cm ⁻³)	0.7884	± 0.0012	0.8415	± 0.0013	0.15 %
SSA (mm ⁻¹)	1.192	± 0.010	0.750	± 0.006	0.81 %
S/V (mm ⁻¹)	8.478	± 0.040	9.108	± 0.043	0.47 %
CP (%) : co-6	2.32	± 0.07	52.74	± 1.63	3.1 %
CP (%) : co-26	2.32	± 0.07	52.03	± 1.61	3.1 %
IC (%) : co-6	88.654	± 0.098	2.883	± 0.003	0.11 %
IC (%) : co-26	88.654	± 0.098	2.883	± 0.003	0.11 %

Table 3.5: Absolute and relative errors for DC-S12 samples.

3.4.5 Key results on error estimations

To sum up, this section distinctly separates the errors made on the calculated microstructural parameters when choosing the resolution, the type of connected voxels and the size of the sample volume. Table 3.4 and Figs. 3.11 and 3.12 showed that the variability of the measurements can be important and is dependent on the depth of the sample. The section also gives the estimation of some calculated parameters along with their errors for all the studied samples. The closed porosity ratio was shown to be completely dependent on ROI size, voxel size and spatial heterogeneities. The proposed connectivity index is a more discriminant parameter to describe the pore closure, as it is foremost dependent on the spatial heterogeneities.

In the following, only samples whose voxel side length is 12 μm are studied and compared. In order to avoid to overload the following figures, the Table 3.5 gives an idea of the absolute uncertainties for two distinct depths of the DC-S12 samples.

3.5 Representative Volume Element in ice

Section 3.4 discussed the representativeness at the scale of samples. In other words it focused on the variability from one sample to another, in particular when size varied. Still the representativeness of a property for one sample needs to be assessed. The problem can be summed up as a question : can we extract a sub-volume from one sample that has the same properties than the total sample volume ? Section 3.4 clearly showed that for the closed porosity ratio, and to a lesser extent for the connectivity index, the DC-S30 exhibited different results than the DC-M30. This should not be very different when extracting sub-volumes from DC-S12 samples. However other properties such as the density or the specific surface area can be checked. Nevertheless a more formal framework should be first described.

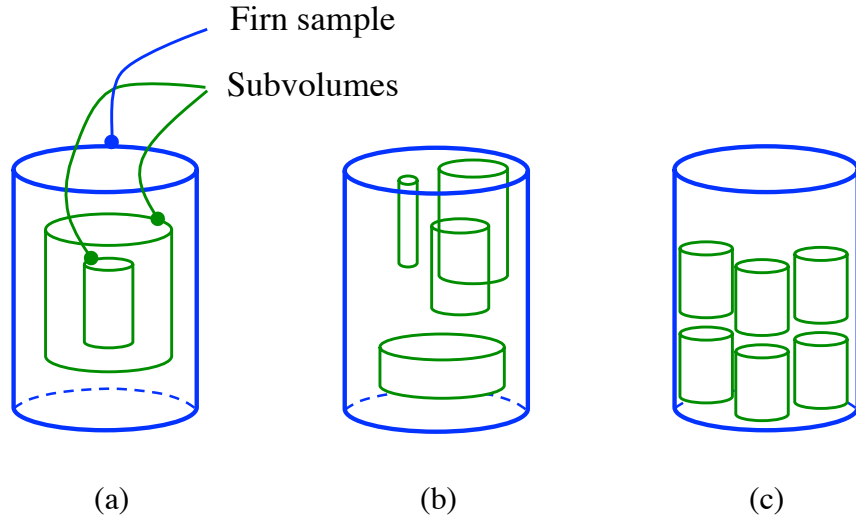


Figure 3.13: Different methods to find the RVE. (a) is called the "deterministic method", (b) the "randomly distributed method" and (c) the "statistical method". All methods aims to determine if the green subvolumes have the same properties than the total sample volume in blue.

3.5.1 Determination methods

An accepted definition of the Representative Volume Element (RVE) is given by [Kanit & Forest \[2003\]](#) : a volume of heterogeneous material sufficiently large to be statistically representative of the microstructural heterogeneities of the material. A RVE is always related to a given property. Three different ways of finding a RVE were numerically tested in this work. The sketch [3.13](#) illustrates this method. First, the extracted sub-volumes were numerically increased by an homothetic transformation in Fig. [3.13a](#). Second, randomly sized subvolumes were extracted from the sample (Fig. [3.13b](#)). Third, a statistical approach to extract non-overlapping subvolumes was used (Fig. [3.13c](#)).

However, the question is: what does "sufficiently large" stand for ? Depending on the property, the RVE can be different. Moreover, finding a RVE for a given property depends only on the error that is acceptable⁶ on the final property value. Figure [3.14](#) illustrates this for the calculation of the relative density ρ_r on all subvolumes for the three methods sketched in Fig. [3.13](#). For a given error of 0.5 % on the relative density of this sample (i.e. $\rho = 0.8383 \pm 0.0042 \text{ g.cm}^{-3} \rightarrow \rho_r = 0.9141 \pm 0.0046 \text{ g.cm}^{-3}$), determining the RVE consists of finding the smallest volume which density is contained within the error bars. In Fig. [3.14a](#) and [3.14b](#) the large red points represent the largest volume whose density is not contained within the error bars. Therefore, for the density of this specific sample, and

⁶ An acceptable error is here an arbitrary choice.

a given relative error of 0.5 %, the RVE is found between these two values. For Fig. 3.14a, it is between 373 and 593 mm³, and for Fig. 3.14b it is above 904 mm³.

These results show quite significant differences between the deterministic (3.14a) and the randomly distributed methods (3.14b). However, Fig. 3.14a could be more discretized with more studied volumes and then could exhibit a larger RVE. Despite being very well discretized (more than 350 volumes), the diagram 3.14b suffers from an undeniable bias because of overlapping samples. Thus, it is safer to determine the proper RVE by using a fit on the lower points of this curve, or on all the points from 3.14a. Figure 3.14c does show a third possibility to find the RVE. This statistical approach uses 4 different sizes of subvolumes. For each size, the maximal number of non-overlapping cylinders was extracted from the sample. This gives a large variability on measurements. However the small red dots show that the mean of each set of measurements is safely included within the error bars. Therefore, the statistical RVE is much smaller than those obtained by the first two other methods. The values obtained for the RVE are given in the following sections.

3.5.2 Formal description of statistical RVEs

From Lantu  joul [1991] and Kanit & Forest [2003]; Kanit et al. [2006], the integral range A_n is a domain size in which the measured properties have a good statistical representativeness such that this domain could represent a larger one. For an ergodic random structure (randomly distributed), these authors claimed that it is a practical measurement of a RVE, as it is used at the scale of the phenomenon. However ergodicity of the structure should be insured. One good estimation of the ergodicity is the covariogram, as already discussed in section 2.3.2.5. The autocorrelation function was thus worked out, and a typical covariogram of one tomographic slice is shown in Fig. 3.15.

One should note that the covariance length obtained for this particular sample ranges between 515 and 734 µm. This length is often used when describing RVE [Rolland du Roscoat et al., 2007]. In our case there is between 16 and 23 heterogeneities in the diameter of the sample. The covariogram clearly indicates that this slice contains enough heterogeneities to be representative in terms of density. Covariance length were also calculated in 3D during the internship of Lucas Milliancourt [Milliancourt, 2017] for a limited amount of samples. It was shown that the porous network is slightly anisotropic depending on the depth of the sample as the covariance length in the core direction is a bit larger than the average of the two other directions ($\approx 5\%$)⁷. However, the mean covariance length was evaluated in average to about 480 µm.

⁷ An appropriate assumption is that pores are more likely to be oriented with the compression direction, i.e. the core axis, because of the vertical stress σ_{zz} on grains.

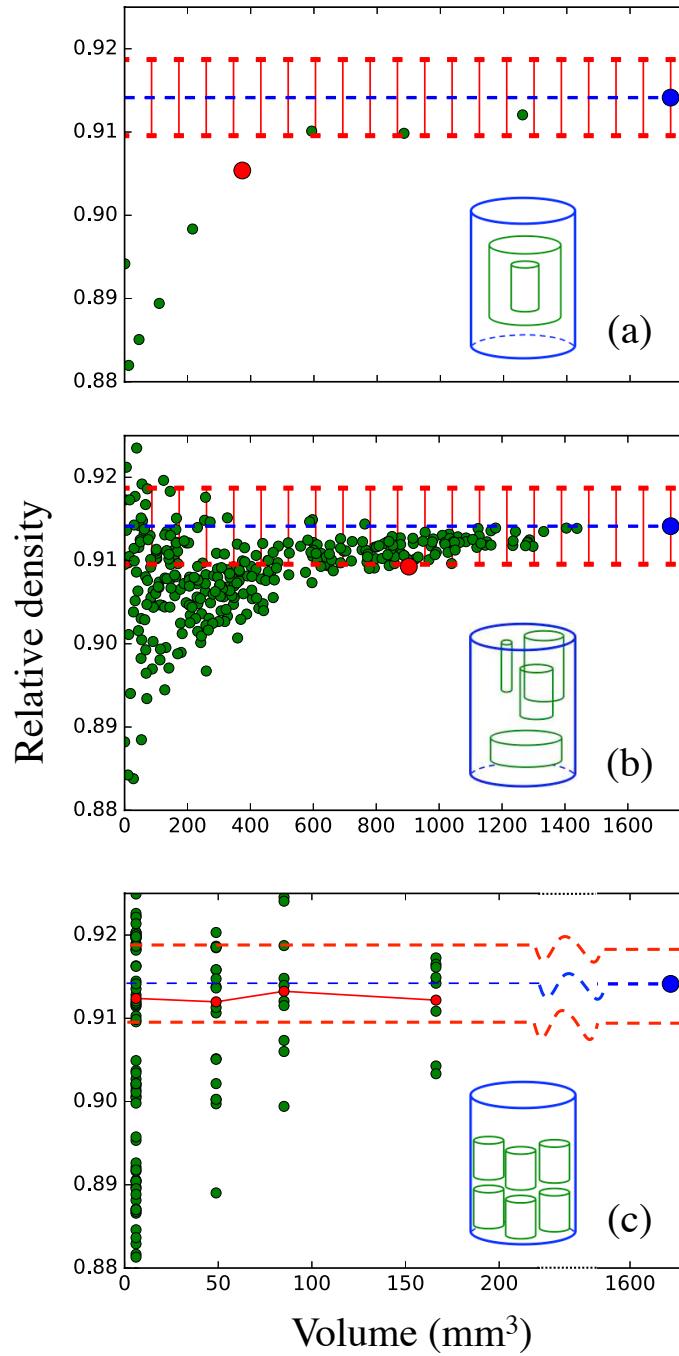


Figure 3.14: An example of RVE determination for a DC-S12 sample from 96 m depth. ρ_r evolution with (a) the deterministic method, (b) the randomly distributed method and (c) the statistical method. The blue dashed line finishing by a point on the three curves corresponds to the density of the total sample volume. The green dots represent the density for all subvolumes. The red error bars on (a) and (b) or dashed line on (c) display the 0.5 % relative error on the density of the total sample volume. Large red points on (a) and (b) depict the largest volume whose density is not contained within the error bars. Small red dots on (c) are the mean density of each set of measurements.

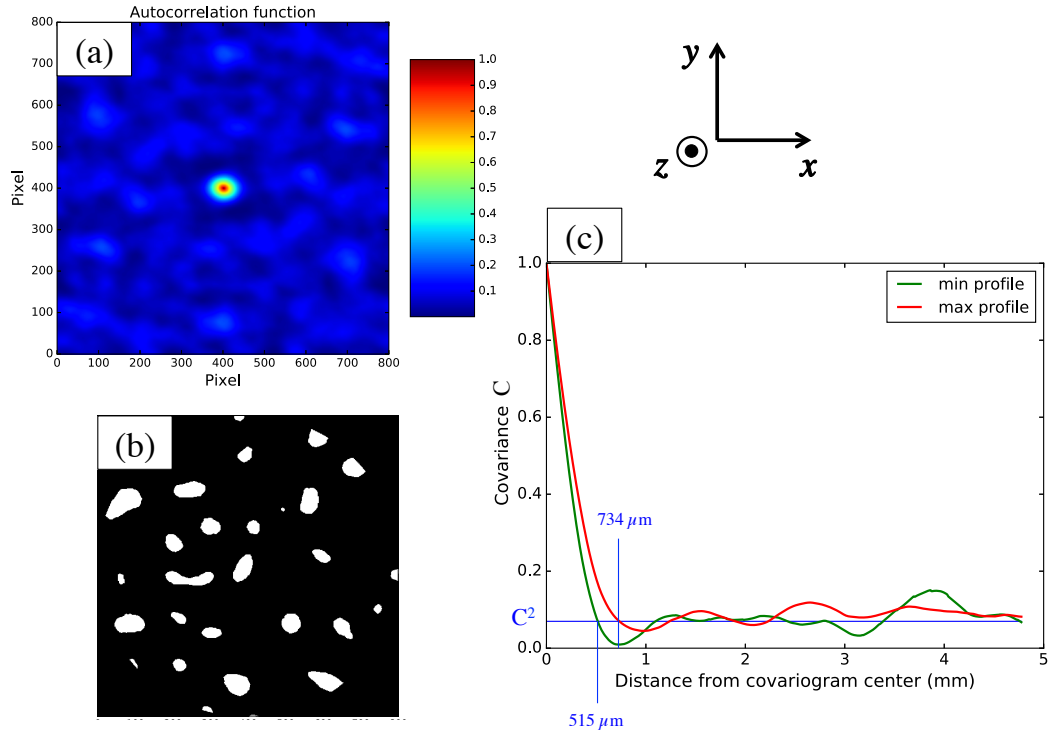


Figure 3.15: (a) Autocorrelation function associated to the slice (b) from a DC-S12 sample 100.33 m deep, as well as its covariogram in the (\mathbf{x}, \mathbf{y}) plane. The covariogram displays the "min" and "max" profile which represents the smallest and largest distance between two heterogeneities as well as their intersection with the squared covariance C^2 . The covariogram procedure used here computes lines in all directions around the center in the (\mathbf{x}, \mathbf{y}) plane, hence the two plotted profiles (which are not x or y-directed profile). Figures are plotted thanks to the AITA toolbox written by [Chauve \[2017a\]](#).

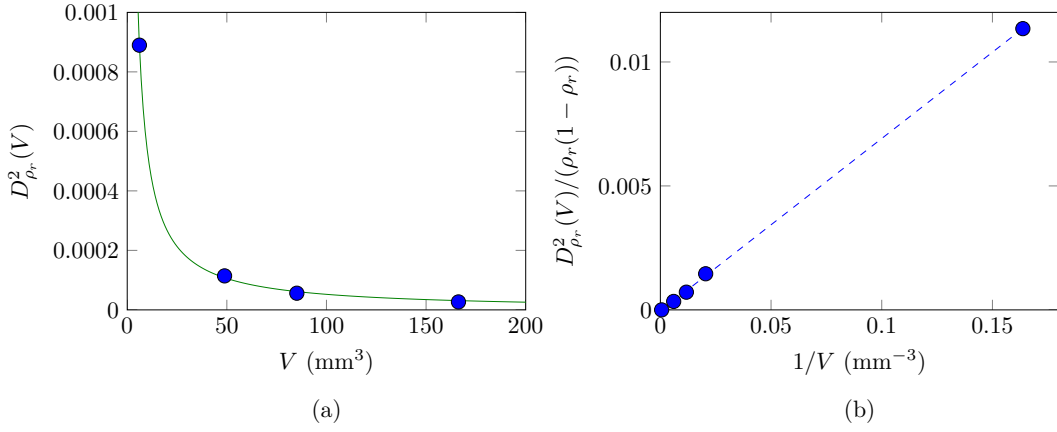


Figure 3.16: (a) Variance and fit for each tested subvolume. (b) Fit of A_3 .

Let be X a given property :

$$\varepsilon_{rel} = \frac{\varepsilon_{abs}}{X} = \frac{2D_X(V)}{X\sqrt{n}} \quad (3.1)$$

with ε_{rel} and ε_{abs} the relative and absolute errors, and n the number of subvolumes. $D_X(V)$ is the square root of the variance related to V by :

$$D_X^2(V) = D_X^2 \frac{A_3}{V} \quad (3.2)$$

with $D_X^2(V)$ the variance of the property X for the subvolume V and A_3 the integral range in 3D. In the case of a two-phase material, the point variance D_X^2 becomes for the volume fraction $X = \rho_r = 1 - \phi$:

$$D_{\rho_r}^2 = \rho_r(1 - \rho_r) \quad (3.3)$$

Combining Eqs. (3.2) and (3.3) leads to :

$$\frac{D_{\rho_r}^2(V)}{\rho_r(1 - \rho_r)} = \frac{A_3}{V} \quad (3.4)$$

From the fit illustrated in Fig. 3.16b, $A_3 = 6.9 \cdot 10^7 \text{ } \mu\text{m}^3$, it is possible to find the RVE for various acceptable relative errors and for a given n , or to find how many subvolumes of given sizes are needed to approach a relative error. This is particularly helpful when running numerical simulations. Thanks to parallel computing, it is faster to perform simulations on numerous small volumes than on a few very large ones. Table 3.6 gives the number of subvolumes required (if this subvolume has a purpose of V_{RVE}) for different

Relative error	0.5 %	1 %	2 %	5 %
$V = 6.11\text{mm}^3$	172	43	11	1
$V = 48.85\text{mm}^3$	22	6	2	1
$V = 85.13\text{mm}^3$	13	3	1	1
$V = 166.25\text{mm}^3$	7	2	1	1

Table 3.6: Number n of necessary subvolumes to approach the mean value of the relative density for relative errors of 0.5, 1, 2 or 5 %, for a DC-S12 sample from 96 m depth.

relative errors on the relative density and for given volumes V as an example :

$$n = \frac{4(1 - \rho_r)A_3}{V_{RVE}\rho_r\varepsilon_{rel}^2} \quad (3.5)$$

For the sample used in Figs. 3.14 and 3.16, it was possible to extract only 130 subvolumes of 6.11 mm^3 , 20 of 48.85 mm^3 , 10 of 85.13 mm^3 and 8 of 166.25 mm^3 . But, the formalism presented here and illustrated numerically in Table 3.6 indicates that this number is largely sufficient to be representative for the relative density property. Nevertheless, results for the 0.5 % relative error mean that this number is a bit short, while Fig. 3.14c states otherwise. Interestingly, if we directly search for the number of subvolumes needed to approach the correct density value at 0.5 %, much less subvolumes are necessary than predicted as shown by Fig. 3.17. Indeed, the maximum observed numbers of subvolumes necessary before having a mean relative density close to the true relative density⁸ at 0.5 % are 50, 11, 5 and 3 for respective subvolumes of 6.11, 48.85, 85.13 and 166.25 mm^3 . Figure 3.17 represents one set of these subvolumes (for sizes 6.11 and 48.85 mm^3). From this discussion and Figs. 3.14c and 3.17, a good statistical V_{RVE} for density and for this specific depth is about 500 mm^3 . Results on the SSA are very similar in terms of subvolume variability but for much larger errors. For the same sample and a typical SSA of 0.78 mm^{-1} , the choice of a $V_{RVE} = 500\text{ mm}^3$ leads to relative errors around 5 %, thus 10 times larger.

Accordingly, in the following we will focus on method (c) from Figs. 3.13 and 3.14 and especially on the practical results for other properties such as the closed porosity ratio and the connectivity index. But we will not estimate the V_{RVE} from statistical theory.

⁸ The true relative density is the relative density of the total sample volume.

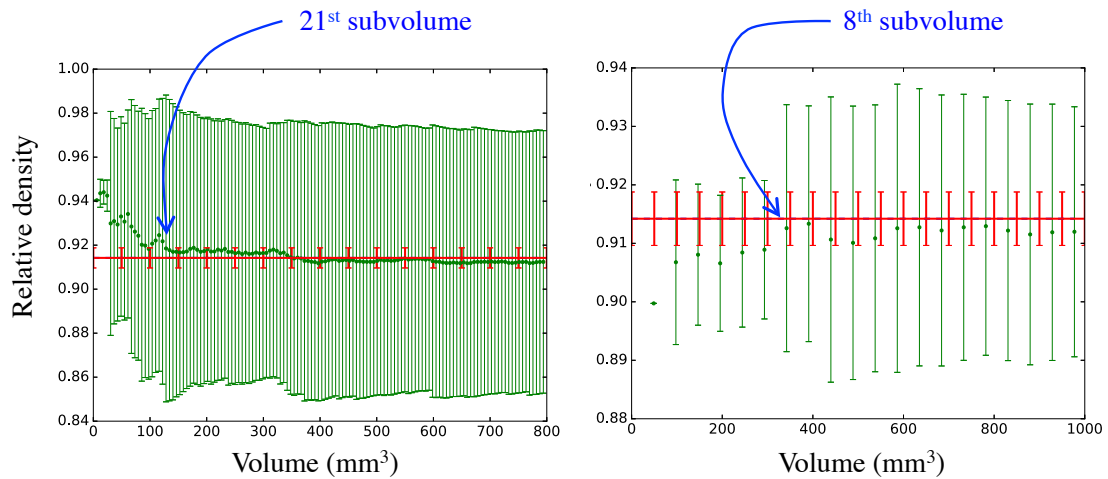


Figure 3.17: Green dots are mean relative densities for the statistical method using non-overlapping subvolumes of size (a) 6.11 mm^3 and (b) 48.85 mm^3 with their associated interval of confidence (2σ) for a DC-S12 sample from 96 m depth. As the volume increases, a new dot representing a new volume appears. Red error bars represent the errors at 0.5 % of the true density. For the smallest size, 21 subvolumes are necessary for the mean relative density to be included within the error bars. It represents only 150 mm^3 , while 8 subvolumes of 48.85 mm^3 (for a total of 400 mm^3 are necessary). Depending of the random set used, this volume can increase to 500 mm^3 .

3.5.3 Representativeness of closed-porosity and connectivity indexes

It is much more challenging to find a statistical RVE for the closed porosity ratio and the connectivity index than for density. Figure 3.18 displays these two properties for the statistical methods. The error chosen for both properties is absolute and equal to 10 %, which represents very large relative errors (more than 50 % for the connectivity index and about 33 % for the closed porosity ratio). For both properties, there is a general trend towards the correct value, however the statistical approach emphasizes a major issue. For volumes below 200 mm^3 , points are mainly outside the error bars especially for the closed porosity ratio. For the connectivity index almost all points are above the value of the total sample volume, and for the closed porosity ratio the majority are below. This demonstrates a clear effect of the subvolume sizes on their mean property values. For density, Fig. 3.14 showed an effect of sample size on the variability but not on the sample mean. In the case of the closed porosity ratio and the connectivity index, multiplying the number of one subvolume size (as for Fig. 3.17) does not change the mean value. Nevertheless, the difference between the connectivity index and the closed porosity ratio is striking in Fig. 3.18. Indeed, when the volume is larger than 1300 mm^3 , the mean

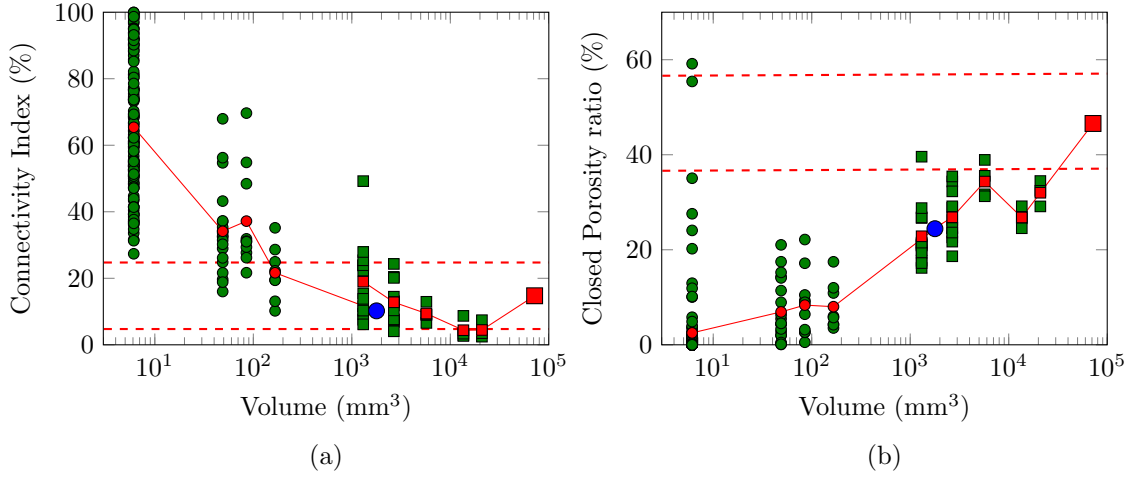


Figure 3.18: Evolution with the volume of (a) the connectivity index and (b) the percentage of the closed porosity ratio. The method used is statistical. The sample is from 95 m depth. Green dots are subvolumes extracted from the DC-S12 sample from this depth. Green squares are subvolumes extracted from the DC-M30. Red dots and squares are the mean property for each set of subvolumes. The red dashed line represents an absolute error of 10 % for both properties. The large blue dots are the property values of the DC-S12 sample and red squares come from the DC-M30 sample from the same depth.

values of the connectivity index are within the error bars, thus finding a RVE is possible. The blue dot, representing the DC-S12 sample at this depth, is rather close to the value of the DC-M30 sample. Therefore, the size of DC-S12 samples is sufficient to evaluate this property. Results for the closed porosity ratio (Fig. 3.18) lead to a very different answer. The subvolume mean property value tends to the correct value. The trend of the curve illustrates what was already noticed on Fig. 3.11, that is, as the volume increases, the closed porosity ratio increases as well. One could argue that the volume is not large enough to have a sufficient number of subvolumes in it to represent correctly the total volume for the closed porosity ratio. In fact, this issue is directly related to the borders, which cut pores that may be closed. In other words, it strongly relies on the volume of the ROI. The adopted definition of a closed pore in this work is a major assumption. However, as already discussed in section 3.4.3, the connectivity index is a good substitute to describe pore closure.

In conclusion, according to Fig. 3.18, it is possible to find a "statistical" RVE for the connectivity index, whereas it is problematic for the closed porosity ratio. Methods (a) and (c) from Fig. 3.13 showed that for 10 % of absolute errors on the connectivity index, a minimal volume of 500 mm^3 is sufficient. The boundaries of the sample play a significant role in the determination of the RVE for some properties such as the closed porosity ratio, and their effects are amplified when reducing the size of the subvolumes. The overlapping

method tends to overestimate the V_{RVE} , thus we will use it as a conservative method for the following maps.

3.5.4 Discussion

The RVE analysis described in this section can be generalized to any kind of properties and for all studied samples. We will focus on giving minimal volumes for different depths and different errors. RVE methods showed that the "randomly distributed" one tends to give an upper bound for the minimal volume possible compared to the "deterministic" and "statistical" ones. Using larger volumes than prescribed should thus work for all methods. In Fig. 3.19, several properties are represented such as the density, the specific surface area, the connectivity index and the closed porosity ratio. On all curves, the white line corresponds to the sample volume at each depth tested. Below, several lines are displaying different absolute errors for each property, determined for the total sample volume. In other words, if one wants to use a smaller volume than scanned, these curves give the precision associated to the volume for the different properties. For instance, taking a subvolume of 983 mm^3 from the 70 m deep sample, the density is known at $\pm 0.005 \text{ g.cm}^{-3}$ (which corresponds to a relative error of 0.66 %).

Between 22 m and 100 m, the density ranges between 0.55 and 0.85 g.cm^{-3} and the specific surface area between 2.6 and 0.7 mm^{-1} . Therefore, the precision annotated on Figs. 3.19a and 3.19b are very small. Subvolumes that are smaller than the DC-S12 samples could be used for other measurements or simulations, without changing much these two properties.

However, it is not the case for the connectivity index and the closed porosity ratio. Precisions on 3.19c and 3.19d are 5, 10 or 20 %. At low depths, these two parameters are known precisely. Indeed, above 80 m pores are well connected, thus the connectivity index is close to 100 % and the closed porosity is close to 0 %. Then, with increasing depth, the results disagree. For the connectivity index there is a peak around 90 m and then it decreases. It is strongly related to the steep drop observed on Fig. 3.12. Indeed a large variability was observed on this curve for shallower depth than 100 m. For Fig. 3.19d, the peak is delayed. When going deeper than 90 m, barely reducing the volume size leads to 30 % of absolute errors on the closed porosity ratio which is aberrant.

From Fig. 3.19d, it is impossible to take a smaller volume without changing drastically the closed porosity ratio. Thus at the close-off depth, the volume of DC-S12 samples is not large enough to quantify the closure process. On the contrary, Fig. 3.19c shows a good precision around the close-off depth. Indeed at 100 m, a subvolume three times smaller can be extracted without changing the connectivity index beyond 5 %. This proves again that the process of closure can be followed with the connectivity index for the DC-S12 samples

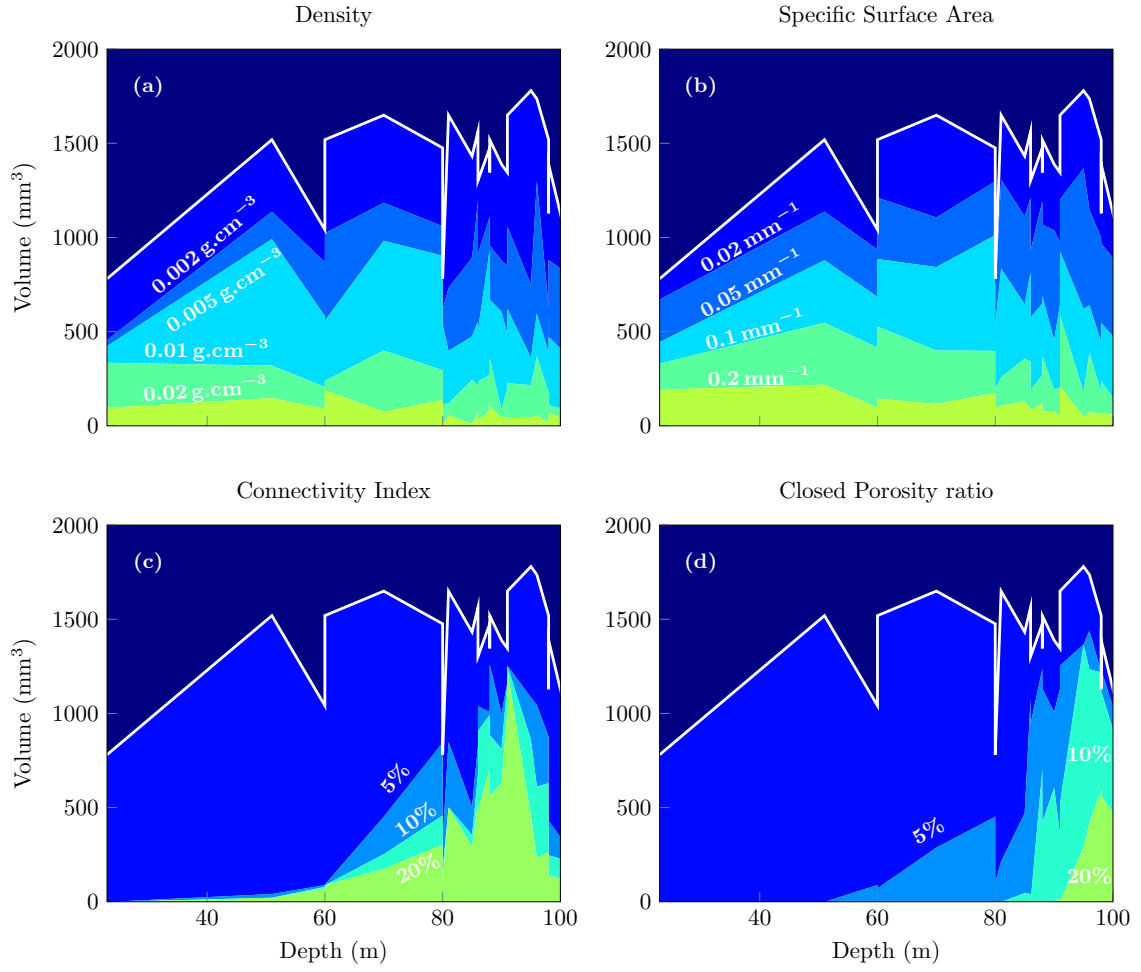


Figure 3.19: Evolution with depth of the minimal volume element for different absolute errors and different properties at Dome C : (a) density, (b) specific surface area, (c) connectivity index and (d) the closed porosity ratio. The white line depicts the total volume of the sample for each tested depths.

sizes. On the contrary, these samples are too small for the closure to be understood with the closed porosity ratio.

3.6 Multi-site comparisons

In this section, we compare our data retrieved from Dome C and Lock In to those originating from WAIS Divide (West Antarctica) and Megadunes (East Antarctica) from [Gregory et al. \[2014\]](#), which were also analyzed with X-ray tomography. We focus on the closed porosity ratio and morphological parameters that can be compared for all four sites. We note however that the depth interval probed for WAIS Divide and Megadunes sites is much smaller than ours. Temperature and accumulation conditions for WAIS Divide and Megadunes are given in Table 3.1, which shows that these two sites have a higher accumulation rate as well as a higher temperature than Dome C and Lock In. Note that the sites Megadunes is peculiar, as it experiences continuous snow deposition on one side or the other of the dunes, and has an average of zero accumulation in "hiatus" zones [[Courville et al., 2007](#); [Severinghaus et al., 2010](#)]. Consequently, porosity is closing at a much shallower depth, between 60 and 80 m for WAIS Divide and Megadunes, as indicated by Fig. 3.20a. In contrast, pore closure occurs below 80 m for Dome C and Lock In. The Lock In site has a more important accumulation rate and is a bit warmer than Dome C but exhibits a deeper (late) closure of pores. When plotting the percentage of closed porosity against density, Fig. 3.20b shows that all points fall approximately on a master curve. This supports the idea that the close-off arises at a particular density.

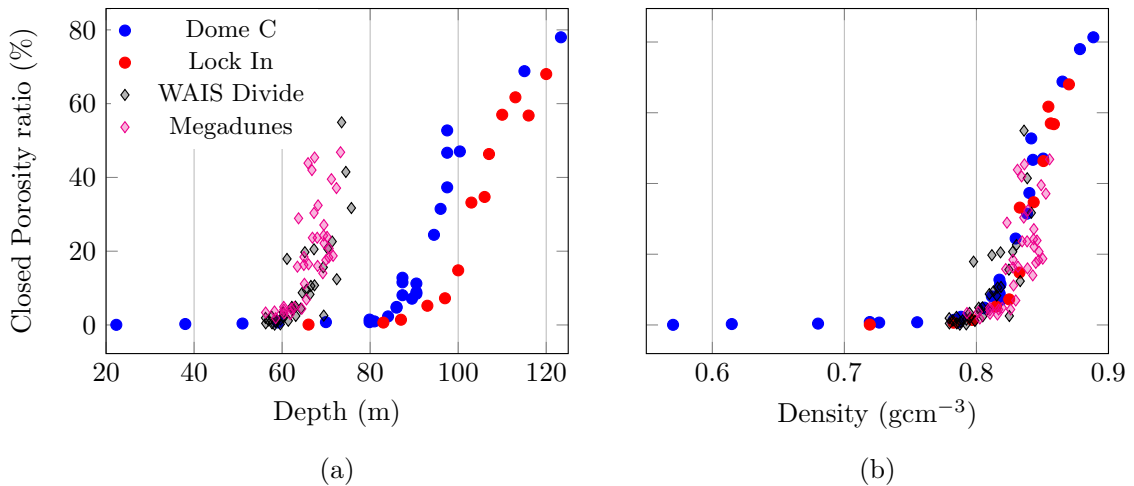


Figure 3.20: Comparison between four polar sites - Dome C, Lock In, WAIS Divide and Megadunes - of the closed porosity evolution with (a) depth and (b) density. Diamonds come from [Gregory et al. \[2014\]](#).

Figure 3.21 shows three morphological parameters of interest (degree of anisotropy,

surface-area-to-volume ratio of pores, and structure model index (SMI)) that can be compared for all four sites. The evolution of these parameters is shown against depth (Figs. 3.21a,c,e) and against density (Figs. 3.21b,d,f). These geometrical parameters give valuable information on the pore network morphology that could be important for firnification understanding.

Figures 3.21a-b show the degree of anisotropy that was determined using the BoneJ plugin [Doubé et al., 2010] on the pore phase. This parameter is calculated using a 3D mean intercept length method that works out directly all the possible directions. An ellipsoid is fitted to the scaled intercepted points, giving eigenvalues for lengths of the ellipsoid axes. The degree of anisotropy of the morphology is 0 for a fully isotropic structure and tends to unity when all objects are aligned along a direction. Figs. 3.21a-b show that for all four sites, the degree of anisotropy is rather low (≤ 0.4), with a mean value of the order of 0.2. No clear trend is observable with depth or density.

The surface-area-to-volume ratio (S/V) of pores is depicted in Figs. 3.21c-d. S/V may be seen as a good indicator of the complexity of the pore network morphology. In the case of pores as shown in Fig. 3.10, pore roughness is similar for both sites (smooth pore surfaces). Therefore, a less tortuous network leads to a smaller S/V value. In contrast with Fig. 3.21a-b, a clear difference is observable between Dome C - Lock In sites and WAIS Divide - Megadunes sites. First we note that our data indicate a clearer trend for Dome C - Lock In sites, whereas WAIS Divide - Megadunes sites [Gregory et al., 2014] is much more scattered on a rather limited interval of depth. It has to be mentioned that Gregory et al. [2014] chose specifically samples from coarse-grained layers and fine-grained layers, which could partly explain the scatter observed in their results. Concentrating on the S/V ratio against density plot (Fig. 3.21d), and focusing on the limited common density interval (0.75-0.85 g.cm⁻³), we note that WAIS Divide exhibits the most tortuous pore network. Megadunes leads to a pore network which S/V values are in between those of Dome C and Lock In, but again with a much larger scatter. Although relatively small, there is a clear hierarchy between Dome C and Lock In, with Dome C consistently exhibiting smaller S/V values as compared to Lock In, whatever density or depth. Dome C and Lock In data points follow approximately a linear evolution. Thus, Lock In presents, for a given depth or density, a more tortuous pore network than Dome C.

The Structure Model Index (SMI) is a popular index in the bone research community and is implemented in the SkyScan software CT-analyzer used by Gregory et al. [2014]. It was also used to analyze snow metamorphism [Schneebeli & Sokratov, 2004; Kaempfer & Schneebeli, 2007]. The SMI describes the shape of pores, with SMI being positive for convex shapes and negative for concave ones. The SMI tends to 0 for plates, 3 for rods

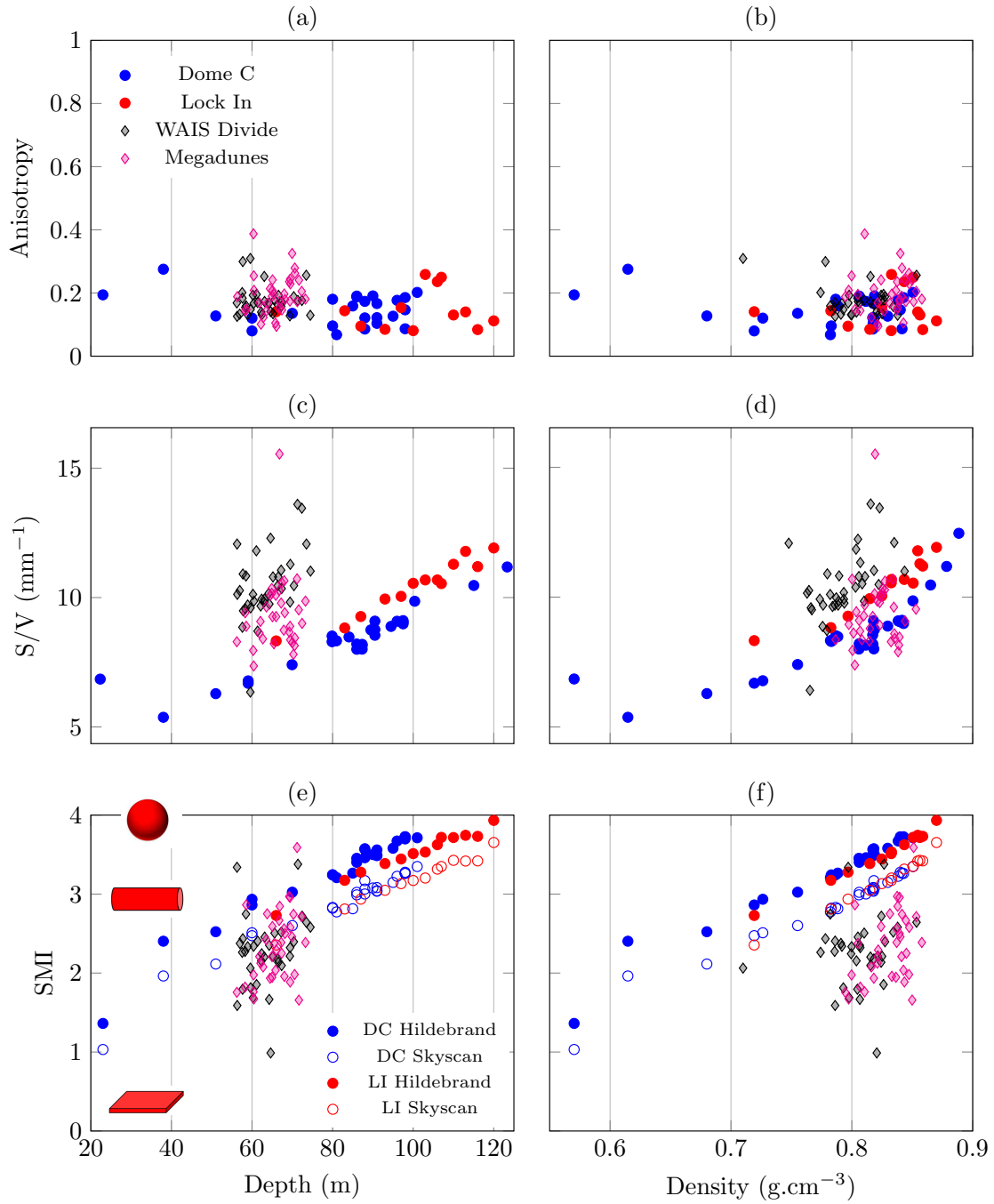


Figure 3.21: Evolution of the anisotropy (a-b), the surface-area-to-volume ratio (c-d) and the Structure Model Index (e-f) against depth and density for Dome C, Lock In (this work) and for WAIS Divide and Megadunes [Gregory et al. \[2014\]](#). The SMI index of Dome C and Lock In is computed using both the Hildebrand method [[Hildebrand & Rüegsegger, 1997](#)] and the Skyscan plugin.

and 4 for spherical particles. Two different methods are available to compute the SMI: the Skyscan plugin and the BoneJ plugin with the Hildebrand algorithms [Hildebrand & Rüegsegger, 1997]. As highlighted by Salmon et al. [2015], the Skyscan plugin consistently leads to smaller SMI values as compared to the Hildebrand plugin.

For sake of comparison with the data of Gregory et al. [2014], Figs. 3.21e-f show the Structure Model Index (SMI) of the porous phase for both methods. Again, as for the S/V parameter, the data of Gregory et al. [2014] (computed with the Skyscan plugin) exhibits a much larger scatter as compared to ours. In other words, the pore shapes measured at WAIS Divide range from semi-cylindrical to nearly spherical for a rather limited span of depth (55 - 70 m) or density. In contrast, data points from Dome C and Lock In follow a clear linear trend, which suggests a simple evolution from rod-like to sphere-like shape for increasing depth or density.

We have checked that the difference between WAIS Divide - Megadunes and Dome C - Lock In data does not originate from the different methodologies used in the two groups by computing the SMI of Dome C and Lock In with the same plugin used for WAIS Divide and Megadunes. As shown by Figs. 3.21e-f, the Skyscan plugin leads indeed to smaller SMI values as compared to Hildebrand. But this does not contradict the general picture that Dome C - Lock In and WAIS Divide - Megadunes sites differ markedly when considering the morphology of pores. In any case, we believe that the linear evolution shown in Figs. 3.21e-f for Dome C - Lock In is pertinent as it correlates well with the change in pore morphology that Fig. 3.10 reveals.

3.7 Refined geometrical parameters for Dome C and Lock In sites

In the preceding section, we have attempted to compare four different sites using the available data from the literature. In this section, we take advantage of the availability of collected 3D images for Dome C and Lock In to compute refined geometrical parameters. These geometrical parameters should bring new insight on the intimate structure of firn and its evolution. They cannot be obtained by air content measurements (such as pycnometry) or by densification models but are very useful properties that can be used for diffusion or permeability modeling and experiments.

We have chosen to plot these parameters as a function of density alone but it is straightforward to retrieve their evolution against depth by using the insert in Fig. 3.9. Figure 3.22 sums up and defines these parameters: maximal path diameter (Fig. 3.22a), Chamber over throat size ratio (Fig. 3.22b), medium chord length (Fig. 3.22c) and connectivity index defined in section 3.4.3 (Fig. 3.22d). The parameters in Figs. 3.22a-c

have been obtained by using the commercial software Geodict [GeoDict, 2014]. Samples DC-C12 and LI-C12 were used, as the software requires parallelepipedic ROIs.

Percolation paths on sub-volumes were calculated in the Z -direction alone, as it is more likely to be the principal flow direction within the firn. It consists in moving the largest sphere possible inside the porosity network, from the top surface to the bottom one. The software gives the diameter above which a sphere cannot pass. For each sample, 10 different percolation paths were calculated, starting with a minimum path diameter of $24\text{ }\mu\text{m}$, and then increasing by $24\text{ }\mu\text{m}$ steps. Figure 3.22a shows the maximal path diameter for those samples. The vertical lines represent the variability of the simulations (all paths that are different), and the dots are the mean of the maximum diameter for those paths. This graph shows a general decrease from approximately $300\text{ }\mu\text{m}$ at 0.55 g.cm^{-3} to zero when reaching approximately 0.83 g.cm^{-3} , which is slightly lower than the close-off density (0.840 g.cm^{-3} , [Martinerie et al., 1992]). Again, there are no noticeable differences between Dome C and Lock In. Both exhibit large variability of the maximal path diameter that can reach $200\text{ }\mu\text{m}$ in the same sample. However these diameters are quantitative information for the path of air (in a given interval), and can be related to the permeability of firn. A noticeable issue of this calculation is that it strongly depends on the size of the chosen sub-volume. Here a ratio of one was used with a cube side of 6.72 mm , which ensures percolation until 0.83 g.cm^{-3} according to Fig. 3.22. The length of the path ranges from 8 to 18 mm , meaning a tortuous structure whatever the depth. This is shown on image A in Fig. 3.22. A larger cube would have lead to a drop of the maximum path diameter to 0 before 0.83 g.cm^{-3} because of the complete structural isotropy of the pore network and the erratic process of closure. A smaller porosity amount is associated with a smaller probability of having a network connecting two opposite faces.

Figure 3.22b is the ratio of the calculated chamber over throat pore size distribution for the 90th percentile. Chamber pore size distribution is worked out using the granulometry over the whole sample, and the throat pore size distribution is obtained here by porosimetry on all samples faces, in the X , Y and Z -directions. Figures 3.22B and 3.22II clarify the throat and chamber concepts. The porosimetry consists of the introduction of a sphere from the top surface, thus mimicking the intrusion of liquid from the specimen surface. Each tested size of spheres in the sample is associated to the volume fraction that the set of spheres cover. In Fig. 3.22II, this is represented by a light blue area in which a particular sphere can circulate. When the space between pores is too small the sphere cannot move down anymore. This is different from the chamber pore size distribution, which is only based on the geometry of the pores. Spheres of different sizes are placed in every available space of the porous network. We chose to display the distribution at the 90th centile, as the porosimetry is difficult to perform for deep sample. This gives the

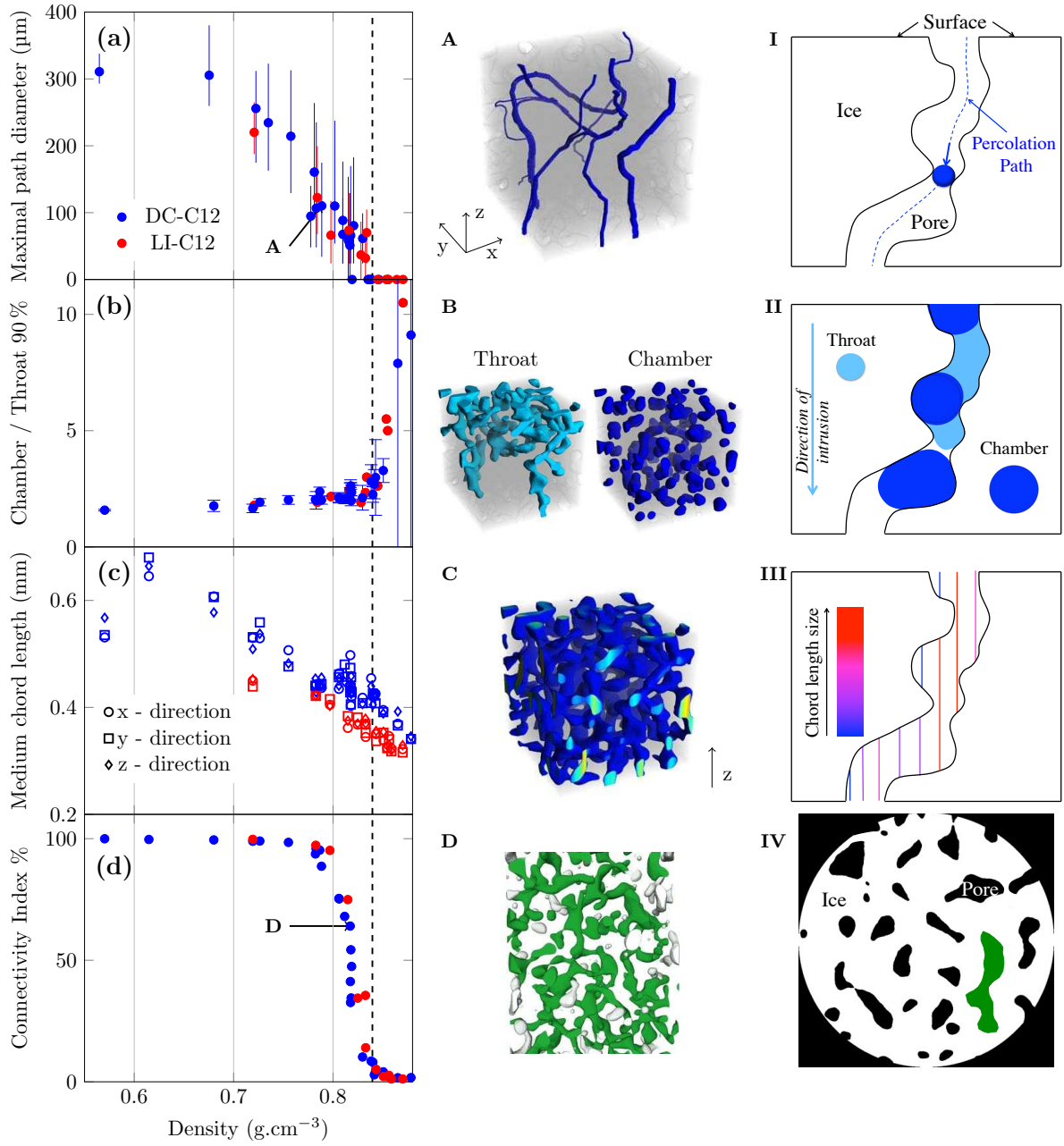


Figure 3.22: Evolution with density of (a) the maximal path diameter, (b) the ratio of chamber size over throat size distribution, (c) the medium chord length and (d) the connectivity index. The black dashed line is the close-off density from [Martinerie et al. \[1992\]](#) for Dome C. 3D images illustrate each parameter on the right hand side (images A-D). Images A-B-C come from the same DC-C12 sample 85m deep, while image D is a picture of a 91 m deep sample. The last column (I-IV) sketches the calculation of the parameters.

general trend of the closure of pores by pinching while still having large globular parts. Error bars are standard deviation from the mean value of the porosimetry results on the six cubic faces. These are shown only for Dome C. After the theoretical close-off density, there is a drastic increase of this ratio, as pinching reduces the throat size. Figures 3.22a-b do not allow for a clear differentiation between the DC-C12 and LI-C12 samples.

Figure 3.22c shows the medium chord length in all three directions. The corresponding sketch only illustrates the intercepts in the z direction. The intercept lengths are measured and averaged for each direction. For a given density, the medium chord length can be considered isotropic. Both DC-C12 and LI-C12 depict a linear decrease of about 50 % from 22.33 m to 100.38 m for DC-S12 samples. The medium chord length of LI-C12 is always smaller than that of the DC-C12 samples. This confirms the more complex shape of pore morphology for Lock In as observed on Fig. 3.21. As for the S/V ratio (Figs. 3.21c-d), we note for Dome C a slight discontinuity of the medium chord length evolution with density at approximately 0.8 g.cm^{-3} . At this density, the medium chord length ceases to decrease. This discontinuity is difficult to interpret but may be linked to the pinching of the thinnest channels that arises at the start of the pore closure.

It is instructive to compare the evolution of the connectivity index in Fig. 3.22d to those of the maximal path diameter and Chamber/Throat (Fig. 3.22a-b). The close-off density as proposed by Martinerie et al. [1992] for Dome C is well correlated to the end of the drop of the connectivity index (black dashed line). It also separates correctly the two regimes observed in Figs. 3.22a-b.

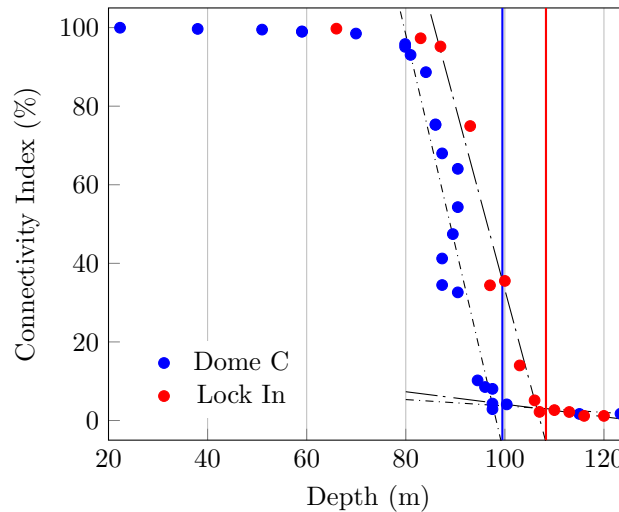


Figure 3.23: Connectivity index for Dome C and Lock In. Vertical solid lines represent the COD from measurements [Landais et al., 2006; Orsi, 2017]. Vertical dashed lines corresponds to the COD_G for temperature of Dome C (-55°C) and Lock In (-53.15°C) and using the evolution of density with depth given in Fig. 3.9. Black dash-dotted lines are linear slopes of the connectivity index that intersects at the COD.

Figure 3.23 compares the evolution of the connectivity index with depth for Dome C and Lock In. When the connectivity index drops to very small values, Fig. 3.23 clearly shows a sharp change in the slope for the two sites. The two linear portions of the curve intersect at depths that are in good agreement both with the ultimate depth where air could be sampled [Landaïs et al., 2006; Orsi, 2017] and with the Goujon et al. [2003] parameterization (used for temperatures of Dome C and Lock In). The blue and red solid lines correspond to the ultimate depths from Dome C (99.5 m [Landaïs et al., 2006]) and Lock In (108.30 m [Orsi, 2017]) respectively. The blue and red dashed lines correspond to the parameterization of Goujon et al. [2003] (ρ_{Gc}), for which the depth COD_G was calculated from our measurements of density (Fig. 3.9). Using the connectivity index evolution thus seems a promising method to locate the depth/density at which pores are fully closed. Its main advantage is that it does not depend on any assumptions or arbitrary choices on the status of pores (closed or open). According to Fig. 3.23, the full close-off depth of Lock In is approximately eight meters below the one from Dome C, consistently with the difference in last firn air sampling depth between these sites.

3.8 Corrected data of Dome C

In order to work out the effective firn diffusivity, models of air transport in firn [Trudinger et al., 1997; Fabre et al., 2000; Severinghaus & Battle, 2006; Witrant et al., 2012], are strongly dependent on the evolution of the fraction of open pores with density [Buizert et al., 2012]. Thus, different parameterizations of the evolution of the closed porosity ratio are proposed in the literature, that do not agree with one another [Schwander, 1989; Goujon et al., 2003; Severinghaus & Battle, 2006; Mitchell et al., 2015; Schaller et al., 2017]. However they are generally based on pycnometric measurements or on the melting-refreezing technique (except for the recent work of Schaller et al. [2017] that uses X-ray tomographic images). Isolated air volume measurements are obtained from sample whose size are close to our M samples ($\approx 60\text{-}100\text{ cm}^3$). Results are usually corrected for the cut-bubble effect as proposed by Martinerie et al. [1990].

In comparison to our work, Schaller et al. [2017] took advantage of X-ray scans on the whole core volume to determine the status of subvolume pores (closed or opened). Section 3.4 discussed the effects of the voxel size by comparing results from samples using 12 and 30 μm . The difference for the closed porosity ratio was less than 7%. Therefore, results obtained by Schaller et al. [2017] with a voxel size of 25 μm should not be too much affected by voxel-related errors. However, their definition of a closed pore still necessitates the knowledge of the status of the surrounding pores. This requires having access to larger volumes than those studied. In our work, only three samples have the diameter of the

core. Besides, as detailed in section 3.4, the voxel size of the largest samples has a great influence on the fraction of closed pores.

Consequently, we propose a correction described in appendix E. The correction assumes that the effect of cut-pores⁹ for the largest samples (L) is negligible. We also assume that the ratio of closed porosity is null above 70 m (below 0.75 g.cm^{-3}) and is 100 % below 101 m (above 0.851 g.cm^{-3}). The correction is further defined by using the known errors between the DC-M30 and DC-M60 samples. Assuming these errors are the same for L60 samples, it enables to obtain new L30 samples (large sample with a voxel side length of $30 \mu\text{m}$). These constraints are used for the correction of DC-S12 and DC-S30 samples to obtain additional L30 samples. In total, we have 71 new L30 samples that originate from L60, DC-S12, DC-S30 corrected samples, and which resolution may be considered as $30 \mu\text{m}$.

The ice density is set to $\rho_{\text{Gice}} = 0.924 \text{ g.cm}^{-3}$ (from Eq. (1.3) [Eq. (7), Goujon et al., 2003]), as if we performed tomographic scans at -55°C . Results for DC-S12 and DC-S30 are thus shifted towards larger densities. Equations for the different parameterizations plotted in Fig. 3.24 are detailed in section 1.1.2 (Eqs. (1.1) to (1.8)). Results of the proposed correction of Dome C is compared with these parameterizations in Fig. 3.24.

We believe the method adopted by Schaller et al. [2017] is appropriate to reasonably limit cut-pore effect and does not suffer much from voxel size issues. However, it is still hindered by the unavoidable possibility of having a large closed pore (larger than the sample) that is wrongly considered open. The use of the connectivity index avoids these issues.

The corrected data set is scattered, with a lower bound close to the parameterization of [Goujon et al., 2003], and an upper bound above the line representing the X-ray tomographic data of Schaller et al. [2017]. Still, the general trend given by our data is smooth, with no abrupt closure in contrast to what Schaller et al. [2017] observed. Although our data come with rather large error bars, it is interesting to note that the shape is closer to what proposed Mitchell et al. [2015] with a stochastic description of pore closure.

Green curves are simple sigmoid functions fitted on a few points that bound our data and give guidance for the eye. The air content related to the mean close-off density can be computed [Rommelaere et al., 1997; Martinerie, 2017] for the upper and lower bounds and compared to measurements of Martinerie et al. [1992]. This gives the density when isolation of air is triggered in terms of pressure, i.e. when air pressure inside pores is not the atmospheric pressure anymore. These are represented by the intersection between colored solid lines and vertical dashed lines. The trend and mean close-off density of the

⁹ In our samples, pores are far from being bubbles, therefore the correction proposed by [Martinerie et al., 1990] can not be used.

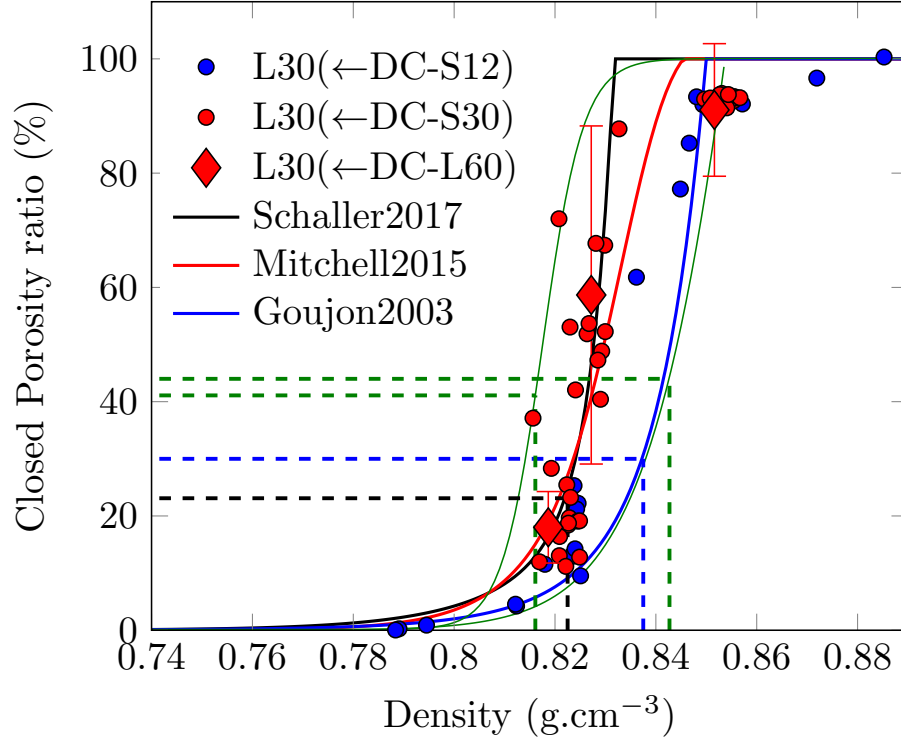


Figure 3.24: Closed porosity ratio after correction of the cut-pores for Dome C. Parameterizations of Schaller et al. [2017]; Mitchell et al. [2015]; Goujon et al. [2003] are shown. Green solid lines represent upper and lower bound of the data. Vertical dashed lines represent the mean close-off density related to air content measurements for the different parameterizations [Martinerie, 2017].

lower bound compares well with the parameterization of Goujon et al. [2003]. Both are consistent with measurements from Martinerie et al. [1992] which gave a close-off density of 0.840 g.cm^{-3} , whereas it is 0.843 g.cm^{-3} for this bound. However, the majority of data is above this lower bound, meaning a lower close-off density. This is in stark disagreement with Fig. 3.22d which showed that the connectivity index agreed well with the close-off density ρ_{Gc} (Eq. 1.2 with $T = -55^\circ\text{C}$).

In brief, we proposed in this section a corrected set of points for the closed-porosity ratio, which seems to underestimate the close-off density as obtained by air content data, but which overlaps parameterizations from Mitchell et al. [2015] and Schaller et al. [2017]. Corrections of points lead to a smooth closure as proposed by Mitchell et al. [2015], and could be used as quantitative input in future works regarding air transport modeling in firn.

3.9 Pore size

In this section we take advantage of the 3D images to determine the size distribution of pores. Figures 3.25 and 3.26 show in (a) the distribution of the total porosity and in (b) the distribution of closed pores. Looking at shallow depths (below 90 m), both figures display small boxplots that are identical between (a) and (b). For the total porosity distribution, there are outliers¹⁰ whose volume are above 100 mm^3 . These come from the large open pores that are present at these depths, and that overcome all others. It should be also noted that the median and mean values of the boxplots are increasing from the shallowest depth (between 10^{-4} and 10^{-3} mm^3) to a region just before the COD (between 10^{-2} and 10^{-1} mm^3). In this region, boxplots from (a) are larger than the ones from (b), and are joining with the outliers. This corresponds well with the steep drop that was noticed in the connectivity index for both sites (see Fig. 3.23). Further, the boxplot size is once more the same for (a) and (b). The median and mean values seem to stagnate between 10^{-2} and 10^{-1} mm^3 .

Figure 3.27 illustrates that the mean pore volume actually decreases after the close-off density. Again, Dome C and Lock In can not be differentiate when data are plotted against density (Fig. 3.27b) but they are different with depth (Fig. 3.27a). A maximum is observed at 100 m depth for Dome C and at 103 m depth for Lock In. However a second maximum is observed at 112 m for Lock In. As it is the mean value, which is plotted, results are very dependent on the statistic of pore size. One large closed pore can increase drastically the mean value, for the same closed porosity ratio. Therefore such parameters

¹⁰ In this section, outliers are points that are significantly separated from boxplots, i.e. more than 1.5 times the interquartile range from the upper quartile, or below 1.5 times the interquartile range from the lower quartile.

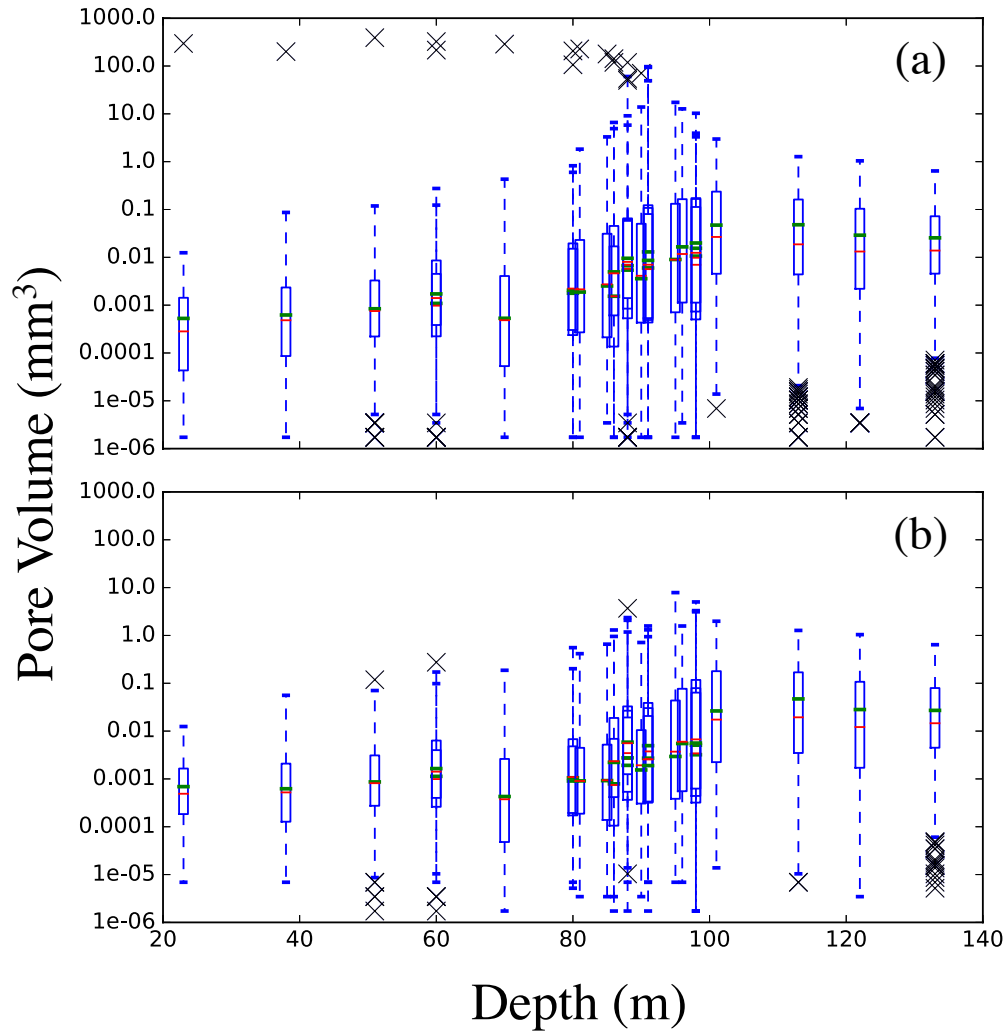


Figure 3.25: Pore size distribution at Dome C for (a) all pores and (b) only closed pores. Boxplots are calculated using [Chambers et al. \[1983\]](#). Crosses are outliers, whose values are above 1.5 the interquartile range (represented by the box) from the upper/lower inner fence. Upper crosses are outliers that correspond to open pores. The green horizontal bar is the median value, while the red square is the mean value.

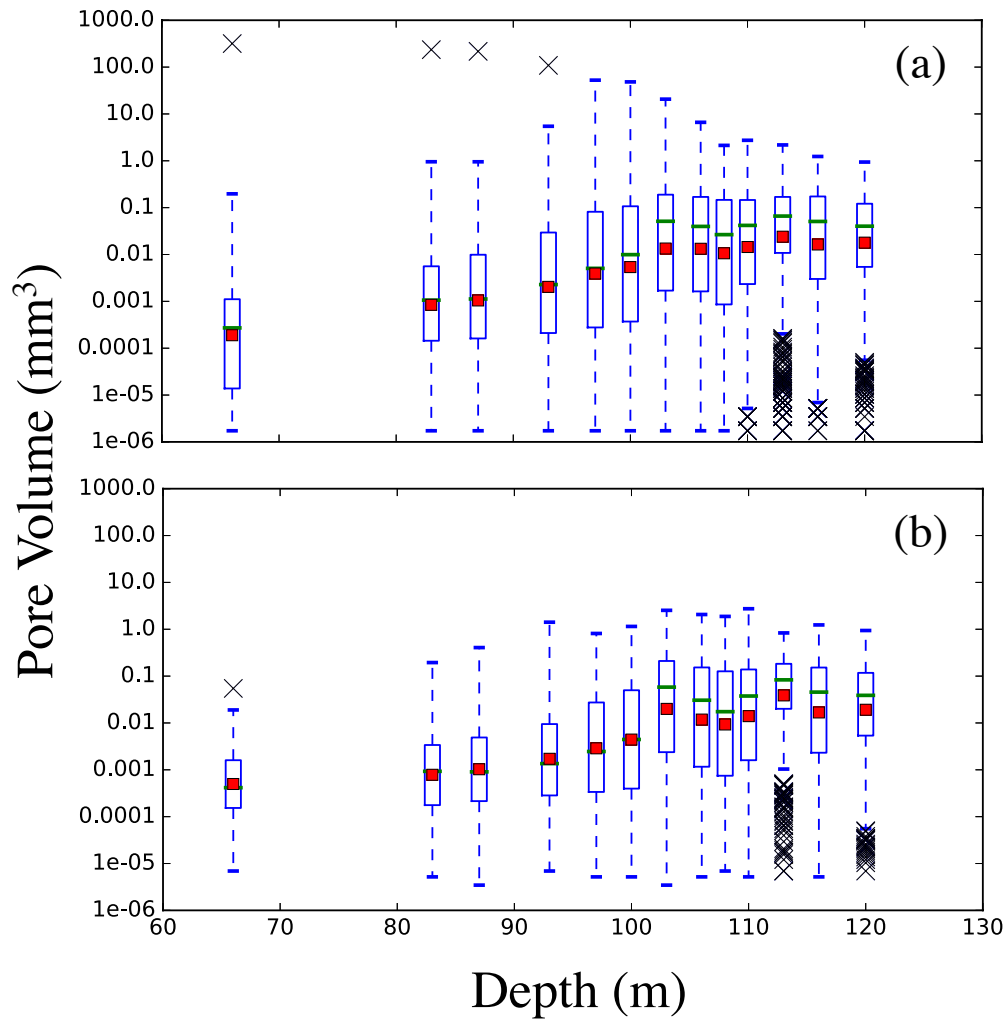


Figure 3.26: Pore size distribution at Lock In for (a) all pores and (b) only closed pores.

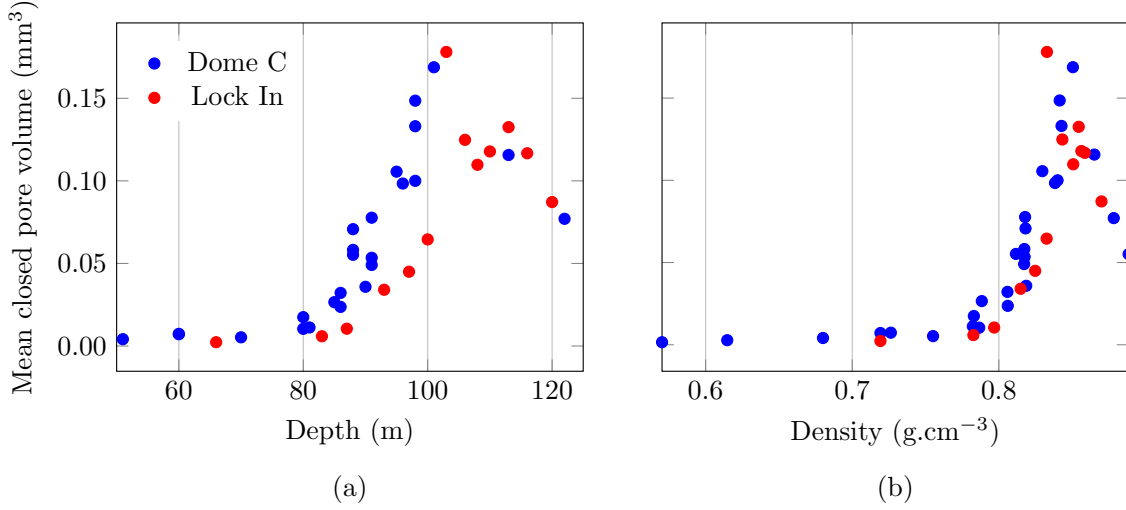


Figure 3.27: Mean volume of closed pores with (a) depth and (b) density for Dome C and Lock In.

is only useful to prove that bubbles are shrinking in average after the COD [e.g., [Arnaud, 1997](#); [Lipenkov et al., 1997](#)].

The similarity between open and closed pores is strongly correlated with the close-off depth (see Figs. 3.25 and 3.26). After the COD, even the pores that were cut off in the surface of the sample have the same size than the inner pores. Hence, all pores are closed, as there is no more distinction in terms of size between the two definitions. Overall, Dome C and Lock exhibit the same distribution of pore size.

3.10 Characterization of the ice phase

3.10.1 Crystallographic orientation

The preparation of thin section of ice was performed thanks to a microtome, and the orientation of grains was determined using an Automatic Ice Texture Analyzer (AITA). It consists of rotating crossed-polarizers in an automatic way, while recording orientation at a pixel level. It produces several data images such as the azimuth and colatitude, the retardation (highest birefringence colour) and quality images for instance. Appendix D compiles all the microstructures obtained for Dome C and Lock In sites. For each sample, the retardation is shown, as well as the azimuth. The azimuth, colatitude and pole figures are obtained thanks to the code from [Chauve \[2017a\]](#), using the data obtained with the AITA. Pole figures are displayed to show the preferential orientation of the fabric for all the thin sections realized (see appendix D). Complete details on the analyzer functioning,

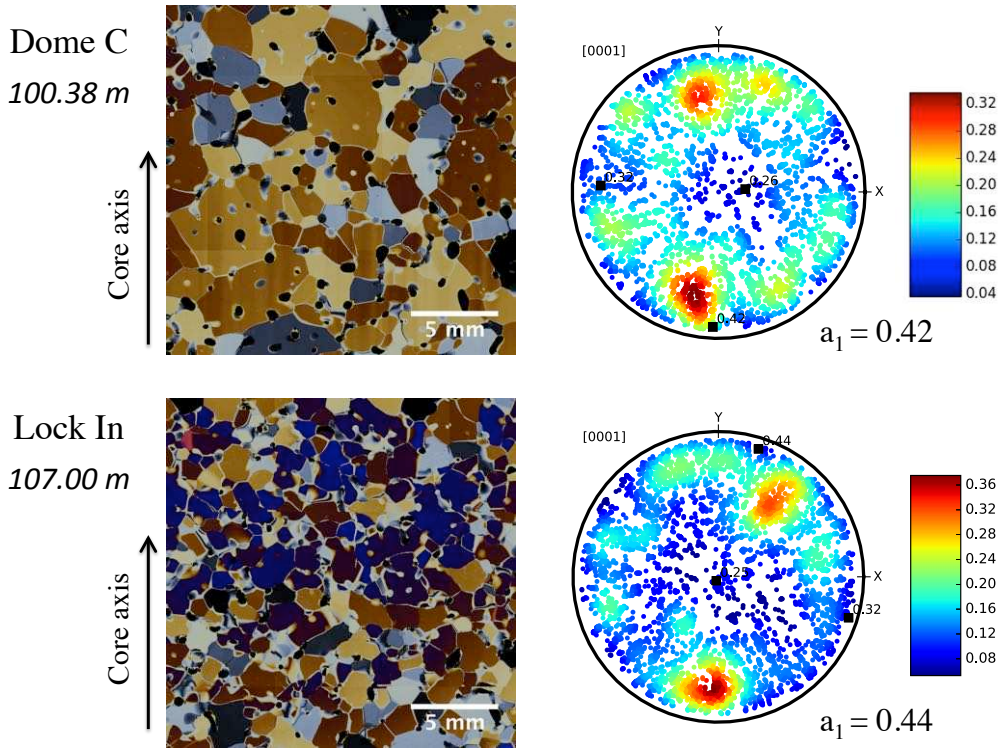


Figure 3.28: Comparison of Pole figures and microstructures between Dome C and Lock In for the same density $\rho = 0.851 \text{g.cm}^{-3}$ (with a_1 , a_2 and a_3 equal to 0.42, 0.32, 0.26 and 0.44, 0.32, 0.25 for Dome C and Lock In respectively).

and on the processing can be found in [Paternell et al. \[2009, 2011\]](#).

Principal directions and eigenvalues of the \mathbf{c} axis can be worked out from the data using the second order tensor \mathbf{a} . Eigenvalues are referred as a_1 , a_2 and a_3 accordingly with section 1.2.3. The eigenvalues verify $a_1 + a_2 + a_3 = 1$. In what follows, we will assume $a_1 \geq a_2 \geq a_3 \geq 0$. Figure D.3 in appendix D illustrates the evolution of the eigenvalues with depth. No general trend can be extrapolated from these measurements. However, some differences between the sites are noteworthy. For Dome C, it appears that $a_1 > a_{2,3}$ and $a_2 \simeq a_3 < \frac{1}{3}$. This means a single maximum fabric for this polar site. [Wang et al. \[2003\]](#) performed fabric analysis for the first 1500 m of the ice core, and stated a quasi random texture at the surface of Dome C. But in their study only two points were available above 100 m. To our knowledge, the last up-to-date fabric analysis on the EPICA Dome C ice core was performed by [Durand et al. \[2009\]](#), who demonstrated the strong development of the texture until reaching the bedrock. Our results do agree with these studies in terms of order of magnitude for a_1 , a_2 and a_3 at shallow depths. Thanks to a larger number of depths studied in our work, we can conclude on a more marked texture of the firn than [Wang et al. \[2003\]](#) suggested. However, no thin sections above 50 m was

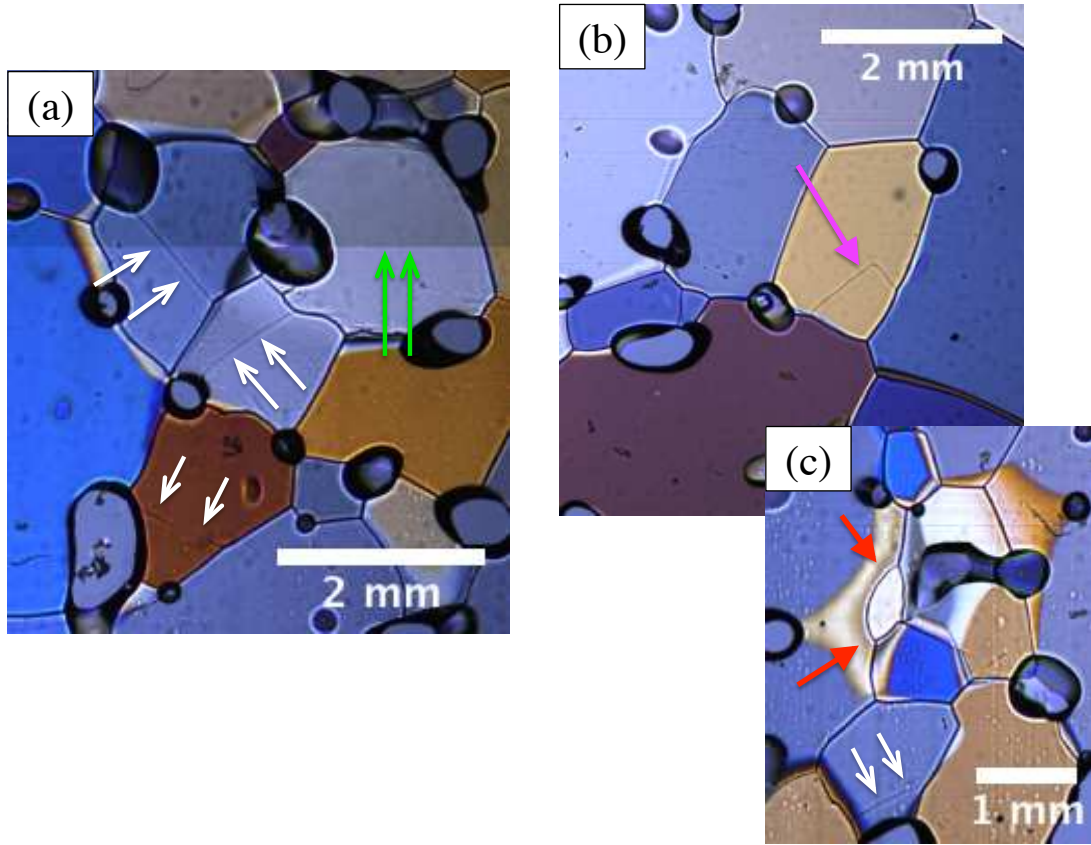


Figure 3.29: Evidence of intragranular deformation on a thin section from Dome C at 100.38 m depth : (a) Subgrain boundaries are pointed by white arrows. Green arrows only show a darker region because of tiles stitching with the AITA. (b) The magenta arrow highlights a "corner" grain. (c) Red arrows point on a possible bulging grain (from strain induced boundary migration) and white arrows on a subgrain boundary. Rounded blue and dark shapes are pores.

analyzed, thus we can only conclude for firn densities above 0.68 g.cm^{-3} . The observed fabric supports the hypothesis that the dome is mainly under uniaxial compression. Lock In fabric also exhibits a relatively pronounced texture. a_2 and a_3 were tighter for Dome C than for Lock In. This can be related to a stress state not only in compression at Lock In, as the eigenvalues do not describe a single-maximum fabric. The site is not exactly at the tip of the Dome so the direction of the flow could be affected by shearing.

Figure 3.28 compares the microstructure and the orientations between Dome C and Lock In for the same density. In terms of texture, the Pole figures are very similar and the density of points is also very close. However, the grain size is visually very different, with a much larger grain size for Dome C than for Lock In. Quantification of the grain size is the topic of the next section (3.10.2).

When high quality images were obtained with the AITA, small features of recrystalliza-

tion and intragranular deformation were observed. White arrows in Fig. 3.29a and 3.29c highlight subgrain boundaries because of intracrystalline deformation. The magenta arrow points to a corner grain which is formed in the vicinity of a pore and a triple junction as already shown by Kipfstuhl et al. [2009]. This could come from rotation recrystallization. Strain induced boundary migration is expected for such depth and density ($\rho = 0.851 \text{ g.cm}^{-3}$ at 100.38 m in Fig. 3.29), leading to nucleation of new grains. Red arrows point on what look to be a new grain on Fig. 3.10c, possibly coming from bulging, and inducing large disorientations of the neighbor grains.

3.10.2 Grain size

Determination of grain size on ice can be done by several ways. One is the mean intercept length method, used by Alley & Woods [1996] on ice from the GISP2 ice core in Greenland. But with the possibility of image processing, 2D techniques enable to directly have the cross-sectional area of the grains. The cross-sectional area is the current definition that the glaciology community uses for grain size.

The grain size of firn from cross-sectional area can be obtained from the technique described by Arnaud [1997]. He used thick sections of ice and coaxial episcopy to distinguish clearly the pores from the grain and the grain boundaries. This method enables the volume fraction of ice to be calculated, as well as the grain size to be determined. But, this type of analysis is hindered by sublimation, which occurs on all grains at different speed, adding micro-pores. An algorithm for segmenting polarized images was proposed by Gay & Weiss [1999] who used this method on the EPICA Dome C ice core. Using this method on images obtained by the AITA tends to increase grain size close to pores and reduce others, as well as removing completely some pores.

Therefore, in our work, a different procedure was adopted. We used directly the quality images captured by the AITA on thin sections. A quality image exhibits darker regions where the analysis is difficult to perform or where it is wrong. When processing orientations for the Pole figure, a threshold is chosen to remove any problematic pixel since it would bias the results. Indeed, usually it leads to a concentration of the \mathbf{c} axes in the center of the stereographic projection. In our case, we take advantage of the low quality at the grain boundaries and at the pores, to threshold grains. Our method, based on the quality images, has a simple algorithm. Typical output images are shown Fig. 3.30. It consists in applying on the 8 bits images the following procedure:

1. Performing an erosion of the grey scale images, i.e. apply a minimum filter. In our case, it consists in replacing a pixel value by the smallest pixel value in its neighborhood. This usually dilates grain boundaries and pores.

2. Performing a median filter. It consists in reducing the noise by replacing pixels value with the median value of their neighborhood.
3. Thresholding.
4. Performing successive close (a dilation followed by an erosion).
5. Removing outliers, as some noise can persist after the median filter.
6. Using the procedure "Analyze Particles" of Fiji [Schindelin et al., 2013] which gives the cross-sectional area.

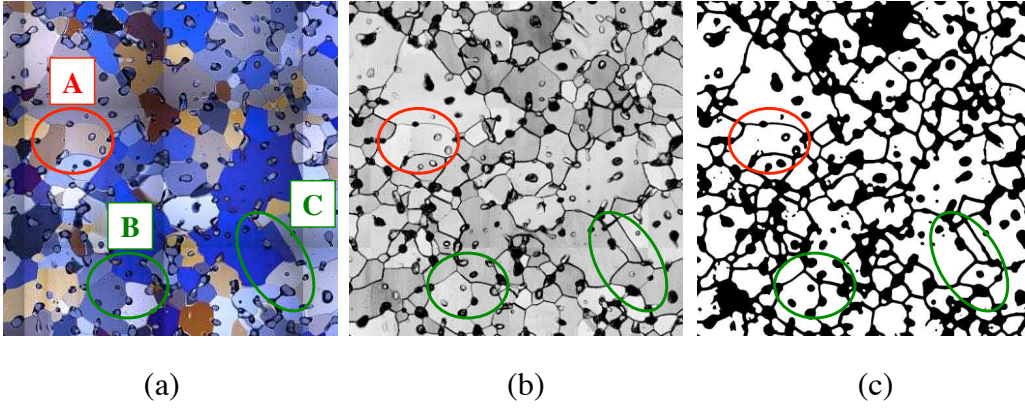


Figure 3.30: Representative image processing procedure to measure grain size. (a) Polarized light image obtained by the AITA. (b) Corresponding grey level quality image. (c) Output of the algorithm. As depicted by area A the quality image does not always able to separate grains after the processing because grain boundaries are too thin and not enhanced by the algorithm. Areas B and C show some features that are correctly captured by the algorithm.

Other algorithms were tested and are shown as dashed line on Fig. 3.31. All dashed error bars that are close to a solid error bar comes from the same quality image of the same sample (at the same depth). They consist of successive close after thresholding, without erosion of grey scale images, but also in reducing the size of the image. The selected method seemed to fall in between others. However, a loss of grains is possible (typically the minimum grain size ranges from $50\mu\text{m}$ to $150\mu\text{m}$), and grain boundaries are usually very thick, which tends to reduce the mean grain size. Overall, the different methods do agree with each other. Following the current grain size definition used by the community, Fig. 3.31 displays the cross-sectional area \bar{A} with depth for Dome C and Lock In. It also shows the mean cross-sectional area $\langle A \rangle$ for different cut-off values. Error bars on Fig. 3.31 is the variability of grain size (equal to one standard deviation).

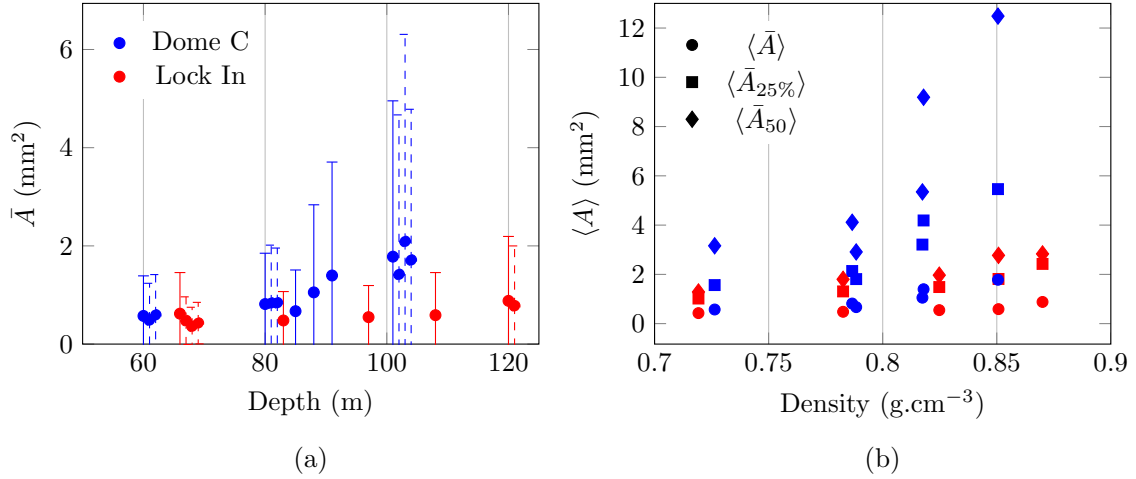


Figure 3.31: Comparison of the cross-sectional area against (a) depth and (b) density for Dome C and Lock In. Dashed error bars represent different image analyses for the same sample and at the same depth than their neighbor solid error bar. $\langle \bar{A} \rangle$ is the mean cross-sectional area of all grains, $\langle \bar{A}_{25\%} \rangle$ is the mean cross sectional area of the 25 % largest grains, and $\langle \bar{A}_{50} \rangle$ of the 50 largest grains. All section dimensions of Dome C are larger than 3 cm x 3 cm (with more than 500 grains). Because of small volumes of firn retrieved from the core of Lock In, section dimensions are above 2 cm x 2 cm (giving more than 300 grains).

Figure 3.31a shows that the mean cross-sectional area of Dome C becomes larger with depth than the one from Lock In. In Fig. 3.31b, it is also the case in terms of density. Moreover, the displayed error bars are also larger for Dome C than for Lock In. As the image processing is the same for both sites, this comes from a much sparser distribution when the grain size increases. Figure 3.31b also displays the mean cross-sectional area for the 25 % larger grains, and for the 50 larger grains. This means that lots of grains were cut off from the analysis. For Dome C, results distinctly show that $\langle \bar{A}_{50} \rangle > \langle \bar{A}_{25\%} \rangle > \langle \bar{A} \rangle$, as the 25 % largest grains contains more than 50 grains. This last remark is also true for Lock In, however the discrepancies between the different mean cross-sectional areas are much smaller. Regarding the isotropy of the grains, these seemed equiaxed. However we did not perform a detail analysis of the grain shape. Gay & Weiss [1999] showed that at a depth of 100 m at Dome C, grain size in the horizontal directions is about 5 % larger than in the vertical (core axis) direction, which is consistent with the fact that grains flatten with increasing depth.

It is difficult to select a pertinent definition for the grain size from Fig. 3.31. In his work, Gow [1969] stated that the 50 largest grains represented about 25 % of the grains contained in the thin section, and that it was representative of the volume. This was since tackled by Gay & Weiss [1999], that showed that the square of the mean linear intercept

length \bar{L}^2 was much closer to $\langle \bar{A} \rangle$ than to $\langle \bar{A}_{25\%} \rangle$ or $\langle \bar{A}_{50} \rangle$. These authors concluded that the mean cross-sectional $\langle \bar{A} \rangle$ is the best measurement to discuss the grain size. When deriving the 3D grain-growth kinetics from thin sections, this method should be preferred. Thus, the grain size is very dependent on the method of estimation. Durand et al. [2006a] also stated that using only a part of the grains is not representative of the whole section. According to these studies, the definition of the mean grain size is the mean grain radius $\langle R \rangle = \frac{1}{N_g} \sum_k^{N_g} \bar{A}_k^{1/2}$, with N_g the number of grains in the analyzed zones. Thus, these authors chose to model the grain by a square. At 100.33 m, the mean grain radius in that case is $\langle R \rangle = 1.04$ mm, while Durand et al. [2006a, 2009] reported 0.9 mm which is close enough. Looking at the cross-sectional area, our value is also slightly larger than that of Gay & Weiss [1999]. These two studies start their analyses from a depth of 100 m, thus we can not conclude on a small overestimation from our part. However, Alley et al. [1982] studied the grain size of the 50 first meters of the firn core. Their results for the mean cross sectional-area are two times larger than ours. They also showed that the firn core is layered with 90 % to 95 % of coarse grains while the remains are fine grains. We did not observe such layering of the firn from our sampling.

In any case, for both sites, there is an overall increase of the grain size. However, Kipfstuhl et al. [2009] performed a thorough study at the micro scale, with grain size down to 65 μm . Using all grains from the thin sections, they showed that grains were not growing with increasing depth for the polar site Dronning Maud Land. They stated that the commonly accepted normal grain growth is not adequate to describe the microstructural evolution of polar firn. The normal grain growth is given by a linear law that relates the age of the ice core to the mean cross-sectional area [Gow, 1969; Stephenson, 1967] :

$$\langle \bar{A} \rangle = \langle \bar{A}_0 \rangle + Kt \quad (3.6)$$

with $\langle \bar{A}_0 \rangle$ the initial mean cross-sectional area and K the growth rate. K depends on temperature and follows an Arrhenius law. The driving force behind this law is the minimization of grain boundary energy. A typical activation energy for grain growth is 49.6 kJ.mol⁻¹ [Arnaud, 1997]. If we assume that the grain growth rate only depends on temperature, it should be about 20 % larger for Lock In than for Dome C with this activation energy. If we also assume that $\langle \bar{A}_0 \rangle$ is identical for both sites, our results could suggest that for the same density, the firn from Dome C is older than from Lock In.

According to the study of Kipfstuhl et al. [2009], above the critical density 0.73 g.cm⁻³, the complex microstructure could only be explained by dynamic recrystallization. Indeed, because of the viscoplastic deformation of firn at high densities, strain induced boundary migration and rotation recrystallization appear and are supposed to be the main processes affecting the firn microstructure. Thus, some grains are growing, and others, smaller, are

nucleating, such that the normal grain growth law cannot hold on average.

Results of [Kipfstuhl et al. \[2009\]](#) were based on high resolution images. Because of the overall quality of our images and our processing, it is possible that lots of small grains were lost, hence a progressive increase of the grain size. Moreover, we did not perform a close analysis of grain boundaries with the microscope. This type of microstructure feature is better followed when the microscope is coupled with an EBSD (electron back scatter diffraction) [[Chauve et al., 2017a](#)].

Although exhibiting a size distribution, grain size measurements showed a larger mean grain size at Dome C than at Lock In. At close-off depths of Dome C (≈ 100 m) and Lock In (≈ 108 m), the mean cross-sectional area was measured from thin sections to be approximately 1.78 mm^2 and 0.59 mm^2 , respectively. We observed that grains in the Dome C firn increased in size with depth (from 0.57 mm^2 at 60 m to 1.78 mm^2 at 100 m) while grains in the Lock In firn showed no clear increase in size in the probed depth range (60-120 m). This information on grain size, together with those on medium chord length (Fig. 3.22) and surface-area-to-volume ratio (Fig. 3.21) suggest a more tortuous pore structure for Lock In which is a bit warmer and with a higher accumulation rate.

3.11 Concluding remarks

X-ray characterization on firn samples was performed on two polar sites, Dome C and Lock In, on a large depth range. We focus on the microstructural markers that accompany the closure of pores. The most obvious method to characterize pore closure is to measure the ratio of closed porosity. However, building on a thorough estimation of the results accuracy after imaging and processing, we have shown that this approach has serious drawbacks as the percentage of closed porosity exhibits large variability with sample size, voxel size, and spatial heterogeneities when characterized by X-ray tomography. This is problematic since most models on air transport in the firn such as [Trudinger et al. \[1997\]](#); [Fabre et al. \[2000\]](#); [Severinghaus & Battle \[2006\]](#); [Witrant et al. \[2012\]](#) rely on a diffusion coefficient that requires the knowledge of the evolution of the closed porosity with depth and/or density. Thus, these models are strongly dependent of a correct parameterization of the volume fraction of closed pores and there is no consensus on those that have been proposed [[Schwander, 1989](#); [Goujon et al., 2003](#); [Severinghaus & Battle, 2006](#); [Mitchell et al., 2015](#); [Schaller et al., 2017](#)]. The cut-bubble effect [[Martinerie et al., 1990](#)] has to be taken into account on the boundaries of the sample.

Here, we have encountered similar difficulties in determining unambiguously the fraction of closed pores. For example, we have determined that near the critical density of 0.84 g.cm^{-3} , it ranges from 31 % to 52 %. This uncertainty results from the conjunction

of three detrimental effects: the sample size, the voxel size (resolution), and an inherent spatial heterogeneity.

If one is interested in the close-off determination while avoiding the aforementioned effects, we propose an alternative parameter: the connectivity index, which is simply the volume of the largest pore, divided by the total pore volume. The main advantage of the connectivity index is that it completely bypasses the issue of cut-pores that undermines the measure of the closed porosity ratio. Before the close-off depth (COD), the connectivity index is essentially affected by spatial heterogeneities in the sample but not much by resolution and sample size. When focusing on the determination of the COD, we have shown that a sample size of the order of 1-2 cm³ is a reasonable choice. In these conditions, the connectivity index accurately predicts the COD as defined by the ultimate air sampling depth [Landais et al., 2006]. It also agrees with the parameterization of Goujon et al. [2003], and therefore with air content measurements from Martinerie et al. [1992, 1994]. When using tomographic data, we propose to use the connectivity index to determine precisely the COD. From this depth, one could infer a relationship between critical fraction of closed pores and COD, assuming a suitable correction has been found.

That being said, the two sites studied in this work (Dome C and Lock In) are both characterized by cold temperatures and low accumulation rates. It would be interesting to use the connectivity index on other polar sites to confirm its pertinence for COD determination. Indeed, further challenging this index on polar sites exhibiting layering such as WAIS Divide, would help determining if this metric is appropriate to characterize closure.

The morphology of pores was compared to data from Gregory et al. [2014] for polar sites WAIS Divide and Megadunes. Their data are very scattered compared to ours, which can be explained by the nature of the studied sites. Indeed, Dome C and Lock In are very cold sites with low accumulation, with Dome C being at the tip of the dome. In contrast, Megadunes is a site exposed to strong winds that redeposit snow from one side of the dune to the other, thus leading to a non-steady state site. WAIS Divide is a warmer site with high accumulation rate. Layering is significant, as high-density layers of fine grains can be found above low-density layers of coarse grains. As Gregory et al. [2014] intentionally extracted their samples from coarse and fine-grained layers, and plotted their data with bulk density, these led to scattered results. The use of local density (density of the scanned sample) may have smoothed their results (as shown by Mitchell et al. [2015]).

The polar sites Dome C and Lock In were extensively compared and are very similar. Shapes of pores, closed porosity and connectivity indices are evolving likewise with density. However, the closure of pores occurs deeper for Lock In than for Dome C (8 meters deeper). Our results on the medium chord length, the surface-area-to-volume ratio and grain size

suggest a more tortuous firn at Lock In than at Dome C. These could have interesting implications on air diffusivity in the firn for the comparison of these two sites. If Lock In is more tortuous, air could have been captured rather soon, meaning a smaller gas-ice age difference at this site than at Dome C.

In conclusion, this chapter gives some quantifiable data useful to improve densification modeling. Evolution of the pore closure is compared with the DEM results on chapter 5. Experimental data as throat size distribution, maximal path diameter or specific surface area can also be helpful for example to model Fick diffusion and permeability in the firn, and the corrected data set for the closed porosity ratio is ready to be used in air transport model for firn.

Chapter 4

In situ compression of natural firn

Contents

4.1	Review of in situ compression on snow and firn	127
4.2	Methods	129
4.2.1	Cold cell for oedometric test	129
4.2.2	Tested samples	131
4.2.3	Digital Volume Correlation	133
4.3	Mechanical behavior	136
4.3.1	Evolution of stresses	136
4.3.2	Pore pressure	138
4.3.3	Specific surface area	141
4.3.4	Grain size and anisotropy	142
4.4	Evolution of pores with artificial densification	144
4.4.1	Effects of densification on pore closure and morphologies	144
4.4.2	Curvatures	144
4.4.3	Discussion	150
4.5	Modeling thermally activated processes	152
4.5.1	Heat treatment	152
4.5.2	Effect of heat treatment on pore closure and morphologies . . .	152
4.5.3	Grain size and texture after heat treatment	159
4.5.4	Curvature minimization modeling	161
4.6	Conclusion	165

4.1 Review of in situ compression on snow and firn

We have seen in chapter 3 the type of information that X-ray tomography observations may offer. Full characterization of the porosity network was performed allowing precise comparison of samples. Results were obtained *ex situ*, meaning that samples were extracted from ice cores and scanned afterwards. One limitation of such study, is that continuous phenomenon cannot be followed as different samples are scanned. In contrast, *in situ* experiments enable to follow densification for instance, as scanning is performed. However, these experiments under X-ray tomography are always challenging to set up. Thus, most X-ray characterizations are done *post-mortem*, i.e. after the experiments took place. For snow, studies concentrate on metamorphism. Indeed, [Schneebeli & Sokratov \[2004\]](#) focused on comparing the effects of thermal gradients on the metamorphism of different types of snow. Results showed that the finer grains were the one that grew the most, with a strong decrease in SSA. However the coarser grains exhibited more changes for grain shapes and curvatures. But snow undergoes also a strong metamorphism when the temperature is kept constant. [Flin et al. \[2004\]](#) quantified the evolution of curvature distributions with time, so that it can be accurately compared to metamorphism model [\[Flin & Brzoska, 2008\]](#). Further on is the recent work of [\[Calonne et al., 2014\]](#), which used X-ray metamorphism experiments to compute several physical properties such as the permeability, the thermal conductivity or the tortuosity. All these authors confirmed by real time 3D observations, that time and temperature lead to rounding and smoothing of snow grains along with grain growth and decrease of the SSA [\[Kaempfer & Schneebeli, 2007; Kerbrat et al., 2007\]](#). They also all denoted the raise of the anisotropy of properties during metamorphism, which is relevant for modeling. Additional worth to cite publications on *in situ* snow metamorphism are the work of [Ebner et al. \[2014, 2015\]](#) who studied the effects of airflow rates, and also [Hammonds et al. \[2014\]](#) that investigated the interface between ice and snow for avalanche understanding.

[Wang & Baker \[2013\]](#) performed compression tests on several types of low density snow at a fixed displacement rate of $3.5 \mu\text{m.s}^{-1}$. These revealed that the deformation of snow was mainly controlled by pressure sintering, thus by the bond size and number of bonds between snow grains. But it is also dependent of the density and the SSA. [Schleef & Löwe \[2013\]](#) performed creep tests on snow about $\rho \approx 0.10 \text{ g.cm}^{-3}$ with extremely low stresses from 0 to 318 Pa. These authors stated that the decrease of the SSA was independent of the stress, or of the initial density during their time scale experiments. However the decrease of the SSA should contribute to densification without overburden load¹ according to these authors. Nevertheless, *in situ* mechanical tests performed on the

¹ In the glaciology community, the "overburden load at a certain depth" is assimilated to the hydrostatic pressure at this particular depth and not to the stress state. When mechanical experiments are performed,

same densities by the same author [Schleef et al. \[2014\]](#) with a microcompression device showed a decrease of the SSA. This was accentuated when the imposed displacement increased. They concluded that this comes from new contacts between snow grains during densification. Displacement rates and stresses were about ten times smaller than [Wang & Baker \[2013\]](#). Using a Maxwell model for the strain rate, and thanks to full relaxation curves, [Schleef et al. \[2014\]](#) obtained a stress exponent $n \approx 2.2$ consistent with low stresses under 0.1 MPa [[Schulson et al., 2009](#)]. [Rolland Du Roscoat et al. \[2011\]](#) were the first to perform X-ray diffraction contrast tomography on snow samples that were slowly crept, allowing the grains to be differentiated from one another (stresses lower than 0.14 MPa and initial densities lower than 0.5 g.cm^{-3}). These authors followed the intragranular deformation of snow grains as small intragranular disorientations were observed. These results emphasized that the anisotropic viscoplasticity of ice crystal should be taken into account even for snow. Thus, [Theile et al. \[2011\]](#) associated in situ creep experiments with finite element simulations to model the deformation of snow of $\rho \approx 0.300 \text{ g.cm}^{-3}$. According to intragranular deformation observed by [Rolland Du Roscoat et al. \[2011\]](#), they used an anisotropic law for the ice, and meshed the grains by beams, enabling simulated and measured viscosities to be compared. [Chandel et al. \[2014\]](#) also performed in situ tests and finite element simulations, but concentrated on mechanical properties with a strong interest on the calculation of the RVE. However, an elastic model was used and justified by the fast applied strain rates (up to $7.2 \cdot 10^{-3} \text{ s}^{-1}$). Similarly, [[Wautier et al., 2015](#)] worked out the elastic modulus of snow by coupling X-ray scans with homogenization techniques using finite element simulations, and extended their work to the snow viscoplastic behavior, for the whole range of density (from snow to ice) [[Wautier et al., 2017](#)].

In situ experiments on snow and coupling mechanical tests with X-ray tomography have become common. However mechanical tests on firn are relatively scarce. To our knowledge, no in situ compression of firn under X-ray microtomography was performed. In other words, the pore closure was never followed during mechanical tests. However some laboratory experiments on dense snow and natural firn do exist. For instance, [Landauer \[1958\]](#) performed uniaxial tests on densities up to 0.63 g.cm^{-3} . This author reported stresses about 0.3 MPa for strain rates of $4 \cdot 10^{-4} \text{ s}^{-1}$. [Ebinuma & Maeno \[1985\]](#) performed creep tests on dense laboratory snow for different initial densities (above 0.55 g.cm^{-3} , similar to natural firn), and went further than 0.85 g.cm^{-3} . They concluded that above a critical density, which depends on the stress, dislocation creep rules the deformation [[Ebinuma & Maeno, 1987](#)]. [Meussen et al. \[1999\]](#) offers a more recent and complete work

the overburden load is the stress from the weight set above the sample. In this chapter, the component σ_{zz} is preferred instead of the "overburden load". The hydrostatic pressure is worked out with the weight of the snow above the point considered. Figure 1.13 depicts its evolution with depth.

on creep experiments on natural firn. Uniaxial creep tests on a large range of densities were performed. Results for densities of approximately 0.85 g.cm^{-3} exhibited less than 1 % of strain for an eighty hours long experiment under 0.5 MPa. Thus, stresses were three orders of magnitude larger than for [Schleef & Löwe \[2013\]](#) and strain was about two orders of magnitude smaller for about the same time. These results exemplify the range of mechanical responses of our material from the extremely porous firn to the extremely dense firn. [Meussen et al. \[1999\]](#) concluded that for those large densities (close to the close-off density), firn exhibits a behavior similar to polycrystalline ice.

A fine characterization of pore closure during mechanical tests is thus non-existent. This chapter focuses on describing such experiments with in situ X-ray tomography, a non-destructive technique. Section 4.2 describes the cold cell used for mechanical experiments, and gives details on how the strain was computed. Results for the strain field are given in section 4.3, with the use of the Digital Volume Correlation. This chapter aims to study firn densification by decoupling the effects of intragranular deformation obtained with oedometric tests (in sections 4.3-4.4) from those of diffusion processes. These are simulated numerically and experimentally by a heat treatment of firn samples (see section 4.5).

4.2 Methods

4.2.1 Cold cell for oedometric test

To perform mechanical tests on firn, a special cold cell was developed. It was designed to be adapted to a micro-compression device lent by Novitom, a French company based in Grenoble. A motor controls the vertical motion of a piston via gears. A load cell is mounted under the piston. A software enables the displacement of the piston to be controlled in a rather large range of velocity (between 0.1 and $10 \mu\text{m.s}^{-1}$). The cell itself is fixed on the micro-compression device. It consists of an air input (similar to the cold cell presented in section 3.3.1), and a cover that bears the compression load. The sample is set between the piston and the cover. The cover was designed to follow several specifications. It should sustain a sufficient load, be thermally insulated and should not absorb too much of the X-rays. A more detailed description of the design and of the specific calibrations is given in appendix F.

Figure 4.1 shows the apparatus inside the laboratory tomograph of CMTC-UGA (Université Grenoble Alpes). The cell is analogous to the one used by [\[Wang & Baker, 2013\]](#), except for the cold air flow as these authors used a cold room. Similarly to ex situ samples, the firn is drilled from a slice of ice core, and the diameter is adjusted to the PMMA socket with a lathe, in order to impose oedometric conditions. These conditions

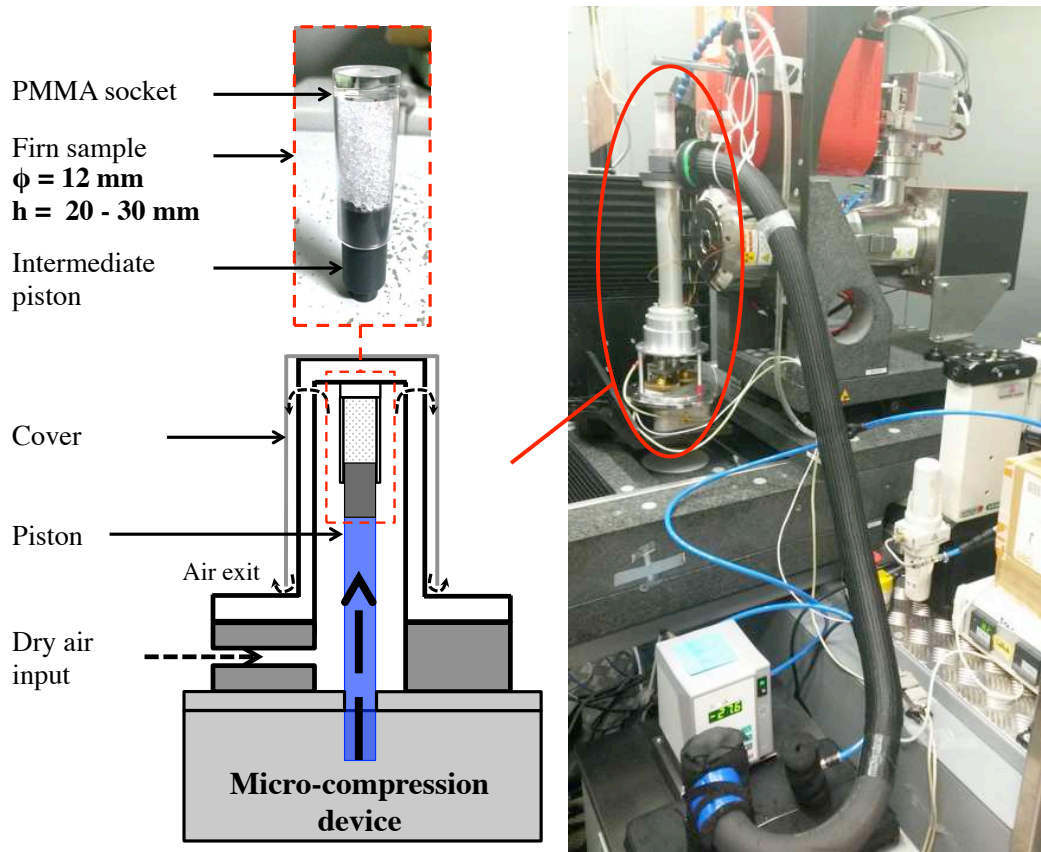


Figure 4.1: The apparatus inside the laboratory tomograph. The red ellipse highlights the microcompression device, and the sample is shown inside its PMMA socket.

are needed to avoid problems that could occur for such a granular material in uniaxial compression (grains may detach easily during the compression and lead to catastrophic failure). Section F.2 describes the stress state of an oedometric test. The oedometric conditions reproduce satisfactorily the stress state imposed in ice caps and soils. The oedometric test is a compaction test, which models an artificial densification of firn

The samples that are mechanically tested are named **in situ** samples in this chapter in contrast with those in chapter 3 that were named **ex situ** samples. They are 12 mm in diameter and their height is in the range 20–30 mm. Acquisition parameters are identical to those used for the DC-S12 samples in section 3.3, except for the voxel side length which is 15 μm to ensure that the oedometer is in the field of view.

4.2.2 Tested samples

The displacement rate of the micro-compression device was always set above $0.08 \mu\text{m.s}^{-1}$ during loading. This led to strain rates faster than 10^{-6} s^{-1} . However, we observed that displacement rates above $1 \mu\text{m.s}^{-1}$ lead to fractures within the firn. It took approximately 8 hours (without scanning time) to densify from 0.785 g.cm^{-3} to $\approx 0.85 \text{ g.cm}^{-3}$.

Four samples were successfully scanned during in situ artificial densification. They originate from the same slice of the Dome C ice core at 79.92 m depth. Table 4.1 gives information on three of these samples. The fourth one is detailed in section 4.5. Samples are named 80m_c as they come from approximately 80 m deep. The "c" stands for "compression".

Table 4.1 shows that three samples were tested at different displacement rates. When the samples seemed in oedometric conditions, a "test velocity" was applied to the piston for samples 80m_c2 and 80m_c3. The test velocity of 80m_c2 is twice the one of 80m_c1, while for the 80m_c3 sample it is three times larger. Figure 4.2 exhibits that it took about 5 hours of compression before the sample was in a correct position, so that the desired speed could be applied.

Figure 4.2a does not take into account the scanning time in the \mathbf{x} axis, which adds about 3 hours to the total time of the experiment. The macroscopic strain ε_{zz} comes from Digital Volume Correlation realized on the tomographic scans. The aim of these experiments is to follow pore closure. However, Fig. 4.2b shows that the density of the close-off ($\rho \approx 0.840 \text{ g.cm}^{-3}$, see chapter 3) is only reached for two experiments. The low strain rates and thus long time needed for these experiments under X-ray, led us to choose samples which pores are about to close.

Name	ρ_i (g.cm ⁻³)	ρ_{btv} (g.cm ⁻³)	ρ_f (g.cm ⁻³)	Test velocity ($\mu\text{m.s}^{-1}$)
80m_c1	0.798	-	0.825	0.0917
80m_c2	0.785	0.799	0.868	0.185
80m_c3	0.785	0.793	0.852	0.270

Table 4.1: Specifications of samples mechanically tested and which compression curves are plotted in Fig. 4.2. ρ_i and ρ_f are the initial density and the final density, respectively. ρ_{btv} is the density prior to the ramp/test velocity. It corresponds to the density before the true oedometric test. Because conditions are not oedometric initially (see section 4.2.3), a slow displacement rate is applied in the meantime. Then, as showed by Fig. 4.2a, when $\varepsilon_{zz} \approx 4\%$, a faster test velocity is applied.

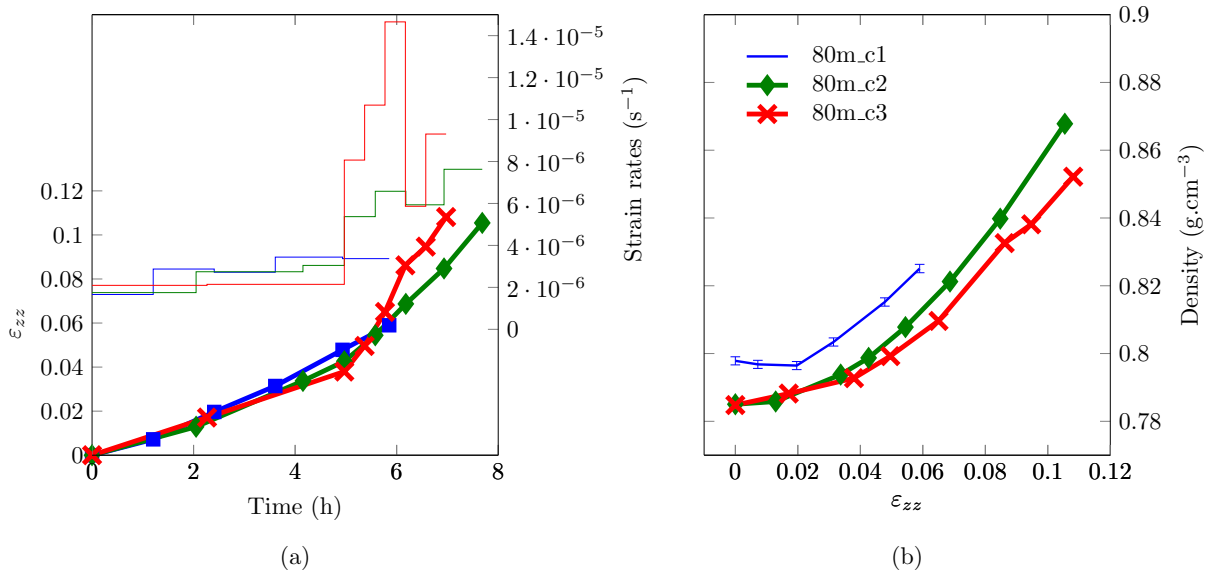


Figure 4.2: (a) Evolution of strains and strain rates during the experiments. All changes in strain rates are related to the points below. At each point, a scan is performed. But scanning time was removed from the scale. (b) Evolution of density with macroscopic logarithmic strain. Strain components are obtained by means of Digital Volume Correlation.

4.2.3 Digital Volume Correlation

The Digital Volume Correlation (DVC) uses in 3D the same methods than described in section 2.3.2. A complete description of the DVC can be found in Gaye [2015]. For samples analyzed in section 2.4.2, we applied a speckle so that the image correlation could be performed. In the case of 3D images, the speckle is not natural or artificial, but it is numerical. This means that the contrast that X-rays offer is used to perform the correlation. In our case of a two-phase material, there is a contrast between the pore phase and the ice phase. However pores are very large and have a low volume fraction (about 14 % for a depth of 80 m). Therefore, the most important point for the correlation is to insure that a subset is not totally located in the ice phase or the pore phase, but that it includes one or two pores. Large subsets are required since pores are large. In order to have a reasonable computation time, a bin of 3 was chosen for the resolution of the scans. For samples 80m_c1-2-3 the correlation is performed on subsets of 40 voxels which side lengths are 45 μm .

To achieve the correlation, CMV3D [Bornert et al., 2004] was performed for the first runs. However, an in-house GPU code was developed at SIMaP-GPM2 and could performed DVC of all deformation steps in a row. This code was preferred and also enabled to track the motion of particles (detailed in section 4.3.2). In practice, CMV3D was used to define the correlation grid as it offers a graphical interface.

The correlation grids were cylindrical for all experiments, so that the whole cylinder could be correlated. As shown by Fig. 4.3, subsets are overlapping one another on the diameter of the cylinder. It is even more pronounced on the diagonals of the grid. However, correlation on regular grids (rectangular parallelepiped with non-overlapping subsets) exhibited negligible differences for the results. Effects of subset size, and systematic errors of 3D correlation were extensively studied by Gaye [2015]. In our study, the DVC gives the mean linearized strain field tensor \mathbf{e} at each strain step in the sample. To evaluate the associated errors, the strain e_{zz}^{DVC} ² is compared with the macroscopic one e_{zz}^{Tomo} calculated from the height of the samples (derived from grey level images) on Fig. 4.4a. More than 50 measurements on the same sample were performed to obtain the height and then calculate the strain with a standard deviation of 0.17 %. This gives the precision on e_{zz}^{Tomo} . In Fig. 4.4, the difference between e_{zz}^{Tomo} and e_{zz}^{DVC} increases with strain, but remains reasonable. As the whole strain field is obtained, DVC is preferred in this chapter for the measurements of macroscopic strain.

Figure 4.4b shows the evolution of radial strains e_{xx} and e_{yy} (obtained by DVC) with the deformation. These strains increase and reach a plateau above 0.80 g.cm⁻³. Depending on the samples, axial strains e_{xx} and e_{yy} range from 1 % to 3 %. These results prove that

² The strain is computed with Cast3m [Cast3m, 2015].

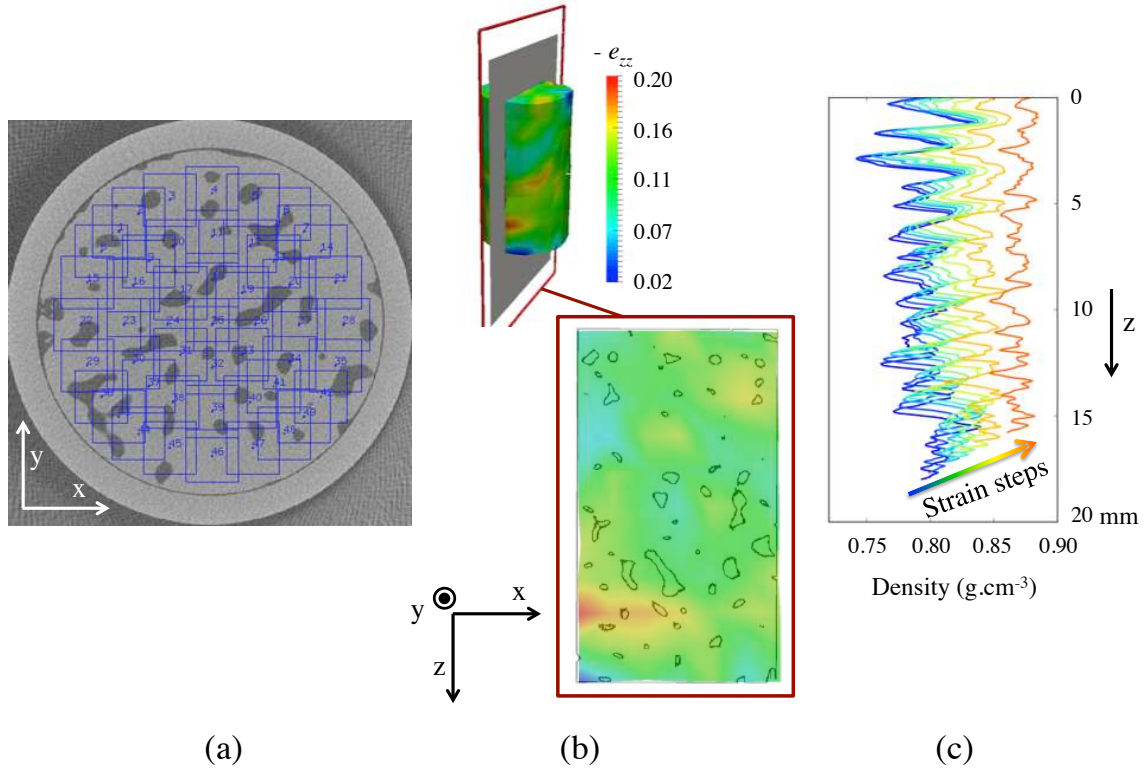


Figure 4.3: Correlation process for sample 80m_c2 with the software CMV3D. (a) The typical cylindrical correlation grid used. Gage length is 1.8 mm. (b) The strain field e_{zz} at the final step of a slice of the sample (visualization is done with ParaView [Ahrens et al., 2005]). A transversal slice superimposes the strain field with the porosity network (in 2D). (c) Evolution of density and sample height for all stages of the densification.

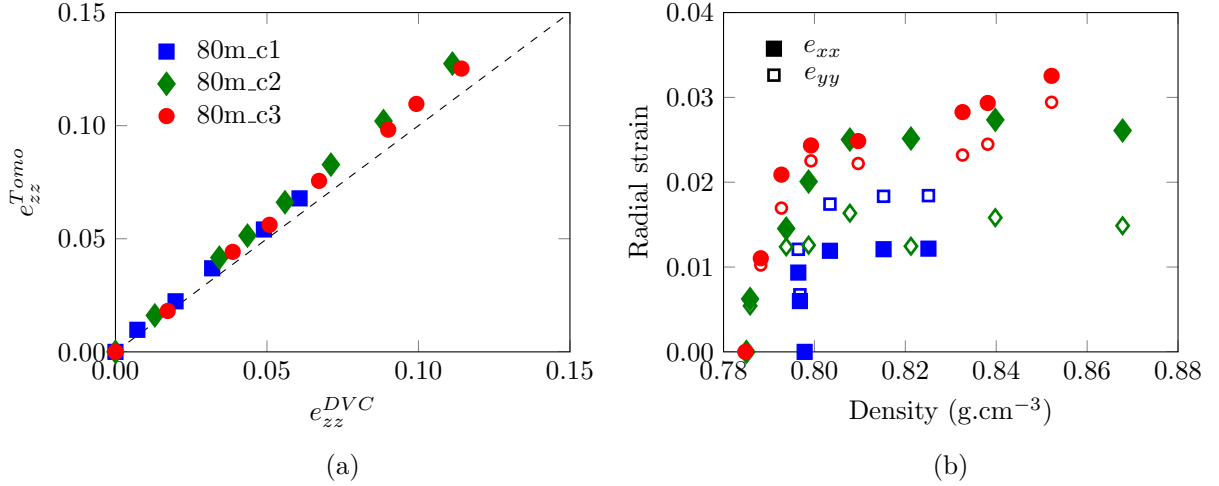


Figure 4.4: (a) Comparison between macroscopic strain calculated from the height of the 3D volume and DVC for the three oedometric tests. (b) Evolution of radial strains with density. Filled markers accounts for e_{xx} while empty ones account for e_{yy} .

the compaction test is not initially in oedometric conditions and that the stress state is closer to a uniaxial state. The sample dimensions obtained with the lathe cannot match the exact diameter of the PMMA socket. This is why the displacement rate was first as slow as possible, so that the sample can deform laterally while avoiding high stresses and microcracking. When the test velocity is set, Fig. 4.4b shows that conditions are oedometric (no more lateral strains).³

Figure 4.3 also illustrates the DVC with results for the strain e_{zz} . The correlation grid is very large with only 6 subsets of 40x40x40 voxels in diameter and 11 planes of subsets in depth. Therefore the resolution of strain is 1.8 mm. The evolution of density through the tomographic slices yields no particular features. The densification seems quite homogeneous, however there are some heterogeneities for the strain field. One transversal slice is represented with its associated pores. Concluding on pore collapse or expansion is difficult from 2D slices, and the strain field has a too low resolution to correlate distinct localized bands with pores.

³ This process was very laborious, and could have been avoided. Indeed a pre-load could have been applied in the cold room. The samples would have crept slowly and would have taken the shape of the PMMA socket.

4.3 Mechanical behavior

4.3.1 Evolution of stresses

The load cell supplied with the micro-compression device gives continuous measurements during experiments. Figure 4.5 depicts a typical stress-time curve for the experiment. The ordinate axis displays the stress σ_{zz} , which is the force divided by a disk area of diameter 12 mm. This means stresses are underestimated from point A to point B as DVC showed radial strains could reach 3%. After point B, sample is considered to be in oedometric conditions and the displacement rate is increased to its test velocity ($0.270 \mu\text{m.s}^{-1}$ in this case). When the target displacement of the piston is reached, we observe a stress relaxation. This drop of the stress illustrates the viscoplasticity of the firn deformation, as the decrease is progressive. After 10 minutes of relaxation, a scan of 25 minutes is performed (and is represented by a red shaded area). The next displacement is imposed three minutes after the scan. This insures that the time between two scans is identical and that these are performed in the same conditions.

The fit of the evolution of density with time that can be derived from Fig. 4.2, allows the evolution of stress with density to be calculated (providing that the relaxation times were removed). However, this fit relies on very few points (6 points for the sample 80m_c1 and 8 for samples 80m_c2-3, corresponding to the loading steps), while the evolution of stress is given at a time resolution of 0.1 s. The large discretization of the experiment for density points, leads to few small artefacts on Fig. 4.6a. For instance, while the stress rises at the beginning of the experiment, the density decreases for samples 80m_c1 and 80m_c3 because of the fit.

Though they are supposed to be constant between each strain steps in Fig. 4.2a, strain rates are clearly evolving during the compaction tests as only the displacement is controlled. Moreover, the scans involved stopping the compression test, leading to a relaxation of stress. The stress evolution is thus discontinuous. Several steps of deformation lead to very different densities. In brief, one can not obtain typical compaction curves from these results⁴.

Despite these issues, some conclusions can still be drawn. First, the stress σ_{zz} necessary to densify the firn at these strain rates goes up to 5 MPa. This is one order of magnitude larger than the hydrostatic pressure at Dome C for these densities (from Fig. 1.13 : at

⁴ To limit these issues, we could have performed scans without stopping the displacement. However the strain rate as well as the stress would still have evolved and images would have been slightly blurred (12.5 pixels of difference in a 25 minutes scans for a speed of $0.1 \mu\text{m.s}^{-1}$). Creep experiments offer on that matter the possibility to select the stress and follow the evolution of strain rates. The main issue is that the necessary weight to apply a 5 MPa stress on the sample involves a completely different apparatus inside the tomograph that we did not attempt to realize.

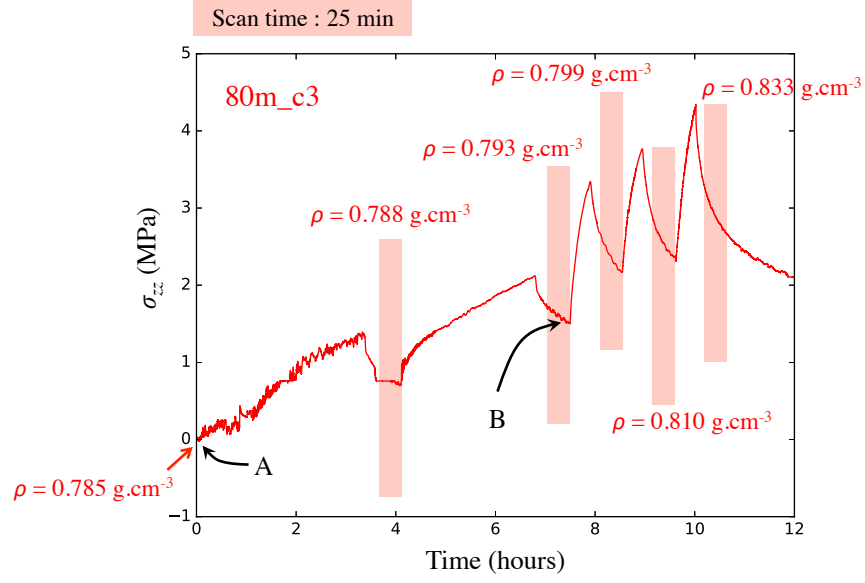


Figure 4.5: A typical stress - time curve, representing here the compaction of sample 80m_c3. Point A illustrates the initial imposition of the displacement of the piston. From A to B, the sample is positioning in the PMMA socket. At point B the test velocity is imposed. Scans are performed during relaxation time, i.e. when the piston does not move, and are represented by red shaded rectangles. The density obtained for each scan is also indicated.

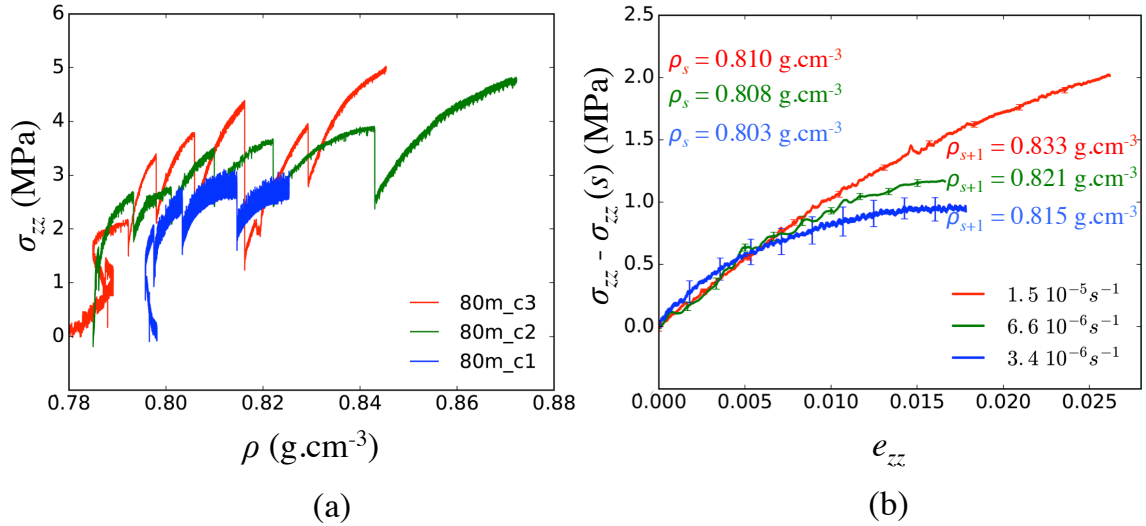


Figure 4.6: (a) Evolution of stress with density for the three samples. (b) Evolution of stress between two scans (between step s and $s + 1$) for the three samples during deformation. Densities at step s are similar. Stresses are shifted to start at 0 MPa ($\sigma_{zz} - \sigma_{zz}(s)$). Stresses are smoothed thanks to a moving average to remove the noise of the measurements that can be observed in (a). Error bars are the standard deviations of this moving average carried out on 20 consecutive points.

80 m depth it is about 0.47 MPa and at 100 m depth it is about 0.63 MPa).

These high stresses are also three orders of magnitude larger than reported by [Schleef et al. \[2014\]](#) for snow (with ρ between 0.120 and 0.150 g.cm⁻³) with the same displacement rates. However compiled data on ice from [Ebinuma & Maeno \[1987\]](#) tend to confirm the order of magnitude of the stress for the strain rates of in situ tests. Secondly, for about the same density, larger strain rates are associated to higher stresses. This is somewhat confirmed by Fig. 4.6b which is a zoom on the evolution of stress between two successive scans (steps s and $s + 1$). For an accurate comparison of the tests, we selected the strain steps that exhibited about the same initial density. In this case the initial density of all three samples is about 0.807 g.cm⁻³. The calculated strain is the incremental strain between the two steps of deformation selected. To ease the comparison, an offset was applied to the stresses so that they start from 0 MPa ($\sigma_{zz} - \sigma_{zz}(s)$). Results show that the slope increases with increasing strain rate. At about 1 % of strain, curves are distinctly parting from one another. Considering the stresses at the end of the deformation steps, and their associated strain rates from Fig. 4.2, the viscosity η can be evaluated. η is dependent of time as the microstructure and density are evolving during compaction tests. Assuming a Newtonian formulation for stress:

$$\sigma_{zz}(t) = \eta(t)\dot{\epsilon}_{zz}(t) \quad (4.1)$$

the viscosity $\eta(t)$ is in between $1 \cdot 10^{11}$ and $1 \cdot 10^{12}$ Pa.s. This is close to what [Theile et al. \[2011\]](#) obtained ($1 \cdot 10^{11}$ Pa.s) for snow with density ranging from 0.200 g.cm⁻³ to 0.350 g.cm⁻³, and larger than the value obtained by [Schleef & Löwe \[2013\]](#) for very porous snow (about $1 \cdot 10^8$ Pa.s for $\rho \approx 0.100$ g.cm⁻³). The range obtained from Eq. (4.1) compares well with the value of $\chi\mu_{basal}$ calculated for ice in chapter 2 (i.e. $4 \cdot 10^{12}$ Pa.s). Viscosity for firn is expected to be lower than for ice as the material is not fully dense. The large stresses obtained in Fig. 4.6 temper the use of a Newtonian flow law as it is likely that the stress exponent is more than unity.

4.3.2 Pore pressure

Other uses of the DVC can be made besides strain calculations. Combining the displacement fields obtained by DVC with the 3D labeling of pores from the Analysis_3D plugin [[Boulos et al., 2013](#)], it is possible to follow each pore at each strain step. Using a cylindrical correlation grid allows more pores in the volume to be tracked. The algorithm allowing this tracking is an in-house code, linked to the DVC algorithm, and which uses the inertia center of the labeled pores. Tracking the pores enables the precise determination of the volume of each particle during the oedometric tests. Considering the air as an ideal gas

and using the Boyle-Mariotte law, one obtains $PV = C$ with P the pressure, V the pore volume and C a constant. Therefore, when a particle is closing, we can thus work out the evolution of the air pressure inside the bubble during its shrinkage.

The following algorithm is used to work out the pressure evolution:

- A pore closing at step 0 is rejected as its internal pressure is not known.
- A pore closes at a step $> 0 \rightarrow$ the assigned value of the initial pressure is 1 bar.
- Only pores that are followed from the step of first appearance to the last strain step are considered. A few pores can be tracked from the beginning of the deformation, be lost by the tracking, and reappear at the end. This case can involve a bad assignment of pores, where two pores are given the same label, leading to inconsistent variations of volume.
- A pore which volume is less than $4 \cdot 10^{-4} \text{ mm}^3$ is rejected as its equivalent radius is smaller than $45 \mu\text{m}$, which is the resolution of the images for the DVC.
- All pores that multiply by two their volume between the initial and final step are rejected as these also come from bad assignment of labels, usually between the penultimate and the last step.

These specifications avoid including some inconsistencies of labels when tracking pores. In fact, errors on labeling come from two sources : the error on the displacement field estimation (from DVC) and a wrong pairing of pores (from tracking). Figure 4.7b depicts a moderate decrease for four different pores in the sample 80m_c2. Pore 71 is already closed at the beginning of the deformation, thus it is not taken into account in the pressure calculation. Pore 22 is not found between steps 1 and 7 and is thus rejected (as all pores in the same situation). Pore 52 and 86 are tracked at each step except for step 0 and are counted in the calculations. This leads to the use of a third of the number of closed pores that were tracked for the sample 80m_c2 and 80m_c3. For sample 80m_c1, this number is very low with only 29 closed pores used at the last strain step.

Figure 4.7 shows two different methods to evaluate the pressure. On Fig. 4.7a, box plots include only the pores that were already closed in the previous steps. Thus, it accounts for the increase of pressure between the steps. The small number of closed pores that are tracked for the first steps and that are indicated above the boxes should temper these statistics. After the strain step 5, the box plots become more significant for samples 80m_c2 and 80m_c3 as it includes more than 10 pores. Our procedure limits the number of closed pores. The correlation grid includes a smaller volume compared to the total volume, which also reduces the closed pore number. However, the median value (represented by a red horizontal bar on fig. 4.7a) increases with strain.

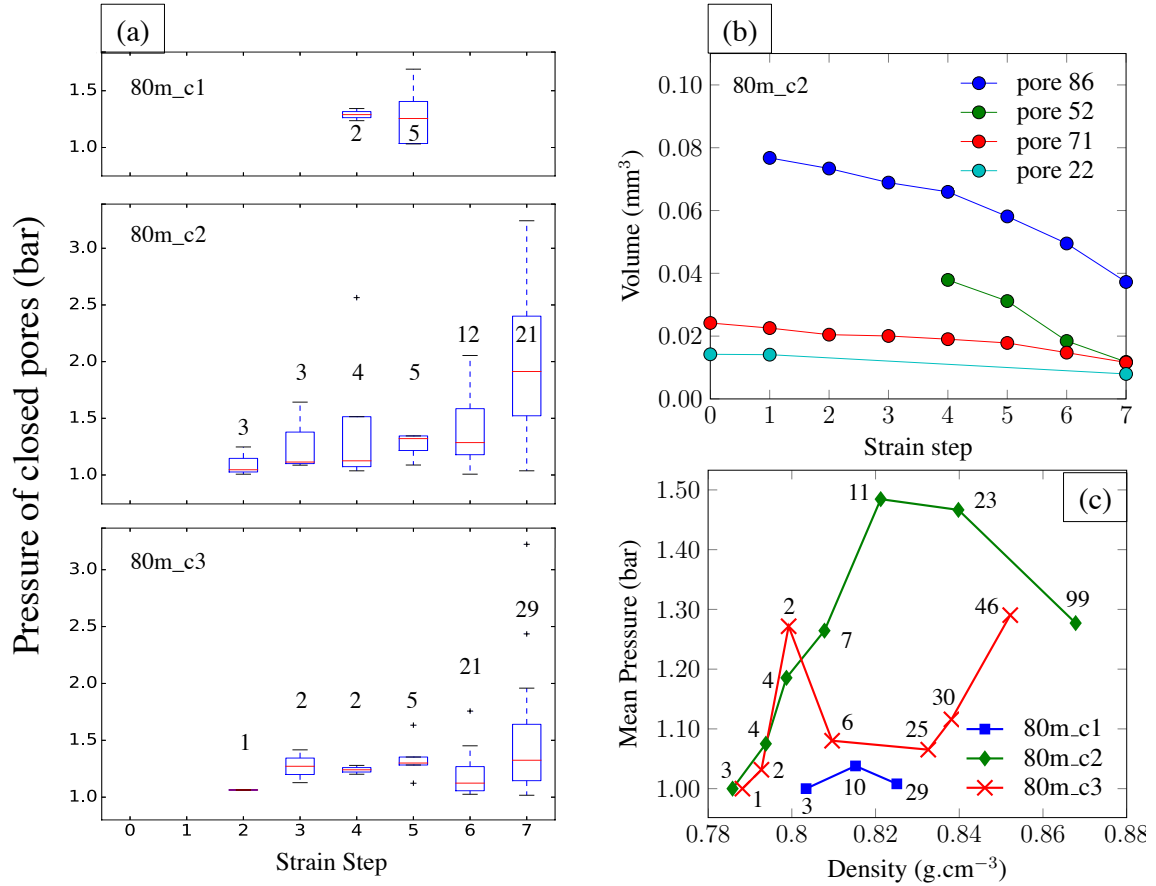


Figure 4.7: (a) Statistical representation of the pressure inside closed pores for all samples. At each strain step, a box plot only contains pores that have closed on the previous steps. The number of closed pores considered is indicated at each strain step. (b) Evolution of the volume of four particular pores for the sample 80m_c2. Pores 71 and 22 are rejected in the calculation of pressure. In fact pore 71 is closed at the beginning of the test and pore 22 is lost for several deformation steps. (c) Evolution of the mean pressure inside the closed pores. Pores that just closed, and that were already closed are considered for the mean pressure. Each point is marked with the number of objects used for the pressure calculation.

The mean value of the pressure is calculated using all closed pores on Fig. 4.7c. In other words, newly closed pores as well as already compacted closed pores are used to determine the mean pressure. The number of closed pores is consistently larger than for Fig. 4.7a. The mean pressure fluctuates with the density as many new closed pores are appearing (thus the pressure 1 bar is assigned to them), but it increases approximately from 1 to 1.3 bar. The maximal mean pressure value is 1.5 bar = 0.15 MPa for the sample 80m_c2, which is more than 20 times smaller than the stress measured at this density (see fig. 4.6). In conclusion, Fig. 4.7c shows that the internal gas pressure is generally negligible as compared to the overall macroscopic stress measured during the oedometric test. However, it cannot be ruled out that a limited number of closed pores may oppose a non-negligible pressure. The maximal pressure observed for one pore was estimated at 0.8 MPa for $\rho = 0.840 \text{ g.cm}^{-3}$ (strain step 6 of sample 80m_c2).

The pressure evolution observed is not particularly marked with density, and is of the same order of magnitude as reported values from the literature. For instance, regarding the Vostok ice core, Lipenkov et al. [1997] obtained a difference of pressure of 0.2 bar between the mean pressure at close-off depth and the atmospheric pressure at this depth. It is roughly 0.3 bar in our case for $\rho = 0.868 \text{ g.cm}^{-3}$. Gow [1968] measured the pressure evolution just after the close-off density, on ice core from the Byrd Station (Antarctica). An increase of approximately 100 % of the pressure inside closed pores were observed in the density range 0.825 g.cm^{-3} to 0.87 g.cm^{-3} . But all the pores were closed in contrast to our experiment. Moreover, in these studies, the pressure measured inside the closed pores deep in the firn was close to the σ_{zz} (with a difference of about 20 % under 2.5 MPa in Gow [1968]). Our results are drastically different. Compaction is facilitated as the few closed pores (and their internal pressure) lead to reduced equivalent stress compared to ice caps. In fact, there are few closed pores in the samples because lots of pores are touching the borders of the sample (enabling air to leak) while in ice caps the air is completely entrapped below the COD.

Finally, the number of closed pores continuously increases with the density as shown by 4.7a-c. Section 4.4 focuses on quantifying the closure and the morphology of the pores.

4.3.3 Specific surface area

The specific surface area characterizes the interactions between air and ice. Figure 4.8a compares ex situ samples to in situ ones. As already shown by the surface-to-volume ratio in Fig. 3.21 (chapter 3), the microstructure of the Lock In site seems more tortuous than at Dome C. Moreover the decline of SSA is linear with the density. The SSA for in situ samples falls on a master curve and exhibits the same trend, with a less abrupt slope than ex situ samples. The SSA is thus not only evolving with density. This difference in

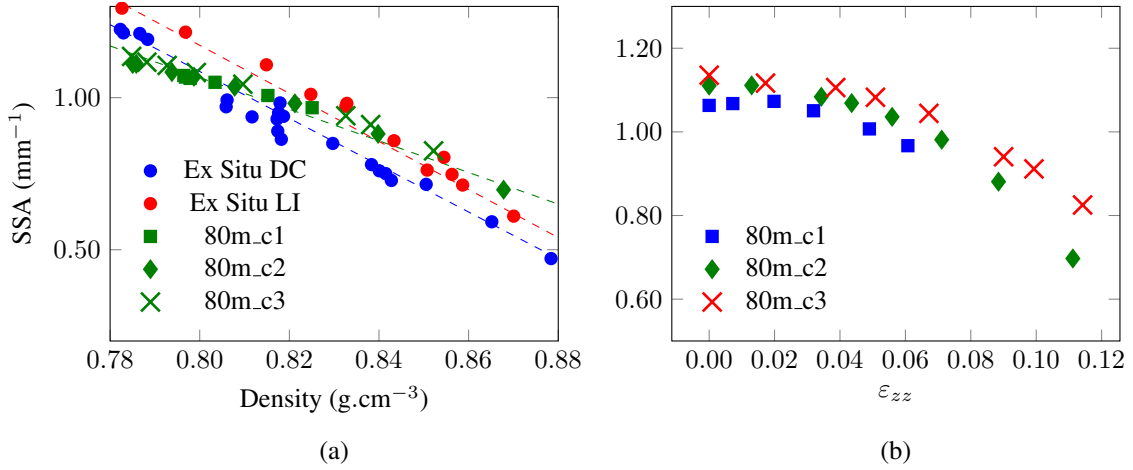


Figure 4.8: Evolution of the SSA with (a) density and (b) logarithmic strain. The dashed lines are trends of the SSA evolution and are only guides to the eye.

trend could be explained by the strain rates and stresses that are larger than for ex situ samples.

Figure 4.8b shows that the SSA of the different samples varies dissimilarly with strain (relative error on the SSA of 0.81 %), with the smaller strain rates exhibiting the largest SSA. However, the initial density is not exactly the same between these samples. Strain rates are 5 to 6 orders of magnitude higher (see Fig. 4.2) and stresses 10 times larger (Fig. 4.6 in the next section) for in situ samples than for ex situ ones. Therefore, the small slope differences on Fig. 4.8a. suggests that the evolution of the SSA is barely dependent of strain rates, relative stresses and initial density for this density range.

4.3.4 Grain size and anisotropy

The compaction tests have also implications on ice grains. From the microstructures presented in Fig. 4.9, two conclusions can be drawn. First, the mean grain size of an ex situ sample is larger than for an in situ sample for the same density ($\rho = 0.851 \text{ g.cm}^{-3}$). This is simply explained by the time of the experiment, which is not sufficient for grain growth evolution. The mean grain size of the initial in situ sample is the one from a slice of ice core from 80 m deep. It was measured to $\langle \bar{A} \rangle = 0.82 \text{ mm}^2$. Grain size of sample 80m_c1 is similar than before compaction, but the final strain was small ($\varepsilon_{zz} = 5.90 \%$). The mean cross-sectional area of the samples 80m_c2 and 80_c3 have lower values around 0.40 mm^2 (with very large standard deviations equivalent to the mean cross-sectional area for all samples). The decrease in grain size for samples 80m_c2-3 could be consistent with an expected recrystallization. However as shown in Table D.3 from appendix D, the quality of the thin sections for these two samples was low with less than a hundred

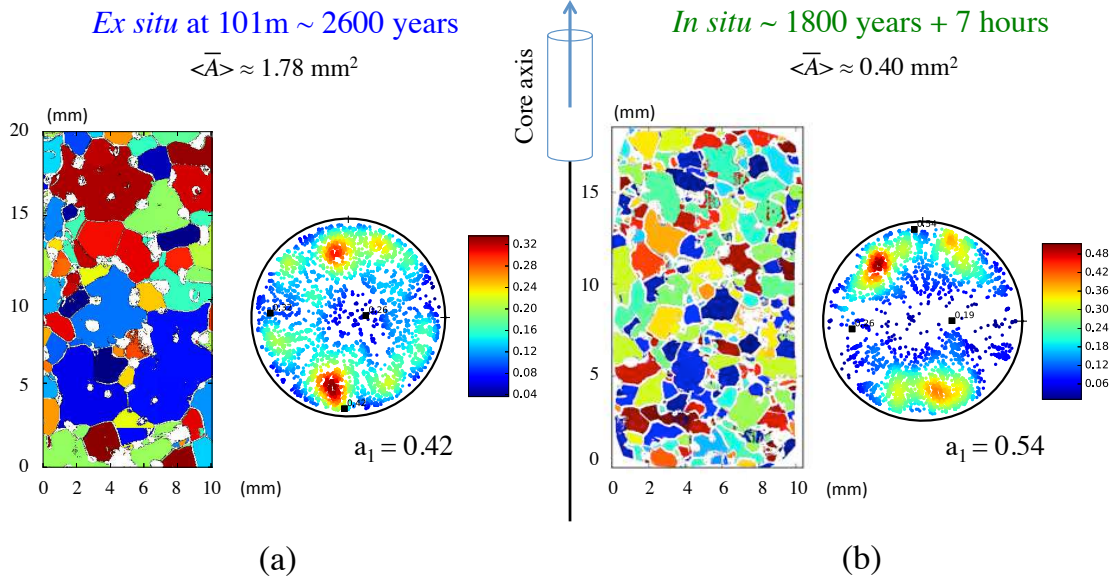


Figure 4.9: Microstructures and pole figures for (a) an ex situ sample from 101 m and (b) the last step of the in situ sample 80m_c3. Both samples have the same density $\rho = 0.851 \text{ g.cm}^{-3}$. Maximum eigenvalues and mean cross-sectional area $\langle \bar{A} \rangle$ are shown.

grains, hindering analyses. In any case, grain growth is excluded. Second, the pole figure on Fig. 4.9b exhibits a more marked anisotropy than for the ex situ sample. Indeed, the maximum eigenvalue a_1 is larger for in situ samples than for ex situ samples. The density of points around poles is also larger, meaning an alignment of **c** axes towards the loading direction, and reminding of a girdle fabric.

All the in situ samples were characterized by the AITA and showed similar results, with a more pronounced texture, and a grain size that does not grow from the initial step. Thin sections and pole figures are given in appendix D. Note that thin sections were closely investigated with the microscope, and some features of dynamic recrystallization were observed⁵. Indeed polygonization (high angle grain boundaries) and subgrain boundaries were observed⁶ as for ex situ slices of ice core (see section 3.10.2). However it is difficult to estimate in which proportion this type of recrystallization occurred.

⁵ To evaluate more precisely grain size and orientations during in situ tests, diffraction contrast tomography was considered, as it already proved to be a very pertinent tool to measure intragranular disorientation [Rolland Du Roscoat et al., 2011]. However, using this technique and analyzing the results turned out to be complicated and time consuming for firn. Hence it was put aside from this work.

⁶ Evidence of important grain nucleation [Chauve et al., 2015] or migration recrystallization [Duval & Castelnau, 1995; Chapelle et al., 1998] were not observed as one could have expected from such high temperature and strains.

4.4 Evolution of pores with artificial densification

4.4.1 Effects of densification on pore closure and morphologies

Similarly to the analysis performed in section 3.6, this section focuses on comparing ex situ and in situ samples coming from the same ice core (Dome C). To that end, Fig. 4.10 shows in (a) the evolution of the closed porosity ratio and in (b) the connectivity index for both type of samples. At a given density, the fraction of closed porosity is larger for ex situ samples. For instance, at 0.85 g.cm^{-3} , there are about 50 % of closed pores for ex situ samples, whereas for in situ samples there are only 20 % of closed pores. Consistently, the connectivity index is larger for in situ samples. In other words, pores are closing at larger densities for in situ samples than for ex situ samples. The right hand side of Fig. 4.10 illustrates this pore closure. Corresponding points are marked both on Figs. 4.10a and b.

The in situ points have been obtained with very different strain rates, but interestingly they all fall on a master curve for the closed porosity ratio and the connectivity index. A strong evolution of the shape of the pores is visible with the increase of density, especially in terms of curvature. This is clearly shown in Fig. 4.11, which depicts the porosity network for the same density (0.85 g.cm^{-3}) of an ex situ sample and an in situ sample. Area Z_1 exhibits very rounded pores with smooth surfaces, whether they are opened or closed. On the contrary, area Z_2 shows acute shapes, with pointy dead-ends. The morphology is clearly sharper than for ex situ results. Surfaces seem also more flat with in situ tests.

The visual inspection gives valuable qualitative information on the porous structure. However, a more precise evaluation of the morphological differences can be realized. The following section concentrates on quantifying these changes in terms of curvatures of pores.

4.4.2 Curvatures

Curvatures of 3D images are usually described with the mean and Gaussian curvatures [Flin et al., 2003, 2004]. Curvatures are supposed to be the driving force of snow metamorphism (surface energy minimization), and are used in codes to model the evolution of snow with time [Flin & Brzoska, 2008]. However, the mean curvature characterizes the convexity or concavity of an object, while the Gaussian curvature aims to differentiate dome-like shape from cylinder and saddle-like shape. It is however difficult to differentiate slight variations of local shapes from a diagram with these two curvatures. On the contrary the two principal curvatures inform only on the local shape and both are needed for this information. Here we take advantage of two other measures of local shape introduced by Koenderink & Doorn [1992]. The shape index is a measure of local shape that also

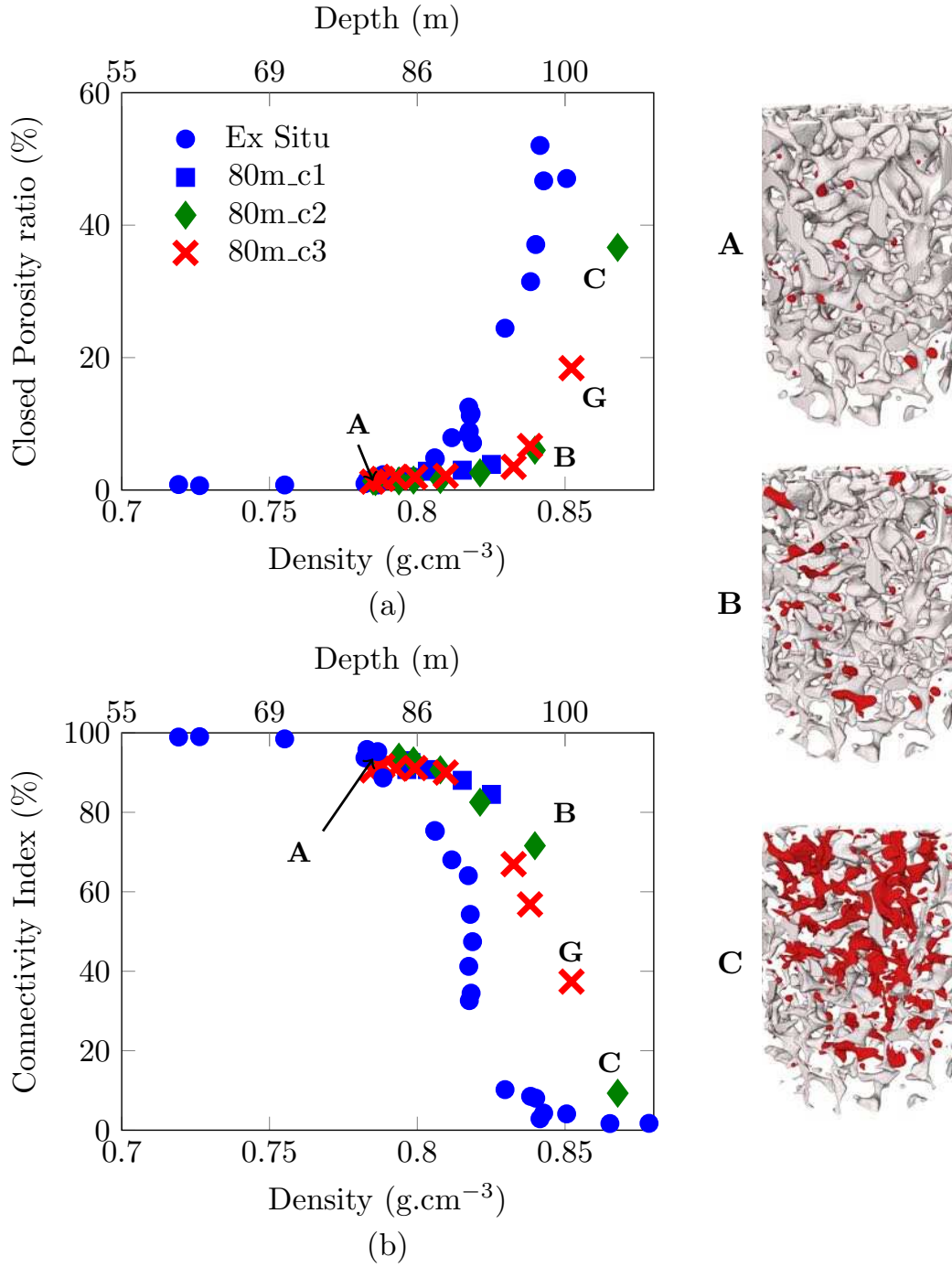


Figure 4.10: Evolution of (a) the closed porosity ratio and (b) the connectivity index with density for ex situ and in situ samples. Different steps of the oedometric test are presented on the right hand side of the figure. The red pores are closed pores. For visualization, figures A, B and C are subvolumes of sample 80m_c2. The pore network of point G is represented in Fig. 4.11b.

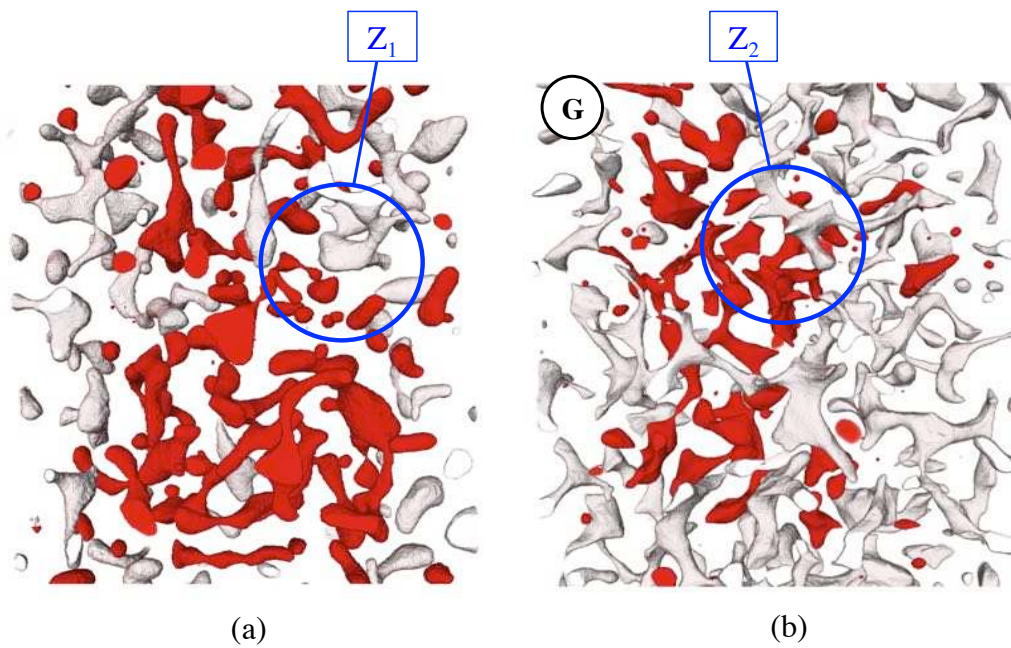


Figure 4.11: Pore morphology at 0.85 g.cm^{-3} density . The porous network on (a) is a zoom inside the DC-S12 sample from 100.38 m deep (**ex situ**), while the porous network named G on (b) is a zoom inside the **in situ** sample 80m_c3 at the end of its compression (Point G from Fig. 4.10). Areas Z_1 and Z_2 (Zone 1 and 2) focus on particular regions and are discussed.

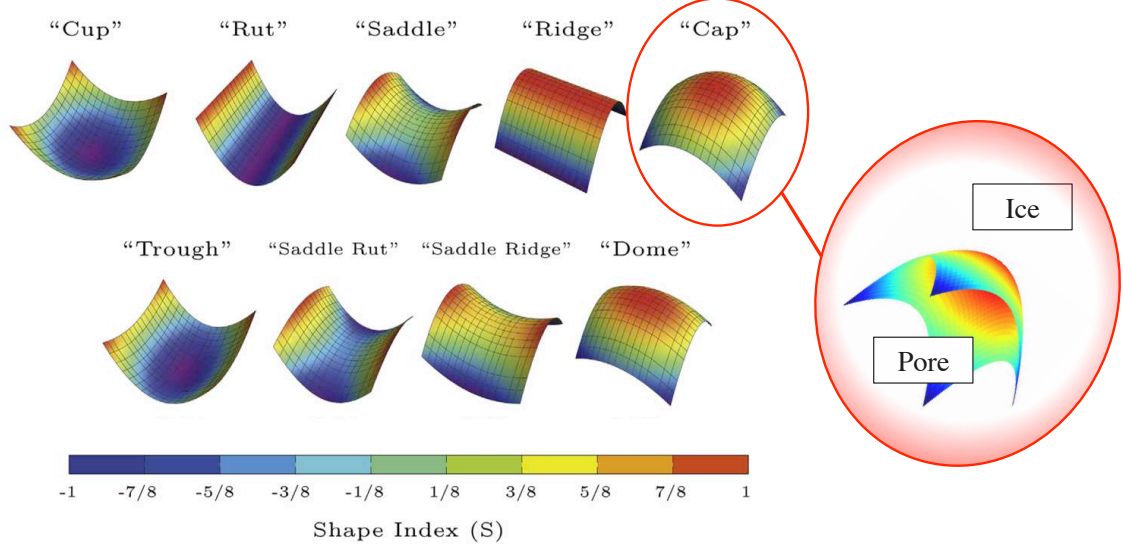


Figure 4.12: Local shapes for different shape indices adapted from [Shahani et al. \[2015\]](#). A zoom on the local surface shows the convention used in this work.

differentiates convexities from concavities. It ranges from -1 to $+1$. The curvedness is a positive value that quantifies the amount of curvature of the shape. It differentiates well flat surfaces from acute shapes for instance. These measures of shape were successfully used in the metallurgy community, to quantify dendritic growth [[Gibbs et al., 2015](#)] or to compare dendrites depending on the solidification method used [[Daudin et al., 2017](#)]. These indices are a powerful tool for comparison and are very appropriate for our case.

In the following, curvatures are investigated from the porosity point of view, such that the surface of an entrapped spherical bubble is convex and not concave. This is important as we adopt the convention $\kappa_1 > \kappa_2$ for principal curvatures. Our convention is thus closer to the one from [Daudin et al. \[2017\]](#) than the one adopted by [Koenderink & Doorn \[1992\]](#). The shape index S writes :

$$S = \frac{2}{\pi} \arctan \left(\frac{\kappa_1 + \kappa_2}{\kappa_1 - \kappa_2} \right) \quad (4.2)$$

The classification of shapes depending on the value of S in the range $[-1; 1]$ is shown in Fig. 4.12. A perfectly spherical pore (cap-like shape) would have a shape index equal to 1, and a perfectly cylindrical pore (ridge-like shape) would have a shape index equal to 0.5. Regarding the curvedness C , it is equal to 0 for a perfectly planar surface (infinite curvature radius), and increases as the curvature radius decreases. Its formulation is:

$$C = \sqrt{\frac{\kappa_1 + \kappa_2}{2}} \quad (4.3)$$

Local curvatures are computed with the software Avizo [[Avizo, 2017](#)]. The generation

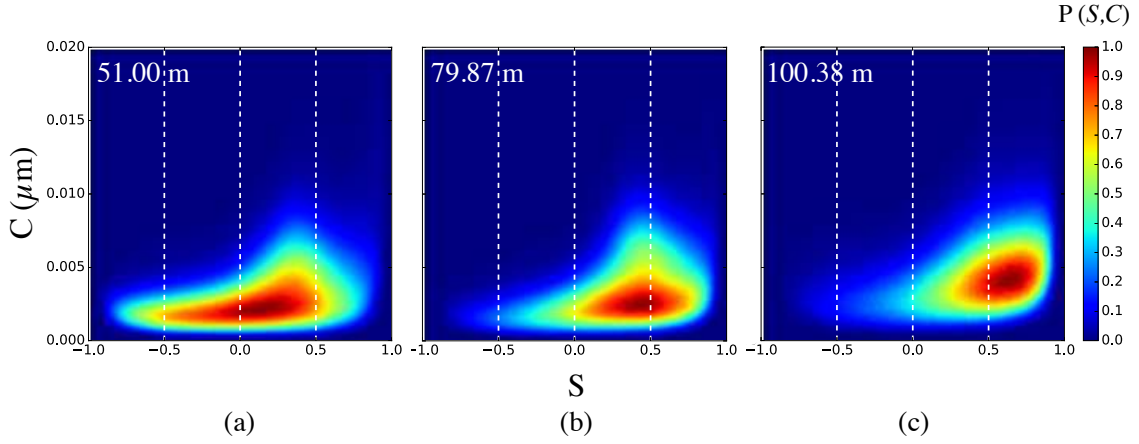


Figure 4.13: Curvature maps of a sample from (a) 51.00 m, (b) 79.87 m and (c) 100.38 m deep. $P(S, C)$ is a density of the two histograms S (Shape Index) and C (Curvedness). For each map, it is scaled by the largest count value, so that it ranges from 0 to 1. Densities at these depths are respectively (a) 0.680 g.cm^{-3} , (b) 0.787 g.cm^{-3} and (c) 0.851 g.cm^{-3} . Computation of S and C is performed on 10 million nodes with their ten nearest neighbors with Avizo [Avizo, 2017].

of the surface mesh implies the choice of a mesh size. It is achieved by selecting a smoothing parameter in Avizo. For the actual calculation of the curvatures, the user also needs to determine how many neighbors are taken into account for the local curvature. It is thus a matter of definition of what is called "local". It strongly depends on the resolution of the tomography. If the voxel size is large (e.g., $15 \mu\text{m}$), using 3 neighbors for a local surface can be similar than using 10 neighbors for a small voxel size (e.g., $4.5 \mu\text{m}$). Thus, a systematic approach was used on some typical case of pores (close to spheres, rounded and sharp pores) to determine the best compromise between speed and accuracy of the results. About 10 millions of nodes on the generated surface are used for our samples. Using the ten closest neighbors for the local curvatures leads to about 10 to 20 minutes of computation time. All curvatures presented in this work are calculated using the same parameters.

Figure 4.13 displays the curvature maps of three firn samples of Dome C from different depths. In fact these are 2D histograms of the curvedness and the shape index. $P(S, C)$ designates a probability density which is scaled. In other words, when a region of the map displays $P(S, C)=1$, it means that the local surface characterized by values S and C is the most abundant in the sample. There is a clear evolution of the distribution of local shapes with depth. The most porous sample (Fig. 4.13a) shows a very sparse horizontal distribution. The maximum density points ($P(S, C) \gtrsim 0.95$) are between 0 and 0.3. Shapes cover the entire shape index but there are more shapes between the saddle and the ridge. With increasing depth, the distribution moves to the right (towards cap

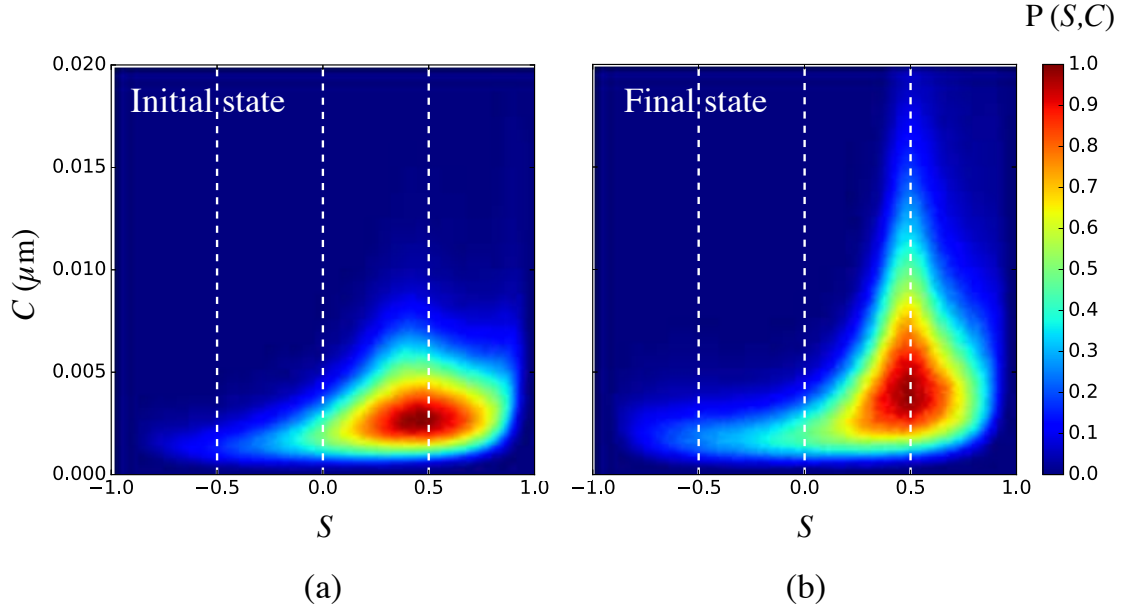


Figure 4.14: Curvatures maps of a sample from 79.92 m deep (a) before ($\rho = 0.785 \text{ g.cm}^{-3}$) and (b) after the compression test ($\rho = 0.868 \text{ g.cm}^{-3}$). $P(S, C)$ is a density of the two histograms S and C . For each map, it is scaled by the maximum count value, so that it ranges from 0 to 1.

or dome-like shapes). On Fig. 4.13b it is more centered around the ridge shape, while on Fig. 4.13c, shapes are mainly between ridges and caps, and are centered around domes. It is consistent with the progressive closure of pores illustrated on Fig. 3.10. Indeed at 100.38 m, lots of pores are closed, thus they are rounding. At 51.00 m, there are very few closed pores, and the pore network is totally connected, which implies more saddle-like shapes. However there are lots of concavities that were not striking at first sight at this depth and which are represented here with a probability density of ≈ 0.7 for rut-like shapes (Fig. 4.13a). On the contrary, the curvedness does not evolve with increasing depth, the 0.1 isovalue staying below $0.01 \mu\text{m}^{-1}$ in all cases.

Figure 4.14 shows the curvature maps of a firn sample from 79.92 m deep that was compacted. The initial state and the final state of the compression are represented. On these maps, local surfaces are neither a perfect cup nor a cap, but they mainly range between the saddle and the dome. The initial state is very close to the map on Fig. 4.13b. The final state shows a distribution more centered around the ridge-like shape than it was initially, and exhibits large contrast with Fig. 4.13c (which density is however smaller). On the contrary to Fig. 4.13, the striking difference between the initial and the final state in Fig. 4.14 comes from the curvedness. After compression, the distribution is sparser. The curvedness is much larger. This represents well the acute shapes that were observed

for the pore morphology on Fig. 4.11. The curvature is much more pronounced locally. Negative values are also slightly more represented in the final state, especially from the saddle to the rut. This underlines the more concave shape of pores. These come from the flattening of pores during the compression.

All compacted samples exhibit the same evolution in terms of curvedness and shape index. These maps are very enlightening and allow the comparison of pore evolution from polar firn densification and from oedometric compaction.

4.4.3 Discussion

In situ characterization revealed large differences with ex situ results both on pore morphology and on pore closure itself. During oedometric tests, viscoplasticity was observed, with stresses about one order of magnitude larger than in firn cores. The strain rates used in the oedometric tests are also large compared to polar firn densification rates (about 6 orders of magnitude larger). The durations involved during in situ tests are much too short for slow thermally activated processes to occur. Figure 4.15 gives an estimation of the evolution of the firn age in the ice core of Dome C. We extrapolated the simulated ages at the different steps of the oedometric tests by fitting density. The eight hours in situ experiment for sample 80m_c2 represents about a thousand years of densification. A correct assumption is that there is no grain growth in that short time and no sintering. Thus, the experiment totally decoupled the plastic deformation from the diffusion effects clarified in section 1.3.4. According to the sharpening of pores, texture observations and strain rates, dislocation creep was the dominant mechanism during compaction (essentially on basal planes). Closure of pores occurred at larger densities than expected by ex situ results. Therefore, the following section aims to study the implications of the diffusion mechanisms on firn densification, as their effects were negligible during in situ oedometric tests.

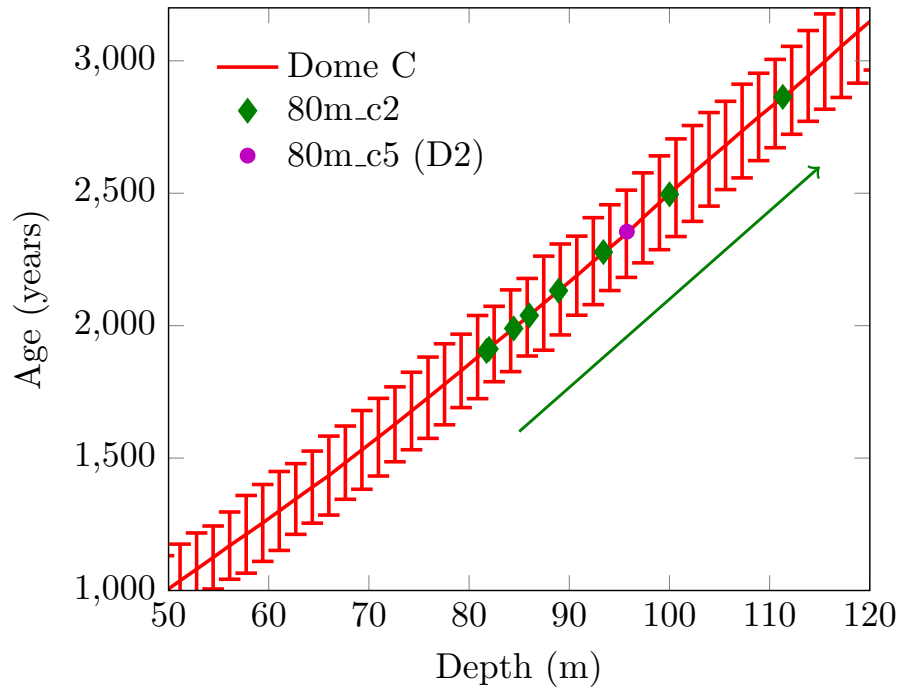


Figure 4.15: Age of the firn from the Dome C ice core [Veres et al., 2013; Bazin et al., 2013]. Fitting the density with depth enables the simulated ages for the compaction tests to be extrapolated. The green arrow represents the direction of the densification for the in situ sample 80m_c2 (duration of the test: 8 hours). Sample 80m_c5 is analyzed in section 4.5.

4.5 Modeling thermally activated processes

4.5.1 Heat treatment

Oedometric tests clearly showed that time is crucial for polar firn densification. Thermally activated processes could not be observed during the short time of the experiment. Additional experiments were carried out in order to understand the contribution of these processes to microstructure evolution. Figure 4.16 summarizes the samples used and the treatments performed. One sample (named 80m_c5) from the same slice of the in situ samples was compacted at a test velocity of $0.185 \mu\text{m.s}^{-1}$ and reached a final density of 0.828 g.cm^{-3} . After the compaction, this sample and others were put in boxes at -2°C , in order to accelerate mechanisms related to diffusion. This holding stage at high temperature is called a heat treatment (HT) in Table 4.2. Two depths were tested (80 and 90 m) with two samples that underwent creep named 80m_c4 and 90m_c1. A load was applied on these samples for the entire duration of the experiment, which was five-month long. We designate reference samples the samples 80m_ref and 90m_ref. These samples are only subjected to a heat treatment in order to understand the benefits of the coupling of creep with diffusion for samples 80m_c4 and 90m_c1.

Two boxes were prepared for this experiment and are shown in Fig. 4.16. One of them hosted samples from 80 m deep (box A), while the other hosted the ones from 90 m deep (box B). In order to avoid sublimation of the firn samples during the five months of the experiment, boxes were filled with snow, ensuring that the relative humidity inside them is close to 100 %. There is equilibrium between the saturating pressure vapour of air and ice in the firn. As samples are also recovered with plastic foils, loss of matter from vapor diffusion should be avoided. The relative humidity of box A stabilised at 99.9%, while the mean value was 74.24 % for box B.

The applied stress on sample 80m_c4 was 0.29 MPa and it was 0.71 MPa for sample 90m_c1. At these depths, the hydrostatic pressures are respectively 0.47 MPa and 0.55 MPa (from Fig. 1.13). In contrast with the 80m_c4 sample, the load was increased from 0.44 MPa to 0.71 MPa during the five months of experiment for the 90m_c1 sample, because no deformation was observed after three months.

4.5.2 Effect of heat treatment on pore closure and morphologies

Figure 4.17 displays the closure of pores after the heat treatment. Error bars are shown for densities and for the y-axes for points D and E. All points linked by an arrow are the same extracted subvolumes after different histories. For instance, a brown arrow that represents the compaction of the sample links D1 to D2. The compaction of 80m_c5 gives

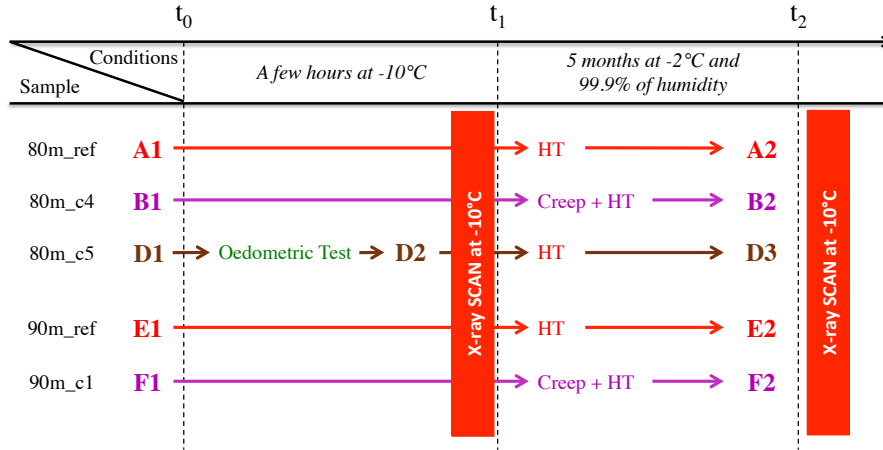


Table 4.2: Description of the heat treatment (HT) applied to various samples with associated times and temperatures. X-ray scans are performed just after the oedometric test on the 80m_c5 sample and on all other samples. The experiment is carried out in a cold room, separately from the tomograph. Five months later, the experiment is stopped and the same samples are scanned again.

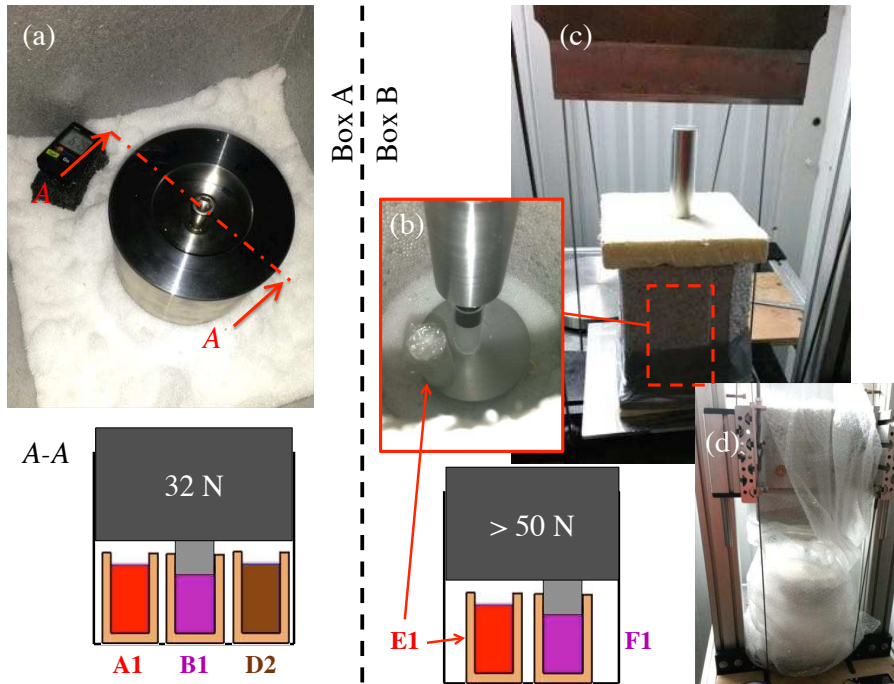


Figure 4.16: Graphical description of the two kinds (A and B) of loadings used on the firm samples. (a) A steel part acts as a simple weight. The second one uses the creep device presented in chapter 2. Picture (b) shows the firm sample inside their PMMA socket in the polystyrene box B (shown in (c)). The box A contains snow around the loading device, and box B is wrapped in bubble wrap so that snow could be introduced around it (d). A continuous measure of humidity is carried out with a recording device Testo 174H (precision $\pm 0.1\%$).

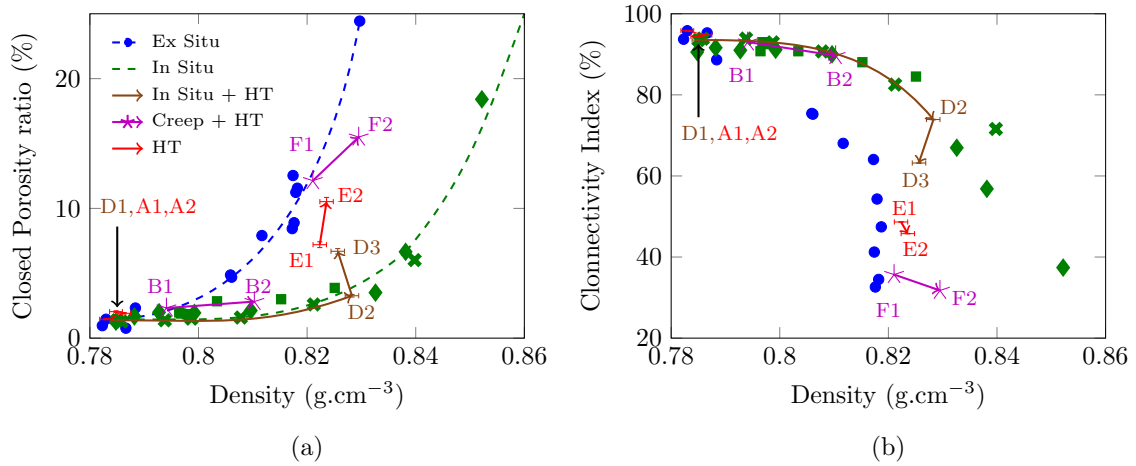


Figure 4.17: Evolution with density of (a) the percentage of closed porosity and (b) the connectivity index. Blue disks (linked by the blue dashed line) are the ex situ samples. Green diamonds, crosses and squares (linked by the green dashed line) are in situ tests performed at -10°C . In agreement with Fig. 4.2, the brown arrow from D1 to D2 illustrates the oedometric test (at -10°C). The arrows linking D2 to D3, and E1 to E2 illustrate the effect of the heat treatment (HT) at -2°C , while A1 and A2 stay close to each other. Purple stars and arrows (B1, B2, F1 and F2) correspond to the creep test with HT at -2°C . Samples A1, B1 and D2 were put in box A, and samples E1 and F1 in box B (Fig. 4.16).

similar results than in situ tests, as D2 falls on the green dashed line. From D2 to D3 the closed porosity ratio increases from 3.3 to 6.7%, while the connectivity index drops from 74 to 63%. The density slightly decreases between D2 and D3. For reference samples, the density stayed within error bars between A1 and A2, or between E1 and E2, but an increase of the closed porosity ratio is only noticed between E1 and E2. Creep tests on samples 80m_c4 (B1) and 90m_c1 (F1) exhibit both a rise in density. However the creep and heat treatment on the deepest sample do close the pores, while they do not for the sample B2. The connectivity index is consistent with what is observed. As for the sample 80m_ref, the time allowed was not enough for the pore channels to disconnect from one another. In brief, oedometric tests tend to increase the density without disconnecting pores, while increasing the temperature tends to unlink the pores for a given density.

Figure 4.18 corresponds to a zoom within the porosity networks after compression test, and then after the five months of heat treatment. The curvedness clearly shows that the acute shapes and pointy dead-ends are starting to round. Concavities also seem to be reduced and some pore channels are disappearing, closing pores in the meantime.

This rounding of pores is confirmed by Fig. 4.19. It compares the local curvatures for sample 80m_c5 after compression and after heat treatment. The curvedness is clearly reduced thanks to time and high temperature. Local surfaces of an ex situ sample from a

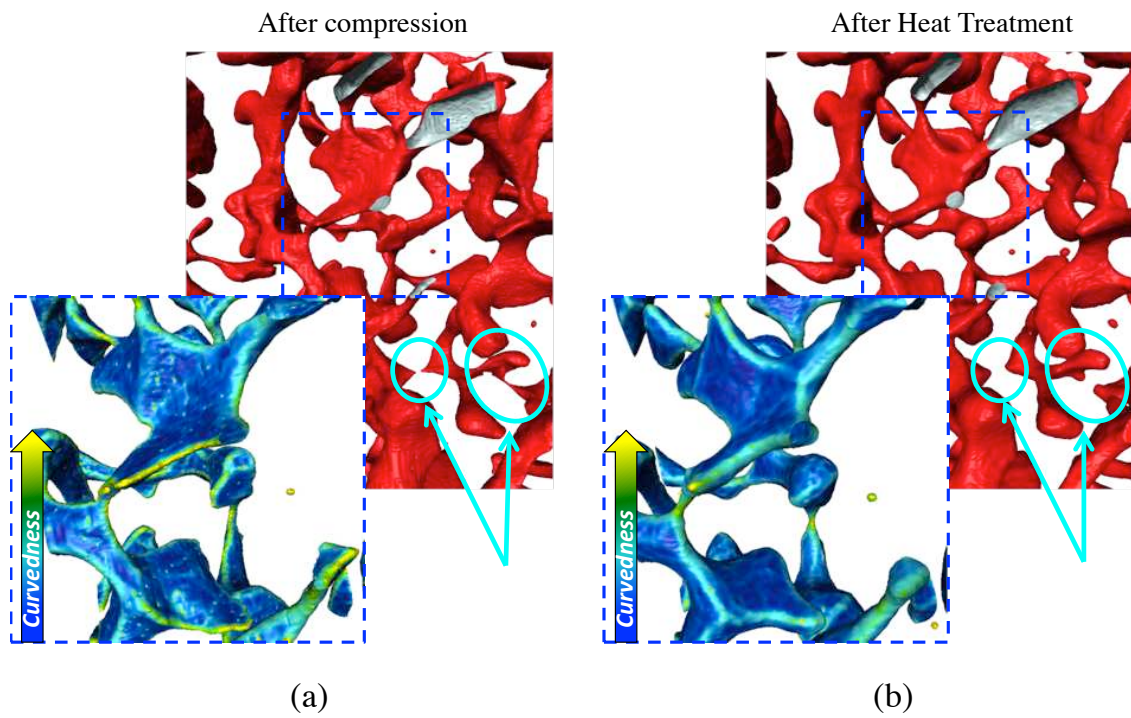


Figure 4.18: Zoom within the porosity network of sample 80m_c5 (a) after compression and (b) after heat treatment. The same region is shown in (a) and (b). Pores are rounding and some pore channels are even closing (pointed out by light blue arrows and ellipses). The curvedness is shown locally on some pores, and illustrates the increase of the local curvature radii.

95 m depth are also plotted on the bottom left for the same density than the sample D3. Although not identical, the local shapes start to look more alike after five months of heat treatment.

High temperature and time enable to close the pores. Closure is also dependent of the microstructure. Indeed, between samples E1 and E2 - E1 was only submitted to a heat treatment - the change in curvatures is minimal. Therefore, the driving force as defined by the difference between the mean curvature with the local curvature, is much less accentuated than for samples D2. However pores are still closing (Fig. 4.17). Curvatures are also similar for samples A1 and A2 but on the contrary to E1, pores do not close. Sections 3.4 to 3.7 demonstrated that closure was heterogeneous between approximately 87 m and 98 m with small pore channels (see Fig. 3.22). This means that closure is particularly accelerated in a certain range of depth (thus for a particular type of microstructure). More samples need to be tested to assess this conclusion more firmly.

The heat treatment described above has lasted five months and was set to a -2°C temperature. These numbers were chosen taking into account time constraint. Still, it is interesting to evaluate very roughly how these parameters (time and temperature) can be linked to the conditions that the natural firn is subjected to. Assuming that the creep rate depends on thermal activation and is described by an Arrhenius exponential term [Hosford, 2010] :

$$\dot{\varepsilon} = \frac{A_1}{T} \exp\left(-\frac{Q}{RT}\right) f(\sigma, d) \quad (4.4)$$

with $f(\sigma, d)$ a function that depends on the stress σ and the grain size d . The pre-exponential term A_1/T does not have a great influence on the results, but is kept here. The strain rate is linked to the densification rate with $\dot{\varepsilon} = -\frac{\dot{\rho}}{\rho}$. For a constant stress, grain size, and temperature, the logarithm of the density is roughly proportional to:

$$\ln(\rho) \propto -\frac{1}{T} \exp\left(-\frac{Q}{RT}\right) f(\sigma, d)t \quad (4.5)$$

Equation (4.5) is based on very strong assumptions (stress and grain size are constant, the activation energy is the same whatever the temperature) that are difficult to ascertain. Still, we should use it as a rough tool in the following discussion.

Fig. 4.20 plots the time necessary at different temperatures and activation energy Q to reach a specific density (according to Eq. (4.5)). For grain growth, which is a thermally activated mechanism, the commonly accepted activation energy is around 50 kJ.mol^{-1} (49.6 kJ.mol^{-1} in Arnaud [1997], 48.6 kJ.mol^{-1} in Gow [1969]). According to Mellor & James [1967] the activation energy for dislocation creep ranges from 44 to 74 kJ.mol^{-1} (dense to porous firn), while Pimienta & Duval [1987] reported a value of 60 kJ.mol^{-1} .

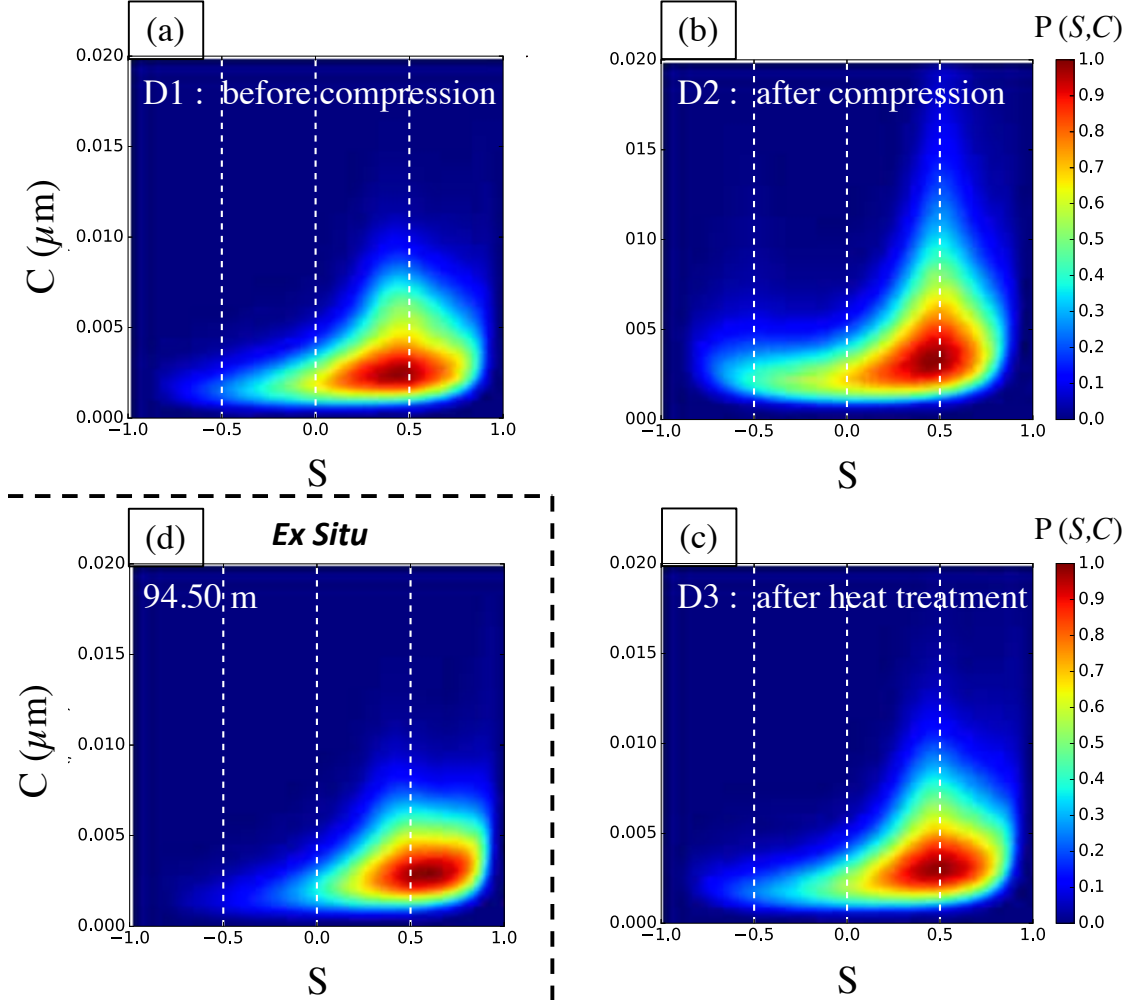


Figure 4.19: Curvature maps of sample 80m_c5. (a) Curvature map from Fig. 4.14b at 79.87 m representing the initial state D1. Maps (b) after compression (D2), and (c) after heat treatment (D3). (d) Curvature map for a 95 m deep DC-S12 sample, which corresponds approximately to the same density than map (c) ($\rho = 0.8256 \text{ g.cm}^{-3}$ for (c) and $\rho = 0.8297 \text{ g.cm}^{-3}$ for (d)).

The x axis in Fig. 4.20 uses the mean annual temperature of Dome C as a reference. A zoom is proposed to relate months at high temperature to years at low temperature. In other words if it takes 200 years for a firn sample to evolve from a microstructure A to B at -55°C , it will only take a bit more than two years at -10°C assuming an activation energy of $50\text{ kJ}\cdot\text{mol}^{-1}$ and for the same stress.

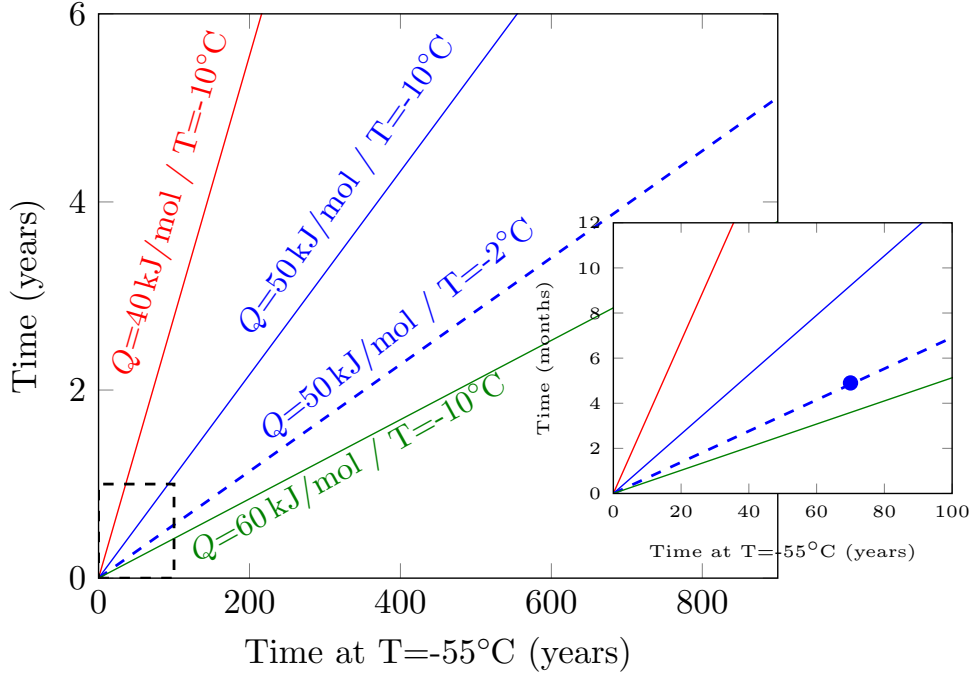


Figure 4.20: Time - Temperature equivalence diagram. The solid lines give the time needed at -10°C and for different activation energy Q to obtain the same strain than at -55°C , according to Eq. (4.5). The blue dashed line corresponds to the conducted experiment at -2°C . The inset is a zoom of the black dashed box. It displays the equivalence of time at low temperature for the 5 month experiment.

For the five month experiment at -2°C of the sample 80m_c5, dislocation creep is negligible, and the densification process is mainly a mix of lattice diffusion (see Fig. 1.14), possibly accompanied by grain growth and other thermally activated mechanisms. The activation energy used⁷ to represent this sample evolution is assumed to be $50\text{ kJ}\cdot\text{mol}^{-1}$. From the inset zoom in Fig. 4.20, it appears that the five month experiment should represent the evolution of the microstructure during 70 years at -55°C . The natural densification of firn from $\rho \approx 0.79\text{ g}\cdot\text{cm}^{-3}$ (about 80 m deep) to $\rho \approx 0.83\text{ g}\cdot\text{cm}^{-3}$ (about 95 m deep) takes about 300 years according to Fig. 4.15. Performing this experiment

⁷ Note that Maeno & Ebinuma [1983] used activation energies of $44\text{ kJ}\cdot\text{mol}^{-1}$ and $66.2\text{ kJ}\cdot\text{mol}^{-1}$ for boundary and lattice diffusion respectively when drawing pressure sintering maps such as Fig. 1.14. Using only one activation energy for a mix of mechanisms is therefore questionable here, but this assumption is made to highlight the importance of microstructure evolution during heat treatment.

barely simulates one fourth of the ageing. However, Fig. 4.20 demonstrates that results are strongly dependent on the assumed activation energy. Indeed increasing the activation energy from 50 to 60 kJ.mol⁻¹ leads to a simulated time three times larger. As already indicated above, these equivalences rely on a strong assumption on the microstructure evolution and we should be cautious when using them as a comparison tool with the ice core, as stresses are not taken into account. Still, it gives a general idea of what happened during the experiments. Figure 4.20 also reveals that three years of storage at -10 °C should accelerate the grain growth of 300 years. It seems important but it is not that much when looking at the grain growth evolution with depth and density from Fig. 3.31. Note that post-coring entrapment in the firn [Aydin et al., 2010] or gas losses [Landais et al., 2012] were observed on collected ice cores, meaning that the microstructure might evolve during storage. ⁸

4.5.3 Grain size and texture after heat treatment

Samples that underwent heat treatment could not be characterized right away by microscopy after X-ray scans. They were kept at -10 °C for five months, thus grain growth should have been limited. However samples B2 and F2 that were crept, have a larger grain size than heat-treated samples (A1 and E2). This observation is shown in Fig. 4.21 and Table D.4. There are no marked differences between the supposed initial microstructure (slice from ice core that was stored at -10 °C) and E2, which was only heat treated at -2 °C. Both exhibit some large and small grains (about ≈ 50). However F2 has only a few grains (≈ 19). Same observations can be made between samples A2 and B2 (shown in Table D.4 from appendix D). According to the colatitude (shown here between $[0, 2\pi]$), **c** axes of F2 are aligning with the loading direction with grain colours close to $\theta = 0, \pi$ or 2π . Therefore the very few present grains lead to an accentuated texture.

Interestingly sample D3 which were deformed by an oedometric test at -10 °C and then heat treated at -2 °C, does not look very different than A2, but its **c** axes are more aligned to the loading direction. For samples 80m_c1 to c3 and even for D3, features of recrystallization are not significant. In situ experiments are rather fast ($> 10^{-6}$ s⁻¹) with large stresses (from 1 MPa to 5 MPa) while the experiment of creep accompanied by a heat treatment is closer to what Chauve et al. [2017a] did, with stresses inferior than 1 MPa. However, nucleation along grain boundaries such as necklaces of grains is not observed for any experiments contrary to what Chauve et al. [2017a] observed at triple junctions in columnar ice. Capolo [2007] also observed drastic recrystallization

⁸ In this work, storage of ice cores from Dome C lasted 5 years at -22 °C, and only 8 months between -10 °C and -15 °C, while samples of Lock In were stored for one or two months at -22 °C after repatriation before scanning.

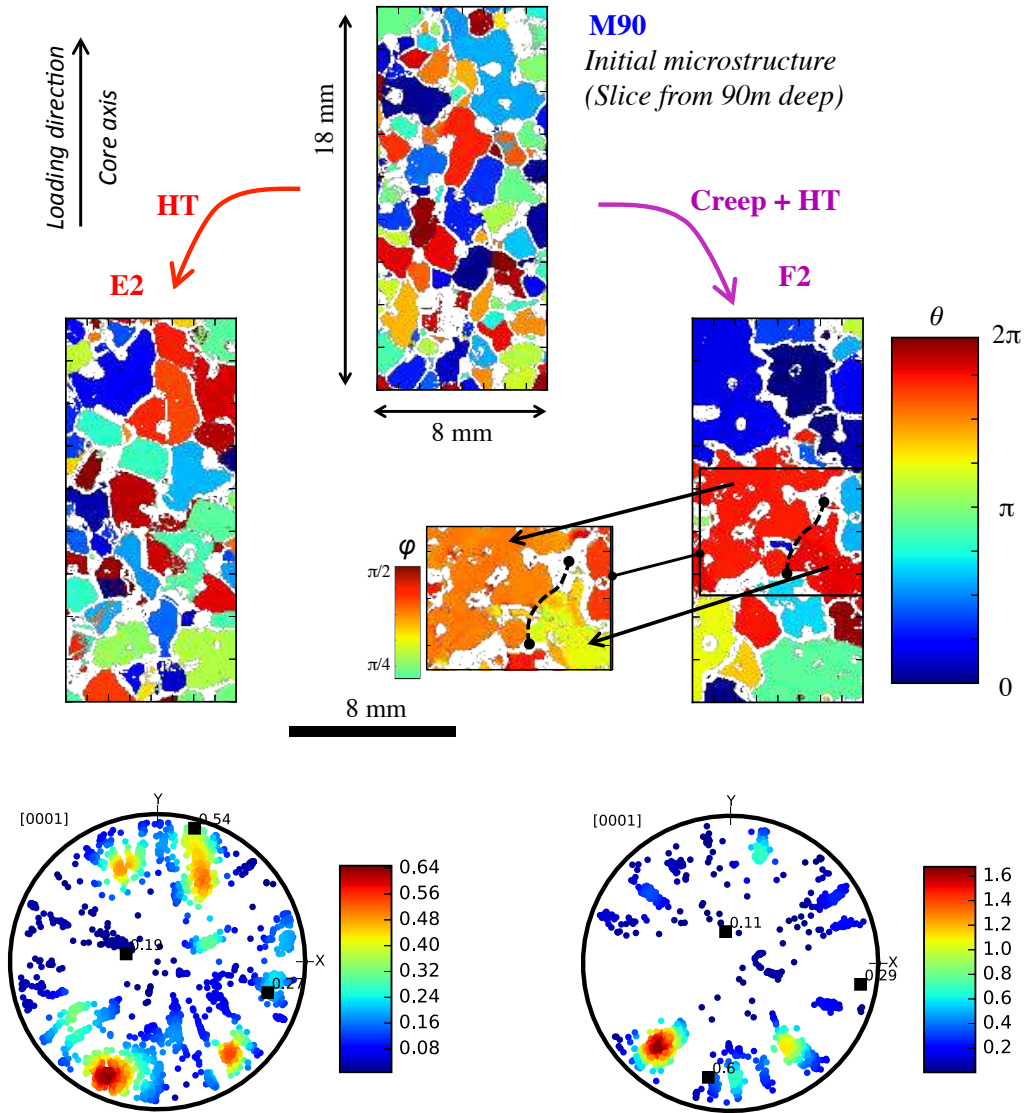


Figure 4.21: Comparison of microstructure originating from the same slice of ice core. The sample M90 is a part of the slice of ice core extracted from 90 m deep. It is typical of the microstructure at this depth. Microstructures of E2 and F2 are shown with their associated Pole figures. On F2, azimuth are really close to 2π for the red grain whereas the colatitude (small zoom) shows the colatitude is different implying the presence of two grains.

after a few hours of creep of ≈ 0.3 MPa on ice tricrystal. Serrated grain boundaries (evidence of grain boundary migration) are also not noticed in contrast to observations from [Montagnat et al. \[2015\]](#) or [Capolo \[2007\]](#). However resolution of our images may hinder close inspection. Examination of thin sections (see Table D.4) reveals there are less small grains (from nucleation or rotation recrystallization) for samples D3 than for in situ and ex situ samples. This could mean a successful annealing of the sample. Nevertheless we would expect the grain to grow in that case and we do not see a particularly marked increase. Again, the small number of observable grains tempers the results.

Samples B2 and F2 respectively reached $e_{zz}^{Tomo} \approx 6.6\%$ and 11.9% , therefore secondary creep was reached, and dynamic recrystallization should take place [[Montagnat et al., 2011](#); [Chauve et al., 2015](#)]. As no small grains are visible, the assumption is that local deformation of grains aligned \mathbf{c} axes of neighbor grains in the same direction and that severe grain boundary migration occurred. This is what happens in the deepest part of ice cores with large grains that are interlocking because of migration recrystallization [[Duval & Castelnau, 1995](#); [Thorsteinsson et al., 1997](#); [Schulson et al., 2009](#), chap. 6]. As the orientation analysis was performed five months after the end of the creep test, we can not exclude annealing which could have occurred at -10°C for samples B2 and F2. High-resolution images and precise measurements of the orientation with the help of EBSD should enhance our comprehension of the underlying mechanisms at work.

4.5.4 Curvature minimization modeling

Section 4.5.2 highlights that time and temperature, on top of compressive stresses, are essential for pore closure. Curvature reduction is possible thanks to surface energy minimization, which induces spherical pores. In theory, if the time is sufficiently long, pores should become spherical, due to this curvature minimization. It is not possible to reproduce polar conditions in cold room, and it is necessary to limit the time of the heat treatment on the firm sample. Thus, we take advantage of modeling techniques to simulate the evolution of microstructure. The DigitalSnow project (ANR-11-BS02-009) proposed a modeling tool that uses 3D binary images to simulate snow metamorphism. The code named Snow3D, was used in our case to let the samples evolve numerically [[Flin et al., 2015](#); [Bretin et al., 2015](#)]. Parallelepipeds had to be extracted from the cylindrical sample volumes to perform the simulations. This leads to a slight decrease for the closed porosity ratio, because of the adopted definition of this property.

The code is based on a phase field approach governed by the Allen-Cahn equation [[Allen & Cahn, 1972](#)]. The interface between air and ice is considered as diffuse with a small thickness (3 voxels in this work). Similarly to the level set method, this approach enables the separation or the coalescence of objects. This computational method also

directly involves the curvature, as the driving force for the evolution comes from the difference between the local and the mean curvatures. The code is constrained to conserve volume. However, discrepancies for the density were observed during modeling, with a slight increase in the beginning and then a decrease after 9 time steps. Differences are reported to be less than 0.2 % with respect to the density of step 00. Complete details of the calculations and of the numerical implementations are given in [Bretin et al. \[2015\]](#)⁹. The simulations were performed using 40 time steps.

Figure 4.22 shows the evolution of sample 80m_c5 (D2) with the Snow3D simulations. Red ellipsoids show the disappearance of some channels from Fig. 4.22a after five months of heat treatment in Fig. 4.22b. This closure is correctly represented by the code Snow3D after 7 (Fig. 4.22c) and 20 (Fig. 4.22d) time steps for instance. The blue circle focuses on a small closed pore, which vanishes with the simulations¹⁰. From Fig. 4.22, 7 time steps are sufficient to simulate correctly the processes of the five month experiments. The green ellipsoid shows a channel that did not close after heat treatment (Fig. 4.22b) but it is closed at the step 20 of the simulation. Therefore, continuing the simulation leads to further closure of pores.

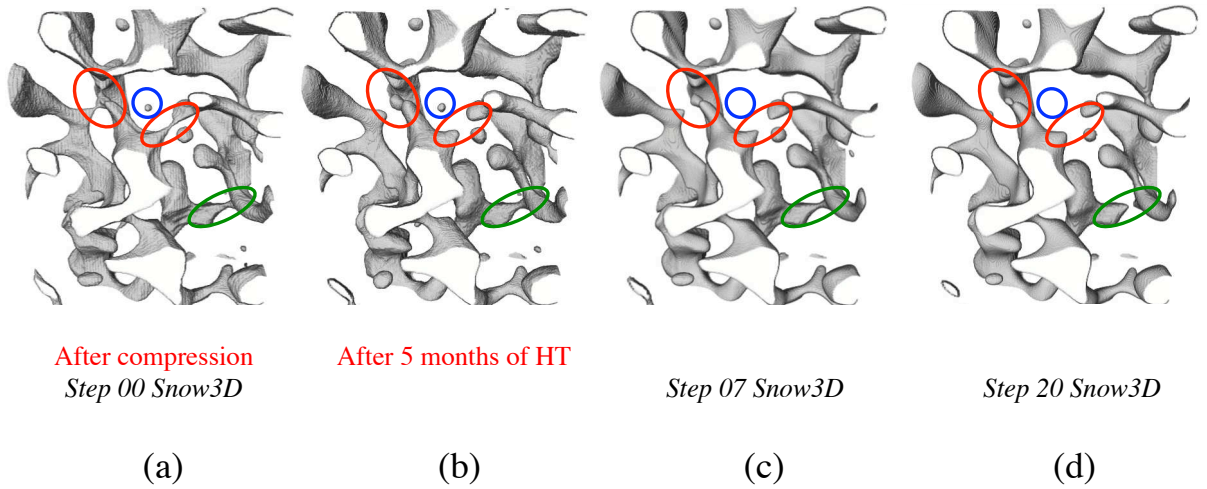


Figure 4.22: Zoom within the binary volume of sample 80m_c5, (a) after compression (D2) and (b) after 5 months of heat treatment (D3). Simulation of the curvature minimization is done with the code Snow3D on image (a) D3. 3D images are obtained after (c) 7 time steps and (d) 20 time steps. Coloured ellipses focus on particular features.

⁹ Note that the code Surface Evolver [[Brakke, 2013](#)] was also tested in this work, but its use involved to mesh large 3D volumes, and to separate almost manually the pores that were disconnecting. Its use on complete 3D images is also not appropriate. The code Snow3D is very interesting in that matter as it only needs raw binary images.

¹⁰ Comparison between the codes Snow3D and Surface Evolver exhibited that small closed pores could progressively be lost with Snow3D (but their volume is not lost), while they stayed indefinitely with Surface Evolver.

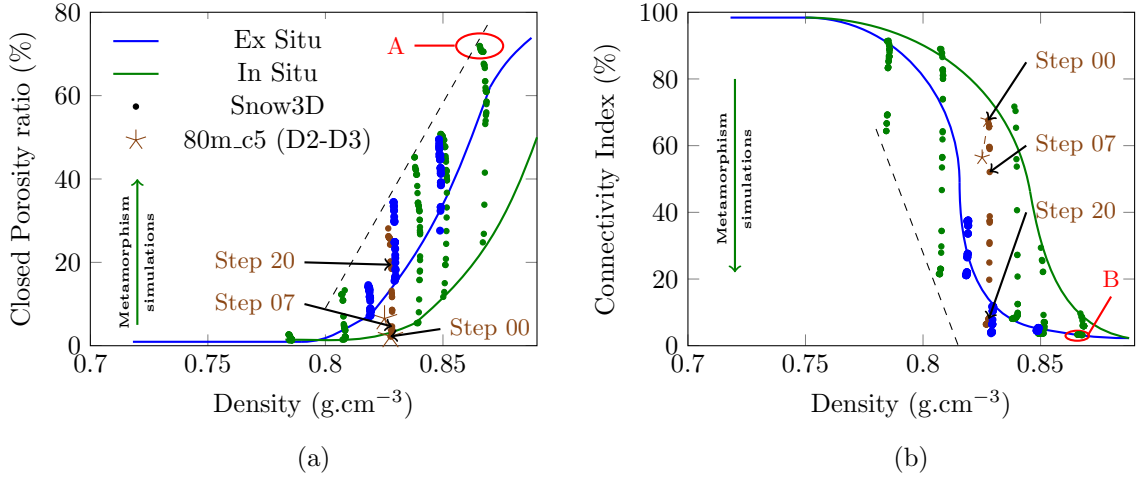


Figure 4.23: Evolution of the (a) closed porosity ratio and (b) connectivity index with density. Ex situ and In situ samples are represented by blue and green solid lines, respectively. The Snow3D results are shown by small dots for several ex situ (blue) and in situ (green) images. Sample 80m_c5 (D2-D3) is represented by stars for experimental data and by brown dots for simulation results. The emphasized steps are the same than in Fig. 4.22. Areas A and B circle several dots for closed porosity and connectivity index, respectively. Ellipses are simulation results from step 28 to 40 for A, and from step 22 to 40 for B. Green arrows indicate the direction of the simulation for increasing steps. The black dashed line represents an upper bound (a) and a lower bound (b) for the results.

Figure 4.23 plots the evolution of the percentage of the closed porosity ratio and of the connectivity index with the use of Snow3D. The simulation disconnects pores (without large variations of density) as observed after heat treatment. Areas A and B focus on the final simulated steps of sample 80m_c2. Area A on Fig. 4.23a includes 12 simulated steps (represented by dots), while area B includes 18 steps on Fig. 4.23b. Simulations on in situ experiments require about 20 steps to reach an equilibrium state. Interestingly, simulation results for ex situ data also exhibit a pore evolution before plateauing. This suggests that ex situ samples are still not totally in a fully equilibrium state, although they are thousand years old. Final dots of the Snow3D simulations also seem to fall on a curve, which could be an upper bound for the closed porosity ratio or a lower bound for the connectivity index representing a steady state microstructure.

The curvatures were also computed for all simulations. Figure 4.24 shows the evolution of the curvature maps of the sample 80m_c5, by displaying the isolines $P(S,C)=0.5$ for comparison. As the simulation proceeds, the decrease in curvedness is clear. The distribution is also shifted to the larger values of the shape index, with more dome local surfaces. The evolution of curvatures with the simulation is very similar between all compacted samples. The sample 80m_c5 allows comparing the experiment results with

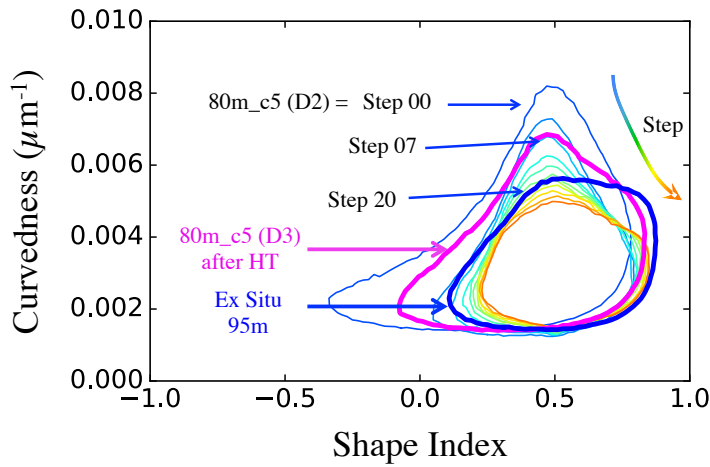


Figure 4.24: Isoline $P(S,C)=0.5$ of the curvature map for the sample 80m_c5. The evolution of colour from blue to orange represents the different simulated steps (from step 00 (D2) to step 40 with Snow3D). The magenta bold line is the isoline for the sample after HT (D3). The blue line is an ex situ sample from 94.5 m deep with about the same density (0.830 g.cm^{-3}).

the simulated surfaces. It is also superimposed to the ex situ results for the same density ($\rho \approx 0.830 \text{ g.cm}^{-3}$ at 94.5 m deep). The isoline that visually corresponds the most to the experiment is the one at step 7. The best match with the ex situ result is the isoline number 20. This comparison can be used as a criterion to stop the simulation to match the corresponding stages. An alternative criterion is to stop the simulation when the closed porosity ratio of the ex situ result is reached. In practice, they give about the same results for the number of simulated steps.

Comparisons for the same density between simulations and ex situ samples lead to the same conclusion. This suggests that Snow3D cannot represent all the microstructural evolution in polar firn. The thermodynamics is not fully represented by the phase field method used in Snow3D. Indeed in the model, the diffusion time of vapor is supposed to be immediate, without considering the pore network. This explains why a closed pore can disappear (blue ellipse in Fig. 4.22). It can interact with an other pore, and can transfer its volume to a larger one, although they are not close to each other. Thus, as the densification goes and the pores disconnect from one another, the code becomes less and less valid. However, the code Snow3D was originally developed to simulate snow

metamorphism, and is used here successfully to represent the closure of pores.

An other important assumption is that we totally decoupled mechanism. It becomes clear that depending of the stress state in the firn, the evolution of the closed porosity ratio with density should be different. We are confident that this evolution is not only dependent on the temperature and density as all proposed parameterizations in literature seem to suggest [Schwander et al., 1993; Severinghaus & Battle, 2006; Goujon et al., 2003; Mitchell et al., 2015]. Simulations on ex situ samples leading to larger closed porosity ratio, this means the equilibrium state was not reached by the polar firn. In ice caps, densification also proceeds because of the overlaying snow and firn, giving a non-negligible stress σ_{zz} . In conclusion, our results showed that the thermo-mechanical coupling might be important for the pore closure.

4.6 Conclusion

This chapter focused on decoupling the effects of dislocation creep from diffusion mechanisms on firn densification. This was performed by in situ oedometric tests on firn under X-ray computed tomography. Samples from the same slice of firn core were extracted, and mechanical tests with oedometric conditions were performed. Effects of stresses (1 MPa to 5 MPa) and strain rates (10^{-5} - 10^{-6} s $^{-1}$) were investigated and did not lead to different results for the closed porosity ratio or the connectivity index. The compaction of firn was shown to be viscoplastic since relaxation and an evolution of crystallographic texture was observed. We can reasonably suggest that the deformation of in situ samples mainly involved dislocation creep. Pores were also reported to close at larger densities for in situ sample than for ex situ ones (analyzed in chapter 3).

The pore morphology was also sharper and the grain size smaller for in situ samples than for ex situ ones with the same density. These differences of curvatures were quantified by the shape index and the curvedness. This peculiar microstructure comes from the very limited time of the experiments compared to the densification of polar firn that lasts thousands of years.

To consider the effect of temperature on the microstructure evolution, a heat treatment was performed on firn samples. Time and temperature consistently increase the closure of pores, and round their morphologies. A phase field method (implemented in the code Snow3D) gave consistent results when comparing simulations to experiments. In this code, microstructure evolution is driven by the difference of local and mean curvatures. Simulations also suggested that ex situ samples are not totally in an equilibrium state despite their old age.

In conclusion, this chapter focused on decoupling the mechanisms of firn densification

and can be summarized with Fig. 4.25. Oedometric tests stand for the viscoplastic part of the densification, that tends to increase the density and to close a few pores. Then, heat treatment allows the activation of diffusion processes that lead mainly to pore closure while little changing the density. The polar firn densification is a concomitance and competition of these two mechanisms.

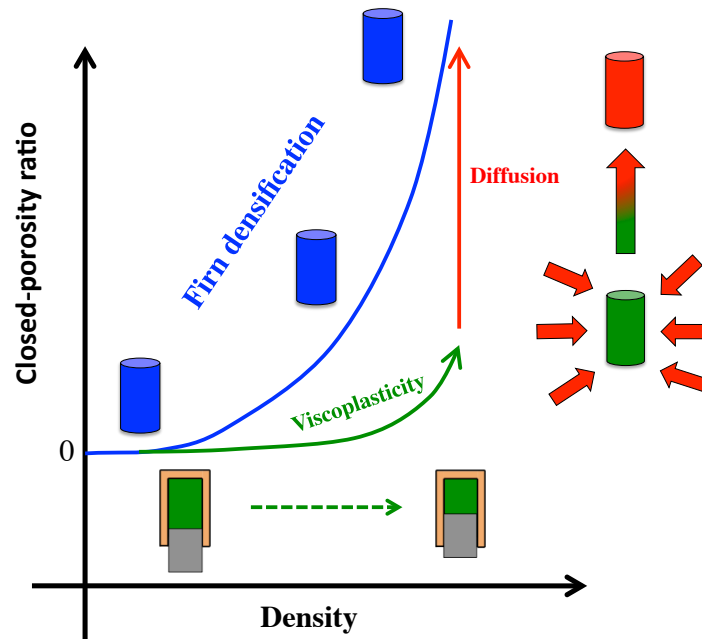


Figure 4.25: Summary diagram of pore closure.

Chapter 5

Discrete Element modeling

Contents

5.1	Principles of the Discrete Element Method	169
5.1.1	Basis of DEM	169
5.1.2	Algorithm	170
5.1.3	Boundary conditions and stress calculation	173
5.1.4	Example of a contact law: elasticity	174
5.1.5	Generating numerical microstructure	176
5.2	Contact law for ice particles	177
5.2.1	Isotropic viscoplastic contact law	179
5.2.2	Viscoplastic anisotropic contact law for ice	180
5.3	Image voxelization	184
5.4	Results of discrete simulations with the anisotropic model . .	185
5.5	Using binary images from in situ X-ray tomography : an attempt	194
5.5.1	Methods	194
5.5.2	Results	196
5.6	Conclusion	199

The densification of snow involves grains rearrangement and sintering until 0.55 g.cm^{-3} . Above this density, these mechanisms are not dominant any more and firnification proceeds mainly by pressure sintering mechanisms and by dislocation creep. Due to snow deposition, agglomeration of grains and their progressive burying in ice caps, firn is a granular material made of ice crystals. Such behavior makes it a good candidate for discrete element simulations. In chapter 2, we described the mutual indentation of two cylinders of ice and the resulting intragranular deformation ruled by *c* axis orientation. An expression for the normal force taking into account those anisotropic effects was proposed. Chapters 3-4 have shown that firn presents some characteristics of a granular behavior. In this chapter, we propose to use the information gathered in chapter 2 on contact to propose a Discrete Element Method (DEM) simulation of firn densification under oedometric conditions.

5.1 Principles of the Discrete Element Method

5.1.1 Basis of DEM

The Discrete Element Method (also denominated sometimes as the Distinct Element Method), models the behavior of a granular medium. The method aims to follow explicitly the motion of each discrete particle that constitutes this granular medium. The evolution of the assembly of particles is given by the second of the Newton's law of motion. Forces on particles are dictated by the interactions between these particles. The discrete elements are usually rigid discs in 2D and rigid spheres in 3D. The deformation of these elements is not accounted for directly but is taken into account indirectly through their mutual indentation. In 3D, spheres will become indented spheres as densification proceeds but the simulated elements will continue to be spheres in the calculation.

Simulating the motion of particles in granular media is of particular interest for geomaterials or civil engineering materials, which exhibit clear granular characteristics (sand, rocks, gravels, concrete, etc ...). The method was originally developed for that purpose [Cundall & Strack, 1979]. For instance, DEM simulations are used to forecast landslide events [Lu et al., 2014] or to model concrete behavior [Camborde et al., 2000]. Closer to the subject treated here, DEM has proved useful to understand snow mechanics [Johnson & Hopkins, 2005; Hagenmuller et al., 2015; Michael, 2014; Gaume et al., 2015]. Applications are also now numerous for material sciences when it comes to simulate powder processes such as powder compaction [Fleck, 1995; Martin et al., 2003] or sintering [Martin et al., 2006; Rasp et al., 2013], but also in industrial chemical engineering processes [Zhu et al., 2008; Xu et al., 2011; Cleary & Sawley, 1999]. More recently, the DEM has also

been used for continuous materials that may develop some discontinuities during their lifetime. For instance, simulating crack propagation or healing may be advantageous with DEM by simply separating particles that were bonded or adding new contacts. Using FEM for such a case usually involves remeshing the volume or assuming some predefined crack path.

As for FEM, parallel computing has proved to be very efficient with a DEM code [Kloss et al., 2012]. Simulating 1.5 millions of particles can be reduced to one hour (with 128 cores [Berger et al., 2015]). In terms of code parallelization, DEM may take advantage of the experience gained in Molecular Dynamics (MD), which is very similar in its essence to DEM. In MD, atoms or molecules are modeled instead of particles and potentials replace interaction forces. However, the basic algorithm is very similar to DEM as shown in the next section.

The DEM description that follows is mostly based on the DEM code `dp3D` (Discrete Powder 3D), which has been developed at SIMaP laboratory and which is dedicated mostly to materials science. For a more general description of available DEM applications, possibilities, and algorithms, the interested reader may refer to Radjai & Dubois [2011].

5.1.2 Algorithm

The main features and assumptions for the DEM in `dp3D` (but also used by many other DEM codes) are listed below :

- Unit particles are spherical;
- Particles interpenetrate without deforming;
- The contact force is separated into two contributions: normal \mathbf{N} and tangential \mathbf{T} ;
- The amplitude of these forces depend on the interpenetration or on the rate of interpenetration and more generally on the relative accumulated displacement between the two particles;
- The contact laws reflects the material behavior;
- Pair interaction is assumed, i.e. the interaction law at a contact between two particles does not depend on the existence of neighboring contacts;
- Inertia terms are neglected;
- The integration scheme is explicit (this makes possible the use of non-linear contact laws and history-dependent laws), therefore the choice of the time step determines stability.

A DEM algorithm is based on a few actions at each time step Δt to simulate the motion of particles. All contacts between particles have to be listed first. This is usually performed with the Verlet-Neighbour list of potential contacts coupled with the linked cell method [Radjai & Dubois, 2011]. This approach involves locating particles in boxes. Only the boxes adjacent to the considered particle are visited for potential contacts. This is advantageous from a CPU point of view as the contact detection problem becomes a $n_p \ln(n_p)$ problem instead of a n_p^2 problem (if n_p is the number of particles). Once contacts are detected, the interaction between particles is ruled by a contact law, which is supposed to represent the considered physical processes.

Different constitutive laws such as elasticity, cohesion, bonding, surface adhesion, friction, plasticity or sintering were studied in the literature [e.g., Johnson, 1987], and were transposed to the contact between two particles. The large majority of these models has been derived for spheres and can be easily generalized to the contact between a sphere and a plane or to the contact of two dissimilar spheres (different material properties or different radii). Analytic derivations or FEM simulations are often used to study closely the contact between two particles and then derive a normal and tangential force law as a function of their relative displacement. Such approaches where particles can overlap/indent each other are classified as soft contact.

For example the elastic contact force between two spherical particles can be derived from Hertz's theory [Hertz, 1882], while the additional effect of surface energy can be accounted for by models derived in the 70's [Johnson et al., 1971; Derjaguin et al., 1994]. Elastoplasticity can be tackled by models that have used analytical derivations and finite element simulations to propose indentation laws between two elastoplastic spherical particles [Mesarovic & Fleck, 1999; Olsson & Larsson, 2014] or two viscoplastic spherical particles [Storåkers et al., 1997, 1999].

Once contact forces are known, the sum of all contact forces on a particle is computed. The second law of Newton is used to obtain the new position of particles. In **dp3D**, the problem is considered quasi-static, which means that inertia terms are neglected. This implies that accelerations are not correct (but sufficiently small to have no effect). A Velocity Verlet algorithm integrates explicitly the second law of Newton. Positions and velocities are obtained at the same time step. Moments and rotations follow the same integration scheme as for forces and translations. Once the new positions and velocities of particles are obtained, a new time step begins. Other examples of DEM codes are **YADE** [Kozicki & Donzé, 2009] or **LIGGGHTS** [Kloss et al., 2012]. The algorithm of **dp3D** is summarized in Fig. 5.1.

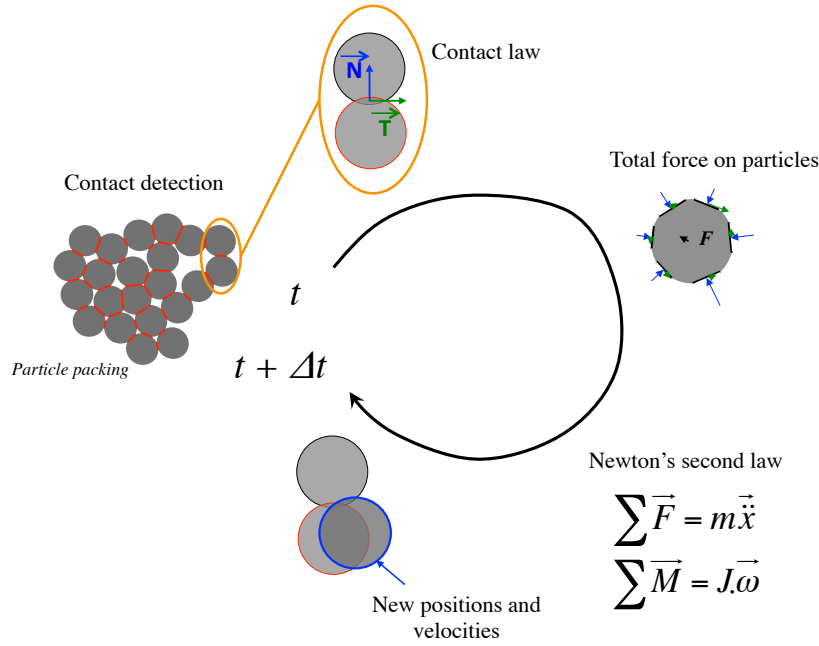


Figure 5.1: Algorithm of the discrete element method as used in dp3D.

The quasi-static equilibrium assumption can be tested in the case of firn by using the inertia number, a dimensionless numerical parameter which writes [MiDi, 2004]

$$I = \dot{\epsilon} \sqrt{\frac{m}{Pd}} \quad (5.1)$$

with m the mass of a particle, P the pressure and d the grain size. Assuming a grain size $d = 1$ mm the mass is $m \approx 5 \cdot 10^{-4}$ g (for a spherical particle of ice). Further, assuming a pressure of the order of $P = 1$ MPa, and a strain rate smaller than $\dot{\epsilon} = 10^{-6}$ s⁻¹ (a very conservative estimate), one obtains $I \approx 10^{-9}$. The system can be considered quasi-static when $I < 10^{-3}$, neglecting inertia terms is thus appropriate in the case of firn densification. Other criteria, based on kinetic energy for example [Agnolin & Roux, 2007], exist. They also confirm the validity of the quasi-static assumption. The advantage that can be gained from this assumption is that the mass of particles can be rescaled (increased artificially) to use a larger time step Δt . This is because Δt writes:

$$\Delta t = 2f_s \sqrt{\frac{m}{K}} \quad (5.2)$$

where K is the contact stiffness and f_s a numerical parameter of the order of 0.1-0.01. In that case, the results of the simulation must be checked to ensure that the quasi-static assumption is still valid even after mass renormalization.

5.1.3 Boundary conditions and stress calculation

There are two types of boundary conditions used in this work:

- **Rigid wall conditions (RWC)** : Rigid walls define the box in which particles are enclosed. These enclosing objects are part of the numerical simulations. The user dictates the motion or the stress applied on these objects. Particles interact with objects via the contact laws and move accordingly. For example, the compaction of a particulate material can be simulated using a cylindrical object as a die and two planes as punches. However, such boundary conditions involve an effect of the walls, as particle configurations close to the walls are different from those far from the wall. This means that the number of particles may affect the macroscopic behavior of the particulate material. At least 4000 particles are necessary to avoid borders effect on the compaction curve [Martin et al., 2003]. A schematic representation of RWC is shown in Fig. 5.2a.
- **Periodic conditions (PC)** : This technique avoids the use of a rigid wall to contain particles. When a particle protrudes outside the periodic cell through a given face, it interacts with the particles on the opposite face. When the center of the particle moves outside the periodic condition, it is translated to the opposite side of the box by a distance equal to the length of the periodic box, L . A simple representation of PC is shown in Fig. 5.2b. The condition is very simple to code. Any distance L_{ij} between centers of particles i and j may be recalculated through:

$$\begin{aligned} \text{if } L_{ij} > 0.5L &\rightarrow L_{ij} = L_{ij} - L \\ \text{if } L_{ij} < -0.5L &\rightarrow L_{ij} = L_{ij} + L \end{aligned} \quad (5.3)$$

Note that RWC and PC can be combined (PC on one direction and RWC on others for example).

The macroscopic stress tensor components σ_{pq} can be calculated on the volume V defined by the simulation box from the contact forces N and T . It has been originally proposed by Weber [Weber, 1966]:

$$\sigma_{pq} = \frac{1}{V} \sum_{\text{contacts}} (N + T)_p \cdot L_{ij,q} \quad (5.4)$$

with $(N + T)_p$ the p th component of the total contact force on a given contact, and $L_{ij,q}$ the q th component of the branch length L_{ij} linking the centres of particles (see Fig. 5.3a). The sum in Eq. (5.4) is made on all contacts in the volume V .

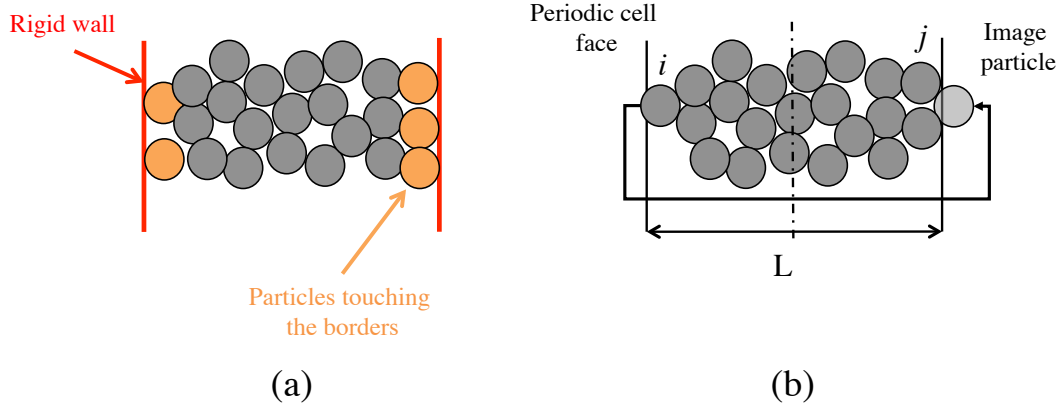


Figure 5.2: (a) Rigid wall conditions. (b) Periodic conditions. Particle i and j are in contact via the periodic condition.

5.1.4 Example of a contact law: elasticity

DEM simulations require contact laws as these represent the first ingredient of a physically based model. Forces are generated when particles form a contact and these forces need to be defined carefully since the physics of the problem to be modeled is very often embedded in these forces. In other words, the local interactions are responsible for the behavior of the particulate material at the macroscopic scale. In the next section, we will describe the generation of the initial assembly of particles that will be used for the DEM simulation of the viscoplastic densification. This generation stage, called jamming, uses a simple elastic contact law between particles. Here we describe the elastic contact law to illustrate the typical set of equations that are necessary to define a contact model. Section 5.2 will describe the specific viscoplastic contact law adopted for ice.

Figure 5.3a illustrates the notation adopted in this work. h characterizes the interpenetration (or indentation), N and T , the normal and tangential forces, respectively. Each particle is defined by its position and its radius. R_i and R_j are the radii of particle i and j in contact and the equivalent radius R^* is used afterwards to account for two particles of different radii:

$$R^* = \frac{R_i R_j}{R_i + R_j} \quad (5.5)$$

During the jamming process, particles are considered elastic. In the following, we describe the contact laws that characterize elastic contacts.

Each particle is assigned a material with given mechanical properties (here Young's modulus E_i , and Poisson's ratio ν_i). Thus composite systems can easily be modeled. An effective Young's modulus E^* accounting for the two materials in contact is defined in

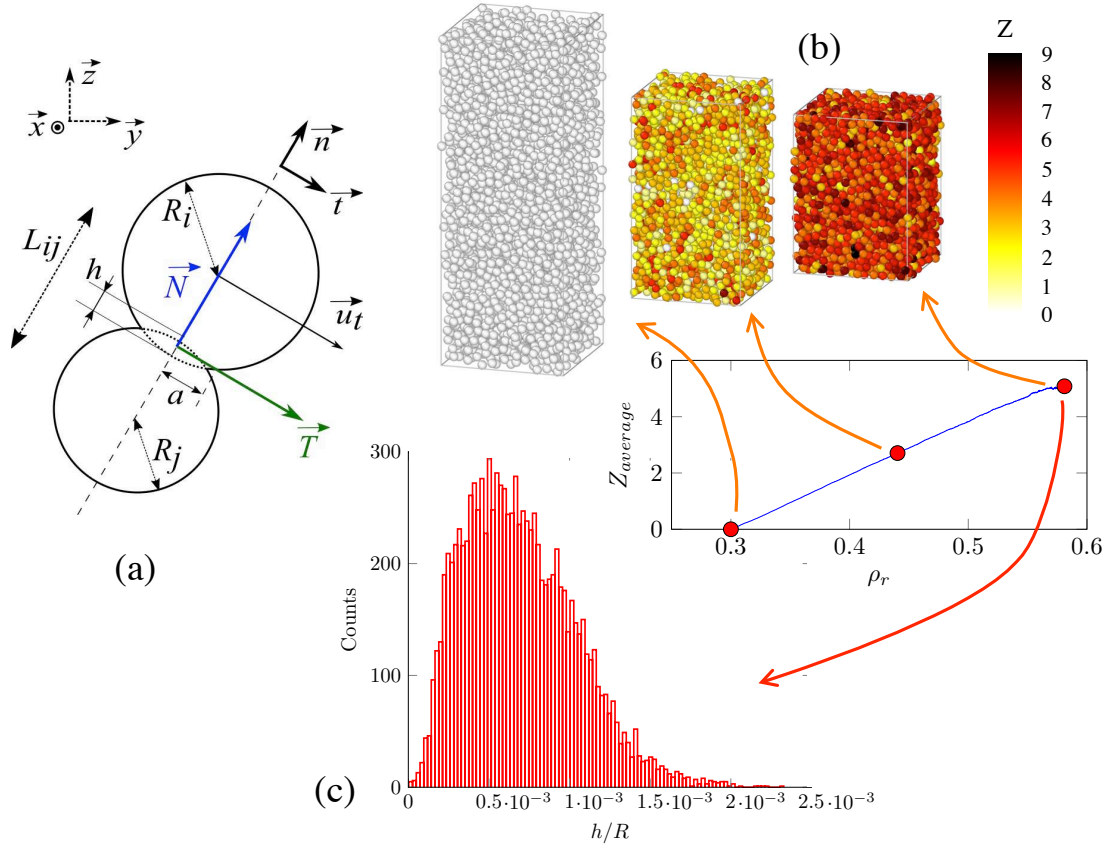


Figure 5.3: (a) Two indented particles and related geometrical parameters. (b) Evolution of the average coordination number $Z_{average}$ against relative density during oedometric jamming for periodic conditions. (c) Contact distribution of h/R for the final step of the jamming ($\rho_r = 0.58$).

that case:

$$\frac{1}{E^*} = \frac{1 - \nu_i^2}{E_i} + \frac{1 - \nu_j^2}{E_j} \quad (5.6)$$

If one considers a monodisperse packing with particles made of the same material, then Eq. (5.5) reduces to $R^* = \frac{R}{2}$ and Eq. (5.6) to $E^* = \frac{E}{2(1-\nu^2)}$.

Particles are in contact when $L_{ij} < R_i + R_j = 2R$. According to elasticity theory, the normal force at the contact writes in that case [Hertz, 1882]:

$$N_e = \frac{4}{3} E^* \sqrt{R^* |h|^3} = \frac{\sqrt{2}}{3} \frac{E}{1 - \nu^2} \sqrt{R |h|^3} \quad (5.7)$$

The contact radius, a_e , associated to the indentation of particles is, in the case of elasticity:

$$a_e^2 = \frac{1}{2} R |h| \quad (5.8)$$

and is actually smaller than the geometrical contact made by two intersecting spheres ($a_g^2 \approx R |h|$).

When friction is considered, the tangential force follows a simplified Hertz-Mindlin model, which is computed from the preceding time step:

$$T_e(t) = T_e(t - \Delta t) - a_e G \frac{du_t}{dt} \Delta t \quad (5.9)$$

with \mathbf{u}_t the relative tangential displacement vector ($\|\mathbf{u}_t\| = u_t$, see Fig. 5.3), and G the shear modulus. The tangential force opposes the relative motion. A Coulomb force serves as an upper bound for the tangential force, with a friction coefficient μ . It is proportional to the normal force:

$$\text{Max}(T_e) = \mu N_e \quad (5.10)$$

5.1.5 Generating numerical microstructure

The whole range of relative density from 0 to 1 could be explored for snow, firn and ice. However, we aim to model the range of density where firn densification proceeds dominantly by dislocation creep. Accordingly, the initial relative density should be larger than $\rho_r \approx 0.55$ (with ρ_r defined with respect to $\rho_{ice} = 0.917 \text{ g.cm}^{-3}$). In this section, we describe the scheme that allows an assembly of particles to be generated and ready for densification.

A gas of particles is first generated. This operation involves particles to be randomly located in the simulated box, without interpenetration. Particles are then packed until they are jammed, because it is difficult to reach relative densities $\rho_r > 0.3$ with a random gas. For monodispersed spherical particles, the relative density in `dp3D` can reach the

Random Close Packing relative density (≈ 0.637), providing particles are frictionless and sufficient CPU time is used to authorize rearrangements [Martin & Bordia, 2008]. Here, smaller relative density are sought for $\rho_r \in [0.55, 0.60]$ and thus the generation by compaction is relatively fast. To perform this operation, an axial strain rate $\dot{\epsilon}_{zz} = 1 \cdot 10^{-4} \text{ s}^{-1}$ is imposed on the upper and lower faces of the cube, and compaction is performed with periodic conditions. Isotropic compaction was also tested and revealed no differences for further simulations. Particles in the gas are gradually touching one another during compaction and contacts are considered fully elastic during this jamming.

Figure 5.3b shows the increase of the coordination number (the average number of contacts per particle) from the generated gas of particles to the packed density. A Young's modulus of $E = 9.33 \text{ GPa}$ [Gammon et al., 1983] is chosen for the compaction but has a limited impact on the jammed assembly. As illustrated by the first box of particles on Fig. 5.3b, there is no contact between particles at the very beginning of the jamming, hence a coordination number equal to 0. As densification proceeds, a contact distribution appears. The average coordination number is increasing until reaching $Z_{average} \approx 5$ for $\rho_r = 0.58$. Interpenetration h between particles at $\rho_r = 0.58$ is very small as $\frac{h}{R}$ stays below ≤ 0.0025 (Fig. 5.3c). This generated microstructure is chosen as the initial state for all simulations in section 5.4.

5.2 Contact law for ice particles

Publications on discrete element modeling of snow particles are very few and to our best knowledge, DEM has not been used for firn. Johnson & Hopkins [2005] used DEM (code μSNOW) to dynamically model dry snow particles whose shape were cylindrical with spherical ends. Johnson & Hopkins [2005] proposed two types of contact: frozen and unfrozen contacts. Both contacts are chosen viscoelastic for normal and tangential forces, with the addition of a viscoelastic bond in the case of frozen contacts. Twisting moments and bending moments are also implemented in the contact law. The bonds are brittle and fail when the tensile stress at the contact exceeds approximately 1.5 MPa at -10°C . This failure is not instantaneous as the bond radius of the contact decreases progressively to 0 when the stress goes over the threshold value. These considerations enabled to replicate accurately the evolution of the snow viscosity with density when creep experiments were simulated. The frozen bonds increased with the coordination number, dictating the evolution of viscoelastic parameters. Grain rearrangement was shown to be dominant for densities below 0.42 g.cm^{-3} thanks to shear at contacts along with grain rotation and twisting. Vedachalam [2011] chose to model the fall of snow particles on an inclined surface (for avalanche applications) using LAMMPS and LIGGGHTS DEM

codes with cohesion models such as the JKR cohesion model [Johnson et al., 1971]. Closer to our work, Hagenmuller et al. [2014] managed to discretize X-ray images of snow to be used in a DEM code.

Hagenmuller et al. [2015] suggested to model grains of snow by clumps of spheres, whose interactions are ruled by elastic, frictional and cohesive laws. In their model, cohesion only exists between particles originating from initial discretized images. During simulation, a cohesive contact may break if a fracture criterion is fulfilled, but new contacts between clumps do not create cohesion. Cohesion of clumps is basically the sum of the cohesion forces of the spheres in contact. Simulations of compression tests revealed the existence of three distinct stages depending on strain: a small elastic phase, then a brittle-frictional phase when cohesion disappears (for $0.02 < \varepsilon_{zz} < 0.3$) and a dense compaction phase, when hardening occurs. Results for stresses showed to be ruled by density, and not by microstructure (densities were lower than 0.4 g.cm^{-3}).

In brief, snow was essentially modeled with elasticity, adding in some cases a viscous damping to dissipate kinetic energy. DEM simulations did not take into account the anisotropy of the ice crystal for the contact (it is however moderate for elastic behavior). Viscoplasticity was set aside because densification of snow occurs mainly by grain rearrangement and fracture. However, Theile et al. [2011] did propose an original approach to model snow densification with FEM. Tomographic images were meshed by hexagonal beam elements representing the ice crystal. The constitutive law used was a simplified Schmidt like relation:

$$\dot{\varepsilon}(\theta) = B(\theta)\sigma^n = 2^{n+1} \sin^{n+1}(\theta) \cos^{n+1}(\theta) B_m \sigma^n \quad (5.11)$$

with $n = 2$ and B_m a viscosity that depends on \mathbf{c} axes orientation. It is equal to $10^{-8} \text{ MPa}^{-2}/\text{s}$ when \mathbf{c} axes are oriented in the range $0 - 3^\circ$ or $87 - 90^\circ$, and $10^{-4} \text{ MPa}^{-2}/\text{s}$ for other orientations. These FEM results were limited to density below 0.345 g.cm^{-3} , thus firm was not considered.

The works described above [Johnson & Hopkins, 2005; Vedachalam, 2011; Hagenmuller et al., 2015] can not be used directly for firm, where dislocation creep is the dominant mechanism. Taking into account the anisotropy of the deformation at the contact between particles has not been attempted yet in a DEM framework. The next two subsections concentrate on a viscoplastic contact law, which can be adjusted for orientation dependency. Moments and rotations due to tangential forces are considered with the laws described hereafter.

5.2.1 Isotropic viscoplastic contact law

5.2.1.1 Normal force

Metallic engineering powders can undergo compaction to form parts. The modeling and simulation of powder compaction require the formulation of indentation (or contact) laws between particles. This is in this context that Storåkers, Fleck and McMeeking proposed a general viscoplastic contact law for powder compaction [Storåkers et al., 1999]. It will be referred as "isotropic law" in the following as it does not take into account any anisotropy. It bears some resemblance to the contact laws described in chapter 2 for cylinders.

We consider a spherical particle i made of a material, which uniaxial stress response is given by:

$$\sigma = \sigma_i \varepsilon^M \dot{\varepsilon}^{\frac{1}{n}} \quad (5.12)$$

with σ_i a material parameter, M a hardening exponent, and n the stress exponent (see also chapter 2). In the case of two spherical particles indenting each other as shown by Fig. 5.3a, the formulation is the same for particle j which is composed of the same material (ice). According to Storåkers et al. [1999], the viscoplastic normal force of indentation writes:

$$N_v = \chi_0 h^{\frac{1}{2}(2+M-\frac{1}{n})} \dot{h}^{\frac{1}{n}} \quad (5.13)$$

By convention, N_v is chosen positive for compression ($\dot{h} > 0$). To simplify the following calculations, we will suppose $M = 0$ for ice (no hardening), which is appropriate according to single crystals experiments [Schulson et al., 2009, chap. 5,]. Equation (5.12) then reduces to Eq. (2.10), and Eq. (5.13) to :

$$N_v = \chi_0 h^{\frac{1}{2}(2-\frac{1}{n})} \dot{h}^{\frac{1}{n}} \quad (5.14)$$

where :

$$\chi_0 = 2^{1-\frac{3}{2n}} 3^{1-\frac{1}{n}} \left(1 + \frac{2}{n}\right) \pi c^{2+\frac{1}{n}} \sigma^* (R^*)^{1-\frac{1}{2n}} \quad (5.15)$$

and:

$$(\sigma^*)^{-n} = \sigma_i^{-n} + \sigma_j^{-n} \quad (5.16)$$

and c is an indentation invariant obtained from finite element simulations [Storåkers et al., 1999] :

$$c^2 = 1.43 * \exp\left(-\frac{0.97}{n}\right) \quad (5.17)$$

Note that the two particles may have two different material parameters σ_i and σ_j but require to have the same stress exponent in the proposed formulation.

In this chapter, simulations were performed only for a viscoplastic Newtonian behavior

for the firm, therefore $n = 1$. Chapter 6 will propose some perspectives using $n = 3$. In the case of a Newtonian behavior, Eq. (5.14) simplifies to :

$$N_v = \frac{3\pi}{2} c^3 (\sigma_i^{-1} + \sigma_j^{-1})^{-1} \sqrt{2R^*} \sqrt{h} \dot{h} \quad (5.18)$$

As mentioned in section 2.4.3 $\chi = \frac{3\pi c^3}{2} \approx 2$. A simple dimensional analysis of N_v shows it is proportional to a squared length. According to Eq. (5.4), the macroscopic behavior of the particulate material is thus independent of the particle size.

The contact radius in the case of isotropic viscoplasticity is related to the indentation h by :

$$a_v^2 = 2c^2 R^* h \quad (5.19)$$

According to Eq. (5.17):

$$a_v^2 = 1.08 R^* h \approx a_g^2 \approx R^* h \quad (5.20)$$

Although this is in line with the theory of Newtonian fluids [Johnson, 1987; Storåkers et al., 1997], this is not an intuitive result, as plastic contact should yield a larger area than the geometrical intersection for which material flow is not taken into account. For example, for a perfectly plastic material ($n \rightarrow \infty$), the contact radius is given by:

$$a_v^2 \rightarrow a_p^2 = 2.86 R^* h \quad (5.21)$$

It should be clear that contact forces in the DEM model used in `dp3D` introduce an indentation h and a rate of approach of the two particles \dot{h} , not a contact size. The choice of a contact size formulation will only have an impact on the voxelization routine that is used to transform numerical microstructures into binary images (see section 5.3).

5.2.1.2 Tangential force

The tangential force is expressed similarly than the normal force and has the same materials parameters. Using Eq. (5.19) for the contact radius, the tangential force writes in the linear case:

$$T_v = \frac{4\pi}{3} c^2 R^* h (\sigma_i^{-1} + \sigma_j^{-1})^{-1} \left(\frac{du_t/dt}{R_i + R_j - h} \right) \quad (5.22)$$

5.2.2 Viscoplastic anisotropic contact law for ice

5.2.2.1 Normal force

To take into account the anisotropy of ice, a model has been developed for the normal force in section 2.2 for a uniaxial stress state (see appendix A.2). It considers that each

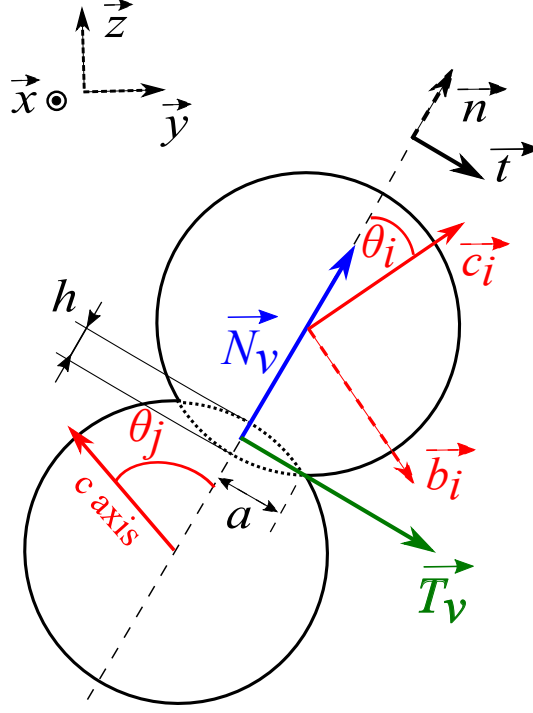


Figure 5.4: Reference and orientations of particles.

spherical particle has an oriented \mathbf{c} axis as illustrated in Fig. 5.4. The angle θ is between the normal direction of the contact \mathbf{n} and \mathbf{c} . The representation is 2D but the azimuth φ also exists and is defined in `dp3D` for each particles. However it does not appear in the calculation of the normal and tangential forces.

Replacing σ_i and σ_j from Eq. (5.18) with Eq. (2.9), and choosing $n = 1$ as well as $\alpha = 1$ (see section 2.2), leads to the following linear formulation of the oriented normal force (Eq. (2.12) proposed a non-linear formulation) :

$$N_v = 9\pi c^3 \mu_{basal} (f(\theta_i) + f(\theta_j))^{-1} \sqrt{2R^*} \sqrt{h} h \quad (5.23)$$

We recall the function $f(\theta)$ for $\alpha = 1$ defined by Eq. (2.7):

$$f(\theta) = 2 \left(1 + 3 \frac{1-\beta}{\beta} \sin^2 \theta \cos^2 \theta \right) \quad (5.24)$$

5.2.2.2 Tangential force

The oriented tangential force was determined in the case of shearing. Appendix A.3 details the calculation used. In reference to Fig. 5.4, it is the shear component of the strain rate tensor $\dot{\epsilon}_{nt}$ which is chosen. Its evolution with θ is displayed in Fig. A.3. Let us consider

the $\frac{\pi}{2}$ periodic function g defined by ($\alpha = 1$) :

$$g(\theta) = \frac{3}{\beta} (1 - 4(1 - \beta) \cos^2(\theta) \sin^2(\theta)) \quad (5.25)$$

Therefore, σ_i writes for the linear case:

$$\sigma_i = 6\mu_{basal} g(\theta_i)^{-1} \quad (5.26)$$

Replacing Eq. (5.26) into Eq. (5.22) leads to :

$$T_v = 12\pi\mu_{basal}(g(\theta_i) + g(\theta_j))^{-1}c^2R^*h \left(\frac{du_t/dt}{R_i + R_j - h} \right) \quad (5.27)$$

5.2.2.3 Comparison of the normal and tangential viscoplastic anisotropic contact laws

The formulation of the normal (Eq. (5.23)) and tangential (Eq. (5.27)) forces for oriented particles are independent from one another. They both depend differently on the orientation of the two particles in contact. Figures 5.5a-b give their evolutions when two particles are submitted to an axial strain rate or a shear rate. We use normalized formulations regarding viscosity and rates (and $R_i = R_j$):

$$\tilde{N}_v = \frac{N_v}{R^2 \frac{h}{R} \mu_{basal}} \quad (5.28)$$

$$\tilde{T}_v = \frac{T_v}{R^2 \mu_{basal} \frac{du_t}{dt} \frac{1}{2R-h}} \quad (5.29)$$

These expressions may be thought of as viscous stiffness for the normal and tangential contact laws. As expected from Fig. 2.1, the normal force is maximum for $\theta = 0$ or $\pi/2$ and is minimum for $\theta = \pi/4$, while it is the opposite for the tangential force. These figures also show that the normal force scales with the root square of the indentation (or equivalently with the radius of the contact) and that the tangential force is nearly linear with h (or equivalently with the square of the radius of the contact). An example of a column of six particles is shown in Figure 5.5. At force equilibrium, the axial deformation of this column of particles leads to very different indentations depending on the relative \mathbf{c} axis orientation of particles. Note that an indentation along \mathbf{n} gives a zero tangential force. Conversely, an imposed shear-rate leads to a non-zero normal force as illustrated by Fig. 5.5d, which shows the normalized normal force evolution when a pair of particles is sheared.

Equations (5.23) and (5.27) come from simplifications performed in appendix A. In

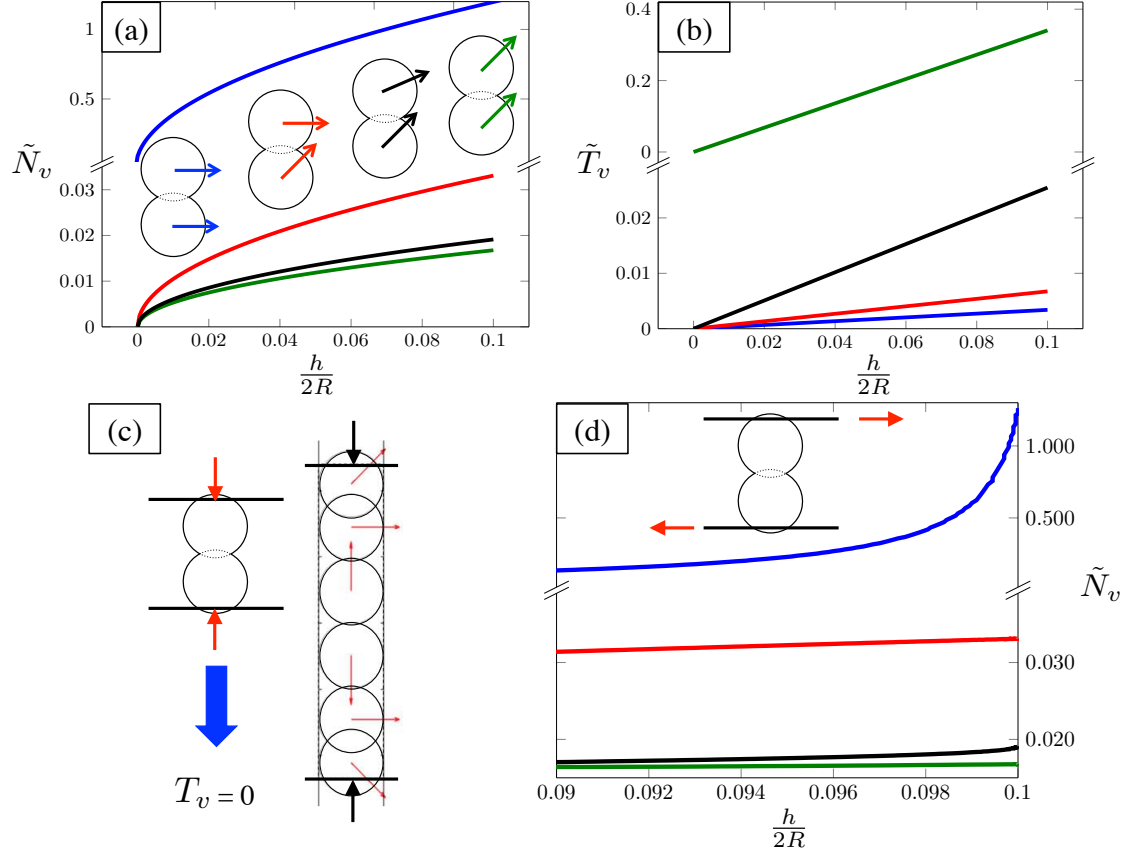


Figure 5.5: Evolution of the normalized (a) normal force and (b) tangential force between two particles for different configurations of \mathbf{c} axes. Diagram (c) illustrates that normal indentation does not induce a tangential force whatever \mathbf{c} axis orientation. Different magnitudes of the indentation are observable on a column of six particles that have different \mathbf{c} axes. (d) Evolution of the normal force when a shear rate is imposed starting from $\frac{h}{2R} = 0.1$. Note that all diagrams have a broken y-axis in order to plot the different force responses on a linear axis.

particular the coupling between shear and normal forces is not taken into account. The shear strain rate induced by a uniaxial stress, as well as the axial strain rate induced by a shear stress, are both neglected. The normal force induced by shear is the consequence of the decrease or increase of h (represented by a reduction of $\frac{h}{2R}$ from 0.1 to 0.09 in Fig. 5.5d).

5.3 Image voxelization

DEM only handles spheres defined by their centers along with their radii. To compare binary images from X-ray tomography (see chapters 3-4) to the results of DEM, **dp3D** proposes a post-treatment voxelization routine that fills particles with matter. It uses the approach of [Sweeney & Martin \[2003\]](#) to detect contours between particles. Shapes of contacts are represented with the geometrical model of [Coble \[1958\]](#) based on volume conservation. The algorithm is described in [[Kallel, 2013](#); [Roussel, 2015](#)]. In brief, it consists in distributing the matter intersected by the two spheres at the particle contact around the neck. Depending on the physical process involved, the matter redistribution is not the same. For instance, a sintered contact will exhibit a larger contact size around the neck than an elastic contact for a given indentation h .

There are two main issues to such a procedure. First, particles should have a sufficient number of voxels to be correctly represented. For instance, [Kallel \[2013\]](#) and [Roussel \[2015\]](#) obtained different results depending on the resolution, when computing the electrical conductivity of voxelized images.

Second, modeling firm involves large densities. However the voxelization routine fails when the relative density reaches 0.9 ($\rho > 0.825 \text{ g.cm}^{-3}$). Neighbor particles can overlap with the redistributed matter, which is then lost. This issue is illustrated in Fig. 5.6a for three particles in contact. In order to reach large densities, the choice was made to use the density obtained by voxelization, and not the relative density computed by the code. Therefore, simulations were performed out for $\rho_r > 1$. Redistribution of the matter around the neck was carried out using a sintered contact size, and the density of images is fitted on the relative density given by **dp3D** (see Fig. 5.6b). The sintered contact radius used for voxelization is [[Coble, 1958](#)]:

$$a_s^2 = 4hR^* \tag{5.30}$$

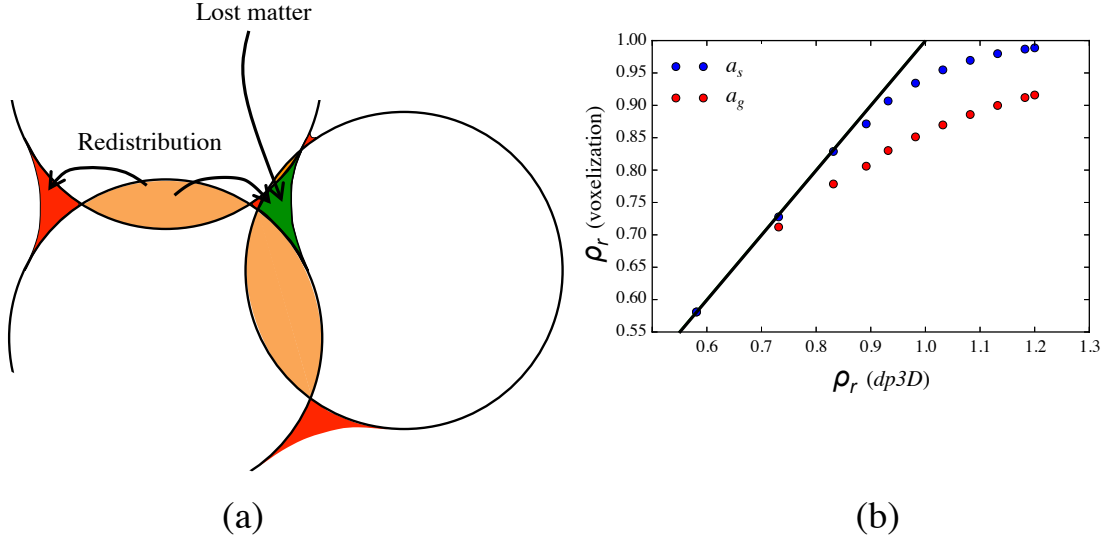


Figure 5.6: (a) Overlapping of the redistributed matter by a particle. The matter to be redistributed is in orange, which has been redistributed in red and which is lost in green. (b) Evolution of the relative density of voxelized images compared to **dp3D** for two contact radius : a_s defined by Eq. (5.30) and a_g defined in Eq. (5.20). The density obtained with the sintered contact a_s is chosen.

5.4 Results of discrete simulations with the anisotropic model

Numerical samples are prepared following steps described in section 5.1.5. The effect of texture is investigated on a packing of 4000 particles with Periodic Boundary conditions. Different cases are shown in this work and are presented in Fig. 5.7. Parameters of the simulations are given in Table 5.1. The compaction is oedometric with an imposed strain rate along the \mathbf{z} direction. Figure 5.9 plots the results for the normal components of the stress tensor. Macroscopic stresses are calculated in the volume delimited by the periodic box, using Eq. (5.4). There are displayed positive in compression and negative in tension. Shear components (σ_{xy} , σ_{xz} , σ_{yz} , not plotted) are oscillating with density, but are always at least one order of magnitude lower than normal components. It should be clear that when tangential forces are fully included in the simulation, moments are effective and particles rotate. Thus, the initial textures sketched in Fig. 5.7 may be modified during compaction as discussed later.

Figure 5.8a shows the evolution of the average coordination number with density for all textures. The coordination number continues to increase as in Fig. 5.3b. However we do not observe any clear effect of the packing texture. Similarly, distributions of indentation

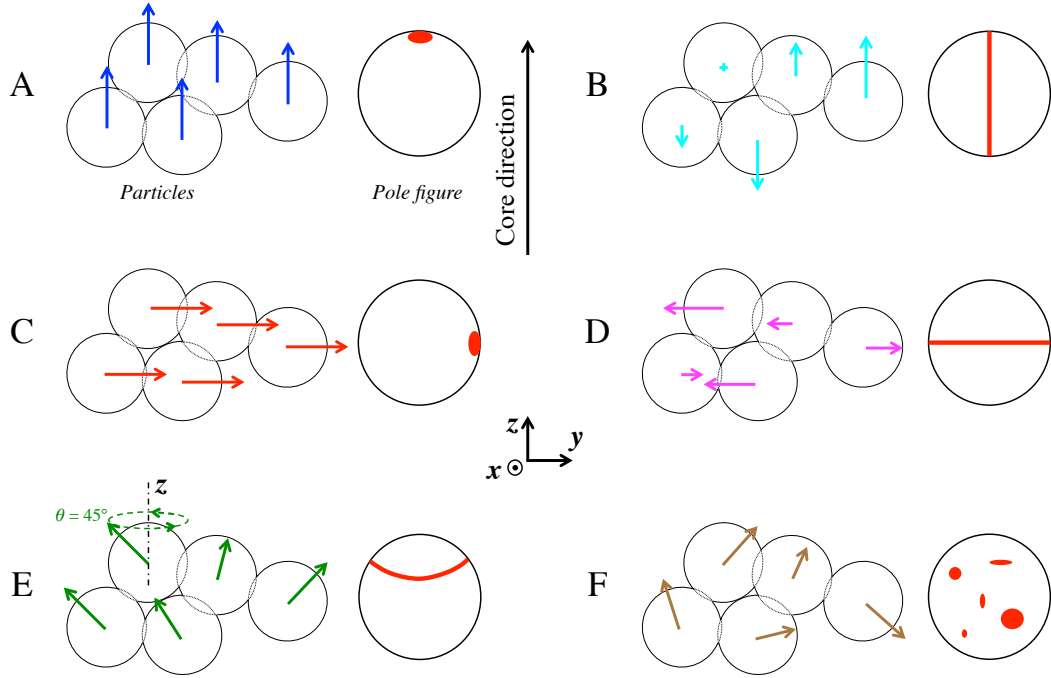


Figure 5.7: Representation of the textures tested in this work with their associated Pole figures. **c** axes of texture A are along the main loading direction **z**, B in the plane (**x**,**z**), C on the **y** direction, D in the plane (**x**,**y**), E at 45° with respect to the **z** axis, F randomly oriented.

Parameters	R (mm)	E (GPa) ^a	ν ^a	μ_{basal} ^b (Pa.s)	$\dot{\epsilon}_{zz}$ (s ⁻¹)	Bound. Cond.
	0.5	9.33 ^c	0.325 ^c	10 ¹²	-10 ⁻⁵	PC

Table 5.1: Parameters for discrete simulations.

^a Used only in section 5.1.5

^b From section 2.4.3

^c Gammon et al. [1983]

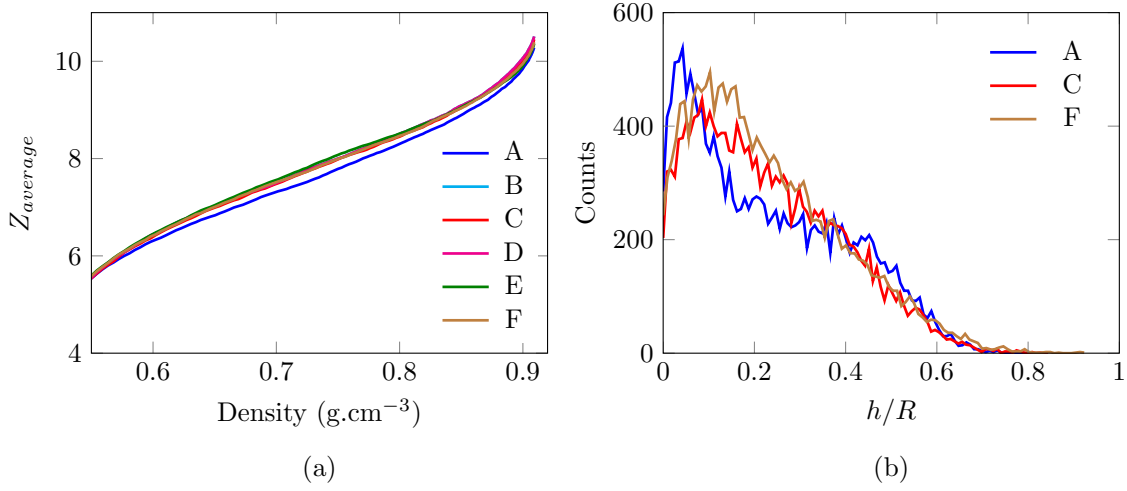


Figure 5.8: (a) Evolution of the average coordination with density for different textures. (b) Indentation distribution for textures A, C and F for $\rho = 0.851 \text{ g.cm}^{-3}$.

h/R (Fig. 5.8b) are rather similar between the different textures, with a peak at small contacts. Differentiating the new detected contacts from those whose \mathbf{c} axis configurations hinder further indentation has not been attempted here. From Fig. 5.5c, one could expect a bimodal distribution of the indentation, with small indented contacts (e.g., the pair $(\theta_i, \theta_j) = (0, \pi/2)$), and large indented contacts (e.g., the pair $(\theta_i, \theta_j) = (\pi/4, \pi/4)$). But, according to Fig. 5.8a, a particle has about 10 contacts with other particles for a density $\rho = 0.9 \text{ g.cm}^{-3}$. Therefore its equilibrium position depends on all those contacts, meaning an averaging of the contact size.

Figure 5.9 clearly differentiates the mechanical response of the various textures. The left hand side column in Fig. 5.9 shows the results when the viscous force T_v is not included, while the right hand side shows the full model with T_v given by Eq. (5.27). The results are qualitatively similar for the two columns but are easier to interpret first with $T_v = 0$.

In that case, textures C and D lead to the largest stresses with normal stresses approximately two times larger than for other textures at the end of the compaction (Fig. 5.9a). While textures A, D, E and F have symmetrical normal stresses with $\sigma_{xx} = \sigma_{yy}$, texture C leads to a clear asymmetrical response with $\sigma_{xx} \leq \sigma_{yy}$. This comes from the loading direction which is perpendicular to \mathbf{c} axes (only along \mathbf{y}) in the case of texture C. On the contrary, texture D does not exhibit such anisotropy because \mathbf{c} axes are randomly oriented in the plane (\mathbf{x}, \mathbf{y}) . We have observed that texture B also displays an asymmetry since $\mathbf{c} \in (\mathbf{x}, \mathbf{z})$, but of much smaller amplitude. For textures A, B, E and F, σ_{xx} and σ_{yy} stresses are approximately two times lower than σ_{zz} .

Using the full anisotropic contact law with the tangential forces, simulation results

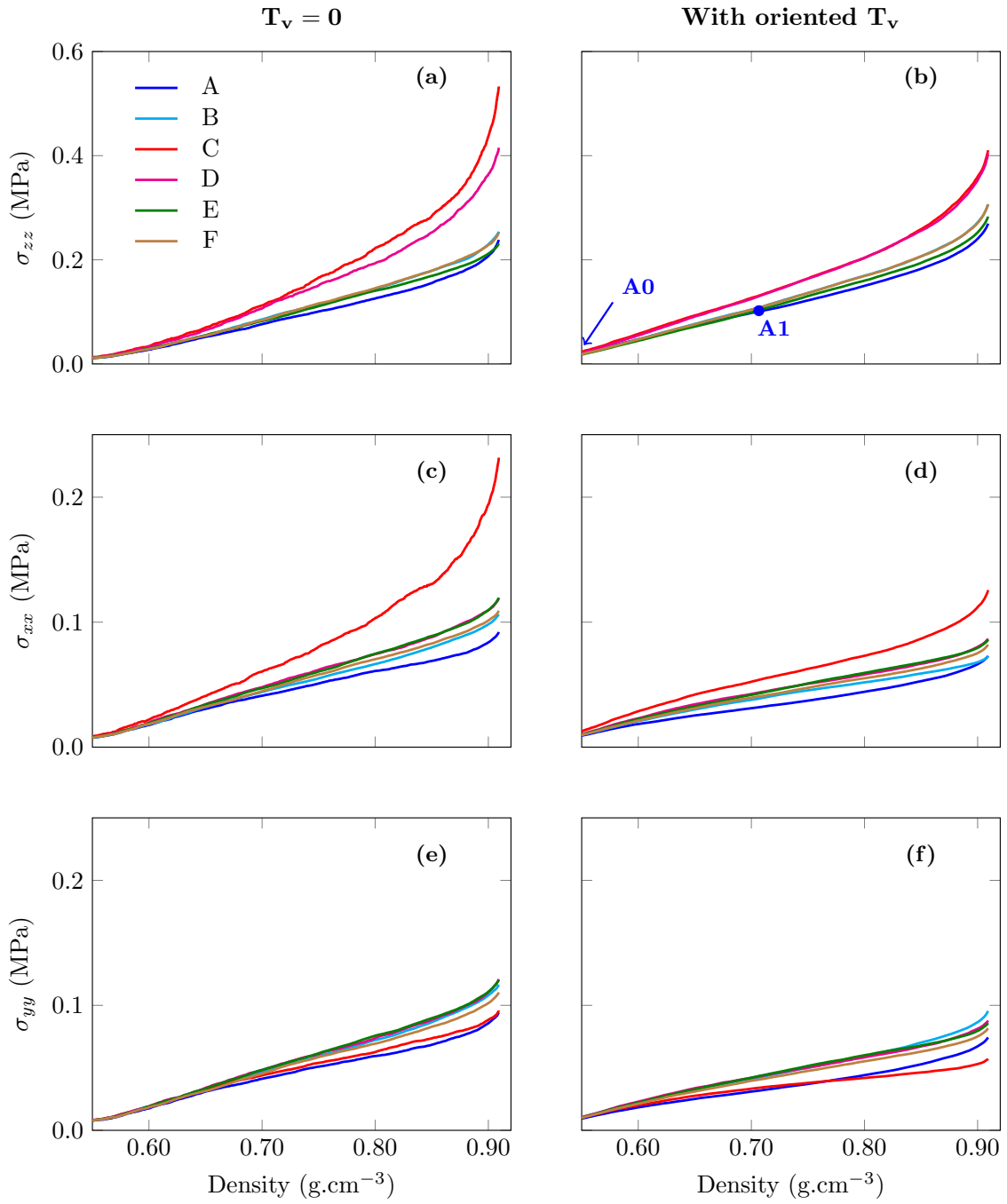


Figure 5.9: Evolution of normal stresses without the tangential force (a,c,e) and with the full oriented viscoplastic contact law (b,d,f). Texture are represented Fig. 5.7. The loading direction is along \mathbf{z} . A0 and A1 correspond to σ_{zz} of texture A for $\rho_r = 0.58$ and $\rho_r = 0.77$ and refer to Fig. 5.13.

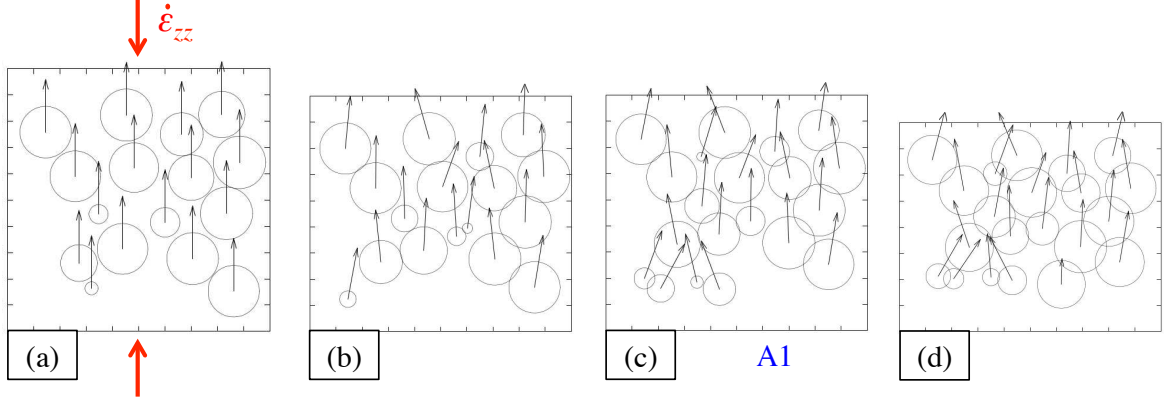


Figure 5.10: Evolution of \mathbf{c} axes with densification for texture A (with \mathbf{c} upward initially). 2D slices of a few particles at (a) $\rho = 0.526 \text{ g.cm}^{-3}$, (b) $\rho = 0.634 \text{ g.cm}^{-3}$, (c) $\rho = 0.716 \text{ g.cm}^{-3}$ and (d) $\rho = 0.851 \text{ g.cm}^{-3}$. A1 refers to Fig. 5.13.

show that σ_{zz} of textures A, B, E and F increases of about 14 to 18% whereas the stress associated with texture C decreased by 15% (Fig. 5.9b). Texture D is unmodified. Thus, the introduction of tangential force leads to less particle rearrangements and to larger stresses, except for the particular texture C. The randomly oriented packing (F) superimposes with texture B (Figs. 5.9a-b) and is between the textures with the largest stress responses (C and D) and the smallest ones (A and E). Lateral stresses σ_{xx} and σ_{yy} (Figs. 5.9d-e) are consistently lower than without tangential forces, texture C showing again an anisotropic behavior. In other words, increasing particle rearrangements in the case of an oedometric compaction, as with $T_v = 0$, tends to a more isotropic stress state as already observed for elastic or plastic compaction of powders [Martin et al., 2003]. Figure 5.10 exemplifies the rotation of \mathbf{c} axes during the packing compaction for a few particles of texture A. It shows that rotation of particles is non-negligible and typically in the order of 10 to 30°. The rotation seems gradual and continues all along the compaction.

The oedometric compaction test also allows for the determination of the Poisson's ratio or more appropriately for finite plastic strains of the Poisson's function:

$$\nu = \frac{\sigma_{xx} + \sigma_{yy}}{\sigma_{xx} + \sigma_{yy} + 2\sigma_{zz}} \quad (5.31)$$

Figure 5.11 depicts a continuous decrease of the Poisson's function with and without tangential forces. ν decreases from 0.4 to 0.2 in the range of investigated densities. The black dashed line in Fig. 5.11 represents the average Poisson's ratio measured by shear waves in firn ($\nu \approx 0.33$) [King & Jarvis, 2007] in the range $0.60 < \rho < 0.85 \text{ g.cm}^{-3}$. Our simulation results that characterize the stress ratio during the oedometric test (Eq. (5.31)) with a purely viscoplastic deformation, may not be compared directly with measures that

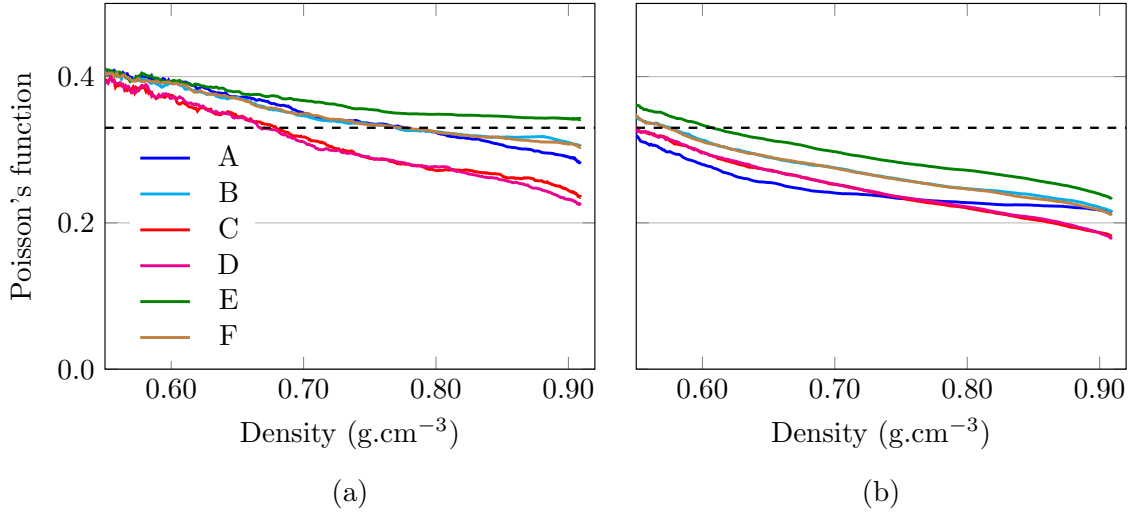


Figure 5.11: Evolution of the Poisson's function with density for DEM simulations (a) with $T_v = 0$ and (b) with N_v and $T_v \neq 0$. $\nu = 0.33$ is represented by the black dashed line [King & Jarvis, 2007].

characterize the elastic behavior of firn.

The above results (Fig. 5.9 and 5.11) can be confronted to those of Fig. 5.12 depicting normal stresses for simulations for which particles cannot rotate. For these simulations, particle rotations were deactivated and thus textures were kept constant all along the densification. Inspection of the curve related to texture A reveals that σ_{zz} is three times larger than when rotations are included (Fig. 5.12a). Also, tensile stresses are generated along \mathbf{x} and \mathbf{y} axes (Figs. 5.12b-c). These odd results mean that a hypothetical auxetic material (negative Poisson's function) is generated with such conditions (Fig. 5.12d). Gaspar [2010] and Kumar et al. [2016] have shown that the necessary ingredients at the contact scale for such a macroscopic behavior is a lower stiffness in the normal direction than in the tangential direction, which is not regular in granular materials¹. This auxetic behavior stems directly from the anisotropic contact law coupled with the deactivation of rotations.

The schematic diagram in Fig. 5.13d illustrates the softer viscoplastic stiffness along the contact normal \mathbf{n} because $\theta_i = \pi/4$ and the stiffer response along \mathbf{t} . This particular configuration, if kept unchanged by deactivating rotations explains the auxetic response of texture A.

Figure 5.12a seems consistent with what one could expect from such textures on a first basis. σ_{zz} is greater for "strong" textures i.e. orientations that are not favorable for deformation (textures A and C) than for "soft" textures such as E. The randomly

¹ Some interesting designs have been proposed in the literature for granular-like materials.

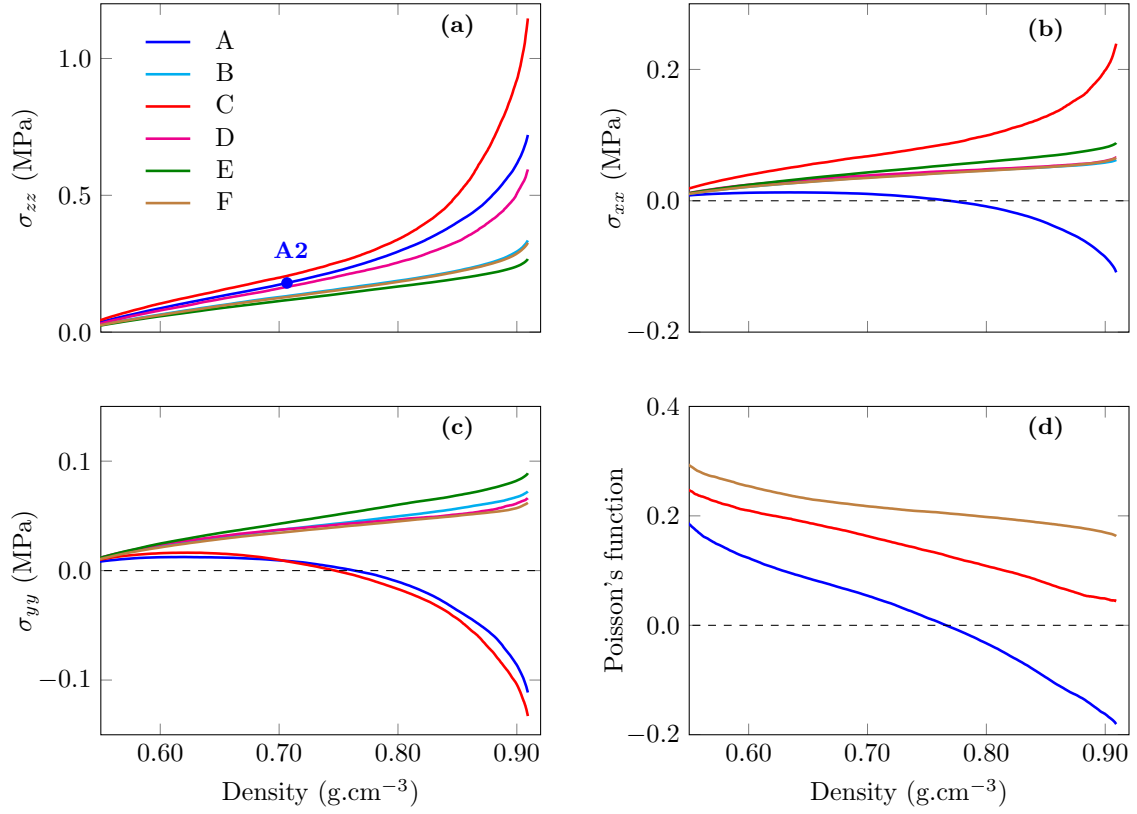


Figure 5.12: (a)-(b)-(c) Evolution of normal stresses when particle rotations are deactivated for the anisotropic viscoplastic contact law. (d) Poisson's function. Textures are represented Fig. 5.7. A2 corresponds to σ_{zz} of texture A for $\rho_r = 0.77$ and refers to Fig. 5.13.

oriented packing (F) is in between these two extremes but still quite close to texture B for Figs. 5.12a, 5.12b and 5.12c meaning that a random texture has approximately the same response than a texture whose **c** axes are in a plane parallel to the compression direction. σ_{xx} and σ_{yy} of texture D are similar than for B and F but σ_{zz} is almost twice as large. Interestingly, texture C is also in tension but only in the **y** direction, which is the **c** axes direction. This starts from about the same density than texture A, i.e. $\approx 0.75 \text{ g.cm}^{-3}$.

When the **c** axis in the initial packing is not constrained to a single non-favorable direction, the stress is drastically decreased when rotation is deactivated. Note that the normal force is 75 times larger for a contact with particles at 0° with respect to **n**, compared to a contact with disorientations of 45° (Eq. (5.24)). Figure 5.12a, indicates that macroscopically, σ_{zz} is only 2.7 times larger for texture A than for E, and Fig. 5.9b gives equal stresses for these textures.

Figure 5.13 attempts to explain such a behavior. The same slice of texture A packing is represented initially (Fig. 5.13a), and at $\rho_r = 0.77$ when the full anisotropic law is used (Fig. 5.13b) and when rotations are deactivated (Fig. 5.13c). Only a typical portion of the 4000 particles packing is represented. Since a substantial axial macroscopic strain is applied to the packing in between slice A0 and slices A1 and A2 (with corresponding particle rearrangements), it is not straightforward to follow individual particles. Still, qualitative information can be gathered from the evolution of the slice. Fig. 5.13a shows that initially all **c** axes are aligned along the loading direction. It should be clear that this does not imply that all particles are characterized by a zero θ angle. Fig. 5.13d shows for example a contact which normal makes a 45° with the loading direction (and thus is characterized by $\theta_i = \theta_j = 45^\circ$). In other words, a very large distribution of angles is obtained between particles, with very few θ equal to 0 or $\pi/2$. Therefore the stress response of the texture cannot be inferred directly from the initial packing. Slice A1 (Fig. 5.13b) illustrates that the smaller stress response obtained on Fig. 5.9d compared to Fig. 5.12a originates from small rearrangements and rotations of **c** axes (also represented in Fig. 5.10). The texture is mainly kept with **c** axes close to the macroscopic loading direction, but a few large disoriented particles are observable. For all textures, we observed that compaction leads to small but finite rotations.

Simulation results are reflecting a few important assumptions of the DEM. In dp3D, rotations arise only from the moment caused by tangential forces and **c** axes are rotated accordingly. However, one of the important result from chapters 2 and 4 was the inevitable rotation of **c** axis during intragranular deformation, which is not taken into account in dp3D. Although, section 2.4.3 showed that truncated cylinders of ice could hinder rotation, they could not avoid it. It is difficult to estimate in which proportion multiple contacts limit rotations. The random texture F stays isotropic with compaction, but such texture

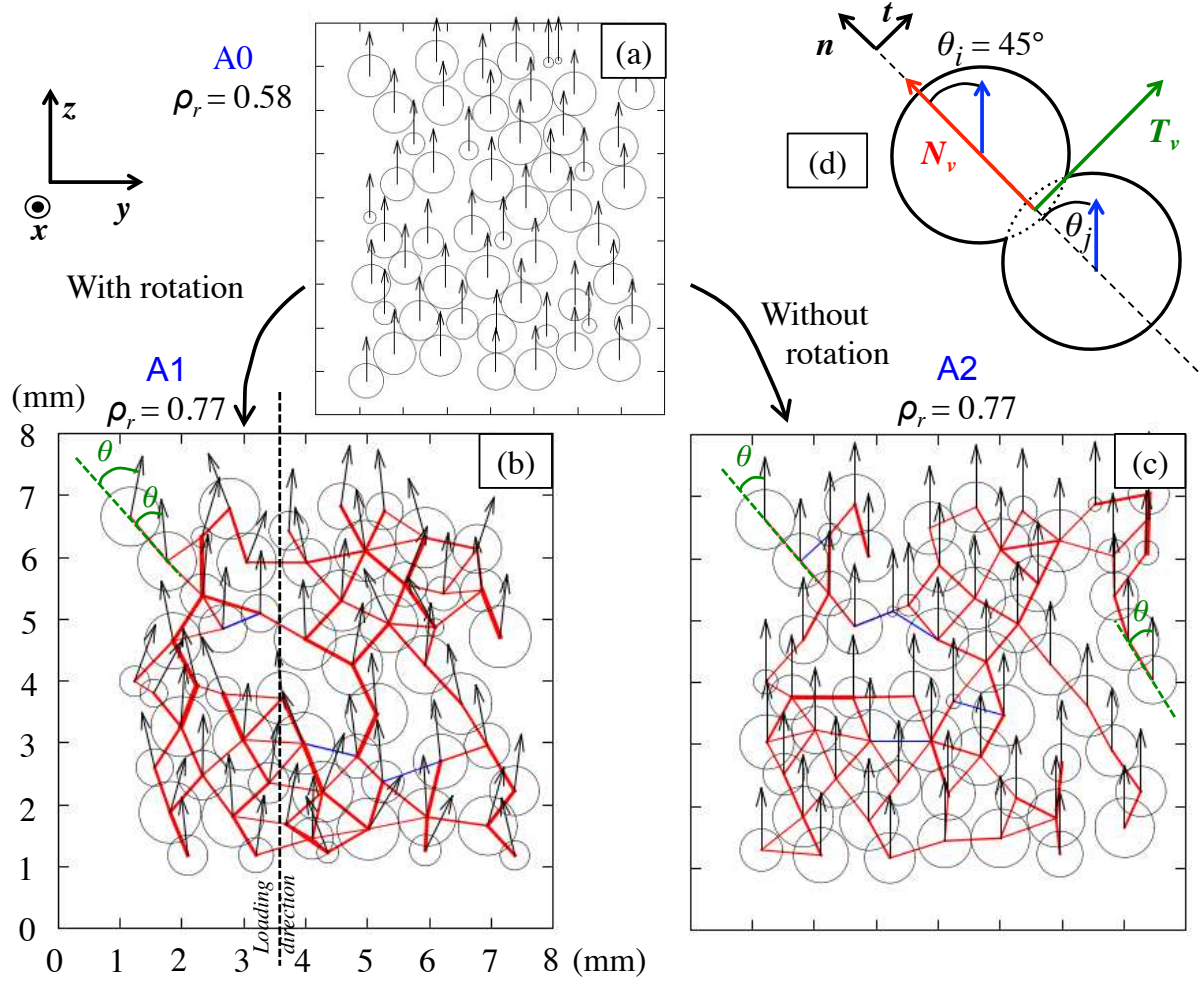


Figure 5.13: 2D slices of texture A (a) before compaction, (b) for point A1 $\rho_r = 0.77$ (see Fig. 5.9b) and (c) for point A2 (see Fig. 5.12a). Red and blue segments connecting particle centers indicate compressive and tensile normal forces, respectively. The thickness of the segment scales with the force amplitude. (d) Schematic of the contact forces for a specific configuration that leads to a negative normal stress σ_{yy} .

should see its \mathbf{c} axes progressively align to the loading direction. It should also be the same for specific textures C and D for instance. However, it is not the case as we did not develop a phenomenological law for the rotation as a function of indentation from results on two contacting cylinders (see section 2.4.2). An other assumption is the omission in DEM of the continuous recrystallization occurring in firn for such densities (observed chapter 3).

Still, different textures could be tested and compared. In this work with a Newtonian anisotropic viscoplastic contact law, results of Fig. 5.9 imply that densification can be about 1.5 longer with texture C than with texture A.

The magnitude of the stress on Fig. 5.9 seems consistent with stresses from firn cores. However the strain rate imposed is 6 to 7 orders of magnitude larger than observed on polar sites. As the contact law used is linear, we only need to multiply the viscosity μ_{basal} by 10^6 . However, $\mu_{basal} = 10^{18}$ Pa.s seems not conceivable. A better solution is to tune the stress exponent to a more relevant value for firn core (typically $n = 3$), which would enable the use of a more appropriate viscosity parameter when density is high. Also a $n = 3$ seems more in line with what has been observed experimentally for polycrystalline ice [e.g., Duval et al., 1983]. An attempt to implement the model for $n = 3$ is described as a possible perspective in chapter 6.

5.5 Using binary images from in situ X-ray tomography : an attempt

5.5.1 Methods

The assembly of 4000 particles studied in the last section is a very idealized microstructure. It is not very representative of the microstructure of firn as observed in chapters 3 and 4. An illustration of pore shapes is proposed in Fig. 5.14a. To start from an initial numerical microstructure that is closer to the real microstructure, X-ray images can be used as a mask for generating the assembly. Such an approach has been used successfully for example to describe the fracture of porous structures digitized by X-ray tomography [Roussel et al., 2016].

The method explained in section 5.1.5 is used first to generate a cylindrical assembly that has the correct size ratio as compared to X-ray images. Firn packings of 50000 particles (FP1) and 150000 particles (FP3) are generated this way (see Table 5.2). Then, samples are homogeneously shrunk to $\rho_r = 1.2$ and the mask of the sample 80m_c2 is applied. Such a relative density means that particles are overlapping one another. With increasing number of particles, the ice phase from binary images is better meshed (see

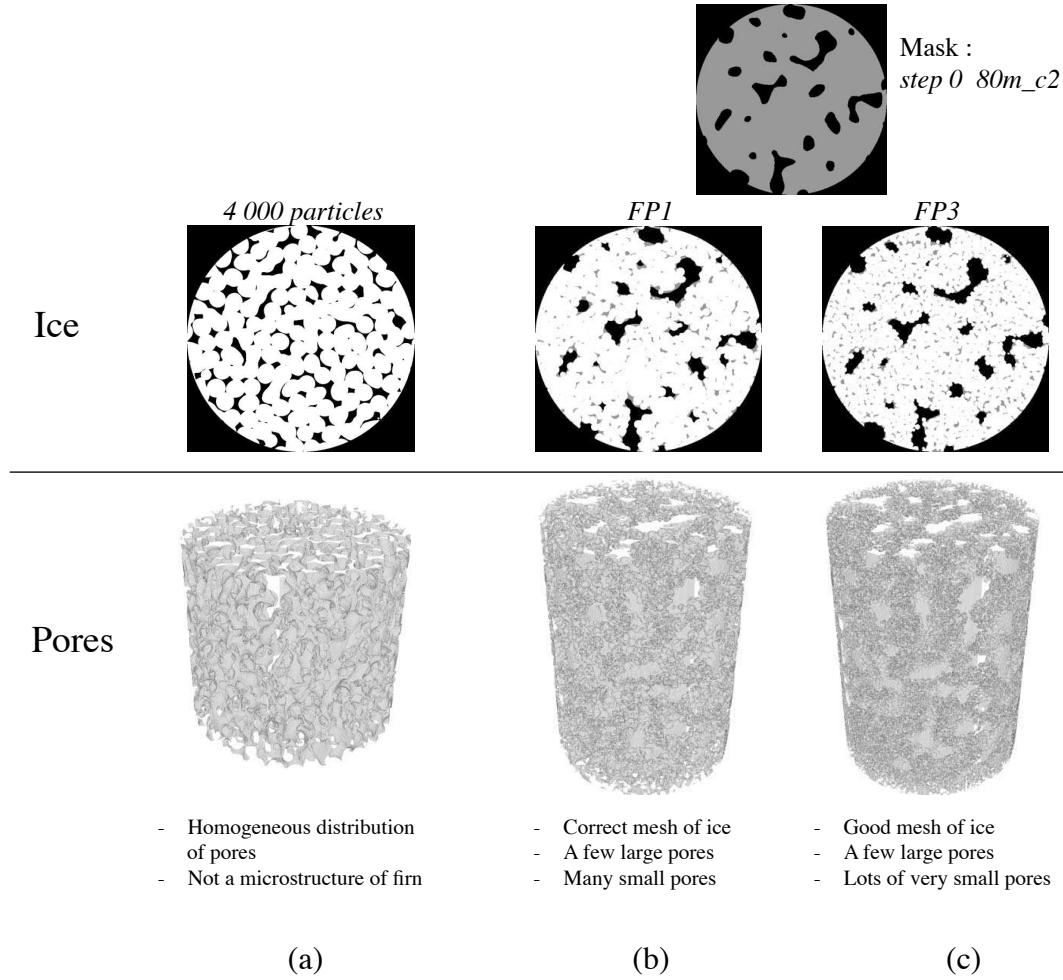


Figure 5.14: Microstructure of cylindrical assemblies after voxelization for about the same density $\approx 0.78 \text{ g.cm}^{-3}$. (a) The packing of 4000 particles studied in section 5.4. Meshing of binary images from sample 80m_c2 with (b) 50000 particles (FP1), and (c) 150000 particles (FP3).

Figs. 5.14b-c). In order to evaluate pore closure after numerical simulations, firm packings are converted to binary images using the voxelization routine (section 5.3). As a result, to keep the total number of voxels reasonable, particles are defined by less voxels for FPs than for the 4000 particles used in section 5.4, once the voxelization routine is performed. The obtained resolution being $30 \mu\text{m}$, errors on the closed porosity ratio and connectivity index are reasonable (report to section 3.4). Moreover the number of small closed pores also increases with the number of particles, as particles are very indented, leaving tiny spaces between them. The relative density of the ice phase filled with particles is not equal to unity, because particles are spherical and matter is lost as illustrated in Fig. 5.6. Thus DEM spherical particles meshing the ice phase should not be thought of as real particles or grains.

Name	Particles	ρ_{r0}
FP1	50000 / monodispersed	0.844
FP2	50000 / uniformly distributed	0.853
FP3	150000 / monodispersed	0.817
FPA	FP1 with texture A	0.844
4000p	4000 / monodispersed	0.58

Table 5.2: Parameters for discrete simulations of firn from granular packings as shown in Fig. 5.14. The initial relative density of sample 80m_c2 is $\rho_{r0} = 0.856$.

An other microstructure is also generated (named FP2) with a dispersion of particle size. Distribution is uniform and ranges between 0.35 and 0.65 mm. This distribution of particles offers the best mesh of the tomographic volume compared to FP1 and FP3, with $\rho_{r0} = 0.853$ after voxelization while the initial relative density of sample 80m_c2 is $\rho_{r0} = 0.856$.

Oedometric tests are performed on the firn packings FP1, FP2, FP3, until $\varepsilon_{zz} = 0.45$. An axial strain rate is imposed ($\dot{\varepsilon}_{zz} = 10^{-5} \text{ s}^{-1}$) with boundary condition RWC and a cylindrical rigid wall is also imposed. Simulations are performed with the isotropic contact law for FP1-3 (section 5.2.1). In order to assess for the effects of the viscoplastic anisotropic contact law on the closure of pores, deformation of firn packing of texture A (FPA) is also simulated with the initial particle assembly from FP1. Other parameters are the same than presented in Table 5.1. Additional details of the simulations are given in Table 5.2.

5.5.2 Results

In situ oedometric tests on sample 80m_c2 led to a maximum density of 0.867 g.cm^{-3} for $\varepsilon_{zz} = 0.105$. However, the deformation of FPs must be $\varepsilon_{zz} \approx 0.35$. A close examination of the dense parts of the firn packings shows (blue ellipse in Fig. 5.15) that relative density is still increasing inside these regions while strain should essentially reduce only the large pores. There is an important loss of matter within these regions, as it cannot be redistributed because of overlapping particles. This is why such a large strain ε_{zz} is required to densify. The definition of density used here (with the voxelized image) has no significance. Indeed one would rather use the density calculated using the strain from simulations and initial density of the digitized in situ sample. However after a strain $\varepsilon_{zz} = 0.45$ the final density should be $\rho = 1.43 \text{ g.cm}^{-3}$ which is not realistic.

Digital volume correlation (DVC) on in situ samples was used in chapter 4, but it required a large subset size that included one or two pores. Thus it was impossible to quantify locally the pore deformation and the ultimate division in new pores. Therefore,

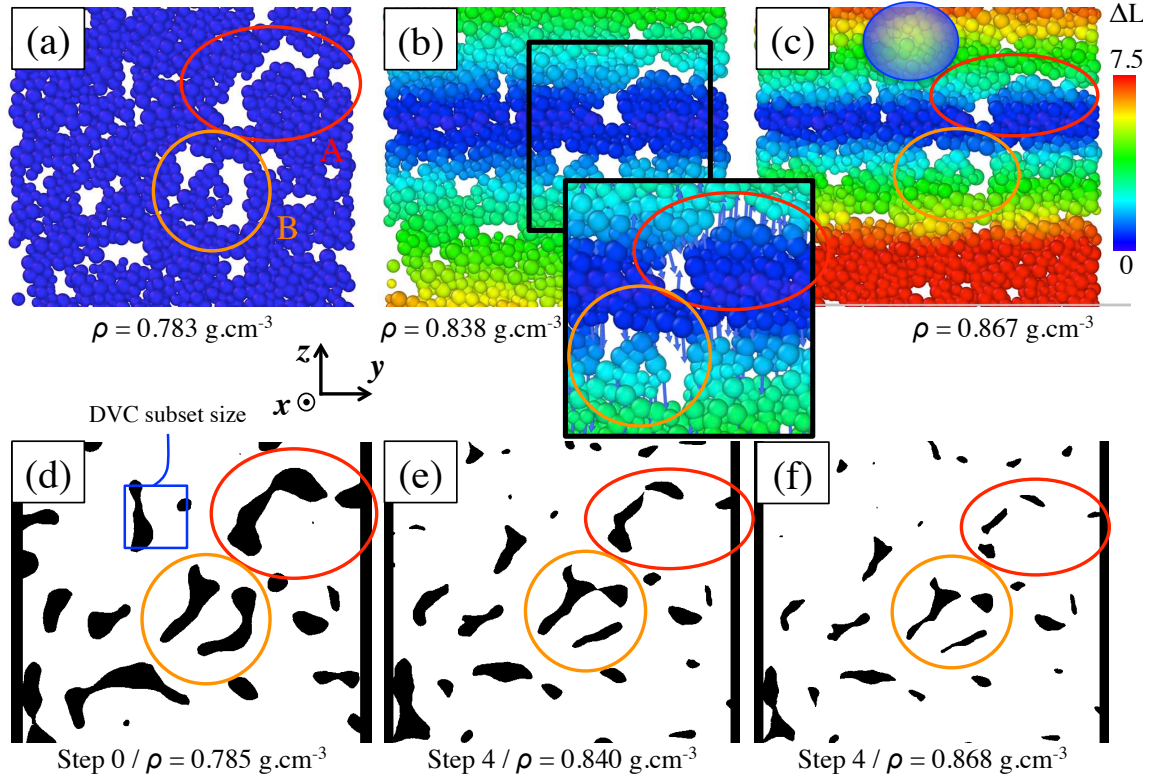


Figure 5.15: Comparison between DEM simulations on FP2 and binary images from in situ sample 80m_c2. Different steps of the simulation a-b-c corresponding to initial step (d), penultimate (e) and last step (f) of in situ deformation are represented. Areas A and B focus on pores that are closing. Arrows on figure (b) show the displacement vectors of each particules.

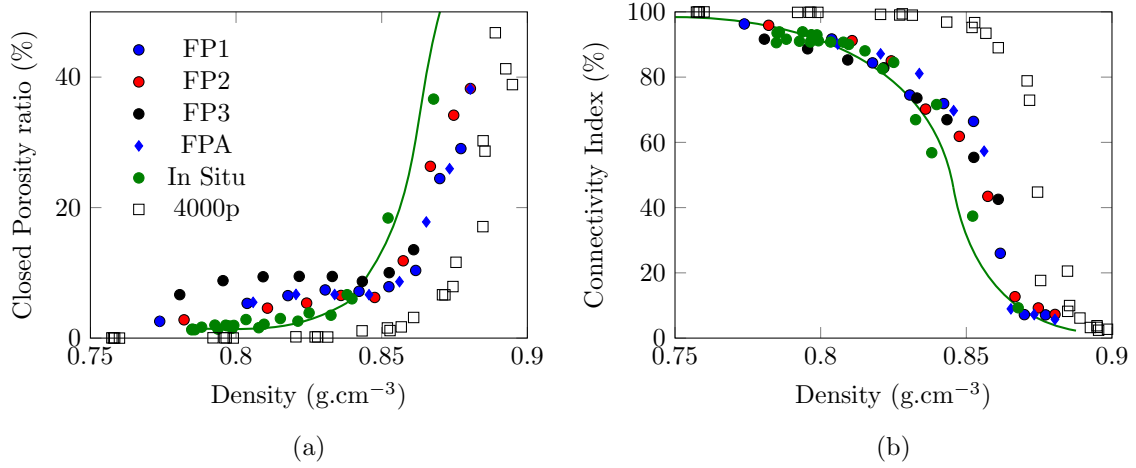


Figure 5.16: Evolution of (a) closed porosity ratio and (b) connectivity index with density (maximal strain $\varepsilon_{zz} = 0.45$). The green solid lines are to guide the eye only. The last points of FP2 and FPA are superimposing. Empty squares 4000p represent the evolution of the packing of 4000 particles from section 5.4 for textures A, E and F, and without textures. All these squares fall on a master curve.

characterizing closure in 3D is challenging for firm. However, thanks to the DEM, it is possible to follow at each time step the ice matrix filled by sphere. Unfortunately, FP's are too dense to be visually followed in 3D. Consequently, Fig. 5.15 compares 2D tomographic slices of in situ sample 80m_c2 with DEM results² of FP2.

All fields are known at the particle scale with DEM, while it was at the scale of the subset with DVC. The displacement field on Fig. 5.15a-b-c seems approximately homogeneous. But a zoom on Fig. 5.15b illustrates the direction of particles and shows local motion in the plane (y, z). The closure of pores in area A seems correctly represented by simulations. The benefit of DEM is interesting in this case. Indeed, meshing firm samples by finite element would have involved the detection of a new contact due to pore closure, while the DEM automatically processes this contact. Area B shows that vertical pores are only being compressed and not separated as in the tomographic slice. However, the view being 2D, slices are not representative of the shape of pores in 3D, and can be slightly tilted.

It is crucial that future work concentrates on tools enabling to compare DEM results with DVC in 3D, but this would need smaller subset size.

The voxelized images of the numerical microstructures obtained after oedometric compaction were treated as for the X-ray images (chapters 3-4) to obtain the closed porosity ratio and the connectivity index. As shown in Fig. 5.16, closure of pores occurs with FP1, FP2 and FPA, and not so much with FP3. Trends are in good agreements with in situ re-

² Visualization of particles is done with the software Ovito [Stukowski, 2010].

sults for FP1, FP2 and FPA. Using the anisotropic contact law has no particular influence on the pore closure compared to the isotropic viscoplastic law. It is worth mentioning again the effect of volume size of the sample used here. In fact, volume of numerical samples FP's and 4000p decreases as the simulation moves forward. Therefore, calculating the closed porosity ratio is done on a reducing volume, while for in situ experiments, a fixed volume was chosen whatever the density in the larger firm sample volume. In other words, numerical and experimental samples are initially the same (with the large approximation of spherical filling of the ice phase), but as the simulation proceeds volumes diverge.

On Fig. 5.16a, this means that final blue and red points would have a larger closed porosity ratio, which is consistent with the in situ trend. As detailed in chapter 3, Fig. 5.16b is not very dependent on the volume reduction from DEM simulations. Curves for FP1 to 3 agree satisfactorily with in situ results.

Assemblies of 4000 particles with different textures and with the use of the isotropic viscoplastic law fall on a master curve for the connectivity index and for the closed porosity ratio. However, the packing 4000p, whose idealized microstructure is very far from the real X-ray tomographic one, exhibits a closure at a significantly larger density ($\approx 0.88 \text{ g.cm}^{-3}$).

5.6 Conclusion

This chapter concentrates on simulating the firm densification with the discrete element method. The anisotropic viscoplastic contact law proposed and validated in chapter 2 is used here to simulate assemblies of ice particles that exhibit textures. Different textures were compared. Results showed that stress response could not be inferred from the initial texture. However textures with **c** axes perpendicular to the loading direction present the largest stress response for σ_{zz} . Hindering rotation greatly limits rearrangement possibilities of particle assemblies especially when **c** axes are parallel to the loading direction. Figure 5.17 shows a normalization of σ_{zz} for the different textures using texture F (random) as a reference. Rotations and the effect of the tangential force are taken into account in this figure (as in Fig. 5.9). A clear effect of textures can be observed with a 30% increase in normal stress for the stiffest texture.

Numerical firm samples were generated and revealed similar results to in situ experiments (detailed in chapter 3), in terms of closed porosity and connectivity index. However, the shapes of pores are very different than observed with ex situ and in situ characterization. Meshing binary images with spheres that follow pore deformation should be enhanced with the work of Gibaud [2017] and allow a finer estimation of the strain field around pores. Indeed, voxelization issues hinder the results shown here. The loss of matter becomes too significant when reaching a relative density of 0.9, leading to a rescaling

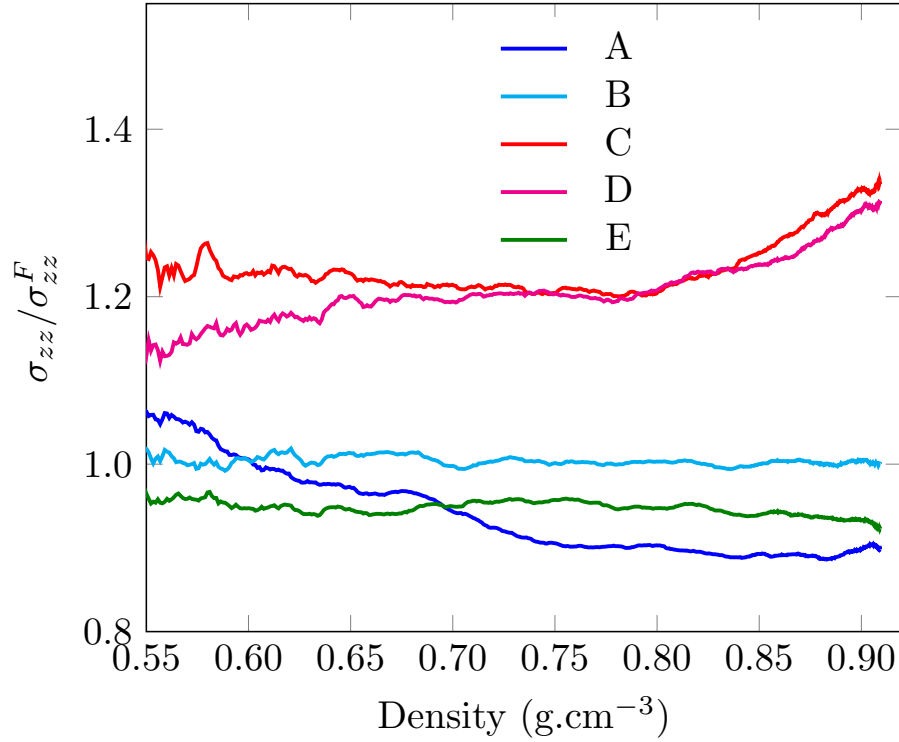


Figure 5.17: Ratio of σ_{zz} for all textures studied with σ_{zz} of texture F in the case of 4000 particles using the anisotropic viscoplastic contact law for ice.

of the density of binary images.

In conclusion, this chapter proposes an estimation of the stress response of different textures for firm, and a proper tool to compare them in the case of a Newtonian flow law.

Future works should try the non-linear formulation of the viscoplastic contact law, as well as more complex cases than oedometric tests.

Chapter 6

Conclusion and future work

Contents

6.1 Conclusion	203
6.2 Future work	205
Numerical simulations on digitized images from X-ray tomography . .	205
Extending X-ray characterization to other sites	207
Coupling Digital Volume Correlation and Diffraction Contrast Tomog- raphy	207
Towards a firm layer modelling	209
Implementation of the anisotropic model in the IGE firm densification model	211

6.1 Conclusion

The densification from firn to ice is a process involving different mechanisms and with important implications for understanding potentially significant climate changes. The progressive capture of air occurs through the closure of pores by pinching. The literature review depicted that ice viscoplasticity is anisotropic because dislocations glide preferentially on basal planes. Up to now, model of densification of firn did not take into account this feature. This thesis aimed to characterize the evolving microstructure of firn with depth and model the densification taking into account the **c** axis orientation of grains (which is perpendicular to basal planes). For that purpose, the discrete element method was selected, as it is an adequate numerical tool for granular material.

A simplified law using the transverse isotropic viscoplastic behavior of the single crystal of ice was chosen to characterize the contact between two particles. Creep experiments performed in laboratory conditions ($T = -10^\circ\text{C}$, $\dot{\epsilon}_{zz} \approx 10^{-5}$ - 10^{-6} s^{-1}) on two ice cylinders were followed by polarized light and digital image correlation and showed good agreement with finite element simulations [Burr et al., 2017]. The evolution of the indentation rate between two particles depending on their initial **c** axis is well captured by the simplified contact law. This anisotropic contact law was implemented in an in-house discrete element code `dp3D`. Starting from a predefined texture or a random texture that characterizes the **c** axis orientation of each particle in the packing, the DEM code enables the stress response to be predicted. Results showed various effects of the different tested textures. Oedometric compaction revealed that the stress response of textures whose **c** axes are perpendicular to the loading direction is the stiffest compared to other textures that present small differences for stresses between one another. When rotation is hindered, results exhibit the possibility to create a hypothetical auxetic material if **c** axes are aligned with the loading direction.

In parallel to this modeling and simulation study, this work also relies on an experimental investigation of the firn microstructure including estimation of grain size and their crystallographic orientation as well as analyzing the pore network. X-ray tomography was mainly used to characterize two polar sites (Dome C and Lock In). In firn, pores revealed to be globular parts separated by channels and to be tortuous. Quantitative data on the closed porosity ratio suffered from voxel size and spatial heterogeneities but foremost from sample size effects. To describe the closure without such effects, a connectivity index defined by the volume of the largest pore divided by the total pore volume is proposed. This parameter reaches values close to 0% for depths and densities close to what was obtained by air pumping [Landais et al., 2006], air content data [Martinerie et al., 1992, 1994] or parameterizations [Goujon et al., 2003]. Conclusions on the comparison of Dome

C and Lock In ice cores are a more tortuous structure for the Lock In firn for similar densities. Although the crystallographic texture of these two sites is comparable, grains at Lock In are smaller than Dome C at the same density. The COD determined by the connectivity index is also deeper at Lock In. A smaller Δ_{age} gas-ice is expected for the firn from Lock In as pore network is more tortuous compared to the firn from Dome C. A correction for firn samples from Dome C was also proposed, so that tomographic data for the closed porosity ratio are readily available for firn air transport models. X-ray tomography reveals to be an appropriate and powerful tool to study locally the range of depths where closure takes place. Besides determining the close-off depth/density, it provides additional microstructural information on all pores that 2D analyses or destructive methods such as pycnometry are not able to deliver. The possibility to have very large volumes with tomography may eventually challenge the relevance of pycnometry.

For the first time, in situ oedometric tests under X-ray tomography at -10°C were performed on firn extracted from the Dome C ice core. The rather large strain rates (10^{-5} - 10^{-6}s^{-1}) and stresses (from 1 MPa to 5 MPa) involved a closure of pores occurring at larger densities than for polar firn densification. Textures and curvatures were also much more accentuated for in situ samples. Creep tests at -2°C were carried out for five months and enabled diffusion creep to proceed in addition to dislocation creep. The microstructures obtained in laboratory conditions came close to those induced by polar firn densification. Diffusion effects were successful to reproduce the pore closure at smaller densities and to reduce local curvatures compared to in situ tests (only dislocation creep). Utilization of a phase field method (code Snow3D [Flin et al., 2015; Bretin, 2009]) was also effective to reproduce this experiment. In conclusion the densification mechanism of firn can be decoupled by an anisotropic viscoplastic contribution and diffusion mechanisms (grain growth, recrystallization, sintering, diffusion creep). Only the first contribution is taken into account in the DEM. Simulating pore closure with DEM was possible by meshing in situ samples with spheres. Performing the same experiment numerically than with x-ray tomography led to correct evolutions of the closed porosity ratio and of the connectivity index with respect to these in situ results.

More generally, the modeling methodology developed in this work can be applied to other fields than firn densification. For example, for strongly anisotropic particulate materials such as magnesium, zinc, or titanium powders, the proposed model taking into account anisotropy at the contact scale may be useful to simulate powder compaction processes. The in-situ experimental tools and the post-processing analysis developed in this work may find applications for snow densification, foam densification or powder compaction. In fact, the thorough study of morphology and shapes of pores can be applied to any granular or porous materials.

6.2 Future work

Several paths for future works can be considered to complement the results on firn densification obtained throughout this thesis. Experimental procedure could also be improved. Some suggestions and guidance are proposed in the following.

Numerical simulations on digitized images from X-ray tomography

A large database of digitized firn samples was obtained in this work. Binary images originating from ice cores (Dome C, Lock In) and from in situ oedometric tests are available.

X-ray data could be further exploited with numerical simulations. In this work, the software Geodict was used to compute some pore properties such as the maximal path diameter or the pore size distribution. However, other physical properties that are of interest for the glaciology community can also be computed. The internship of Lucas Milliancourt [Milliancourt, 2017] proposed a few advances on this front, using the tomographic data gathered in this work. In particular, the thermal conductivity, the effective diffusion and the permeability are properties that could be of use in densification and air transport models for firn. For instance, the thermal conductivity is needed in the heat transfer module of the Goujon et al. [2003] model. Results obtained for these properties also complete the work of Calonne et al. [2011, 2012] that was restricted to snow at lower densities than 0.544 g.cm^{-3} . Figure 6.1 depicts the effective diffusion of several types of snow including binary images from in situ and ex situ samples. The new data enable the whole range of density from snow to ice to be characterized. Interestingly, preliminary results on the effective diffusion showed a marked anisotropy in the ice core direction when reaching densities of about 0.800 g.cm^{-3} . This could mean that the closure of pores, or their pinching is preferentially occurring in the lateral directions (parallel to the snow surface). Open pores should be oriented vertically if such results are confirmed. Moreover, the diffusion coefficient is calculated equal to zero below 95 m deep at Dome C (for density $\rho > 0.829 \text{ g.cm}^{-3}$), meaning a close-off at slightly shallower depth than obtained with the connectivity index ($\approx 98 \text{ m}$). As only a few images were tested and a large amount of data is at hand, this calls for further studies (in particular with the use of the Lock In site digitized images).

On that scope, the thesis of Fourteau [2019] should help in understanding the link between air diffusion in the closure region with the closed porosity ratio evolution. Combining methane concentrations in firn layers¹ with pycnometry and X-ray tomography, is expected to inform on the firn layering (thus the age distribution) and may enable a

¹ In closed firn layers, methane concentration is lower than in open firn layers, as air from the past has a fewer concentration of methane compared to the present one.

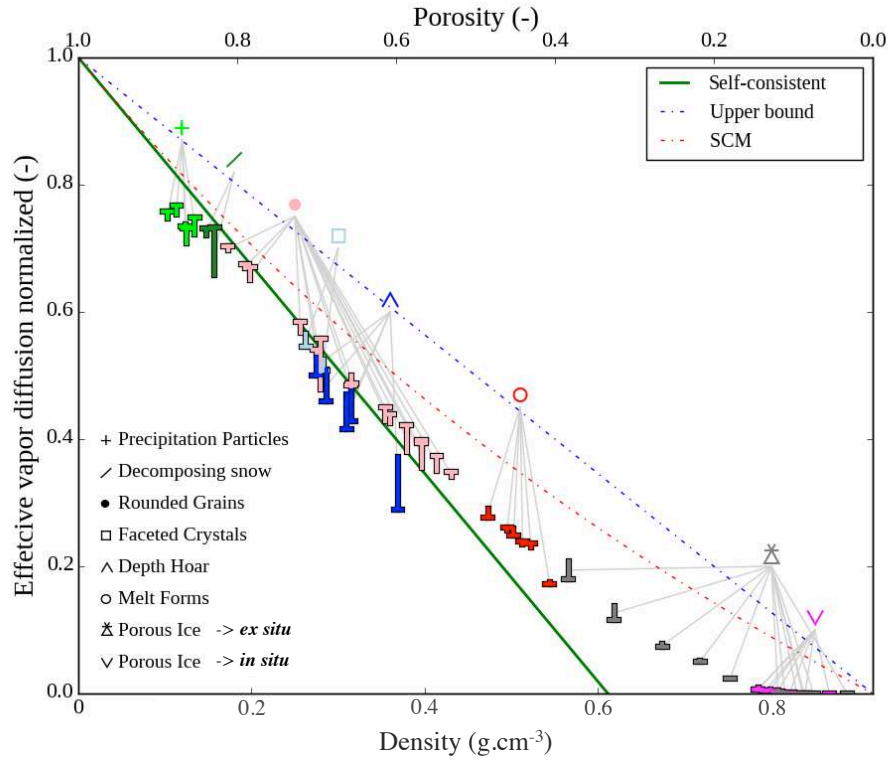


Figure 6.1: Evolution of effective diffusion with density and for different microstructure from [Milliancourt, 2017]. Different models are shown, and markers account for the anisotropy of the diffusion values. Ex situ (in grey) and in situ (in magenta) results are on the bottom right. Other experimental data were collected by Calonne [2014]. T shape markers give values along the core direction (the tip of "T") and in the plane parallel to the surface (the horizontal bar of "T"). The self-consistent, and SCM curves are two self-consistent models, while the upper bound represents only the evolution of the fraction of air multiplied by the effective vapor diffusion.

velocity of the closure process to be estimated.

Concerning mechanical properties, these data also offer some interesting prospects. The elastic properties were computed by Milliancourt [2017] and complement the work of Wautier et al. [2015]. A great addition to the understanding of the viscoplastic behavior of firn is to use digitized images from our work and especially the ones from in situ tests with the homogenization procedure and subsequent calculations with ABAQUS proposed by Wautier et al. [2017]. The thorough analysis of the RVE realized in this manuscript should be done again for these properties, to speed up the simulations.

Extending X-ray characterization to other sites

The X-ray characterization performed in this work relied on two cold sites with low accumulation rates. The next step is to challenge our results, particularly the connectivity index with warmer polar sites and different accumulation rates. Moreover, chapter 4 emphasized that microstructure of polar firn is controlled by stress and temperature, as phase field simulations showed the firn was not at an equilibrium state for a particular density. At warm polar sites with high accumulation rates, the close-off density is reached at shallower depth and microstructural mechanisms are then expected to be controlled by diffusion. The applied stress on firn at close-off density is also smaller than for colder sites (less overlaying firn). But, this induces a larger densification rate, therefore dislocation creep could be the dominant mechanism (Fig. 1.3.4). A still on-going work is to determine in which proportion stress, accumulation rate, temperature (promoting curvature minimization) or even dust content [Hörhold et al., 2012] are controlling the closed porosity ratio. Despite the rather large strain rates required for laboratory experiments, we proved that these tests are essential to understand pore closure. Different microstructures from various polar sites could be tested with this methodology in future works.

Coupling Digital Volume Correlation and Diffraction Contrast Tomography

Chapter 4 proved that digital volume correlation was suited to evaluate strain during oedometric compression. Thanks to DVC and a homemade algorithm, closed pores were tracked enabling their volume evolution to be studied.

Tomographic data and grain characteristics were decoupled in this thesis, as X-ray images only provided the pores and the ice skeleton. On their side, grains were obtained only by 2D microscopy. With the help of Diffraction Contrast Tomography, each grain of ice could be separated from one another in firn samples. This technique consists in coupling the absorption volume from tomography with the different diffraction spots of the grain, which are obtained when the Bragg condition is met. For example, the technique used at the European Synchrotron Research Facility (ESRF, Grenoble) relies on the matching of Friedel's pair - as the sample completes a full rotation, two identical diffraction spots are found at 180° - to find the position and the shape of grains in the sample volume [Ludwig et al., 2008; Reischig et al., 2013]. Coupling this technique with other methods is challenging but offers a full understanding of underlying processes at work. For instance, Proudhon et al. [2016] showed that crystal plasticity resolved by FEM could predict the global behavior and lattice rotation observed by DCT. The use of 6D algorithm as proposed by Viganò et al. [2016] also proved to be a great advance in

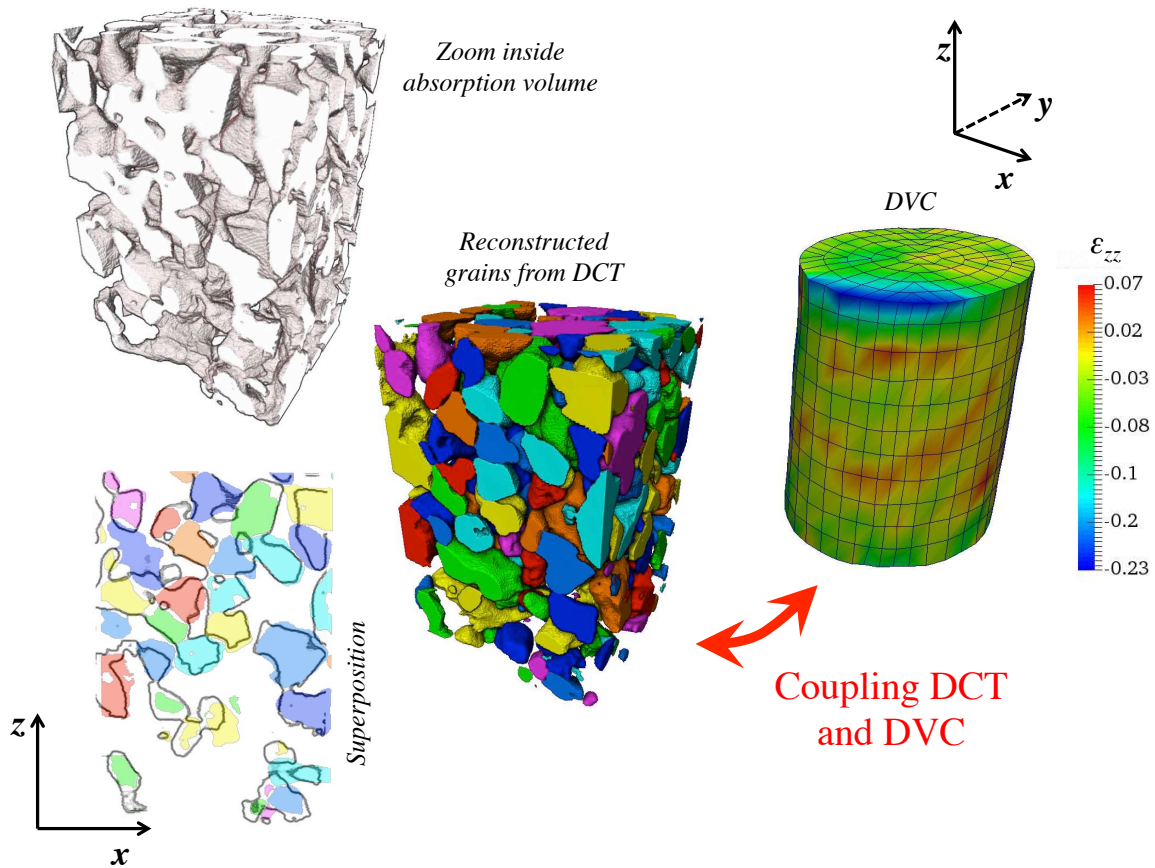


Figure 6.2: Parallelepipedic subvolumes of a snow sample, showing the absorption volume with the corresponding grains as reconstructed by DCT in this work. Subvolume size is $2.00 \times 1.75 \times 3.00 \text{ mm}^3$. A 2D superposition of grains and binary slice illustrates that shapes of grains are approximately retrieved. The DVC was performed on the whole sample and the calculated strain ε_{zz} is shown for the last step of strain. Sample size used for correlation is 3.38 mm in diameter and 4.13 mm in height.

reconstructing deformed grains that exhibit intragranular disorientations.

A very promising prospect is to couple DCT with DVC. In that case, the particles to track would be grains rather than porosities. This would enable the progressive change of grain orientation to be related to a strain field. Therefore one should be able to determine which grains deform the most according to their c axis rotations and their surrounding neighbors. Figure 6.2 illustrates this possible coupling of DCT with DVC which should greatly improve our understanding of the granular behavior of firn. The example that illustrates this scheme comes from experimental data obtained on ID19 at the ESRF in the framework of the ANR Snow White. Creep tests were performed on snow samples from different origins and with different grain sizes. Results lead to the publication of Rolland Du Roscoat et al. [2011], however much more data are available and could be exploited. During my PhD, digital volume correlation and DCT reconstruction was performed on

one particular sample presented in Fig. 6.2.

The sample reconstructed in Fig. 6.2 is much more porous than firn samples from chapter 4 ($\rho = 0.43 \text{ g.cm}^{-3}$). Therefore, studying firn sample with DCT involves the cold cell used in chapter 4 to be adapted. Indeed, according to the different trials to reconstruct the grains from the DCT data, samples should only contain a few hundred grains, and ice crystals should not be too much perfect. Creep tests may be the natural choice. However, it proved to be not very reliable on the snow tested in the ANR Snow White, and very difficult to perform on firn as stresses become too large. We recommend using the in situ cold cell developed in this work, which allows for a well-controlled procedure.

Towards a firn layer modeling

In this work, discrete element simulations were performed in the simple case of an oedometric compression with an applied fixed strain rate. A potentially interesting extension of this work is to study the compaction of particles in a more realistic case, pertinent for the densification of firn. In that case, it is necessary to follow a slice of the firn as it is subjected to increasing normal stress.

To that end an assembly of 4000 particles is generated and compacted to a relative density of $\rho_r = 0.58$ ($\rho = 0.53 \text{ g.cm}^{-3}$). Then, a series of stress plateaus, each corresponding to the weight of the above layers of firn, is applied on the packing. The imposed stress is increased to the value of the next plateau once the increase in relative density attains $\Delta\rho_r = 0.005$.

The overall stress increase corresponding to these successive plateaus is plotted in Fig. 6.3a against relative density. Different tests are proposed. The anisotropic contact law is used with $n = 1$ for three types of texture proposed in chapter 5. The viscosity is fitted so that the correct order of magnitude for strain rates is respected. For textures A, E and F, $\mu_{\text{basal}} = 3.5 \cdot 10^{18} \text{ Pa.s}$. Texture F needs 73 years more than E to reach a density of $\rho = 0.82 \text{ g.cm}^{-3}$ (Fig. 6.3b). The profile of the beginning of the curve is satisfactorily close to the density profile obtained by measurements (for $0.53 < \rho < 0.70 \text{ g.cm}^{-3}$), however when $\rho > 0.70 \text{ g.cm}^{-3}$, simulated curves are almost linear and diverge from the experimental curve.

The overestimation of the reached density at large times shown in Fig. 6.3b is linked to our simplistic contact law that only proposes a linear hardening as particles indent each other. An improvement for packings at large densities was implemented by Kallel [2013] in dp3D for the compaction of metallic powders. It uses the result of FEM simulations by Harthong et al. [2009] and proposes a simple hardening function that requires to be implemented in the contact law to take into account the departure from the indentation law of Storåkers et al. [1999]. This more realistic contact law for large densities has been

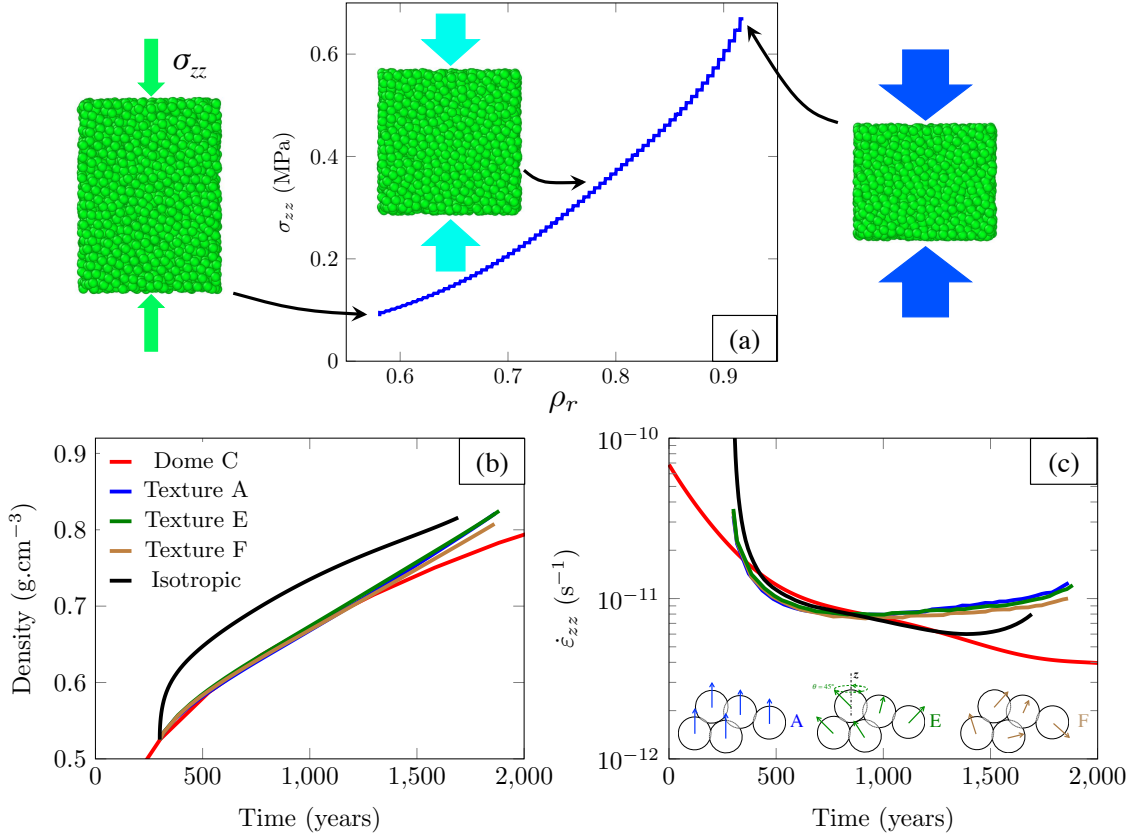


Figure 6.3: (a) Evolution of the applied stress on a packing of 4000 particles. Arrows illustrate the increasing stress that is applied. Evolution with time of (b) the density and (c) the strain rate $\dot{\epsilon}_{zz}$ using the isotropic and anisotropic viscoplastic laws. The red curve on (b) and (c) depicts measurements at Dome C using [Veres et al., 2013; Bazin et al., 2013; Bréant et al., 2017]. The blue, green and brown solid lines represent the different textures tested with $n = 1$ for the anisotropic viscoplastic contact law. The black line is the isotropic viscoplastic contact law with $n = 3$.

implemented for the isotropic viscoplastic law with $n = 3$ and $\mu_{basal} = 2.1 \cdot 10^9 \text{ Pa}^3\text{s}$ (values from Frost & Ashby [1982]). This model is represented by the black solid line in Fig. 6.3b-c. Its use here gives a time of densification in the right order of magnitude compared to measurements, without any fit of the viscosity. However, the beginning of the curve does not have the correct shape. The strain rate (defined by $\dot{\epsilon}_{zz} = -\frac{\dot{\rho}}{\rho}$) of Dome C is surprisingly well simulated by this law in the range $0.64 < \rho < 0.77 \text{ g.cm}^{-3}$ (shown Fig. 6.3c).

Measurements show a continuous decrease of the axial strain rate while simulations that only take a linear hardening into account lead to a constant or even to an increase of the axial strain rate after 500 years. Texture A has consistently larger strain rates than F and E. When density reaches 0.8 g.cm^{-3} , the competition between density and increase of

the stress leads to an increase of the strain rate, while measurements depict a continuous drop. As the imposed stress increases with density, the viscosity should evolve during densification but was chosen constant in this example. Further studies could adopt a linear formulation at the beginning of the densification (see Fig. 6.3b-c) and then change the stress exponent accordingly to the increase of stress.

Improvements could also be made to the DEM code in order to take into account additional mechanisms to dislocation creep: diffusion effects such as grain growth, diffusion creep (see Fig. 1.3.4) or recrystallization. However these require the derivation of contact laws for forces that are far from being obvious.

Implementation of the anisotropic model in the IGE firn densification model

The firn densification model used in the IGE laboratory takes into account the coupling of simplified mechanisms as grain rearrangement and pressure sintering [Arnaud et al., 2000] with thermal gradient and diffusion inside the firn [Goujon et al., 2003]. The thesis of Bréant [2017] focused on improving the model with a sensitive study of the temperature by adjusting activation energies but also took into account soluble impurities that soften the firn. The modeled Δ_{age} gas-ice was reduced compared to previous estimations for East Antarctica polar sites (Dome C, Vostok and Dome Fuji) with significant repercussions for the phasing of temperature and gas concentrations in ice cores [Bréant et al., 2017]. This led to a better agreement of the modeled Δ_{age} gas-ice with data at very cold sites with low accumulation rates. Taking into account the evolution of textures of polar firn as we demonstrated that it has an effect on densification could enhance the densification model of the IGE. Including a parameter that would be appropriately tuned depending on the texture of the polar site studied should be an improvement.

Bibliography

Bibliography

- Agnolin, I. & Roux, J.-N. (2007). Internal states of model isotropic granular packings. I. Assembling process, geometry, and contact networks. *Phys. Rev. E*, 76, 61302. (Cited on page [172](#).)
- Ahmad, S., Shearwood, C., & Whitworth, R. (1992). Dislocation multiplication mechanisms in ice. *Physics and Chemistry of ice*, (pp. 492–496). (Cited on page [16](#).)
- Ahmed, M., Anchukaitis, K. J., Asrat, A., Borgaonkar, H. P., Braida, M., Buckley, B. M., Büntgen, U., Chase, B. M., Christie, D. A., Cook, E. R., et al. (2013). Continental-scale temperature variability during the past two millennia. *Nature geoscience*, 6(5), 339. (Cited on page [3](#).)
- Ahrens, J., Geveci, B., Law, C., Hansen, C., & Johnson, C. (2005). Paraview: An end-user tool for large-data visualization. *The visualization handbook*, 717. (Cited on page [134](#).)
- Allais, L., Bornert, M., Bretheau, T., & Caldemaison, D. (1994). Experimental characterization of the local strain field in a heterogeneous elastoplastic material. *Acta Metallurgica et Materialia*, 42(11), 3865–3880. (Cited on pages [47](#), [48](#), and [49](#).)
- Allen, S. M. & Cahn, J. W. (1972). Ground state structures in ordered binary neighbor interactions. *Acta Metallurgica*, 20(March), 423–433. (Cited on page [161](#).)
- Alley, R. (1987). Firn Densification By Grain-Boundary Sliding : a First Model. *Le Journal de Physique Colloques*, 48(C1), C1–249–C1–256. (Cited on pages [5](#), [28](#), and [39](#).)
- Alley, R. B. (1992). Flow-law hypothesis for ice-sheet modeling. *Journal of Glaciology*, 38(129), 245–256. (Cited on page [25](#).)
- Alley, R. B., Bolzan, J. F., & Whillans, I. M. (1982). Polar firn densification and grain growth. *Annals of Glaciology*, 3(415), 7–11. (Cited on page [121](#).)
- Alley, R. B. & Woods, G. A. (1996). Impurity influence on normal grain growth in the GISP2 ice core, Greenland. *Journal of Glaciology*, 52(141), 255–260. (Cited on pages [32](#) and [118](#).)

- Ammann, C. M., Joos, F., Schimel, D. S., Otto-bliesner, B. L., & Tomas, R. A. (2007). Solar influence on climate during the past millennium : Results from transient simulations with the NCAR Climate System Model. *Proceedings of the National Academy of Sciences*, 104(10), 3713–3718. (Cited on page 3.)
- Anderson, D. L. & Benson, C. S. (1963). The densification and diagenesis of snow. In W. Kingery (Ed.), *Ice and snow: properties, processes, and applications* chapter 30, (pp. 391–411). Cambridge, MA, MIT Press. (Cited on page 5.)
- Arnaud, L. (1997). *Modélisation de la transformation de la neige en glace à la surface des calottes polaires ; Etude du transport des gaz dans ces milieux poreux*. PhD thesis, Université Joseph Fourier - Grenoble 1. (Cited on pages 115, 118, 121, and 156.)
- Arnaud, L., Barnola, J. M., & Duval, P. (2000). Physical modeling of the densification of snow/firn and ice in the upper part of polar ice sheets. *Physics of Ice Core Records*. (Cited on pages 28, 29, 34, 70, and 211.)
- Arnaud, L., Lipenkov, V., Barnola, J., Gay, M., & Duval, P. (1998). Modelling of the densification of polar firn: characterization of the snow-firn transition. *Annals of Glaciology*, 26, 39–44. (Cited on pages 28 and 39.)
- Arthern, R. J., Vaughan, D. G., Rankin, A. M., Mulvaney, R., & Thomas, E. R. (2010). In situ measurements of Antarctic snow compaction compared with predictions of models. *Journal of Geophysical Research: Earth Surface*, 115(3), 1–12. (Cited on page 30.)
- Arzt, E. (1982). The influence of an increasing particle coordination on the densification of spherical powders. *Acta Materialia*, 30, 1883–1890. (Cited on pages 28 and 39.)
- Augustin, L., Barbante, C., & Barnes, P. (2004). Eight glacial cycles from an Antarctic ice core. *Nature*, (pp. 623–628). (Cited on pages 3 and 73.)
- Avizo (2017). Avizo lite 9.2.0. <https://www.fei.com/software/avizo-for-materials-science/>. (Cited on pages 147 and 148.)
- Aydin, M., Montzka, S. A., Battle, M. O., Williams, M. B., Bruyn, W. J. D., Butler, J. H., & Verhulst, K. R. (2010). Post-coring entrapment of modern air in some shallow ice cores collected near the firn-ice transition : evidence from CFC-12 measurements in Antarctic firn air and ice cores. *Atmospheric Chemistry and Physics*, 10, 5135–5144. (Cited on page 159.)
- Babin, P., Valle, G. D., Chiron, H., Cloetens, P., & Hoszowska, J. (2006). Fast X-ray tomography analysis of bubble growth and foam setting during breadmaking. *Journal of Cereal Science*, 43, 393–397. (Cited on page 89.)

- Babout, L., Marrow, T. J., Mummery, P. M., & Withers, P. J. (2006). Mapping the evolution of density in 3D of thermally oxidised graphite for nuclear applications. *Scripta Materialia*, 54(5), 829–834. (Cited on page 89.)
- Bader, H. (1964). *Density of ice as a function of temperature and stress*. Cold Regions Research and Engineering Laboratory, US Army Material Command. (Cited on pages 9 and 285.)
- Ballot, C. (2016). *Etude par tomographie de la densification d'un névé de Dôme C*. Technical report, Grenoble INP Phelma. (Cited on pages 80 and 83.)
- Barnett, M. R. (2003). A Taylor Model Based Description of the Proof Stress of Magnesium AZ31 during Hot Working. *Metallurgical and Materials Transactions A*, 34(9), 1799–1806. (Cited on page 22.)
- Barnola, J., Pierritz, R., Goujon, C., Duval, P., & Bollor, E. (2004). 3d reconstruction of the vostok firn structure by x-ray tomography. *Mater. Glyatsiol. Issled./Data Glaciol. Stud*, 97, 80–84. (Cited on pages 69, 70, 72, 74, and 75.)
- Barnola, J.-M., Pimienta, P., Raynaud, D., & Korotkevich, Y. S. (1991). CO₂-climate relationship as deduced from the Vostok ice core: a re-examination based on new measurements and on a re-evaluation of the air dating. *Tellus B*, 43(2), 83–90. (Cited on pages 3, 28, 29, and 70.)
- Baruchel, J., Philip, A., & Tafforeau, P. (2013). Nouvelles applications de l'imagerie aux rayons X en utilisant le rayonnement synchrotron. *Reflets de la physique*, (34-35), 32–37. (Cited on page 45.)
- Battle, M., Bender, M. L., Sowers, T., Tans, P. P., Butler, J., Elkins, J., Ellis, J., Conway, T. J., Zhang, N., Lang, P., & Clarke, A. (1996). Atmospheric gas concentrations over the past century measured in air from firn at the South Pole. *Nature*, 383. (Cited on page 3.)
- Battle, M. O., Severinghaus, J. P., Sofen, E. D., Plotkin, D., Orsi, A. J., Aydin, M., Montzka, S. A., Sowers, T., & Tans, P. P. (2011). Controls on the movement and composition of firn air at the West Antarctic Ice Sheet Divide. *Atmospheric Chemistry and Physics*, 11(21), 11007–11021. (Cited on page 74.)
- Bazin, L., Landais, A., Lemieux-Dudon, B., Toyé Mahamadou Kele, H., Veres, D., Parrenin, F., Martinerie, P., Ritz, C., Capron, E., Lipenkov, V., Loutre, M. F., Raynaud, D., Vinther, B., Svensson, A., Rasmussen, S. O., Severi, M., Blunier, T., Leuenberger, M., Fischer, H., Masson-Delmotte, V., Chappellaz, J., & Wolff, E. (2013). An optimized

- multi-proxy, multi-site Antarctic ice and gas orbital chronology (AICC2012): 120-800 ka. *Climate of the Past*, 9(4), 1715–1731. (Cited on pages 4, 30, 31, 151, and 210.)
- Bereiter, B., Eggleston, S., Schmitt, J., Nehrbass-ahles, C., Stocker, T. F., Fischer, H., Kipfstuhl, S., & Chappellaz, J. (2015). Revision of the EPICA Dome C CO₂ record from 800 to 600 kyr before present. *Geophysical Research Letters*, 42(2), 542–549. (Cited on pages 3 and 4.)
- Berger, R., Kloss, C., Kohlmeyer, A., & Pirker, S. (2015). Hybrid parallelization of the LIGGGHTS open-source DEM code. *Powder Technology*, 278, 234–247. (Cited on page 170.)
- Blackford, J. R. (2007). Sintering and microstructure of ice: a review. *Journal of Physics D: Applied Physics*, 40(21), R355–R385. (Cited on pages 26 and 27.)
- Bornert, M., Brémand, F., Doumalin, P., Dupré, J. C., Fazzini, M., Grédiac, M., Hild, F., Mistou, S., Molimard, J., Orteu, J. J., Robert, L., Surrel, Y., Vacher, P., & Wattrisse, B. (2009). Assessment of digital image correlation measurement errors: Methodology and results. *Experimental Mechanics*, 49(3), 353–370. (Cited on pages 53 and 54.)
- Bornert, M., Doumalin, P., & Maire, É. (2004). Mesure tridimensionnelle des champs de déformation par corrélation d’images microtomographiques. In *Colloque Photomécanique* (pp.33). (Cited on page 133.)
- Boulos, V., Fristot, V., Houzet, D., Salvo, L., & Lhuissier, P. (2013). Investigating performance variations of an optimized GPU-ported granulometry algorithm To cite this version : Investigating performance variations of an optimized GPU-ported granulometry algorithm. In *Design and Architectures for Signal and Image Processing (DASIP), 2012 Conference on, Oct 2012, Karlsruhe, Germany* (pp. 1–6). (Cited on pages 80, 81, 82, and 138.)
- Bourcier, M. (2012). *Étude multi-échelle des mécanismes de déformation ductile de polycristaux synthétiques de chlorure de sodium*. PhD thesis, Ecole Polytechnique. (Cited on page 47.)
- Bourcier, M., Bornert, M., Dimanov, A., Héripré, E., & Raphanel, J. L. (2013). Multiscale experimental investigation of crystal plasticity and grain boundary sliding in synthetic halite using digital image correlation. *Journal of Geophysical Research: Solid Earth*, 118(2), 511–526. (Cited on pages 49, 50, 59, and 63.)
- Brakke, K. (2013). Surface evolver. <http://facstaff.susqu.edu/brakke/evolver/evolver.html>. (Cited on page 162.)

- Bréant, C. (2017). *Variabilité régionale de la densification de la neige polaire lors des grandes transitions climatiques*. PhD thesis, Université Paris Saclay. (Cited on page 211.)
- Bréant, C., Martinerie, P., Orsi, A., Arnaud, L., & Landais, A. (2017). Modelling the firn thickness evolution during the last deglaciation: constraints on sensitivity to temperature and impurities. *Climate of the Past*, 13, 833–853. (Cited on pages 6, 29, 30, 31, 74, 210, and 211.)
- Bretin, E. (2009). *Mouvements par courbure moyenne et méthode de champs de phase*. PhD thesis, Institut Polytechnique de Grenoble. (Cited on page 204.)
- Bretin, É., Denis, R., Flin, F., Oudet, É., & Roussillon, T. (2015). *Discrete-Continuous approach for deformable partitions*. Technical report. (Cited on pages 161 and 162.)
- Brown, A. M. & Ashby, M. F. (1980). On the power-law creep equation. *Scripta Metallurgica*, 14, 1297–1302. (Cited on page 22.)
- Brown, R. L. (1980). A volumetric constitutive law for snow based on a neck growth model. *Journal of Applied Physics*, 51(1), 161–165. (Cited on page 39.)
- Buizert, C., Martinerie, P., Petrenko, V. V., Severinghaus, J. P., Trudinger, C. M., Witrant, E., Rosen, J. L., Orsi, A. J., Rubino, M., Etheridge, D. M., Steele, L. P., Hogan, C., Laube, J. C., Sturges, W. T., Levchenko, V. A., Smith, A. M., Levin, I., Conway, T. J., Dlugokencky, E. J., Lang, P. M., Kawamura, K., Jenk, T. M., White, J. W. C., Sowers, T., Schwander, J., & Blunier, T. (2012). Gas transport in firn: Multiple-tracer characterisation and model intercomparison for NEEM, Northern Greenland. *Atmospheric Chemistry and Physics*, 12(9), 4259–4277. (Cited on pages 10, 69, and 109.)
- Burr, A., Noël, W., Trecourt, P., Bourcier, M., Gillet-Chaulet, F., Philip, A., & Martin, C. L. (2017). The anisotropic contact response of viscoplastic monocrystalline ice particles. *Acta Materialia*, 132, 576–585. (Cited on pages 37 and 203.)
- Calonne, N. (2014). *Physique des métamorphoses de la neige sèche : de la microstructure aux propriétés macroscopiques*. PhD thesis, Université de Grenoble. (Cited on pages 72 and 206.)
- Calonne, N., Flin, F., Geindreau, C., Lesaffre, B., & Rolland du Roscoat, S. (2014). Study of a temperature gradient metamorphism of snow from 3-D images : time evolution of microstructures , physical properties and their associated anisotropy. *The Cryosphere*, 8, 2255–2274. (Cited on pages 78 and 127.)

- Calonne, N., Flin, F., Morin, S., Lesaffre, B., Roscoat, S. R., & Geindreau, C. (2011). Numerical and experimental investigations of the effective thermal conductivity of snow. *Geophysical Research Letters*, 38(August), 1–6. (Cited on page 205.)
- Calonne, N., Geindreau, C., Flin, F., Morin, S., Lesaffre, B., Rolland Du Roscoat, S., & Charrier, P. (2012). 3-D image-based numerical computations of snow permeability: Links to specific surface area, density, and microstructural anisotropy. *Cryosphere*, 6(5), 939–951. (Cited on page 205.)
- Camborde, F., Mariotti, C., & Donzé, F. V. (2000). Numerical study of rock and concrete behaviour by discrete element modelling. *Computers and Geotechnics*, 27, 225–247. (Cited on page 169.)
- Capolo, L. (2007). *Contribution à l'étude des hétérogénéités de déformation viscoplastique de la glace Ih mono et multi cristalline : essais de compression in-situ sous rayonnement X*. PhD thesis, Université Joseph Fourier - Grenoble 1. (Cited on pages 19, 159, and 161.)
- Cast3m (2015). Cast3m 2015. <http://www-cast3m.cea.fr/>. (Cited on page 133.)
- Castelnau, O. (1996). *Modelisation du comportement mécanique de la glace polycristalline par une approche auto-cohérente ; application au développement de textures dans les glaces des calottes polaires*. PhD thesis, Université Joseph Fourier - Grenoble 1. (Cited on pages 19 and 22.)
- Castelnau, O., Canova, G. R., Lebensohn, R. A., & Duval, P. (1997). Modelling viscoplastic behavior of anisotropic polycrystalline ice with a self-consistent approach. *Acta Materialia*, 45(11), 4823–4834. (Cited on page 19.)
- Chambers, J. M., Cleveland, W. S., Kleiner, B., Tukey, P. A., et al. (1983). *Graphical methods for data analysis*, volume 5. Wadsworth Belmont, CA. (Cited on page 113.)
- Chandel, C., Srivastava, P. K., & Mahajan, P. (2014). Micromechanical analysis of deformation of snow using X-ray tomography. *Cold Regions Science and Technology*, 101, 14–23. (Cited on page 128.)
- Chapelle, S. D. L., Castelnau, O., Lipenkov, V., & Duval, P. (1998). Dynamic recrystallization and texture development in ice as revealed by the study of deep ice cores in Antarctica and Greenland. *Journal of Geophysical Research*, 103(B3), 5091–5105. (Cited on page 143.)
- Chauve, T. (2017a). Aita toolbox. <https://github.com/ThomasChauve/aita>. (Cited on pages 95, 115, and 265.)

- Chauve, T. (2017b). *La recristallisation dynamique dans les matériaux anisotropes*. PhD thesis, Communauté Université Grenoble Alpes. (Cited on pages 26, 53, and 255.)
- Chauve, T., Montagnat, M., Barou, F., Hidas, K., Tommasi, A., & Mainprice, D. (2017a). Investigation of nucleation processes during dynamic recrystallization of ice using cryo-EBSD. *Philosophical Transactions of the Royal Society A: Mathematical, Physical and Engineering Sciences*, 375(2086), 20150345. (Cited on pages 52, 56, 122, and 159.)
- Chauve, T., Montagnat, M., Piazzolo, S., Journaux, B., Wheeler, J., Barou, F., Mainprice, D., & Tommasi, A. (2017b). Non-basal dislocations should be accounted for in simulating ice mass flow. *Earth and Planetary Science Letters*, 473, 247–255. (Cited on page 19.)
- Chauve, T., Montagnat, M., & Vacher, P. (2015). Strain field evolution during dynamic recrystallization nucleation; A case study on ice. *Acta Materialia*. (Cited on pages 52, 56, 143, and 161.)
- Chevy, J., Louchet, F., Duval, P., & Fivel, M. (2012). Creep behaviour of ice single crystals loaded in torsion explained by dislocation cross-slip. *Philosophical Magazine Letters*, 92(6), 262–269. (Cited on pages 16, 41, and 66.)
- Chu, T. C., Ranson, W. F., & Sutton, M. A. (1985). Applications of digital-image-correlation techniques to experimental mechanics. *Experimental Mechanics*, 25(3), 232–244. (Cited on page 47.)
- Cleary, P. & Sawley, M. L. (1999). Three-dimensional modelling of industrial granular flows. *Second international conference on CFD in the minerals and process industries*, 12(December), 95–100. (Cited on page 169.)
- Coble, R. L. (1958). Initial Sintering of Alumina and Hematite. *Journal of the American Ceramic Society*, 41(2), 55–62. (Cited on page 184.)
- Colbeck, S. (1983). Theory of Metamorphism of Dry Snow. *Journal of Geophysical Research*, 88(C9), 5475–5482. (Cited on page 5.)
- Coléou, C., Lesaffre, B., Brzoska, J. B., Ludwig, W., & Bollor, E. (2001). Three-dimensional snow images by X-ray microtomography. *Annals of Glaciology*, 32, 75–81. (Cited on pages 69, 71, and 72.)
- COMSOL (2013). Comsol multiphysics 5.2.0. <https://www.comsol.com>. (Cited on page 288.)

- Courville, Z., Hörhold, M., Hopkins, M., & Albert, M. (2010). Lattice-Boltzmann modeling of the air permeability of polar firn. *Journal of Geophysical Research: Earth Surface*, 115(4), 1–11. (Cited on page [71](#).)
- Courville, Z. R., Albert, M. R., Fahnestock, M. A., Cathles, I. M., & Shuman, C. A. (2007). Impacts of an accumulation hiatus on the physical properties of firn at a low-accumulation polar site. *Journal of Geophysical Research: Earth Surface*, 112(2), 1–11. (Cited on page [102](#).)
- Cummings, E., Johnson, J., & Brinkerhoff, D. (2013). Development of a finite element firn densification model for converting volume changes to mass changes. c, 9. (Cited on page [30](#).)
- Cundall, P. a. & Strack, O. D. L. (1979). A discrete numerical model for granular assemblies. (Cited on page [169](#).)
- Daudin, R., Terzi, S., Lhuissier, P., Tamayo, J., Scheel, M., Babu, N. H., Eskin, D. G., & Salvo, L. (2017). Particle-induced morphological modification of Al alloy equiaxed dendrites revealed by sub-second in situ microtomography. *Acta Materialia*, 125, 303–310. (Cited on page [147](#).)
- Del Río, M. S. & Dejus, R. J. (2011). Xop v2. 4: recent developments of the x-ray optics software toolkit. In *Proc. SPIE*, volume 8141 (pp. 814115). (Cited on page [289](#).)
- Derjaguin, B., Muller, V., & Toporov, Y. (1994). Effect of contact deformations on the adhesion of particles. *Progress in Surface Science*, 45(3), 131–143. (Cited on page [171](#).)
- Diprinzio, C. L., Wilen, L. A., Alley, R. B., Fitzpatrick, J. J., Spencer, M. K., & Gow, A. J. (2005). Fabric and texture at Siple Dome , Antarctica. *Journal of Glaciology*, 51(173), 281–290. (Cited on page [24](#).)
- Doake, C. & Wolff, E. (1985). Flow law for ice in polar ice sheets. *Nature*, 314(21), 255–257. (Cited on pages [22](#) and [66](#).)
- Domine, F., Albert, M., Huthwelker, T., Jacobi, H.-W., Kokhanovsky, A. A., Lehning, M., Picard, G., & Simpson, W. R. (2008). Snow physics as relevant to snow photochemistry. *Atmospheric Chemistry and Physics*, 8(2), 171–208. (Cited on page [83](#).)
- Doube, M., Kłosowski, M. M., Arganda-Carreras, I., Cordelières, F. P., Dougherty, R. P., Jackson, J. S., Schmid, B., Hutchinson, J. R., & Shefelbine, S. J. (2010). Bonej: free and extensible bone image analysis in imagej. *Bone*, 47(6), 1076–1079. (Cited on page [103](#).)

- Doumalin, P. (2000). *Microextensométrie locale par corrélation d'images numériques. Application aux études micromécaniques par microscopie à balayage*. PhD thesis, Ecole Polytechnique. (Cited on pages [47](#) and [52](#).)
- Durand, G., Gagliardini, O., Thorsteinsson, T., Svensson, A., Kipfstuhl, J., & Dahl-Jensen, D. (2006a). Ice microstructure and fabric : an up-to-date approach for measuring textures. *Journal of Glaciology*, 52(179), 1–12. (Cited on page [121](#).)
- Durand, G., Gillet-Chaulet, F., Svensson, A., Gagliardini, O., Kipfstuhl, S., Meyssonier, J., Parrenin, F., Duval, P., & Dahl-Jensen, D. (2007). Change in ice rheology during climate variations – implications for ice flow modelling and dating of the EPICA Dome C core. *Climate of the Past*, 3(1998), 155–167. (Cited on pages [24](#) and [39](#).)
- Durand, G., Persson, A., Samyn, D., & Svensson, A. (2008). Relation between neighbouring grains in the upper part of the NorthGRIP ice core - Implications for rotation recrystallization. *Earth and Planetary Science Letters*, 265(3-4), 666–671. (Cited on page [25](#).)
- Durand, G., Svensson, A., Persson, A., Gagliardini, O., Gillet-Chaulet, F., Sjolte, J., Montagnat, M., & Dahl-Jensen, D. (2009). Evolution of the texture along the EPICA Dome C ice core. *Low Temperature Science*, 68, 91–105. (Cited on pages [24](#), [25](#), [116](#), and [121](#).)
- Durand, G., Weiss, J., Lipenkov, V., Barnola, J. M., Krinner, G., Parrenin, F., Delmonte, B., Ritz, C., Duval, P., Röthlisberger, R., & Bigler, M. (2006b). Effect of impurities on grain growth in cold ice sheets. *Journal of Geophysical Research: Earth Surface*, 111(1), 1–18. (Cited on pages [32](#) and [74](#).)
- Duva, J. M. & Crow, P. D. (1994). Analysis of consolidation of reinforced materials by power-law creep. *Mechanics of Materials*, 17(1), 25–32. (Cited on page [291](#).)
- Duval, P., Ashby, M. F., & Andermant, I. (1983). Rate-Controlling Processes in the Creep of Polycrystalline Ice. *Journal of Physical Chemistry*, 87(1), 4066–4074. (Cited on pages [18](#), [32](#), [39](#), [41](#), [59](#), [62](#), [66](#), and [194](#).)
- Duval, P. & Castelnau, O. (1995). Dynamic Recrystallization of Ice in Polar Ice Sheets. *Journal de Physique IV*, 5(C3), 197–203. (Cited on pages [143](#) and [161](#).)
- Ebinuma, T. & Maeno, N. (1985). Experimental studies on densification and pressure-sintering of ice. *Annals Of Glaciology*, 6, 83–86. (Cited on pages [39](#) and [128](#).)

- Ebinuma, T. & Maeno, N. (1987). Particle Rearrangement and dislocation creep in a snow-densification process. *Le Journal de Physique Colloques*, 48(C1), C1–263–C1–269. (Cited on pages [128](#) and [138](#).)
- Ebner, P. P., Grimm, S. A., Schneebeli, M., & Steinfeld, A. (2014). An instrumented sample holder for time-lapse microtomography measurements of snow under advective airflow. *Geoscientific Instrumentation, Methods and Data Systems*, 3(2), 179–185. (Cited on pages [72](#) and [127](#).)
- Ebner, P. P., Schneebeli, M., & Steinfeld, A. (2015). Tomography-based monitoring of isothermal snow metamorphism under advective conditions. *The Cryosphere*, 9(4), 1363–1371. (Cited on pages [72](#) and [127](#).)
- Enting, I. G. (1993). Statistics of firn closure: a simulation study. *Journal of Glaciology*, 39(131), 133–142. (Cited on page [12](#).)
- Fabre, A., Barnola, J. M., Arnaud, L., & Chappellaz, J. (2000). Determination of gas diffusivity in polar firn: Comparison between experimental measurements and inverse modeling. *Geophysical Research Letters*, 27(4), 557–560. (Cited on pages [109](#) and [122](#).)
- Fischer, H., Severinghaus, J., Brook, E., Wolff, E., Albert, M., Alemany, O., Arthern, R., & Bentley, C. (2013). Where to find 1.5 million yr old ice for the IPICS “ Oldest-Ice ” ice core. *Climate of the Past*, 9, 2489–2505. (Cited on page [3](#).)
- Fleck, N. (1995). On the cold compaction of powders. *Journal of the Mechanics and Physics of Solids*, 43(9), 1409–1431. (Cited on page [169](#).)
- Fletcher, N. H. (1970). The chemical physics of ice. *The Chemical Physics of Ice*, by NH Fletcher, Cambridge, UK: Cambridge University Press, 2009. (Cited on pages [15](#) and [40](#).)
- Flin, F. & Brzoska, J. B. (2008). The temperature-gradient metamorphism of snow: Vapour diffusion model and application to tomographic images. *Annals of Glaciology*, 49(1), 17–21. (Cited on pages [127](#) and [144](#).)
- Flin, F., Brzoska, J.-B., Lesaffre, B., Coléou, C., & Pieritz, R. A. (2003). Full three-dimensional modelling of curvature-dependent snow metamorphism: first results and comparison with experimental tomographic data. *Journal of Physics D: Applied Physics*, 36(10A), A49–A54. (Cited on pages [26](#), [70](#), [72](#), and [144](#).)
- Flin, F., Brzoska, J. B., Lesaffre, B., Coléou, C., & Pieritz, R. A. (2004). Three-dimensional geometric measurements of snow microstructural evolution under isothermal conditions. *Annals of Glaciology*, 38, 39–44. (Cited on pages [26](#), [127](#), and [144](#).)

- Flin, F., Calonne, N., Denis, R., Caneill, R., Lesaffre, B., Dufour, A., Philip, A., Roulle, J., Roscoat, S. R., & Geindreau, C. (2015). 3D Growth Rates from Tomographic Images : Local Measurements for a Better Understanding of Snow Metamorphism - Application to Isothermal Metamorphism and Comparison with a Phase-Field Model. In *American Geophysical Union (AGU) Fall Meeting: American Geophysical Union (AGU) Fall Meeting*, San Fransisco, USA, 14-18 December, 2015. (Cited on pages [161](#) and [204](#).)
- Fourteau, K. (2019). *Physique de la fermeture des pores dans le névé polaire, implications pour la compréhension des rétroactions passées entre cycle du carbone et climat, in progress*. PhD thesis, Communauté Université Grenoble Alpes. (Cited on pages [74](#) and [205](#).)
- Fourteau, K., Faïn, X., Martinerie, P., Landais, A., Ekaykin, A. A., Lipenkov, V. Y., & Chappellaz, J. (2017). Analytical constraints on layered gas trapping and smoothing of atmospheric variability in ice under low accumulation conditions. *Climate of the Past Discussions*, 2017, 1–28. (Cited on page [30](#).)
- Freitag, J., Dobrindt, U., & Kipfstuhl, J. (2002). A new method for predicting transport properties of polar firn with respect to gases on the pore-space scale. *Annals of Glaciology*, 35, 538–544. (Cited on page [71](#).)
- Freitag, J., Kipfstuhl, S., & Faria, S. (2008). The connectivity of crystallite agglomerates in low-density firn at Kohnen station, Dronning Maud Land, Antarctica. *Annals of Glaciology*, 49(1), 114–120. (Cited on page [71](#).)
- Freitag, J., Kipfstuhl, S., & Laepple, T. (2013a). Core-scale radiosopic imaging : a new method reveals density – calcium link in Antarctic firn. 59(218), 1009–1014. (Cited on page [72](#).)
- Freitag, J., Kipfstuhl, S., Laepple, T., & Wilhelms, F. (2013b). Impurity-controlled densification: A new model for stratified polar firn. *Journal of Glaciology*, 59(218), 1163–1169. (Cited on page [30](#).)
- Freitag, J., Wilhelms, F., & Kipfstuhl, S. (2004). Microstructure-dependent densification of polar firn derived from X-ray microtomography. *Journal of Glaciology*, 50(169), 243–250. (Cited on pages [32](#), [70](#), [71](#), and [74](#).)
- Frost, H. J. & Ashby, M. F. (1982). *Deformation mechanism maps: the plasticity and creep of metals and ceramics*. Pergamon press. (Cited on pages [32](#) and [210](#).)

- Fujita, S., Okuyama, J., Hori, A., & Hondoh, T. (2009). Metamorphism of stratified firn at Dome Fuji, Antarctica: A mechanism for local insolation modulation of gas transport conditions during bubble close off. *Journal of Geophysical Research*, 114, 1–21. (Cited on pages 70 and 74.)
- Gagliardini, O. (1999). *Simulation numérique d'un écoulement bidimensionnel de glace polaire présentant une anisotropie induite évolutive*. PhD thesis, Université Joseph Fourier - Grenoble 1. (Cited on page 21.)
- Gagliardini, O. & Meyssonier, A. (1997). Flow simulation of a firn-covered cold glacier. *Annals of Glaciology*, 24, 242–248. (Cited on page 291.)
- Gagliardini, O., Zwinger, T., Durand, G., Favier, L., Fleurian, B. D., Greve, R., & Malinen, M. (2013). Capabilities and performance of Elmer / Ice, a new-generation ice sheet model. *Geoscience Model Development*, 6, 1299–1318. (Cited on page 63.)
- Gammon, P. H., Kieft, H., Clouter, M. J., & Dennert, W. W. (1983). Elastic constants of artificial and natural ice samples by Brillouin spectroscopy. *Journal of Glaciology*, 29(103), 433–460. (Cited on pages 15, 177, and 186.)
- Gaspar, N. (2010). A granular material with a negative poisson's ratio. *Mechanics of Materials*, 42(7), 673–677. (Cited on page 190.)
- Gaume, J., Herwijnen, A. V., Chambon, G., Birkeland, K., Schweizer, J., & Gaume, J. (2015). Modeling of crack propagation in weak snowpack layers using the discrete element method. *The Cryosphere*, 9, 1915–1932. (Cited on page 169.)
- Gautier, E., Savarino, J., Erbland, J., Lanciki, A., & Possenti, P. (2016). Variability of sulfate signal in ice core records based on five replicate cores. *Climate of the Past*, 12(1), 103–113. (Cited on page 73.)
- Gay, M. & Weiss, J. (1999). Automatic reconstruction of polycrystalline ice microstructure from image analysis: Application to the EPICA ice core at Dome Concordia, Antarctica. *Journal of Glaciology*, 45(151), 547–554. (Cited on pages 118, 120, and 121.)
- Gaye, A. (2015). *Analyse multi-échelle des mécanismes de déformation du sel gemme par mesures de champs surfaciques et volumiques*. PhD thesis, Université Paris-Est. (Cited on pages 47 and 133.)
- GeoDict (2014). Geodict 2014 - porodict module. <https://www.math2market.de/>. (Cited on page 106.)

- Gerland, S., Oerter, H., Kipfstuhl, J., Wilhelms, F., Miller, H., & Miners, W. D. (1999). Density log of a 181 m long ice core from Berkner Island, Antarctica. *Annals of Glaciology*, 29, 215–219. (Cited on page 32.)
- Gibaud, R. (2017). *Application of the Discrete Element Method to finite elastic strain in Multi-Materials*. PhD thesis, Communauté Université Grenoble Alpes. (Cited on page 199.)
- Gibbs, J., Mohan, K. A., Gulsoy, E., Shahani, A., Xiao, X., Bouman, C., De Graef, M., & Voorhees, P. (2015). The Three-Dimensional Morphology of Growing Dendrites. *Scientific reports*, (pp. 1–9). (Cited on page 147.)
- Gillet-Chaulet, F. (2006). *Modélisation de l'écoulement de la glace polaire anisotrope et premières applications au forage de Dôme C*. PhD thesis, Université Joseph Fourier - Grenoble 1. (Cited on pages 19 and 63.)
- Gillet-Chaulet, F., Gagliardini, O., Meyssonier, J., Montagnat, M., & Castelnau, O. (2005). A user-friendly anisotropic flow law for ice-sheet modeling A user-friendly anisotropic flow law for ice-sheet modelling. *Journal of Glaciology*, 51(172), 3–14. (Cited on pages 23 and 63.)
- Gillet-Chaulet, F., Hindmarsh, R. C. A., Corr, H. F. J., King, E. C., & Jenkins, A. (2011). In-situ quantification of ice rheology and direct measurement of the Raymond Effect at Summit , Greenland using a phase-sensitive radar. *Geophysical Research Letters*, 38, 1–6. (Cited on page 66.)
- Goujon, C., Barnola, J.-M., & Ritz, C. (2003). Modeling the densification of polar firn including heat diffusion: Application to close-off characteristics and gas isotopic fractionation for Antarctica and Greenland sites. *Journal of Geophysical Research: Atmospheres*, 108(D24), n/a–n/a. (Cited on pages xviii, 9, 10, 11, 29, 69, 88, 90, 109, 110, 111, 112, 122, 123, 165, 203, 205, 211, 283, and 284.)
- Gow, A. (1969). On the rates of growth of grains and crystals in south polar firn. *Journal of Glaciology*, 8(53), 241–252. (Cited on pages 120, 121, and 156.)
- Gow, A. J. (1968). Bubbles and bubble pressures in Antarctic glacier ice. *Journal of Glaciology*, 7(50), 167–182. (Cited on page 141.)
- Gregory, S. A., Albert, M. R., & Baker, I. (2014). Impact of physical properties and accumulation rate on pore close-off in layered firn. *Cryosphere*, 8(1), 91–105. (Cited on pages 32, 70, 73, 74, 75, 84, 90, 102, 103, 104, 105, and 123.)

- Grennerat, F. (2011). *Hétérogénéités de déformation au cours du fluage transitoire de la glace polycristalline*. PhD thesis, Université de Grenoble. (Cited on page [53](#).)
- Grennerat, F., Montagnat, M., Castelnau, O., Vacher, P., Moulinec, H., Suquet, P., & Duval, P. (2012). Experimental characterization of the intragranular strain field in columnar ice during transient creep. *Acta Materialia*, 60(8), 3655–3666. (Cited on page [52](#).)
- Hagenmuller, P., Calonne, N., Chambon, G., Flin, F., Geindreau, C., & Naaïm, M. (2014). Characterization of the snow microstructural bonding system using the minimum cut density. *Cold Regions Science and Technology*, 108, 72–79. (Cited on page [178](#).)
- Hagenmuller, P., Chambon, G., & Naaïm, M. (2015). Microstructure-based modeling of snow mechanics: a discrete element approach. *The Cryosphere*, 9, 1969–1982. (Cited on pages [39](#), [169](#), and [178](#).)
- Hammonds, K., Lieb-lappen, R., Courville, Z., Song, A., Wang, X., & Baker, I. (2014). Laboratory investigations on the thermophysical properties of the ice-snow interface while under a controlled temperature gradient. In *Proceedings, International Snow Science Workshop, Banff* (pp. 35–42). (Cited on pages [71](#), [78](#), and [127](#).)
- Harthong, B., Jérïer, J.-F., Dorémus, P., Imbault, D., & Donzé, F.-V. (2009). Modeling of high-density compaction of granular materials by the Discrete Element Method. *International Journal of Solids and Structures*, 46(18-19), 3357–3364. (Cited on page [209](#).)
- Hegerl, G. C., Hasselmann, K., Cubasch, U., Mitchell, J. F. B., Roeckner, E., Voss, R., & Waszkewitz, J. (1997). Climate Dynamics Multi-fingerprint detection and attribution analysis of greenhouse gas, greenhouse gas-plus-aerosol and solar forced climate change. *Climate Dynamics*, 13, 613–634. (Cited on page [3](#).)
- Herron, M. M. & Langway, C. C. J. (1980). Firn densification: an empirical model. *Journal of Glaciology*, 25(93), 373–385. (Cited on pages [28](#), [30](#), [39](#), and [70](#).)
- Hertz, H. (1882). Ueber die Berührung fester elastischer Körper. *Journal für die reine und angewandte Mathematik (Crelle's Journal)*, 1882, 156–171. (Cited on pages [171](#) and [176](#).)
- Higashi, A., Koinuma, S., & Mae, S. (1964). Plastic Yielding in Ice Single Crystals. *Japanese Journal of Applied Physics*, 3(10), 610–616. (Cited on pages [16](#) and [41](#).)
- Higashi, A., Nakawo, M., & Enomoto, H. (1983). The bubble close-off density of ice in Antarctica ice sheets. *Memoirs of National Institute of Polar Research. Special Issue*, 29, 135–148. (Cited on page [10](#).)

- Hildebrand, T. & Rüegsegger, P. (1997). A new method for the model-independent assessment of thickness in three-dimensional images. *Journal of Microscopy*, 185(1), 67–75. (Cited on pages [104](#) and [105](#).)
- Hobbs, P. V. & Radke, L. F. (1967). The role of volume diffusion in the metamorphism of snow. *Journal of Glaciology*, 6(48), 879–891. (Cited on page [26](#).)
- Hondoh, T. (2000). Nature and behavior of dislocations in ice. *Physics of Ice Core Records*, (pp. 3–24). (Cited on pages [16](#) and [17](#).)
- Honeycombe, R. W. K. (1975). The plastic deformation of metals. (Cited on page [56](#).)
- Hörhold, M. (2010). *The layering of polar firn*. PhD thesis, Bremen University. (Cited on page [32](#).)
- Hörhold, M. W., Albert, M. R., & Freitag, J. (2009). The impact of accumulation rate on anisotropy and air permeability of polar firn at a high-accumulation site. *Journal of Glaciology*, 55(192), 625–630. (Cited on page [71](#).)
- Hörhold, M. W., Kipfstuhl, S., Wilhelms, F., Freitag, J., & Frenzel, A. (2011). The densification of layered polar firn. *Journal of Geophysical Research: Earth Surface*, 116(1), 1–15. (Cited on pages [32](#), [70](#), and [74](#).)
- Hörhold, M. W., Laepple, T., Freitag, J., Bigler, M., Fischer, H., & Kipfstuhl, S. (2012). On the impact of impurities on the densification of polar firn. *Earth and Planetary Science Letters*, 325–326, 93–99. (Cited on pages [5](#), [30](#), and [207](#).)
- Hosford, W. F. (2010). *Mechanical behavior of materials*. Cambridge University Press. (Cited on page [156](#).)
- Johnson, J. B. & Hopkins, M. A. (2005). Identifying microstructural deformation mechanisms in snow using discrete-element modeling. *Journal of Glaciology*, 51(174), 432–442. (Cited on pages [169](#), [177](#), and [178](#).)
- Johnson, K. L. (1987). *Contact mechanics*. Cambridge university press. (Cited on pages [44](#), [171](#), and [180](#).)
- Johnson, K. L., Kendall, K., & Roberts, A. D. (1971). Surface Energy and the Contact of Elastic Solids. *Proceedings of the Royal Society A: Mathematical, Physical and Engineering Sciences*, 324(1558), 301–313. (Cited on pages [171](#) and [178](#).)
- Jones, S. J. & Glen, J. W. (1969). The mechanical properties of single crystals of pure ice. *Journal of Glaciology*, 8(54), 463–473. (Cited on page [18](#).)

- Jouzel, J., Masson-Delmotte, V., Cattani, O., Dreyfus, G., Falourd, S., Hoffmann, G., Minster, B., Nouet, J., Barnola, J.-M., Chappellaz, J., Fischer, H., Gallet, J.-C., Johnsen, S., Leuenberger, M., Loulergue, L., Luethi, D., Oerter, H., Parrenin, F., Raisbeck, G., Raynaud, D., Schilt, A., Schwander, J., Selmo, E., Souchez, R., Spahni, R., Stauffer, B., Steffensen, J. P., Stenni, B., Stocker, T. F., Tison, J. L., Werner, M., & Wolff, E. W. (2007). Orbital and Millennial Antarctic Climate Variability over the Past 800,000 Years. *Science*, 317, 793–796. (Cited on page 3.)
- Kaempfer, T. U. & Schneebeli, M. (2007). Observation of isothermal metamorphism of new snow and interpretation as a sintering process. *Journal of Geophysical Research*, 112(D24), D24101. (Cited on pages 79, 103, and 127.)
- Kallel, A. (2013). *Compaction à chaud de nanopoudres SiGe : du process aux propriétés thermoélectriques : Hot pressing of thermoelectric materials for high temperature energy harvesting*. PhD thesis, Université de Grenoble. (Cited on pages 184 and 209.)
- Kamb, W. B. (1961). The glide direction in ice. *Journal of Glaciology*, 3(30), 1097–1106. (Cited on page 19.)
- Kanit, T. & Forest, S. (2003). Determination of the size of the representative volume element for random composites: statistical and numerical approach. *International Journal of solids and structures*, 40(13), 3647–3679. (Cited on pages 92 and 93.)
- Kanit, T., N’Guyen, F., Forest, S., Jeulin, D., Reed, M., & Singleton, S. (2006). Apparent and effective physical properties of heterogeneous materials: Representativity of samples of two materials from food industry. *Computer Methods in Applied Mechanics and Engineering*, 195(33-36), 3960–3982. (Cited on page 93.)
- Kerbrat, M., Pinzer, B., Huthwelker, T., Gäggeler, H. W., Ammann, M., & Schneebeli, M. (2007). Measuring the specific surface area of snow with X-ray tomography and gas adsorption: comparison and implications for surface smoothness. *Atmospheric Chemistry and Physics Discussions*, 7(4), 10287–10322. (Cited on page 127.)
- King, E. C. & Jarvis, E. P. (2007). Use of Shear Waves to Measure Poisson’s Ratio in Polar Firn. *Journal of Environmental & Engineering Geophysics*, 12(1), 15–21. (Cited on pages 189 and 190.)
- Kipfstuhl, S., Faria, S. H., Azuma, N., Freitag, J., Hamann, I., Kaufmann, P., Miller, H., Weiler, K., & Wilhelms, F. (2009). Evidence of dynamic recrystallization in polar firn. *Journal of Geophysical Research: Solid Earth*, 114(5), 1–10. (Cited on pages 25, 118, 121, and 122.)

- Kloss, C., Goniva, C., Hager, A., Amberger, S., & Pirker, S. (2012). Models, algorithms and validation for opensource DEM and CFD-DEM. *Progress in Computational Fluid Dynamics*, 12(2-3), 140–152. (Cited on pages [170](#) and [171](#).)
- Koenderink, J. J. & Doorn, A. J. V. (1992). Surface shape and curvature scales. *Image Vision Comput.*, 10(8), 557–564. (Cited on pages [144](#) and [147](#).)
- Kozicki, J. & Donzé, F. V. (2009). YADE-OPEN DEM : an open-source software using a discrete element method to simulate granular material. *Engineering Computations*, 26(7), 786–805. (Cited on page [171](#).)
- Kumar, R., Rommel, S., Jauffrès, D., Lhuissier, P., & Martin, C. L. (2016). Effect of packing characteristics on the discrete element simulation of elasticity and buckling. *International Journal of Mechanical Sciences*, 110, 14–21. (Cited on page [190](#).)
- Landais, A., Barnola, J. M., Kawamura, K., Caillon, N., Delmotte, M., Van Ommen, T., Dreyfus, G., Jouzel, J., Masson-Delmotte, V., Minster, B., Freitag, J., Leuenberger, M., Schwander, J., Huber, C., Etheridge, D., & Morgan, V. (2006). Firn-air $\delta^{15}\text{N}$ in modern polar sites and glacial-interglacial ice: A model-data mismatch during glacial periods in Antarctica? *Quaternary Science Reviews*, 25(1-2), 49–62. (Cited on pages [30](#), [32](#), [71](#), [73](#), [74](#), [87](#), [88](#), [90](#), [108](#), [109](#), [123](#), [203](#), and [284](#).)
- Landais, A., Dreyfus, G., Capron, E., Jouzel, J., Masson-Delmotte, V., Roche, D. M., Prié, F., Caillon, N., Chappellaz, J., Leuenberger, M., Laurantou, A., Parrenin, F., Raynaud, D., & Teste, G. (2013). Two-phase change in CO₂, Antarctic temperature and global climate during Termination II. *Nature Geoscience*, 6(12), 1062–1065. (Cited on page [3](#).)
- Landais, A., Dreyfus, G., Capron, E., Pol, K., Loutre, M. F., Raynaud, D., Lipenkov, V. Y., Arnaud, L., Masson-delmotte, V., Paillard, D., Jouzel, J., & Leuenberger, M. (2012). Towards orbital dating of the EPICA Dome C ice core using $\delta\text{O}_2/\text{N}_2$. *Climate of the Past*, 8, 191–203. (Cited on page [159](#).)
- Landauer, J. K. (1958). The Creep of Snow under Combined Stress. *Journal of Rheology*, 2(1), 175. (Cited on page [128](#).)
- Lantuéjoul, C. (1991). Ergodicity and integral range. *Journal of Microscopy*, 161(3), 387–403. (Cited on page [93](#).)
- Leballeur, M. L., Picard, G., Mialon, A., Arnaud, L., Lefebvre, E., & Possenti, P. (2015). Modeling L-band brightness temperature at Dome C, Antarctica and comparison with

- SMOS observations. *IEEE Transactions on Geoscience and Remote Sensing*, 53(7), 4022–4032. (Cited on page [283](#).)
- Lebensohn, R. A., Montagnat, M., Mansuy, P., Duval, P., Meysonnier, J., & Philip, A. (2009). Modeling viscoplastic behavior and heterogeneous intracrystalline deformation of columnar ice polycrystals. *Acta Materialia*, 57(5), 1405–1415. (Cited on pages [22](#) and [56](#).)
- Lebensohn, R. A. & Tomé, C. N. (1993). A self-consistent anisotropic approach for the simulation of plastic deformation and texture development of polycrystals : application to zirconium alloys. *Acta Metallurgica et Materialia*, 41(9), 2611–2624. (Cited on page [22](#).)
- Li, J. & Zwally, H. J. (2011). Modeling of firn compaction for estimating ice-sheet mass change from observed ice-sheet elevation change. *Annals of Glaciology*, 52(59), 1–7. (Cited on page [30](#).)
- Lide, D. R. et al. (1947). Crc handbook of chemistry and physics. *12J204*. (Cited on page [5](#).)
- Linow, S., Hörhold, M. W., & Freitag, J. (2012). Grain-size evolution of polar firn: a new empirical grain growth parameterization based on X-ray microcomputer tomography measurements. *Journal of Glaciology*, 58(212), 1245–1252. (Cited on pages [71](#) and [83](#).)
- Lipenkov, V. Y., Salamatin, A. N., & Duval, P. (1997). Bubbly-ice densification in ice sheets: II. Applications. *Journal of Glaciology*, 43(145), 397–407. (Cited on pages [22](#), [115](#), and [141](#).)
- Lomonaco, R., Albert, M., & Baker, I. (2011). Microstructural evolution of fine-grained layers through the firn column at Summit, Greenland. *Journal of Glaciology*, 57(204), 755–762. (Cited on pages [32](#), [70](#), [71](#), and [74](#).)
- Lorensen, W. E. & Cline, H. E. (1987). Marching cubes: A high resolution 3d surface construction algorithm. In *ACM siggraph computer graphics*, volume 21 (pp. 163–169).: ACM. (Cited on page [83](#).)
- Loulergue, L., Schilt, A., Spahni, R., Masson-Delmotte, V., Blunier, T., Lemieux, B., Barnola, J.-M., Raynaud, D., Stocker, T. F., & Chappellaz, J. (2008). Orbital and millennial-scale features of atmospheric CH₄ over the past 800,000 years. *Nature Letters*, 453(May), 383–386. (Cited on page [3](#).)

- Löwe, H., Spiegel, J. K., & Schneebeli, M. (2011). Interfacial and structural relaxations of snow under isothermal conditions. *Journal of Glaciology*, 57(203), 499–510. (Cited on page 71.)
- Lowe, P. R. & Ficke, J. M. (1974). *The computation of saturation vapor pressure*. Technical Report March. (Cited on page 78.)
- Lu, C.-Y., Tang, C.-L., Chan, Y.-C., Hu, J.-C., & Chi, C.-C. (2014). Forecasting landslide hazard by the 3D discrete element method : A case study of the unstable slope in the Lushan hot spring district, central Taiwan. *Engineering Geology*, 183, 14–30. (Cited on page 169.)
- Ludwig, W., Schmidt, S., Lauridsen, E. M., & Poulsen, H. F. (2008). X-ray diffraction contrast tomography : a novel technique for three-dimensional grain mapping of polycrystals . I . Direct beam case. *Journal of Applied Crystallography*, 41, 302–309. (Cited on page 207.)
- Lüthi, D., Bereiter, B., Stauffer, B., Winkler, R., Schwander, J., Kindler, P., Leuenberger, M., Kipfstuhl, S., Capron, E., Landais, A., et al. (2010). Co₂ and o₂/n₂ variations in and just below the bubble-clathrate transformation zone of antarctic ice cores. *Earth and planetary science letters*, 297(1), 226–233. (Cited on page 6.)
- Lüthi, D., Le Floch, M., Bereiter, B., Blunier, T., Barnola, J.-m., Siegenthaler, U., Raynaud, D., Jouzel, J., Fischer, H., Kawamura, K., & Stocker, T. F. (2008). High-resolution carbon dioxide concentration record. *Nature Letters*, 453(May), 379–382. (Cited on page 3.)
- Maeno, N. & Ebinuma, T. (1983). Pressure Sintering of Ice and Its Implication to the Densification of Snow at Polar Glaciers and Ice Sheets. *Journal Physical Chemistry*, 169(87), 4103–4110. (Cited on pages 5, 26, 32, 33, 34, and 158.)
- Mansuy, P. (2001). *Contribution à l'étude du comportement viscoplastique d'un multicristal de glace : hétérogénéité de la déformation et localisation, expériences et modèles*. PhD thesis, Université Joseph Fourier - Grenoble 1. (Cited on pages 19, 22, 46, and 56.)
- Mansuy, P., Meyssonier, J., & Philip, A. (1999). Modelling the ice single-crystal Viscoplastic Behaviour. *Advances in cold-region thermal . . .* (Cited on pages 46 and 247.)
- Mansuy, P., Meyssonier, J., & Philip, A. (2002). Localization of deformation in polycrystalline ice: experiments and numerical simulations with a simple grain model. *Computational Materials Science*, 25(1-2), 142–150. (Cited on pages 19, 41, 42, 62, 247, 249, and 251.)

- Mansuy, P., Philip, A., & Meyssonier, J. (2001). Localization of deformation in polycrystalline ice. *Journal of Physics IV*, 11, 267–274. (Cited on page [21](#).)
- Martín, C., Gudmundsson, G. H., Pritchard, H. D., & Gagliardini, O. (2009). On the effects of anisotropic rheology on ice flow, internal structure, and the age-depth relationship at ice divides. *Journal of Geophysical Research: Earth Surface*, 114(4), 1–18. (Cited on page [39](#).)
- Martin, C. F., Josserond, C., Salvo, L., Blandin, J. J., Cloetens, P., & Boller, E. (2000). Characterization by X-ray micro-tomography of cavity coalescence during superplastic deformation. *Scripta Materialia*, 42(4), 375–381. (Cited on page [89](#).)
- Martin, C. L. & Bordia, R. K. (2008). Influence of adhesion and friction on the geometry of packings of spherical particles. *Phys. Rev. E*, 77, 31307. (Cited on page [177](#).)
- Martin, C. L., Bouvard, D., & Shima, S. (2003). Study of particle rearrangement during powder compaction by the Discrete Element Method. *Journal of the Mechanics and Physics of Solids*, 51(4), 667–693. (Cited on pages [169](#), [173](#), and [189](#).)
- Martin, C. L., Schneider, L. C. R., Olmos, L., & Bouvard, D. (2006). Discrete element modeling of metallic powder sintering. *Scripta Materialia*, 55, 425–428. (Cited on page [169](#).)
- Martin, G., Sinclair, C. W., & Lebensohn, R. A. (2014). Microscale plastic strain heterogeneity in slip dominated deformation of magnesium alloy containing rare earth. *Materials Science and Engineering A*, 603(March), 37–51. (Cited on pages [22](#) and [47](#).)
- Martin, G., Sinclair, C. W., & Schmitt, J. H. (2013). Plastic strain heterogeneities in an Mg-1Zn-0.5Nd alloy. *Scripta Materialia*, 68(9), 695–698. (Cited on page [47](#).)
- Martinerie, P. (2017). personal communication. (Cited on pages [74](#), [110](#), and [111](#).)
- Martinerie, P., Lipenkov, V. Y., & Raynaud, D. (1990). Correction of air-content measurements in polar ice for the effect of cut bubbles at the surface of the sample. *Journal of Glaciology*, 36(124), 299–303. (Cited on pages [9](#), [109](#), [110](#), and [122](#).)
- Martinerie, P., Lipenkov, V. Y., Raynaud, D., Chappellaz, J., & Lorius, C. (1994). Air content paleo record in the Vostok ice core (Antarctica): A mixed record of climatic and glaciological parameters. *Journal of Geophysical Research*, 99(D5), 10565–10576. (Cited on pages [9](#), [69](#), [88](#), [123](#), and [203](#).)
- Martinerie, P., Raynaud, D., Etheridge, D. M., Barnola, J. M., & Mazaudier, D. (1992). Physical and climatic parameters which influence the air content in polar ice. *Earth*

- and *Planetary Science Letters*, 112(1-4), 1–13. (Cited on pages [9](#), [69](#), [88](#), [90](#), [106](#), [107](#), [108](#), [110](#), [112](#), [123](#), and [203](#).)
- Masson-Delmotte, V., Dreyfus, G., Braconnot, P., Johnsen, S., Jouzel, J., Kageyama, M., Landais, A., Loutre, M.-F., Nouet, J., Parrenin, F., Raynaud, D., Steni, B., & Tüenter, E. (2006). Temperature reconstructions from Antarctic ice cores of the Past. Past temperature reconstructions from deep ice cores : relevance for future climate change. *Climate of the Past*, 2, 145–165. (Cited on page [3](#).)
- Mellor, M. & James, H. (1967). Instructions for use Creep of Snow and Ice. *US Army Cold Regions Research and Engineering Laboratory*, (pp. 843–855). (Cited on page [156](#).)
- Mesarovic, S. D. & Fleck, N. A. (1999). Spherical indentation of elastic-plastic solids. *Proceedings of the Royal Society of London A: Mathematical, Physical and Engineering Sciences*, 455(1987), 2707–2728. (Cited on page [171](#).)
- Meussen, B., Mahrenholtz, O., & Oerter, H. (1999). Creep of polar firn. *Cold Regions Science and Technology*, 29, 177–200. (Cited on pages [128](#) and [129](#).)
- Meyssonier, J. & Philip, A. (1996). A model for the tangent viscous behaviour of anisotropic polar ice. *Annals of Glaciology*, 23, 253–261. (Cited on pages [14](#), [19](#), [41](#), [62](#), and [247](#).)
- Meyssonier, J. & Philip, A. (1999). Remarks on Self-Consistent Modelling of Polycrystalline Ice. *Advances in cold-region thermal engineering sciences, technological, environmental and climatological impact, Lecture Notes in Physics*, 533, 225–236. (Cited on page [19](#).)
- Michael, M. (2014). *A Discrete Approach to Described the Kinematics between Snow and a Tire Tread*. PhD thesis, Université du Luxembourg. (Cited on page [169](#).)
- MiDi, G. (2004). On dense granular flows. *European Physical Journal E-Soft Matter*, 14(4). (Cited on page [172](#).)
- Milliancourt, L. (2017). *Effective properties of the firn and the porous ice from Dome C ice core: Thermal conductivity, diffusion, permeability, elasticity*. Technical report, Grenoble INP ENSE3. (Cited on pages [93](#), [205](#), and [206](#).)
- Mitchell, L. E., Buizert, C., Brook, E. J., Breton, D. J., Fegyveresi, J., Baggenstos, D., Orsi, A., Severinghaus, J., Alley, R. B., Albert, M., Rhodes, R. H., McConnell, J. R., Sigl, M., Maselli, O., Gregory, S., & Ahn, J. (2015). Observing and modeling the influence of layering on bubble trapping in polar firn. *Journal of Geophysical Research*

- Atmospheres*, 120(6), 2558–2574. (Cited on pages [xviii](#), [10](#), [11](#), [69](#), [71](#), [109](#), [110](#), [111](#), [112](#), [122](#), [123](#), [165](#), [283](#), and [284](#).)
- Montagnat, M. (2001). *Contribution à l'étude du comportement viscoplastique des glaces des calottes polaires : Modes de déformation et simulation du développement des textures*. PhD thesis, Université Joseph Fourier - Grenoble 1. (Cited on page [22](#).)
- Montagnat, M., Azuma, N., Dahl-Jensen, D., Eichler, J., Fujita, S., Gillet-Chaulet, F., Kipfstuhl, S., Samyn, D., Svensson, A., & Weikusat, I. (2014). Fabric along the NEEM ice core, Greenland, and its comparison with GRIP and NGRIP ice cores. *The Cryosphere*, 8(4), 1129–1138. (Cited on pages [24](#) and [25](#).)
- Montagnat, M., Blackford, J. R., Piazzolo, S., Arnaud, L., & Lebensohn, R. A. (2011). Measurements and full-field predictions of deformation heterogeneities in ice. *Earth and Planetary Science Letters*, 305(1-2), 153–160. (Cited on pages [39](#) and [161](#).)
- Montagnat, M., Buiron, D., Arnaud, L., Broquet, A., Schlitz, P., Jacob, R., & Kipfstuhl, S. (2012). Measurements and numerical simulation of fabric evolution along the Talos Dome ice core, Antarctica. *Earth and Planetary Science Letters*, 357, 168–178. (Cited on page [25](#).)
- Montagnat, M., Chauve, T., Barou, F., Tommasi, A., Beausir, B., & Fressengeas, C. (2015). Analysis of Dynamic Recrystallization of Ice from EBSD Orientation Mapping. *Frontiers in Earth Science*, 3(81), 1–13. (Cited on page [161](#).)
- Montagnat, M. & Duval, P. (2000). Rate controlling processes in the creep of polar ice, influence of grain boundary migration associated with recrystallization. *Earth and Planetary Science Letters*, 183(1-2), 179–186. (Cited on page [40](#).)
- Nakaya, U. (1958). *The deformation of single crystal of ice*. Technical report. (Cited on page [16](#).)
- Olsson, E. & Larsson, P. L. (2014). On the tangential contact behavior at elastic-plastic spherical contact problems. *Wear*, 319(1-2), 110–117. (Cited on page [171](#).)
- Orozco-Caballero, A., Lunt, D., Robson, J. D., & Quinta da Fonseca, J. (2017). How magnesium accommodates local deformation incompatibility : A high-resolution digital image correlation study. *Acta Materialia*, 133, 367–379. (Cited on page [22](#).)
- Orsi, A. J. (2017). personal communication. (Cited on pages [73](#), [74](#), [108](#), and [109](#).)
- Parrenin, F., Dreyfus, G., Durand, G., Fujita, S., Gagliardini, O., Gillet, F., Jouzel, J., Kawamura, K., Lhomme, N., Masson-Delmotte, V., Ritz, C., Schwander, J., Shoji, H.,

- Uemura, R., Watanabe, O., & Yoshida, N. (2007). Ice flow modelling at EPICA Dome C and Dome Fuji, East Antarctica. *Climate of the Past Discussions*, 3(1), 19–61. (Cited on page 4.)
- Passalacqua, O. (2017). *Localiser une archive glaciaire de 1.5 millions d'années par une approche multi-modèles*. PhD thesis, Communauté Université Grenoble Alpes. (Cited on page 3.)
- Peternell, M., Kohlmann, F., Wilson, C. J. L., Seiler, C., & Gleadow, A. J. W. (2009). A new approach to crystallographic orientation measurement for apatite fission track analysis: Effects of crystal morphology and implications for automation. *Chemical Geology*, 265(3-4), 527–539. (Cited on page 116.)
- Peternell, M., Russell-Head, D. S., & Wilson, C. J. L. (2011). A technique for recording polycrystalline structure and orientation during in situ deformation cycles of rock analogues using an automated fabric analyser. *Journal of Microscopy*, 242(2), 181–188. (Cited on page 116.)
- Peters, W. & Ranson, W. (1982). Digital imaging techniques in experimental stress analysis. *Optical Engineering*, 21(3), 427–431. (Cited on page 47.)
- Petit, J. R., Raynaud, D., Basile, I., Chappellaz, J., Ritz, C., Delmotte, M., Legrand, M., Lorius, C., & Pe, L. (1999). Climate and atmospheric history of the past 420,000 years from the Vostok ice core, Antarctica. *Nature*, 399, 429–436. (Cited on page 3.)
- Petrenko, V. F. & Whitworth, R. W. (1999). *Physics of ice*. (Cited on pages 12, 13, 19, 39, 41, 56, and 59.)
- Philip, A., Capolo, L., Meyssonier, J., & Baruchel, J. (2015). Inception and movement of a 'subgrain boundary precursor' in ice under an applied stress, observed by X-ray synchrotron radiation Bragg imaging. *Journal of Applied Crystallography*, 48, 672–678. (Cited on page 19.)
- Pimienta, P. & Duval, P. (1987). Rate controlling processes in the creep of polar glacier ice. *Journal de Physique*, 48, 243–248. (Cited on pages 22, 29, 33, and 156.)
- Proudhon, H., Li, J., Reischig, P., Guéninchault, N., Forest, S., & Ludwig, W. (2016). Coupling Diffraction Contrast Tomography with the Finite Element Method. *Advanced Engineering Materials*, 18(6), 903–912. (Cited on page 207.)
- Radjai, F. & Dubois, F. (2011). *Discrete-element modeling of granular materials*. Wiley-Iste. (Cited on pages 170 and 171.)

- Rasp, T., Kraft, T., & Riedel, H. (2013). Discrete element study on the influence of initial coordination numbers on sintering behaviour. *Scripta Materialia*, 69(11-12), 805–808. (Cited on page [169](#).)
- Raynaud, D., Delmas, R., Ascencio, J. M., & Legrand, M. (1982). Gas extraction from polar ice cores: a critical issue for studying the evolution of atmospheric CO₂ and ice-sheet surface elevation. *Annals of Glaciology*, 3, 265–268. (Cited on pages [10](#) and [69](#).)
- Raynaud, D. & Lebel, B. (1979). Total gas content and surface elevation of polar ice sheets. *Nature*, 281(5729), 289–291. (Cited on page [10](#).)
- Reischig, P., King, A., Nervo, L., Viganó, N., Guilhem, Y., Palenstijn, W. J., Batenburg, K. J., Preuss, M., & Ludwig, W. (2013). Advances in X-ray diffraction contrast tomography: Flexibility in the setup geometry and application to multiphase materials. *Journal of Applied Crystallography*, 46(2), 297–311. (Cited on page [207](#).)
- Rolland du Roscoat, S., Decain, M., Thibault, X., Geindreau, C., & Bloch, J. F. (2007). Estimation of microstructural properties from synchrotron X-ray microtomography and determination of the REV in paper materials. *Acta Materialia*, 55(8), 2841–2850. (Cited on pages [71](#) and [93](#).)
- Rolland Du Roscoat, S., King, A., Philip, A., Reischig, P., Ludwig, W., Flin, F., & Meyssonier, J. (2011). Analysis of Snow Microstructure by Means of X-Ray Diffraction Contrast Tomography. *Advanced Engineering Materials*, 13(3), 128–135. (Cited on pages [39](#), [72](#), [128](#), [143](#), and [208](#).)
- Rommelaere, V., Arnaud, L., & Barnola, J.-M. (1997). Reconstructing recent atmospheric trace gas concentrations from polar firn and bubbly ice data by inverse methods. *Journal of Geophysical Research*, 102(D25), 30,069–30,083. (Cited on pages [69](#) and [110](#).)
- Roussel, D. (2015). *Optimisation d'architecture d'électrode poreuse pour pile à combustible à oxyde solide*. PhD thesis, Université de Grenoble. (Cited on page [184](#).)
- Roussel, D., Lichtner, A., Jauffrès, D., Villanova, J., Bordia, R. K., & Martin, C. L. (2016). Strength of hierarchically porous ceramics: Discrete simulations on x-ray nanotomography images. *Scripta Materialia*, 113, 250–253. (Cited on page [194](#).)
- Rubino, M., Etheridge, D. M., Trudinger, C. M., Allison, C. E., Battle, M. O., Langenfelds, R. L., Steele, L. P., Curran, M., Bender, M., White, J. W. C., Jenk, T. M., Blunier, T., & Francey, R. J. (2013). A revised 1000 year atmospheric d¹³C-CO₂ record from Law Dome and South Pole, Antarctica. *Journal of Geophysical Research: Atmospheres*, 118, 8482–8499. (Cited on page [3](#).)

- Salm, B. (1982). Mechanical properties of snow. *Reviews of Geophysics*, 20(1), 1–19. (Cited on page [39](#).)
- Salmon, P. L., Ohlsson, C., Shefelbine, S. J., & Doube, M. (2015). Structure model index does not measure rods and plates in trabecular bone. *Frontiers in Endocrinology*, 6(OCT), 1–10. (Cited on page [105](#).)
- Schaller, C. F., Freitag, J., & Eisen, O. (2017). Gas enclosure in polar firn follows universal law. *Climate of the Past Discussions*, 1, 1–12. (Cited on pages [xviii](#), [10](#), [11](#), [12](#), [69](#), [72](#), [109](#), [110](#), [111](#), [112](#), [122](#), and [283](#).)
- Schindelin, J., Arganda-carreras, I., Frise, E., Kaynig, V., Pietzsch, T., Preibisch, S., Rueden, C., Saalfeld, S., Schmid, B., Tinevez, J.-y., White, D. J., Hartenstein, V., Tomancak, P., & Cardona, A. (2013). Fiji - an Open Source platform for biological image analysis. *Nature Methods*, 9(7). (Cited on pages [46](#), [79](#), [119](#), and [255](#).)
- Schleef, S. & Löwe, H. (2013). X-ray microtomography analysis of isothermal densification of new snow under external mechanical stress. *Journal of Glaciology*, 59(214), 233–243. (Cited on pages [71](#), [72](#), [127](#), [129](#), and [138](#).)
- Schleef, S., Löwe, H., & Schneebeli, M. (2014). Hot-pressure sintering of low-density snow analyzed by X-ray microtomography and in situ microcompression. *Acta Materialia*, 71(JUNE 2014), 185–194. (Cited on pages [128](#) and [138](#).)
- Schneebeli, M. & Sokratov, S. A. (2004). Tomography of temperature gradient metamorphism of snow and associated changes in heat conductivity. *Hydrological Processes*, 18(September), 3655–3665. (Cited on pages [70](#), [71](#), [103](#), and [127](#).)
- Schulson, E. M., Duval, P., et al. (2009). *Creep and fracture of ice*, volume 1. Cambridge University Press Cambridge. (Cited on pages [14](#), [15](#), [19](#), [21](#), [41](#), [56](#), [128](#), [161](#), and [179](#).)
- Schwander, J. (1989). The Transformation of Snow to Ice and the Occlusion of Gases. In *The Environmental Record in Glaciers and Ice Sheets* (pp. 53–67). (Cited on pages [9](#), [11](#), [69](#), [109](#), and [122](#).)
- Schwander, J., Barnola, J.-M., Andri , C., Leuenberger, M., Ludin, A., Raynaud, D., & Stauffer, B. (1993). The age of the air in the firn and the ice at Summit, Greenland. *Journal of Geophysical Research*, 98(D2), 2831–2838. (Cited on pages [4](#), [7](#), [69](#), and [165](#).)
- Schwander, J., Sowers, T., Barnola, J.-M., Blunier, T., Fuchs, A., & Malaiz , B. (1997). Age scale of the air in the summit ice : Implication for glacial-interglacial temperature change. *Journal of Geophysical Research*, 102(D16), 19483–19493. (Cited on page [283](#).)

- Schwander, J. & Stauffer, B. (1984). Age difference between polar ice and the air trapped in its bubbles. *Nature*, 311(5981), 45–47. (Cited on pages 4, 10, and 69.)
- Schwander, J., Stauffer, B., & Sigg, A. (1988). Air mixing in firn and the age of the air at pore close-off. *Annals of Glaciology*, 10, 141–145. (Cited on pages 4 and 12.)
- Scott, G. D. & Kilgour, D. M. (1969). The density of random close packing of spheres. *Journal of Physics D: Applied Physics*, 2(6), 863. (Cited on page 5.)
- Severinghaus, J. P., Albert, M. R., Courville, Z. R., Fahnestock, M. A., Kawamura, K., Montzka, S. A., Mühle, J., Scambos, T. A., Shields, E., Shuman, C. A., Suwa, M., Tans, P., & Weiss, R. F. (2010). Deep air convection in the firn at a zero-accumulation site, central Antarctica. *Earth and Planetary Science Letters*, 293(3-4), 359–367. (Cited on pages 74 and 102.)
- Severinghaus, J. P. & Battle, M. O. (2006). Fractionation of gases in polar ice during bubble close-off: New constraints from firn air Ne, Kr and Xe observations. *Earth and Planetary Science Letters*, 244(1-2), 474–500. (Cited on pages 7, 9, 11, 69, 109, 122, and 165.)
- Shahani, A. J., Gulsoy, E. B., Roussochatzakis, V. J., Gibbs, J. W., Fife, J. L., & Voorhees, P. W. (2015). The dynamics of coarsening in highly anisotropic systems : Si particles in Al – Si liquids. *Acta Materialia*, 97, 325–337. (Cited on page 147.)
- Shapiro, L. H., Johnson, J. B., Sturm, M., & Blaisdell, G. L. (1997). *Snow Mechanics : Review of the State of Knowledge and Applications*. Technical report, CREEL Hanover NH. (Cited on page 15.)
- Solidworks (2013). Solidworks 2013 x64 edition. <http://www.solidworks.com>. (Cited on pages 77 and 288.)
- Sowers, T., Bender, M., Raynaud, D., & Korotkevich, Y. (1992). $\delta^{15}\text{N}$ of N_2 in air trapped in polar ice: A tracer of gas transport in the firn and a possible constraint on ice age-gas age differences. *Journal of Geophysical Research: Atmospheres*, 97(D14), 15683–15697. (Cited on page 5.)
- Spaulding, N., Meese, D., & Baker, I. (2011). Advanced microstructural characterization of four East Antarctic firn / ice cores. *Journal of Glaciology*, 57(205), 796–810. (Cited on page 25.)
- Stauffer, B., Schwander, J., & Oeschger, H. (1985). Enclosure of air during metamorphosis of dry firn to ice. *Annals of Glaciology*, 6(1), 108–112. (Cited on page 10.)

- Stephenson, P. J. (1967). Some Considerations of snow metamorphism in the Antarctic Ice Sheet in the Light of Ice Crystal Studies. *Physics of Snow and Ice : proceedings*, 1(2), 725–740. (Cited on page [121](#).)
- Storåkers, B., Biwa, S., & Larsson, P.-L. (1997). Similarity analysis of inelastic contact. *International Journal of Solids and Structures*, 34(24), 3061–3083. (Cited on pages [43](#), [44](#), [171](#), and [180](#).)
- Storåkers, B., Fleck, N., & McMeeking, R. (1999). The viscoplastic compaction of composite powders. *Journal of the Mechanics and Physics of Solids*, 47, 785–815. (Cited on pages [43](#), [61](#), [171](#), [179](#), and [209](#).)
- Stukowski, A. (2010). Visualization and analysis of atomistic simulation data with OVITO – the Open Visualization Tool. *Modelling and Simulation in Materials Science and Engineering*, 18. (Cited on page [198](#).)
- Sutton, M., Wolters, W., Peters, W., Ranson, W., & McNeill, S. (1983). Determination of displacements using an improved digital correlation method. *Image and Vision Computing*, 1(3), 133–139. (Cited on page [47](#).)
- Sweeney, S. M. & Martin, C. L. (2003). Pore size distributions calculated from 3-D images of DEM-simulated powder compacts. *Acta Materialia*, 51(12), 3635–3639. (Cited on page [184](#).)
- Tett, S. F. B., Stott, P. A., Allen, M. R., Ingram, W. J., & Mitchell, J. F. B. (1999). Causes of twentieth-century temperature change near the Earth’s surface. *Nature*, 399, 569–572. (Cited on page [3](#).)
- Theile, T., Löwe, H., Theile, T. C., & Schneebeli, M. (2011). Simulating creep of snow based on microstructure and the anisotropic deformation of ice. *Acta Materialia*, 59(18), 7104–7113. (Cited on pages [39](#), [71](#), [128](#), [138](#), and [178](#).)
- Thorsteinsson, T., Kipfstuhl, J., & Miller, H. (1997). Textures and fabrics in the GRIP ice core. *Journal of Geophysical Research*, 102(C12), 26583. (Cited on pages [24](#), [25](#), and [161](#).)
- Triconnet, K., Derrien, K., Hild, F., & Baptiste, D. (2009). Parameter choice for optimized digital image correlation. *Optics and Lasers in Engineering*, 47(6), 728–737. (Cited on page [53](#).)
- Trudinger, C. M., Enting, I. G., Etheridge, D. M., Francey, R., Levchenko, V. A., & Steele, L. P. (1997). Modeling air movement and bubble trapping in firn. *Journal of Geophysical Research*, 102(D6), 6747–6763. (Cited on pages [7](#), [69](#), [109](#), and [122](#).)

- Vedachalam, V. (2011). *Discrete Element Modelling Of Granular Snow Particles Using LIGGGHTS*. PhD thesis, The University of Edinburgh. (Cited on pages [177](#) and [178](#).)
- Veres, D., Bazin, L., Landais, A., Toyé Mahamadou Kele, H., Lemieux-Dudon, B., Parrenin, F., Martinerie, P., Blayo, E., Blunier, T., Capron, E., et al. (2013). The Antarctic ice core chronology (AICC2012): An optimized multi-parameter and multi-site dating approach for the last 120 thousand years. *Climate of the Past*, 9(4), 1733–1748. (Cited on pages [4](#), [30](#), [31](#), [151](#), and [210](#).)
- Verfaillie, D., Fily, M., Meur, E. L., Magand, O., Jourdain, B., Arnaud, L., & Favier, V. (2012). Snow accumulation variability derived from radar and firn core data along a 600 km transect in Adelie Land, East Antarctic plateau. *The Cryosphere*, 6, 1345–1358. (Cited on page [73](#).)
- Viganò, N., Tanguy, A., Hallais, S., Dimanov, A., Bornert, M., Batenburg, K. J., & Ludwig, W. (2016). Three-dimensional full-field X-ray orientation microscopy. *Scientific reports*, 6, 20618. (Cited on page [207](#).)
- Wang, X. & Baker, I. (2013). Observation of the microstructural evolution of snow under uniaxial compression using X-ray computed microtomography. *Journal of Geophysical Research: Atmospheres*, 118(22), 12,371–12,382. (Cited on pages [71](#), [127](#), [128](#), and [129](#).)
- Wang, Y., Kipfstuhl, S., Azuma, N., Thorsteinsson, T., & Miller, H. (2003). Ice-fabrics study in the upper 1500 m of the Dome C (East Antarctica) deep ice core. *Annals Of Glaciology*, 37(1), 97–104. (Cited on pages [24](#) and [116](#).)
- Wautier, A., Geindreau, C., & Flin, F. (2015). Linking snow microstructure to its macroscopic elastic stiffness tensor: A numerical homogenization method and its application to 3-D images from X-ray tomography. *Geophysical Research Letters*, 42(19), 8031–8041. (Cited on pages [71](#), [128](#), and [206](#).)
- Wautier, A., Geindreau, C., & Flin, F. (2017). Numerical homogenization of the viscoplastic behavior of snow based on X-ray tomography images. *The Cryosphere*, 11(3), 1465–1485. (Cited on pages [39](#), [128](#), and [206](#).)
- Weber, J. (1966). Recherches concernant les contraintes intergranulaires dans les milieux pulvérulents. *Bulletin de Liaison des Ponts-et-chaussées*, 20, 1–20. (Cited on page [173](#).)
- Wilkinson, D. (1988). A pressure-sintering model for the densification of polar firn and glacier ice. *Journal of Glaciology*, 34(116), 40–45. (Cited on page [32](#).)
- Wilkinson, D. S. & Ashby, M. F. (1975). Pressure sintering by power law creep. *Acta Metallurgica*, 23, 1277–1285. (Cited on pages [28](#) and [29](#).)

- Wittrant, E., Martinerie, P., Hogan, C., Laube, J. C., Kawamura, K., Capron, E., Montzka, S. A., Dlugokencky, E. J., Etheridge, D., Blunier, T., & Sturges, W. T. (2012). A new multi-gas constrained model of trace gas non-homogeneous transport in firn: Evaluation and behaviour at eleven polar sites. *Atmospheric Chemistry and Physics*, 12(23), 11465–11483. (Cited on pages [7](#), [10](#), [69](#), [74](#), [87](#), [109](#), and [122](#).)
- Xu, J., Qi, H., Fang, X., Lu, L., Ge, W., Wang, X., Xu, M., Chen, F., He, X., & Li, J. (2011). Quasi-real-time simulation of rotating drum using discrete element method with parallel GPU computing. *Particuology*, 9(4), 446–450. (Cited on page [169](#).)
- Zhu, H. P., Zhou, Z. Y., Yang, R. Y., & Yu, A. B. (2008). Discrete particle simulation of particulate systems: A review of major applications and findings. *Chem. Eng. Sci.*, 62, 5728–5770. (Cited on page [169](#).)
- Zwally, H. J. & Jun, L. (2002). Seasonal and interannual variations of firn densification and ice-sheet surface elevation at the Greenland summit. *Journal of Glaciology*, 48(161). (Cited on page [30](#).)

Appendices

Appendix A

The transverse isotropic viscoplastic law

A.1 Analytical description for the behaviour of ice single crystal

In this section, the general description of the non-linear transverse isotropic law for the viscoplastic behavior of ice is derived from [Meyssonnier & Philip \[1996\]](#). In sections [A.2](#) and [A.3](#), the cases of a uniaxial stress and of shearing are studied, as well as possible simplifications. To be consistent with previous publications [Meyssonnier & Philip \[1996\]](#); [Mansuy et al. \[1999, 2002\]](#), the model is described in a local reference frame (see [Fig. A.1](#)) named $\mathcal{R} = (\mathbf{x}, \mathbf{y}, \mathbf{z})$. A global reference frame associated to the crystal orientation $\bar{\mathcal{R}} = (\bar{\mathbf{x}}, \bar{\mathbf{y}}, \bar{\mathbf{z}})$, with the \mathbf{c} axis along \mathbf{z} is also used. We recall that the ratio of the axial viscosity along the \mathbf{c} axis to the axial viscosity normal to the \mathbf{c} axis is denominated α .

With respect to the local reference, the transverse isotropic law of ice writes [[Mansuy](#)

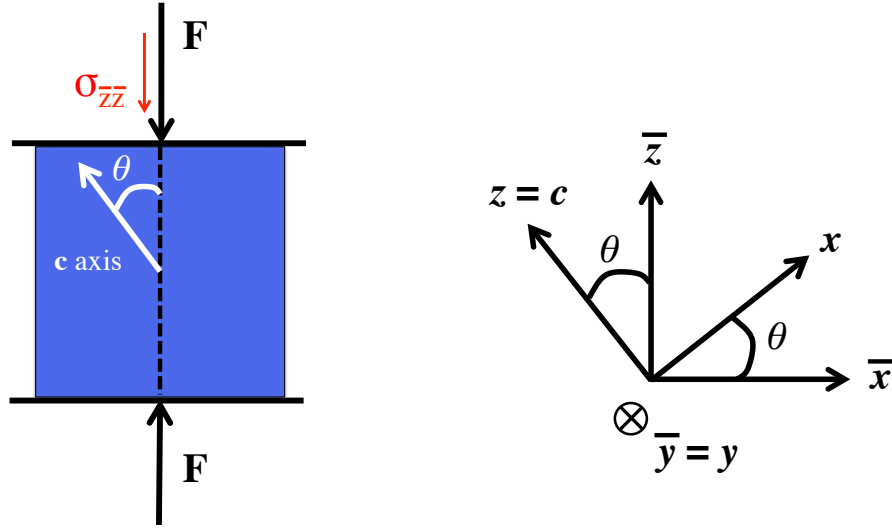


Figure A.1: Diagram of the test under a uniaxial load and with associated reference frame. \mathbf{c} axis is along \mathbf{z} .

et al., 2002]:

$$S_{xx} - S_{yy} = 2\eta_{xy}^*(D_{xx} - D_{yy}) \quad (\text{A.1})$$

$$S_{xx} = 2\eta_{xy}^*(D_{xx} - \frac{2}{3}(\alpha - 1)D_{zz}) \quad D_{xx} = \frac{1}{2\eta_{xy}^*}(S_{xx} + \frac{2(\alpha - 1)}{4\alpha - 1}S_{zz}) \quad (\text{A.2})$$

$$S_{yy} = 2\eta_{xy}^*(D_{yy} - \frac{2}{3}(\alpha - 1)D_{zz}) \quad D_{yy} = \frac{1}{2\eta_{xy}^*}(S_{yy} + \frac{2(\alpha - 1)}{4\alpha - 1}S_{zz}) \quad (\text{A.3})$$

$$S_{zz} = 2\eta_{xy}^* \left(\frac{4\alpha - 1}{3} \right) D_{zz} \quad \Leftrightarrow \quad D_{zz} = \frac{3S_{zz}}{2\eta_{xy}^*(4\alpha - 1)} \quad (\text{A.4})$$

$$S_{yz} = 2\eta_{xy}^*\beta D_{yz} \quad D_{yz} = \frac{S_{yz}}{2\eta_{xy}^*\beta} \quad (\text{A.5})$$

$$S_{zx} = 2\eta_{xy}^*\beta D_{zx} \quad D_{zx} = \frac{S_{zx}}{2\eta_{xy}^*\beta} \quad (\text{A.6})$$

$$S_{xy} = 2\eta_{xy}^* D_{xy} \quad D_{xy} = \frac{S_{xy}}{2\eta_{xy}^*} \quad (\text{A.7})$$

with D_{ij} the local strain rates components, S_{ij} the local deviatoric stress components and

η_{xy}^* an apparent shear viscosity in the basal plane that writes :

$$\eta_{xy}^* = A_n^{-1} \tau_{\diamond}^{1-n} \quad (\text{A.8})$$

with A_n a numerical fit parameter, n the stress exponent equal to 1 for a Newtonian flow (usually for low stresses < 0.1 MPa) and to 3 for laboratory experiments (for high stresses). τ_{\diamond} is given by [Mansuy et al., 2002]:

$$\tau_{\diamond}^2 = \frac{3}{4\alpha - 1} \tau_{ax}^2 + \tau_{\perp}^2 + \frac{\tau_{\parallel}^2}{\beta} \quad (\text{A.9})$$

The three terms that appear in the expression of τ_{\diamond}^2 write:

$$\tau_{ax}^2 = \frac{3}{4} S_{zz}^2 \quad (\text{A.10})$$

$$\tau_{\perp}^2 = \frac{(S_{xx} - S_{yy})^2}{4} + S_{xy}^2 \quad (\text{A.11})$$

$$\tau_{\parallel}^2 = S_{yz}^2 + S_{zx}^2 \quad (\text{A.12})$$

This leads to :

$$\eta_{xy}^* = A_n^{-1} \left(\frac{9S_{zz}^2}{4(4\alpha - 1)} + \frac{(S_{xx} - S_{yy})^2}{4} + S_{xy}^2 + \frac{S_{yz}^2 + S_{zx}^2}{\beta} \right)^{\frac{1-n}{2}} \quad (\text{A.13})$$

A.2 Case 1 : Simplifications for an applied uniaxial stress

In the global reference, the stress tensor of a uniaxial stress is simply:

$$\bar{\sigma} = \begin{pmatrix} 0 & 0 & 0 \\ 0 & 0 & 0 \\ 0 & 0 & \sigma_{\bar{z}\bar{z}} \end{pmatrix}_{(\bar{\mathbf{x}}, \bar{\mathbf{y}}, \bar{\mathbf{z}})} \quad (\text{A.14})$$

From the rotation matrix, one can deduce the stress tensor in the local reference :

$$\sigma = {}^t R \bar{\sigma} R \quad (\text{A.15})$$

with :

$$R = \begin{pmatrix} \cos(\theta) & 0 & -\sin(\theta) \\ 0 & 1 & 0 \\ \sin(\theta) & 0 & \cos(\theta) \end{pmatrix} \quad (\text{A.16})$$

$${}^t\mathbf{R} = \begin{pmatrix} \cos(\theta) & 0 & \sin(\theta) \\ 0 & 1 & 0 \\ -\sin(\theta) & 0 & \cos(\theta) \end{pmatrix} \quad (\text{A.17})$$

$$\boldsymbol{\sigma} = \begin{pmatrix} \sigma_{\bar{z}\bar{z}} \sin^2(\theta) & 0 & \sigma_{\bar{z}\bar{z}} \cos(\theta) \sin(\theta) \\ 0 & 0 & 0 \\ \sigma_{\bar{z}\bar{z}} \cos(\theta) \sin(\theta) & 0 & \sigma_{\bar{z}\bar{z}} \cos^2(\theta) \end{pmatrix}_{(\mathbf{x}, \mathbf{y}, \mathbf{z})} \quad (\text{A.18})$$

The deviatoric stress tensor is derived locally from the constitutive law thanks to the fluidity tensor \mathbf{N} . The strain rate tensor in the local reference $\mathbf{D}_{\text{Voigt}}$ is then derived as follows.

$$\mathbf{S} = \boldsymbol{\sigma} - \frac{\text{tr}(\boldsymbol{\sigma})}{3} \mathbf{I} \quad (\text{A.19})$$

$$\mathbf{S} = \sigma_{\bar{z}\bar{z}} \begin{pmatrix} -\frac{1}{3} \cos^2(\theta) + \frac{2}{3} \sin^2(\theta) & 0 & \cos(\theta) \sin(\theta) \\ 0 & -\frac{1}{3} \cos^2(\theta) - \frac{1}{3} \sin^2(\theta) & 0 \\ \cos(\theta) \sin(\theta) & 0 & \frac{2}{3} \cos^2(\theta) - \frac{1}{3} \sin^2(\theta) \end{pmatrix}_{(\mathbf{x}, \mathbf{y}, \mathbf{z})} \quad (\text{A.20})$$

With the Voigt notation, \mathbf{S} writes :

$$\mathbf{S}_{\text{Voigt}} = \sigma_{\bar{z}\bar{z}} \begin{pmatrix} -\frac{1}{3} \cos^2(\theta) + \frac{2}{3} \sin^2(\theta) \\ -\frac{1}{3} \cos^2(\theta) - \frac{1}{3} \sin^2(\theta) \\ \frac{2}{3} \cos^2(\theta) - \frac{1}{3} \sin^2(\theta) \\ 0 \\ \cos(\theta) \sin(\theta) \\ 0 \end{pmatrix}_{(\mathbf{x}, \mathbf{y}, \mathbf{z})} \quad (\text{A.21})$$

and \mathbf{N} :

$$\mathbf{N} = \frac{1}{2\eta_{xy}^*} \begin{pmatrix} 1 & 0 & \frac{2(\alpha-1)}{4\alpha-1} & 0 & 0 & 0 \\ 0 & 1 & \frac{2(\alpha-1)}{4\alpha-1} & 0 & 0 & 0 \\ \frac{2(\alpha-1)}{4\alpha-1} & \frac{2(\alpha-1)}{4\alpha-1} & \frac{2\alpha+1}{4\alpha-1} & 0 & 0 & 0 \\ 0 & 0 & 0 & \frac{2}{\beta} & 0 & 0 \\ 0 & 0 & 0 & 0 & \frac{2}{\beta} & 0 \\ 0 & 0 & 0 & 0 & 0 & 2 \end{pmatrix}_{(\mathbf{x}, \mathbf{y}, \mathbf{z})} \quad (\text{A.22})$$

$$\mathbf{D}_{\text{Voigt}} = \mathbf{N} \cdot \mathbf{S}_{\text{Voigt}} \quad (\text{A.23})$$

Using the Voigt notation, the strain rate tensor is:

$$\mathbf{D}_{\text{voigt}} = \frac{\sigma_{\bar{z}\bar{z}}}{2\eta_{xy}^*} \begin{pmatrix} -\frac{1}{3}(\cos^2(\theta) - 2\sin^2(\theta) - \frac{2(2\cos^2(\theta) - \sin^2(\theta))(\alpha-1)}{4\alpha-1}) \\ -\frac{1}{3}(\cos^2(\theta) + \sin^2(\theta) - \frac{2(2\cos^2(\theta) - \sin^2(\theta))(\alpha-1)}{4\alpha-1}) \\ \frac{2\cos^2(\theta) - \sin^2(\theta)}{(4\alpha-1)} \\ 0 \\ \frac{2\cos(\theta)\sin(\theta)}{\beta} \\ 0 \end{pmatrix}_{(\mathbf{x}, \mathbf{y}, \mathbf{z})} \quad (\text{A.24})$$

$$\bar{\mathbf{D}} = \mathbf{R}\mathbf{D}^t\mathbf{R} \quad (\text{A.25})$$

The strain rates tensor in the global reference thus writes:

$$D_{\bar{x}\bar{x}} = \frac{\sigma_{\bar{z}\bar{z}}}{2\eta_{xy}^*(4\alpha-1)} (-2\cos^4(\theta) - \sin^4(\theta) + 2\alpha\cos^2(\theta)\sin^2(\theta)) \quad (\text{A.26})$$

$$+ \frac{\sigma_{\bar{z}\bar{z}}}{2\eta_{xy}^*(4\alpha-1)} \left(-\frac{2(4\alpha-1)-\beta}{\beta} \cos^2(\theta)\sin^2(\theta) + \cos^2(\theta) \right) \quad (\text{A.27})$$

$$D_{\bar{y}\bar{y}} = -\frac{\sigma_{\bar{z}\bar{z}}}{6\eta_{xy}^*} \left(\cos^2(\theta) + \sin^2(\theta) - (2\cos^2(\theta) - \sin^2(\theta)) \left(\frac{2(\alpha-1)}{4\alpha-1} \right) \right) \quad (\text{A.28})$$

$$D_{\bar{z}\bar{z}} = \frac{\sigma_{\bar{z}\bar{z}}}{2\eta_{xy}^*(4\alpha-1)} \left(3\cos^4(\theta) + 2\alpha\sin^4(\theta) + \frac{2(4\alpha-1)-\beta}{\beta} \sin^2(\theta)\cos^2(\theta) - \cos^2\theta \right) \quad (\text{A.29})$$

$$D_{\bar{x}\bar{z}} = \frac{\sigma_{\bar{z}\bar{z}}}{2\eta_{xy}^*(4\alpha-1)} \cos(\theta)\sin(\theta) (\sin^2(\theta) - \cos^2(\theta)) \left(2\alpha + 1 - \frac{4\alpha-1}{\beta} \right) \quad (\text{A.30})$$

The case being in two dimensions, components $D_{\bar{x}\bar{y}} = D_{\bar{y}\bar{z}} = 0$. As axial viscosities are similar along the \mathbf{c} - axis and the basal plane [Mansuy et al., 2002], α is approximated to 1, hence :

$$D_{\bar{x}\bar{x}} = -\frac{\sigma_{\bar{z}\bar{z}}}{6\eta_{xy}^*} \left(1 + 6\frac{1-\beta}{\beta} \cos^2(\theta)\sin^2(\theta) \right) \quad (\text{A.31})$$

$$D_{\bar{y}\bar{y}} = -\frac{\sigma_{\bar{z}\bar{z}}}{6\eta_{xy}^*} \quad (\text{A.32})$$

$$D_{\bar{z}\bar{z}} = \frac{\sigma_{\bar{z}\bar{z}}}{6\eta_{xy}^*} 2 \left(1 + 3\frac{1-\beta}{\beta} \cos^2(\theta)\sin^2(\theta) \right) \quad (\text{A.33})$$

$$D_{\bar{x}\bar{z}} = \frac{\sigma_{\bar{z}\bar{z}}}{2\eta_{xy}^*} \cos(\theta)\sin(\theta)(\cos^2(\theta) - \sin^2(\theta)) \left(\frac{1-\beta}{\beta} \right) \quad (\text{A.34})$$

Figure A.2 displays the evolution of strain rates components in the global frame for a uniaxial stress and with $\beta = 0.01$, which value comes from Mansuy et al. [2002]. The

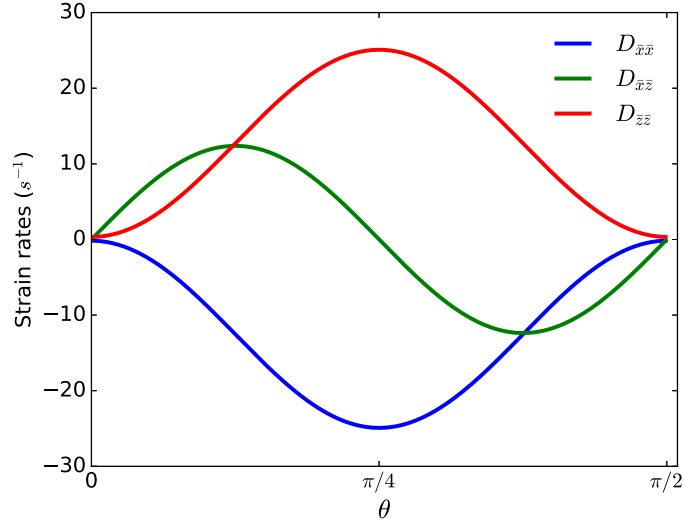


Figure A.2: Strain rates in the global reference in the uniaxial case for $n = 1$, $\sigma_{\bar{z}\bar{z}} = -1\text{Pa}$, $\alpha = 1$, $\beta = 0.01$ et $\eta_{xy}^* = \eta_{xy} = 1\text{Pa.s}$.

applied stress $\sigma_{\bar{z}\bar{z}}$ is set to -1Pa for compression, and $\eta_{xy}^* = \eta_{xy} = 1\text{Pa.s}$, which are arbitrary values. $D_{\bar{z}\bar{z}}$ and $D_{\bar{x}\bar{x}}$ are symmetrical with respect to $y = 0$. Both are respectively minimum and maximum at $\theta = \pi/4$. $D_{\bar{x}\bar{z}}$ is negative when $\theta < \pi/4$ and positive above. The shear component is significant, its maximum being more than half the maximum of $D_{\bar{x}\bar{x}}$, however it is totally neglected in the formulation of the anisotropic contact law in chapters 2 and 5.

A.3 Case 2 : Simplifications for an applied shear stress

For the case of an applied shear stress, the stress tensor writes:

$$\bar{\sigma} = \begin{pmatrix} 0 & 0 & \sigma_{\bar{x}\bar{z}} \\ 0 & 0 & 0 \\ \sigma_{\bar{x}\bar{z}} & 0 & 0 \end{pmatrix}_{(\bar{\mathbf{x}}, \bar{\mathbf{y}}, \bar{\mathbf{z}})} \quad (\text{A.35})$$

Using the same method from section A.2 for a uniaxial stress, the strain rate in the

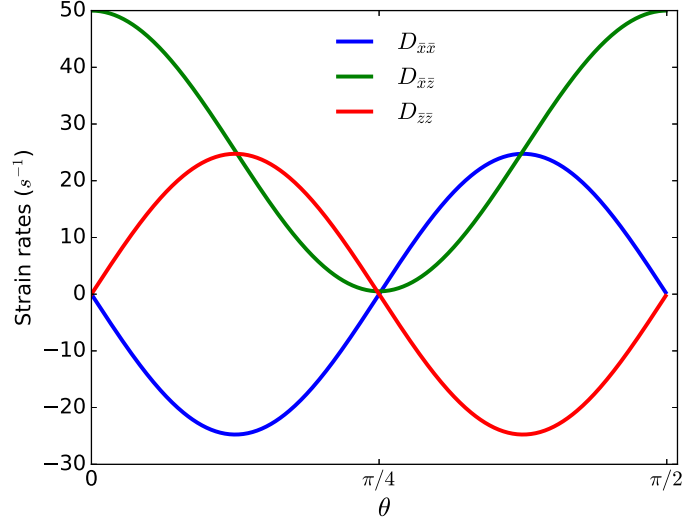


Figure A.3: Strain rates in the global reference in the shearing case for $n = 1$, $\sigma_{\bar{z}\bar{z}} = 1\text{Pa}$, $\alpha = 1$, $\beta = 0.01$ et $\eta_{xy}^* = \eta_{xy} = 1\text{Pa.s}$.

global frame is :

$$D_{\bar{z}\bar{z}} = \frac{\sigma_{\bar{x}\bar{z}} \cos(\theta) \sin(\theta)}{2\eta_{xy}^*(4\alpha - 1)} \left(4\alpha \sin^2(\theta) + 2 \sin^2(\theta) - 6 \cos^2(\theta) + 2 \frac{(4\alpha - 1)(\cos^2(\theta) - \sin^2(\theta))}{\beta} \right) \quad (\text{A.36})$$

$$D_{\bar{x}\bar{x}} = \frac{\sigma_{\bar{x}\bar{z}} \cos(\theta) \sin(\theta)}{2\eta_{xy}^*(4\alpha - 1)} \left(4\alpha \cos^2(\theta) + 2 \cos^2(\theta) - 6 \sin^2(\theta) - 2 \frac{(4\alpha - 1)(\cos^2(\theta) - \sin^2(\theta))}{\beta} \right) \quad (\text{A.37})$$

$$D_{\bar{x}\bar{z}} = \frac{\sigma_{\bar{x}\bar{z}}}{2\eta_{xy}^*(4\alpha - 1)} \left(4 \cos^2(\theta) \sin^2(\theta) (2 + \alpha) + \frac{(4\alpha - 1)(\cos^2(\theta) - \sin^2(\theta))^2}{\beta} \right) \quad (\text{A.38})$$

Again imposing $\alpha = 1$, one obtains :

$$D_{\bar{z}\bar{z}} = \frac{\sigma_{\bar{x}\bar{z}}}{\eta_{xy}^*} \cos(\theta) \sin(\theta) (\cos^2(\theta) - \sin^2(\theta)) \left(\frac{1 - \beta}{\beta} \right) \quad (\text{A.39})$$

$$D_{\bar{x}\bar{x}} = -\frac{\sigma_{\bar{x}\bar{z}}}{\eta_{xy}^*} \cos(\theta) \sin(\theta) (\cos^2(\theta) - \sin^2(\theta)) \left(\frac{1 - \beta}{\beta} \right) \quad (\text{A.40})$$

$$D_{\bar{x}\bar{z}} = \frac{\sigma_{\bar{x}\bar{z}}}{6\eta_{xy}^*} \frac{3}{\beta} (1 - 4(1 - \beta) \cos^2(\theta) \sin^2(\theta)) \quad (\text{A.41})$$

Figure A.3 thus illustrates the evolution of the strain rate components in the global frame for a shearing stress.

Similarly to Fig. A.2, components $D_{\bar{z}\bar{z}}$ and $D_{\bar{x}\bar{x}}$ are symmetrical with respect to $y = 0$.

However applying a shear stress induces larger values for $D_{\bar{x}\bar{z}}$ than for other components. In the case of a uniaxial stress, the component $D_{\bar{z}\bar{z}}$ (Eq. (A.33)) of the strain rate is used when deriving the normal force of the contact law between two single crystals of ice (see chapter 2 and 5). Similarly, in the case of an applied shear stress, the component $D_{\bar{x}\bar{z}}$ (Eq. (A.41)) is used for the tangential force as proposed in chapter 5. However, as illustrated by both figures A.2 and A.3, using only one component of the strain rate tensor is a strong simplification. In the case of uniaxial stress and shear stress, $D_{\bar{x}\bar{z}}$ (Fig. A.2) and $D_{\bar{z}\bar{z}}$ (Fig. A.3) are not taken into account while they are far from being negligible comparing respectively to $D_{\bar{z}\bar{z}}$ and $D_{\bar{x}\bar{z}}$. However, in the case of the normal force, section 2.5 showed that using only the component $D_{\bar{z}\bar{z}}$ (Eq. (A.33)) is appropriate to model the indentation of two monocrystalline ice particles.

Appendix B

Errors on macroscopic strain calculation

B.1 Choice of the macroscopic strain calculation

The macroscopic deformation can be computed by DIC. However, as pointed out in [Chauve \[2017b\]](#), this macroscopic deformation obtained from DIC softwares becomes wrong when large strain heterogeneities arise. As shown by the experiments (see chapter 2), very large heterogeneities appear, thus, there is not a representative volume element for strain. In the study of two cylinders of ice (see section 2.4.2), the user must manually removed on CMV, the correlation domain from the grid that are not on the cylinders speckle. Associating these issues, the macroscopic strains directly calculated by CMV is not correct. However, it is possible to follow each correlation domain individually. Hence, the approximate subsets located in the center of each cylinder were followed, and the black curve in Fig. B.1 illustrates the resulting logarithmic strain between these two centers. Similarly, the mean position of the top and the bottom line of the grid correlation were worked out, and the strain computed (red line). Finally, the blue line shows the logarithmic strain calculated from image analysis (with Fiji [[Schindelin et al., 2013](#)]), by following the displacement of the rigid plane (see section 2.3.1).

Mismatches between the curves tend to increase with time, but the blue curve looks like a good compromise for strain. Moreover, the DIC curves have major drawbacks. The DIC-centers one relies on only two subsets, which means that when large heterogeneities as shear bands appear (see section 2.4), these specific subsets have large displacements along the y axis. In the meantime the neighbor subset could be unaffected. The DIC-lines curve represents a mean, which should limit this effect. However it suffers other issues. First the progressive flattening of the cylinder with the rigid plane tends to underestimate the strain, as the displacement field of the line of subsets is not homogeneously downward.

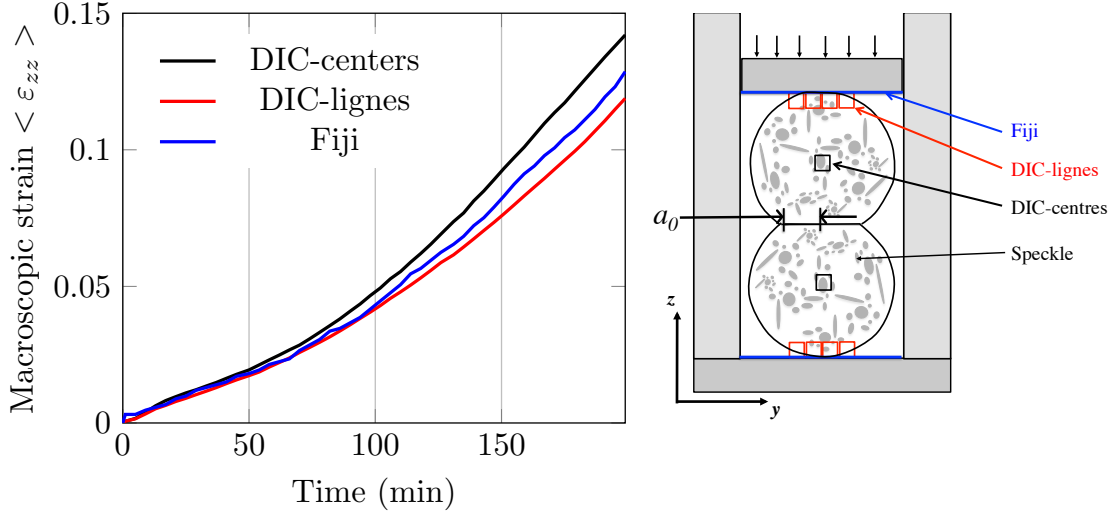


Figure B.1: Comparison of logarithmic strain curves obtained by DIC (CMV) and by image analysis (Fiji). These curves come from the indentation of two cylinders with $a_0/R = 0.20 - 34^\circ/65^\circ - 53\text{ N}$ (see table C.2).

Second, when looking at deviation around the mean position of the line, non-negligible discrepancies can appear because of the large heterogeneities. These several points make the Fiji measurement more reliable, as it only consists in following the pixels of the rigid plane (and resolution does not change during each experiment so errors are limited).

B.2 Methods for errors calculation

For the whole chapter 2, the following errors propagation formulation was chosen. For a given function $f(x_i)$:

$$\Delta f^2 = \sum_i \left[\left(\frac{\partial f(x_i)}{\partial x_i} \right)^2 \Delta x_i^2 \right] \quad (\text{B.1})$$

Typically for the logarithmic strain $\varepsilon_{zz} = \ln \left(1 + \frac{\delta L}{L_0} \right)$ with $\delta L = L_0 - L$, one obtains :

$$\Delta \varepsilon_{zz} = \left(\frac{L}{2L_0 - LL_0} \right) \sqrt{\Delta L_0^2 + \left(\frac{L_0}{L} \right)^2 \Delta L^2} \quad (\text{B.2})$$

Repetitions of the measurements of the length on Fiji were performed and the standard deviation for each particular length was computed. For instance, in the configuration proposed in section 2.4.2, ΔL , ΔL_0 and ΔR (uncertainty on the cylinder radius) were measured at 5 pixels, while it is $\Delta a = 10$ pixels for the neck size because of difficulties to define it visually. These lead to relative errors on the strain ε_{zz} of less than 0.3% in

section 2.3. Moreover, Fig. 2.12 displays very small error bars. Let us pose $J = \varepsilon_{zz} \sqrt{\frac{a_0}{R}}$

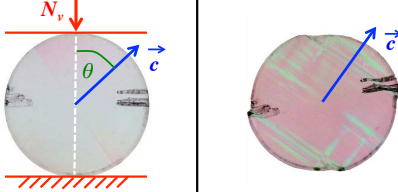
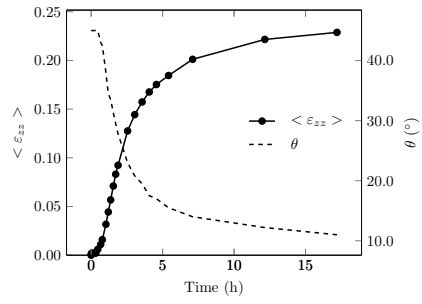
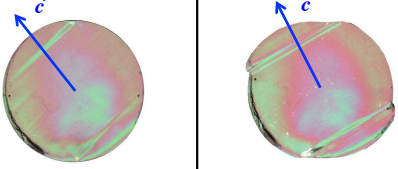
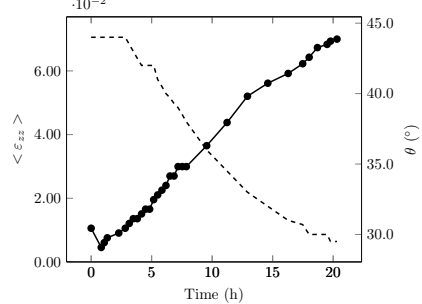
$$\begin{aligned}
 \Delta J^2 &= \left[\frac{\partial}{\partial \varepsilon_{zz}} \varepsilon_{zz} \sqrt{\frac{a_0}{R}} \right]^2 \Delta \varepsilon_{zz}^2 + \left[\frac{\partial}{\partial a_0} \varepsilon_{zz} \sqrt{\frac{a_0}{R}} \right]^2 \Delta a_0^2 + \left[\frac{\partial}{\partial R} \varepsilon_{zz} \sqrt{\frac{a_0}{R}} \right]^2 \Delta R^2 \\
 &= \frac{a_0}{R} \Delta \varepsilon_{zz}^2 + \frac{\varepsilon_{zz}^2}{4a_0 R} \Delta a_0^2 + \frac{\varepsilon_{zz}^2 a_0}{4R^3} \Delta R^2 \\
 \Rightarrow \left[\frac{\Delta J}{J} \right]^2 &= \frac{\Delta \varepsilon_{zz}^2}{\varepsilon_{zz}^2} + \frac{\Delta a_0^2}{a_0^2} + \frac{\Delta R^2}{R^2}
 \end{aligned} \tag{B.3}$$

$$\Rightarrow \Delta J = \varepsilon_{zz} \sqrt{\frac{a_0}{R}} \sqrt{\frac{\Delta \varepsilon_{zz}^2}{\varepsilon_{zz}^2} + \frac{\Delta a_0^2}{a_0^2} + \frac{\Delta R^2}{R^2}} \tag{B.4}$$

Appendix C

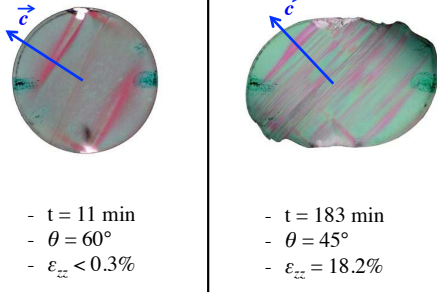
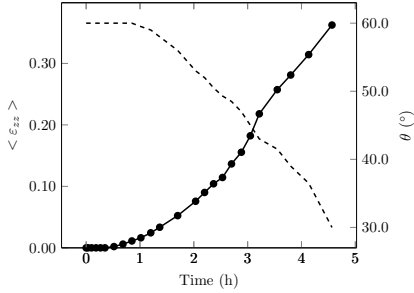
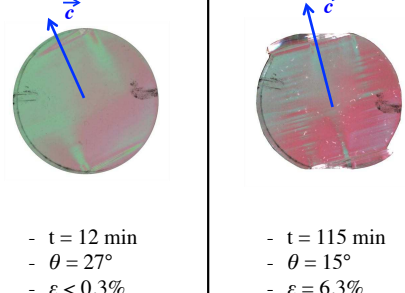
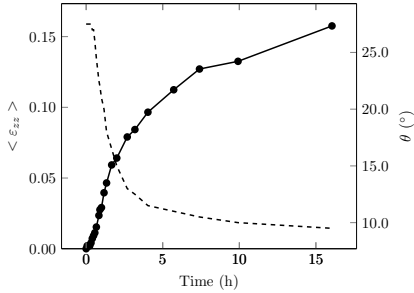
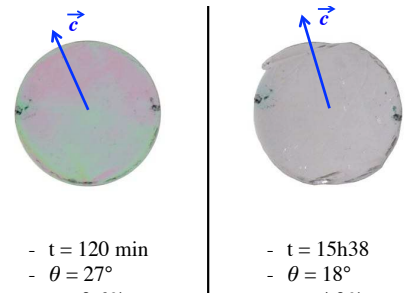
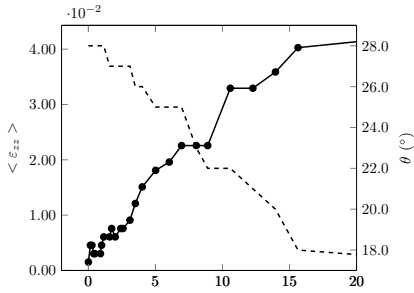
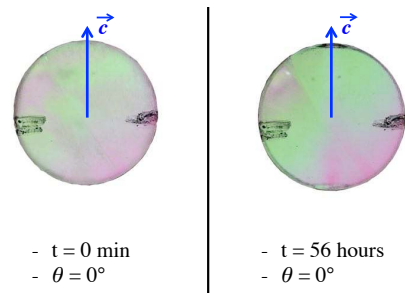
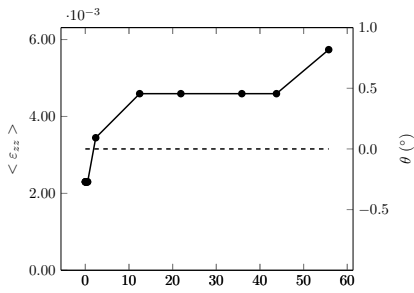
Creep test on monocrystalline cylinders

Table C.1: Creep of monocrystalline ice cylinders followed by polarized light.

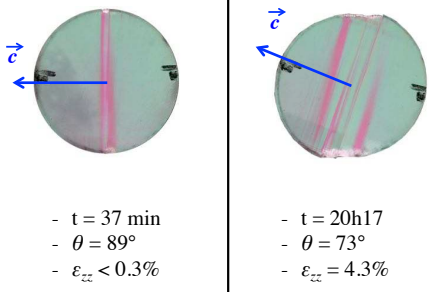
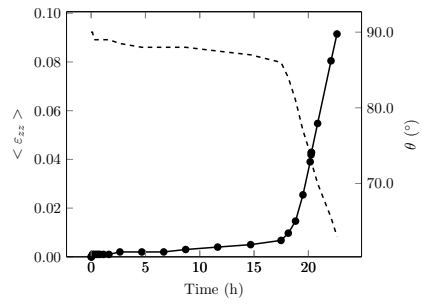
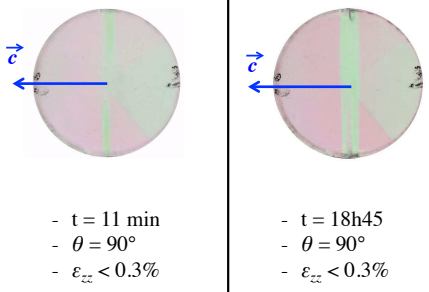
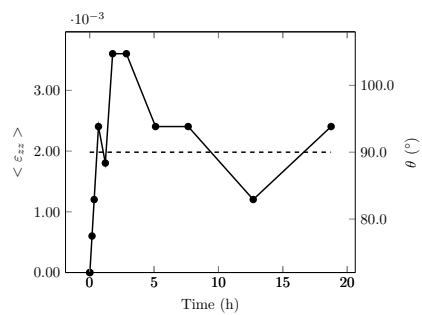
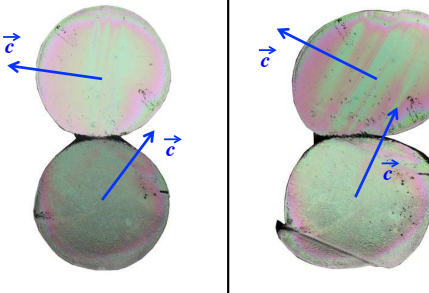
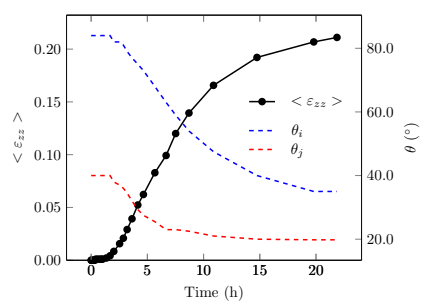
Sample	Polarized light	Logarithmic strain
45°-105 N	 <ul style="list-style-type: none"> - Before loading - $\theta = 45^\circ$ - $t = 82 \text{ min}$ - $\theta = 35^\circ$ - $\varepsilon_{zz} = 5.7\%$ 	
44°-34 N	 <ul style="list-style-type: none"> - $t = 95 \text{ min}$ - $\theta = 44^\circ$ - $\varepsilon_{zz} = 0.8\%$ - $t = 20\text{h}18$ - $\theta = 29.5^\circ$ - $\varepsilon_{zz} = 7.0\%$ 	

Continued on next page ...

APPENDIX C. CREEP TEST ON MONOCRYSTALLINE CYLINDERS

Sample	Polarized light	Logarithmic strain
60°-109 N	 <ul style="list-style-type: none"> - $t = 11$ min - $\theta = 60^\circ$ - $\varepsilon_{zz} < 0.3\%$ <ul style="list-style-type: none"> - $t = 183$ min - $\theta = 45^\circ$ - $\varepsilon_{zz} = 18.2\%$ 	
27°-108 N	 <ul style="list-style-type: none"> - $t = 12$ min - $\theta = 27^\circ$ - $\varepsilon < 0.3\%$ <ul style="list-style-type: none"> - $t = 115$ min - $\theta = 15^\circ$ - $\varepsilon = 6.3\%$ 	
28°-34 N	 <ul style="list-style-type: none"> - $t = 120$ min - $\theta = 27^\circ$ - $\varepsilon = 0.6\%$ <ul style="list-style-type: none"> - $t = 15\text{h}38$ - $\theta = 18^\circ$ - $\varepsilon = 4.0\%$ 	
0°-50 N	 <ul style="list-style-type: none"> - $t = 0$ min - $\theta = 0^\circ$ - $\varepsilon_{zz} = 0\%$ <ul style="list-style-type: none"> - $t = 56$ hours - $\theta = 0^\circ$ - $\varepsilon_{zz} < 0.6\%$ 	

Continued on next page ...

Sample	Polarized light	Logarithmic strain
90°-54 N	 <ul style="list-style-type: none"> - $t = 37 \text{ min}$ - $\theta = 89^\circ$ - $\varepsilon_{zz} < 0.3\%$ - $t = 20\text{h}17$ - $\theta = 73^\circ$ - $\varepsilon_{zz} = 4.3\%$ 	
90°-50 N	 <ul style="list-style-type: none"> - $t = 11 \text{ min}$ - $\theta = 90^\circ$ - $\varepsilon_{zz} < 0.3\%$ - $t = 18\text{h}45$ - $\theta = 90^\circ$ - $\varepsilon_{zz} < 0.3\%$ 	
84°/40°-53 N	 <ul style="list-style-type: none"> - $t = 152 \text{ min}$ - $\theta_i = 82^\circ / \theta_j = 37^\circ$ - $\varepsilon_{zz} = 1.6\%$ - $t = 7\text{h}31$ - $\theta_i = 59^\circ / \theta_j = 23^\circ$ - $\varepsilon_{zz} = 12.8\%$ 	

Continued on next page ...

APPENDIX C. CREEP TEST ON MONOCRYSTALLINE CYLINDERS

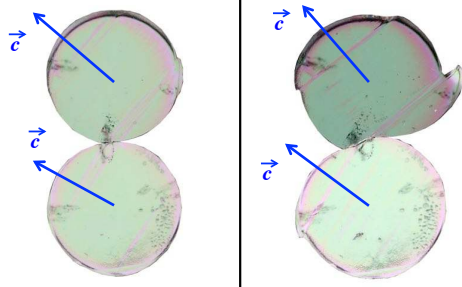
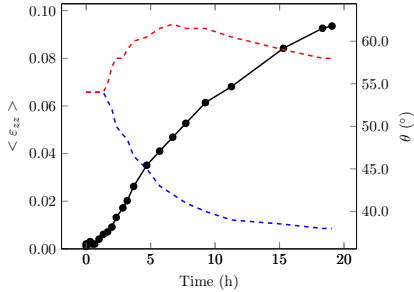
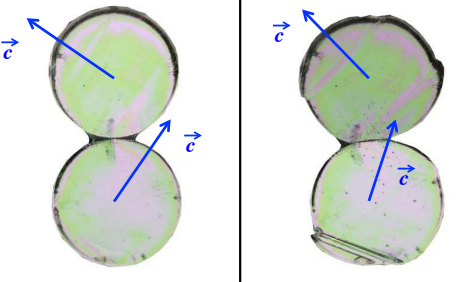
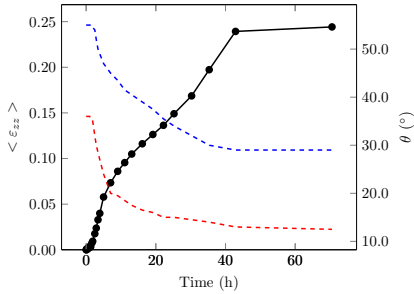
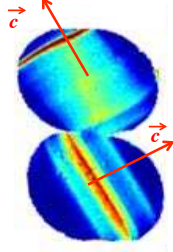
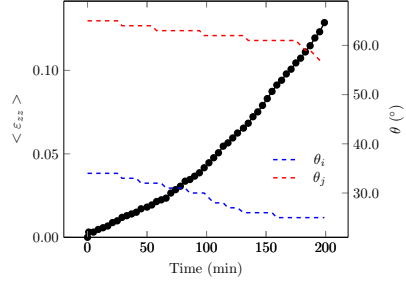
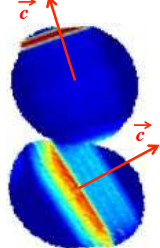
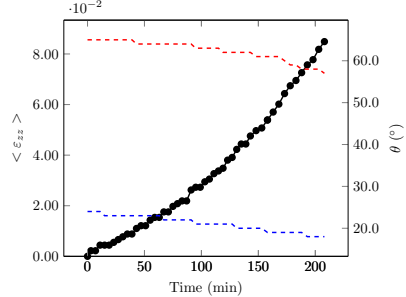
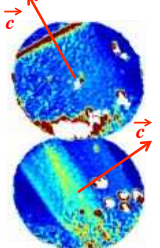
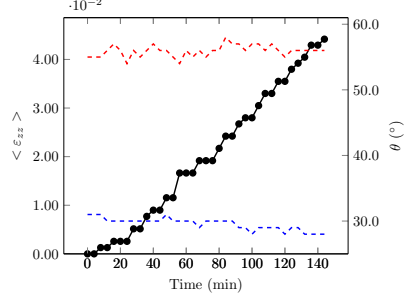
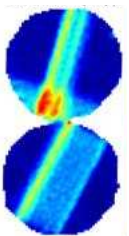
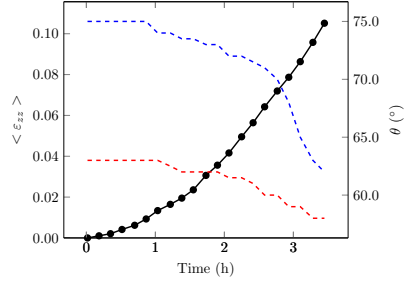
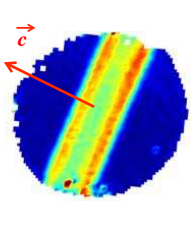
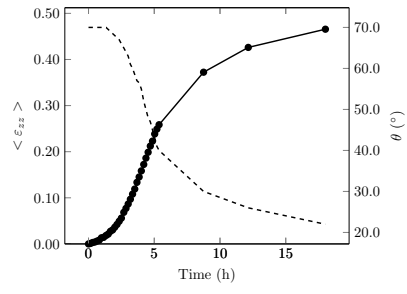
Sample	Polarized light	Logarithmic strain
54°/54°-53 N	 <ul style="list-style-type: none"> - $t = 171 \text{ min}$ - $\theta_i = 49^\circ / \theta_j = 58^\circ$ - $\varepsilon_{zz} = 1.7\%$ <ul style="list-style-type: none"> - $t = 19\text{h}04$ - $\theta_i = 38^\circ / \theta_j = 58^\circ$ - $\varepsilon_{zz} = 9.4\%$ 	
54°/36°-53 N	 <ul style="list-style-type: none"> - $t = 46 \text{ min}$ - $\theta_i = 55^\circ / \theta_j = 36^\circ$ - $\varepsilon_{zz} = 0.3\%$ <ul style="list-style-type: none"> - $t = 7\text{h}01$ - $\theta_i = 45^\circ / \theta_j = 20^\circ$ - $\varepsilon_{zz} = 7.3\%$ 	

Table C.2: Digital Image Correlation on monocrystalline cylinders.

Sample	DIC specifications	Logarithmic strain						
$a_0/R = 0.20 - 34^\circ/65^\circ - 53 \text{ N}$	<div></div> <div><ul style="list-style-type: none">- $t = 200 \text{ min}$- $\theta_i = 25^\circ / \theta_j = 57^\circ$- $\epsilon_{zz} = 12.9\%$<table><tr><td>Pixel size (μm)</td><td>12.6 ± 0.05</td></tr><tr><td>Autocorrelation radius (pix)</td><td>≈ 2.6</td></tr><tr><td>Gage length (μm)</td><td>504 ± 2</td></tr></table></div>	Pixel size (μm)	12.6 ± 0.05	Autocorrelation radius (pix)	≈ 2.6	Gage length (μm)	504 ± 2	
Pixel size (μm)	12.6 ± 0.05							
Autocorrelation radius (pix)	≈ 2.6							
Gage length (μm)	504 ± 2							
$a_0/R = 0.32 - 24^\circ/65^\circ - 53 \text{ N}$	<div></div> <div><ul style="list-style-type: none">- $t = 208 \text{ min}$- $\theta_i = 18^\circ / \theta_j = 57^\circ$- $\epsilon_{zz} = 8.5\%$<table><tr><td>Pixel size (μm)</td><td>16.0 ± 0.05</td></tr><tr><td>Autocorrelation radius (pix)</td><td>≈ 3.25</td></tr><tr><td>Gage length (μm)</td><td>608 ± 2</td></tr></table></div>	Pixel size (μm)	16.0 ± 0.05	Autocorrelation radius (pix)	≈ 3.25	Gage length (μm)	608 ± 2	
Pixel size (μm)	16.0 ± 0.05							
Autocorrelation radius (pix)	≈ 3.25							
Gage length (μm)	608 ± 2							
$a_0/R = 0.35 - 31^\circ/55^\circ - 53 \text{ N}$	<div></div> <div><ul style="list-style-type: none">- $t = 144 \text{ min}$- $\theta_i = 28^\circ / \theta_j = 56^\circ$- $\epsilon_{zz} = 4.4\%$<table><tr><td>Pixel size (μm)</td><td>13.0 ± 0.05</td></tr><tr><td>Autocorrelation radius (pix)</td><td>$\approx 4.6 - 4.9$</td></tr><tr><td>Gage length (μm)</td><td>520 ± 2</td></tr></table></div>	Pixel size (μm)	13.0 ± 0.05	Autocorrelation radius (pix)	$\approx 4.6 - 4.9$	Gage length (μm)	520 ± 2	
Pixel size (μm)	13.0 ± 0.05							
Autocorrelation radius (pix)	$\approx 4.6 - 4.9$							
Gage length (μm)	520 ± 2							
$75^\circ/63^\circ - 54 \text{ N}$	<div></div> <div><ul style="list-style-type: none">- $t = 83 \text{ min}$- $\theta_i = 73.5^\circ / \theta_j = 62^\circ$- $\epsilon_{zz} = 2.0\%$<table><tr><td>Pixel size (μm)</td><td>21.6 ± 0.05</td></tr><tr><td>Autocorrelation radius (pix)</td><td>≈ 2.2</td></tr><tr><td>Gage length (μm)</td><td>864 ± 2</td></tr></table></div>	Pixel size (μm)	21.6 ± 0.05	Autocorrelation radius (pix)	≈ 2.2	Gage length (μm)	864 ± 2	
Pixel size (μm)	21.6 ± 0.05							
Autocorrelation radius (pix)	≈ 2.2							
Gage length (μm)	864 ± 2							

Continued on next page ...

APPENDIX C. CREEP TEST ON MONOCRYSTALLINE CYLINDERS

Sample	DIC specifications	Logarithmic strain						
70° - 54N	<div><div></div><div><ul style="list-style-type: none">- t = 140 min- θ = 67°- ε_zz = 4.9%<table><tr><td>Pixel size (μm)</td><td>10.1 ± 0.05</td></tr><tr><td>Autocorrelation radius (pix)</td><td>≈ 3 - 5</td></tr><tr><td>Gage length (μm)</td><td>604 ± 2</td></tr></table></div></div>	Pixel size (μm)	10.1 ± 0.05	Autocorrelation radius (pix)	≈ 3 - 5	Gage length (μm)	604 ± 2	
Pixel size (μm)	10.1 ± 0.05							
Autocorrelation radius (pix)	≈ 3 - 5							
Gage length (μm)	604 ± 2							

Appendix D

Evolution of firn microstructure at Dome C and Lock In

D.1 Frame of reference

Be \vec{z} the ice core axis (a vertical axis towards the surface). The Pole figures are represented in the (X,Y) in a direct reference (see Fig. D.1). Thus the orientation of the ice core is denoted accordingly to these coordinates. For instance in Table D.1, the sample microstructure shown at 51 m has its \vec{z} -axis coming toward the reader (it is noted $\vec{z} = Z$). In other words the plane shown is parallel to the ice core surface, whereas at 59.05 m deep it is perpendicular. Digitized grains used for the Pole figure are obtained with the AITA python toolbox [Chauve, 2017a]. Grain colors represent \mathbf{c} axis orientations according to the colorwheel in Fig. D.1. Note that colors separated by an angle of π , i.e. from opposite sides on the colorwheel, illustrate the same direction of \mathbf{c} axes.

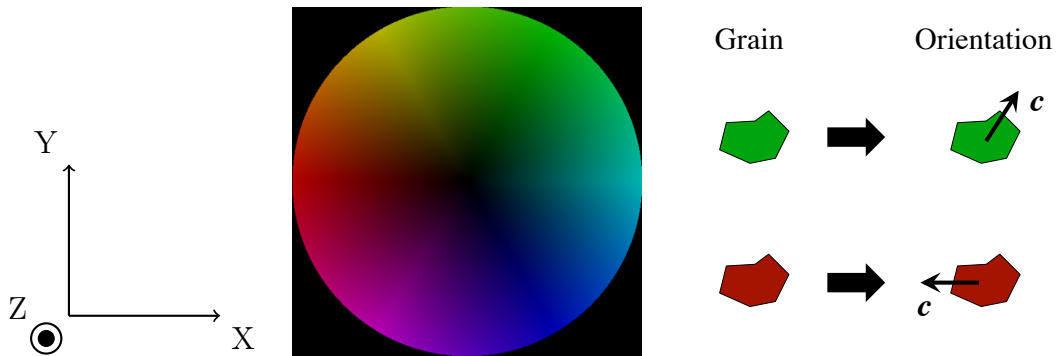
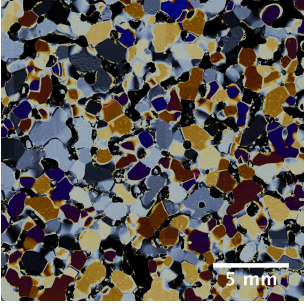
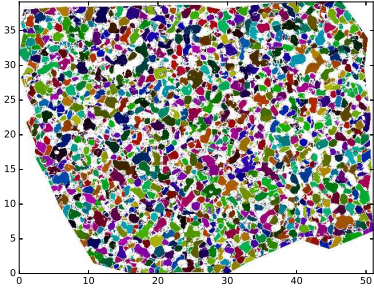
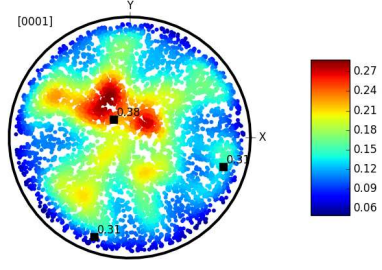
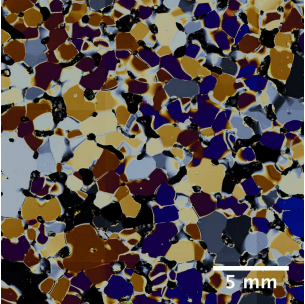
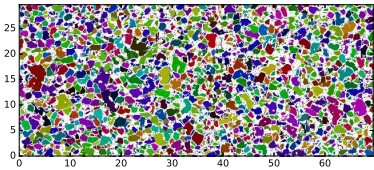
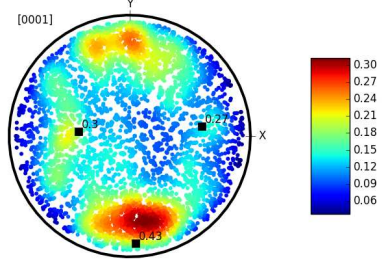
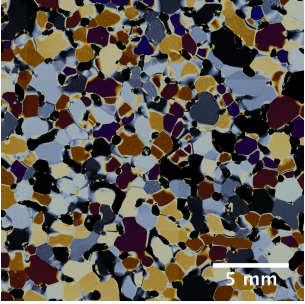
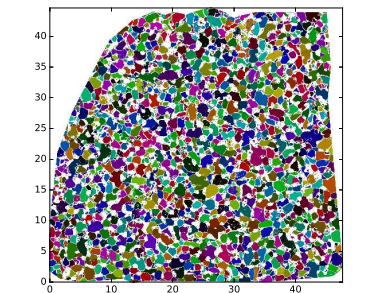
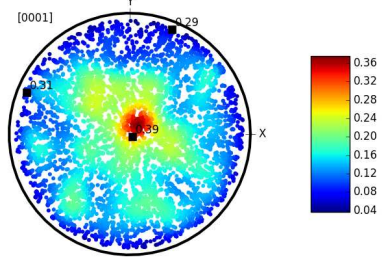
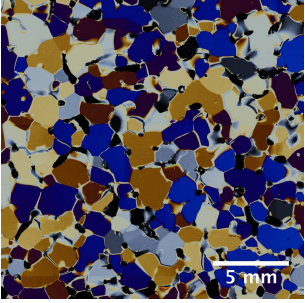
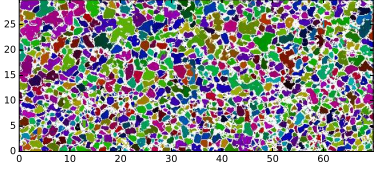
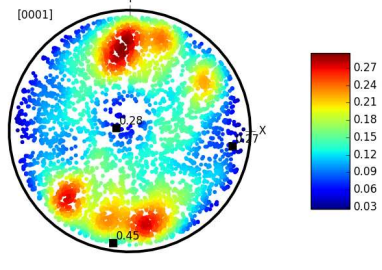


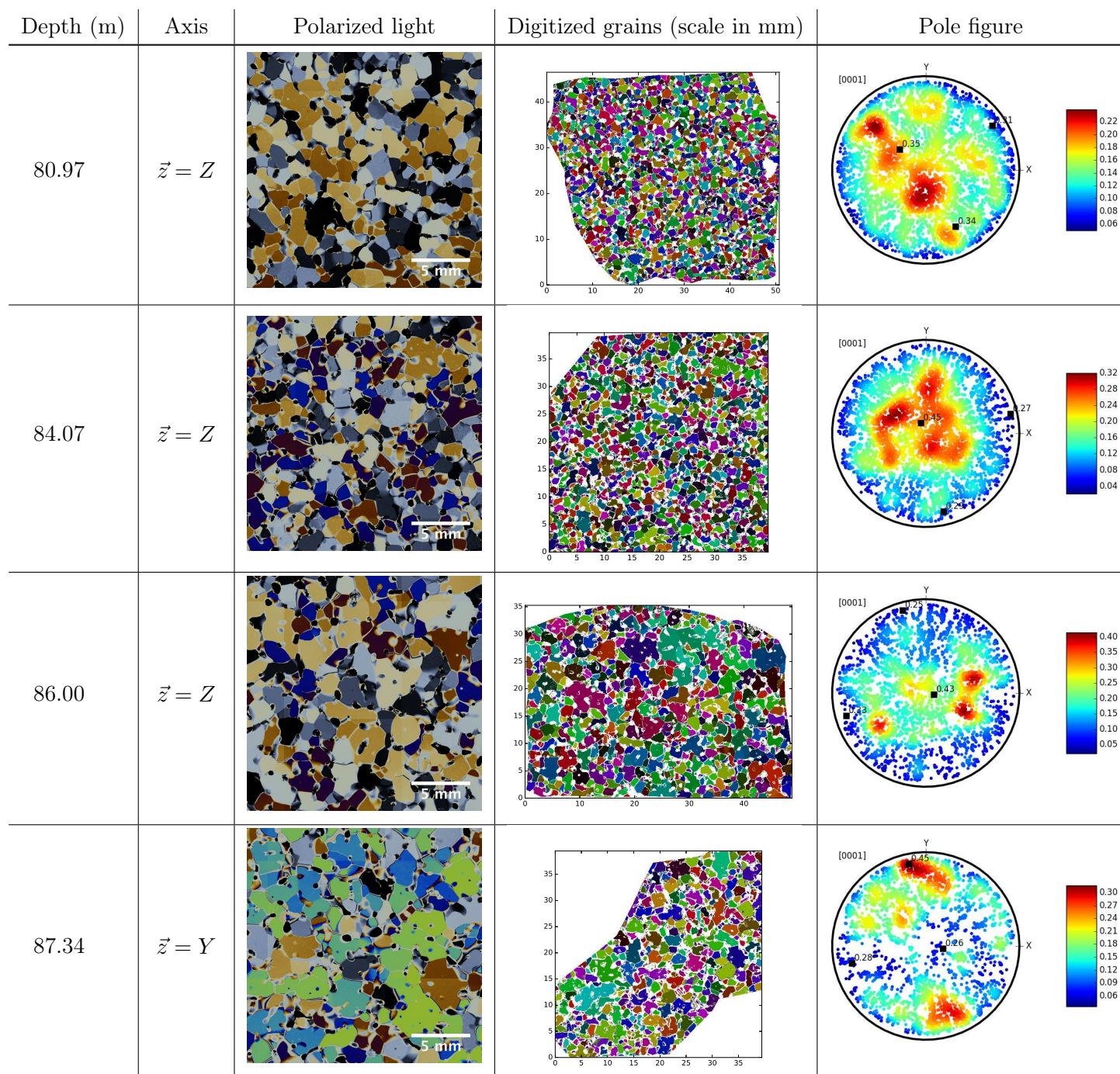
Figure D.1: Reference of the Pole figures and colorwheel for the digitized grains along with an explanation for color reading.

D.2 Dome C

Table D.1: Microstructure of Dome C firn core for several depths.

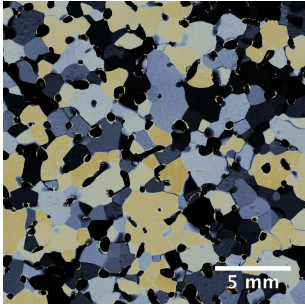
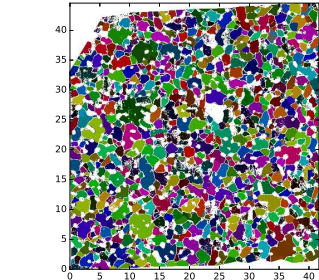
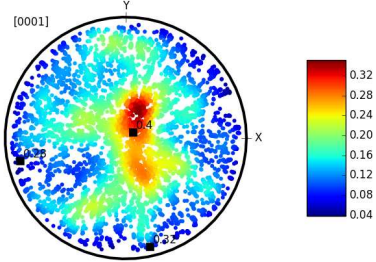
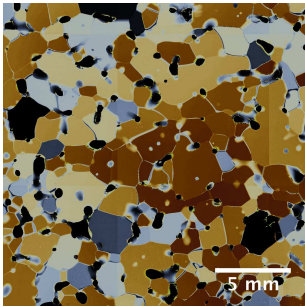
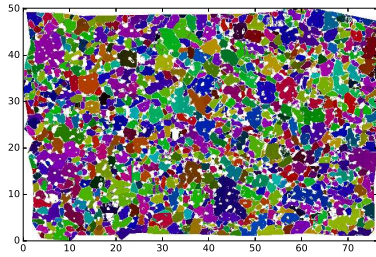
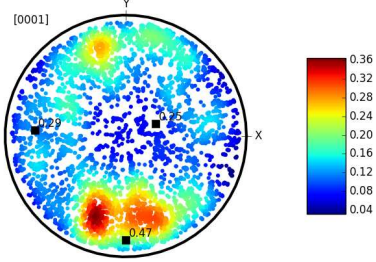
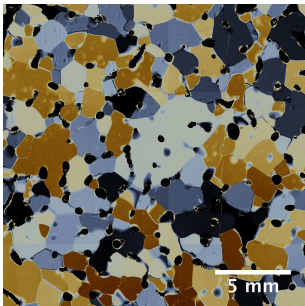
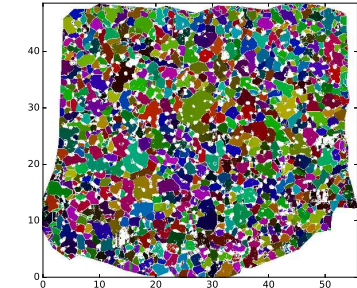
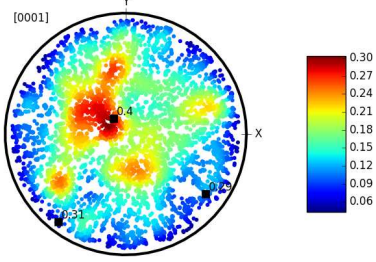
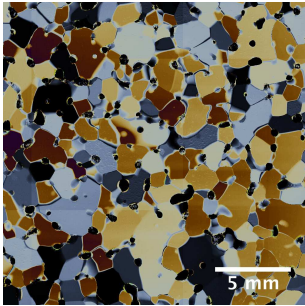
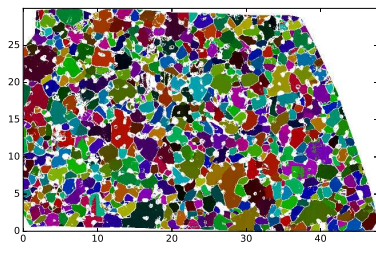
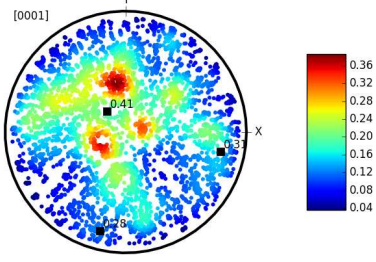
Depth (m)	Axis	Polarized light	Digitized grains (scale in mm)	Pole figure
51.00	$\vec{z} = Z$			
59.05	$\vec{z} = Y$			
69.95	$\vec{z} = Z$			
79.87	$\vec{z} = Y$			

Continued on next page ...

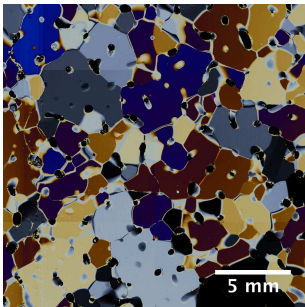
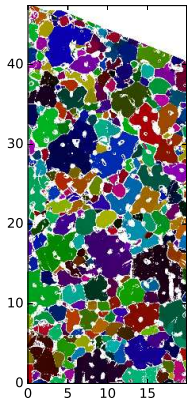
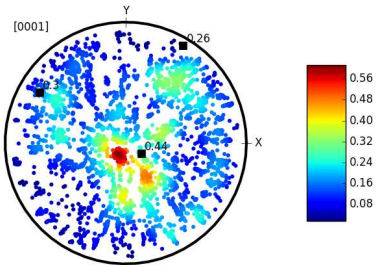
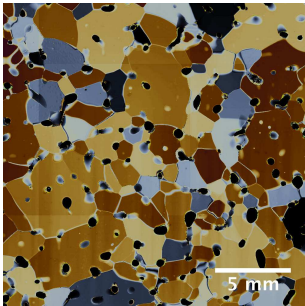
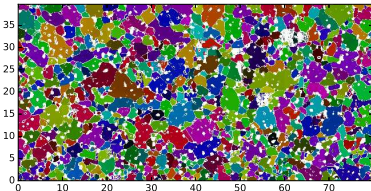
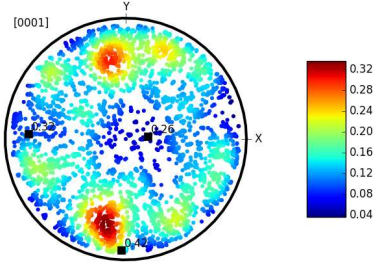
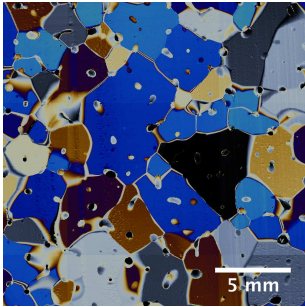
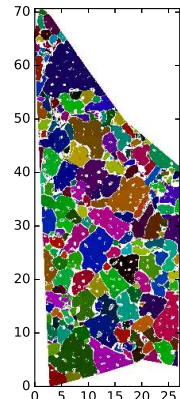
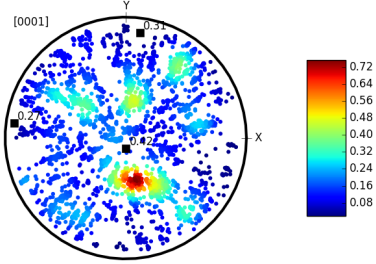


Continued on next page ...

APPENDIX D. EVOLUTION OF FIRN MICROSTRUCTURE AT DOME C AND LOCK IN

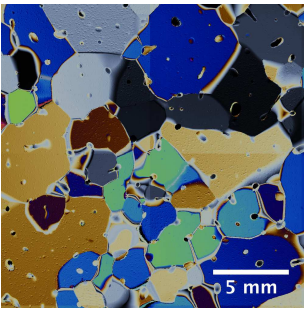
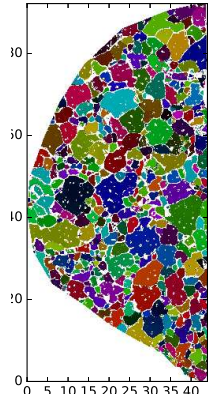
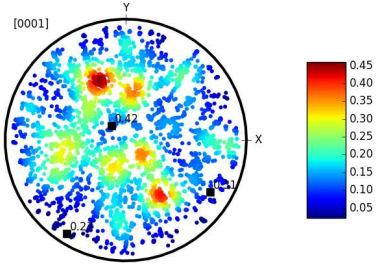
Depth (m)	Axis	Polarized light	Digitized grains (scale in mm)	Pole figure
89.50	$\vec{z} = Z$			
90.50	$\vec{z} = Y$			
94.50	$\vec{z} = Z$			
96.00	$\vec{z} = Z$			

Continued on next page ...

Depth (m)	Axis	Polarized light	Digitized grains (scale in mm)	Pole figure
97.50	$\vec{z} = Z$			
100.38	$\vec{z} = Y$			
123.34	$\vec{z} = Z$			

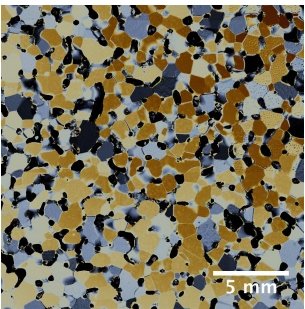
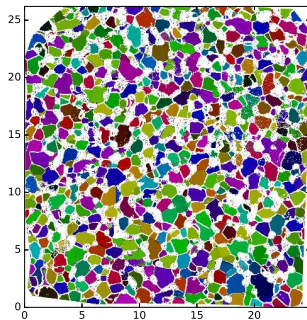
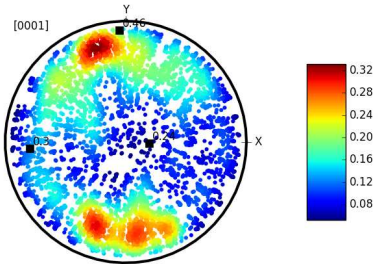
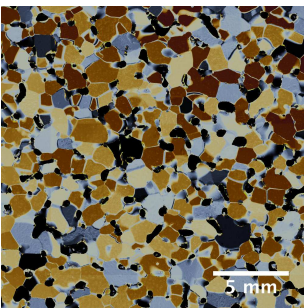
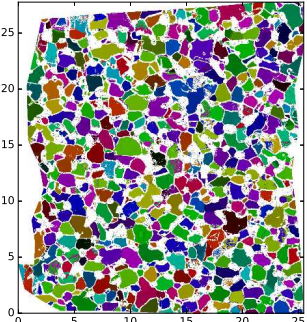
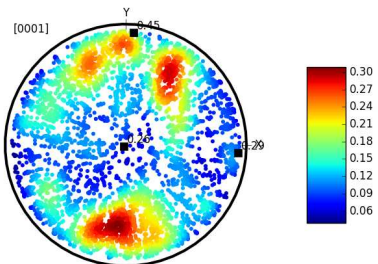
Continued on next page ...

APPENDIX D. EVOLUTION OF FIRN MICROSTRUCTURE AT DOME C AND LOCK IN

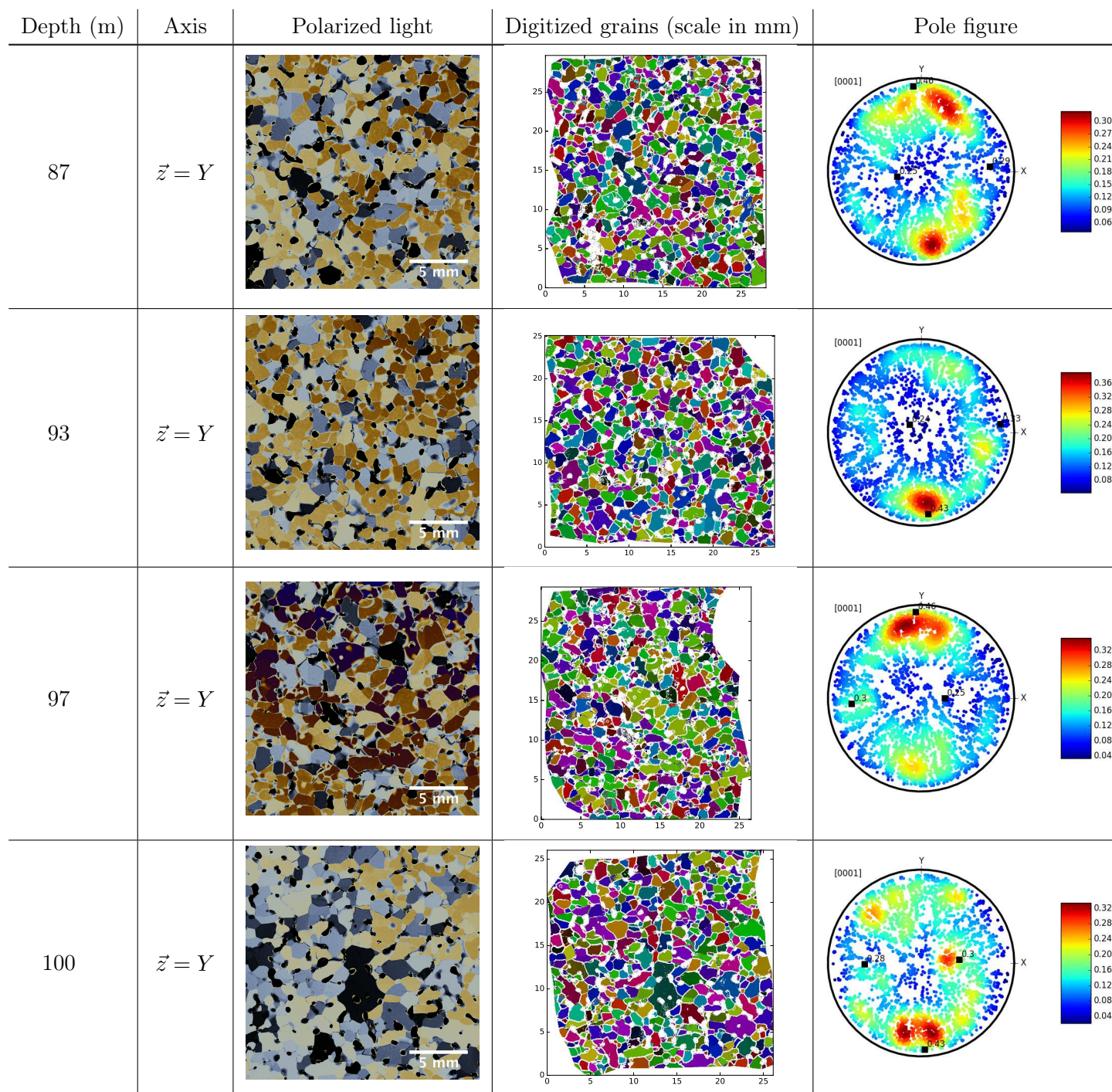
Depth (m)	Axis	Polarized light	Digitized grains (scale in mm)	Pole figure
132.07	$\vec{z} = Z$			

D.3 Lock In

Table D.2: Microstructure of Lock In firn core for several depths.

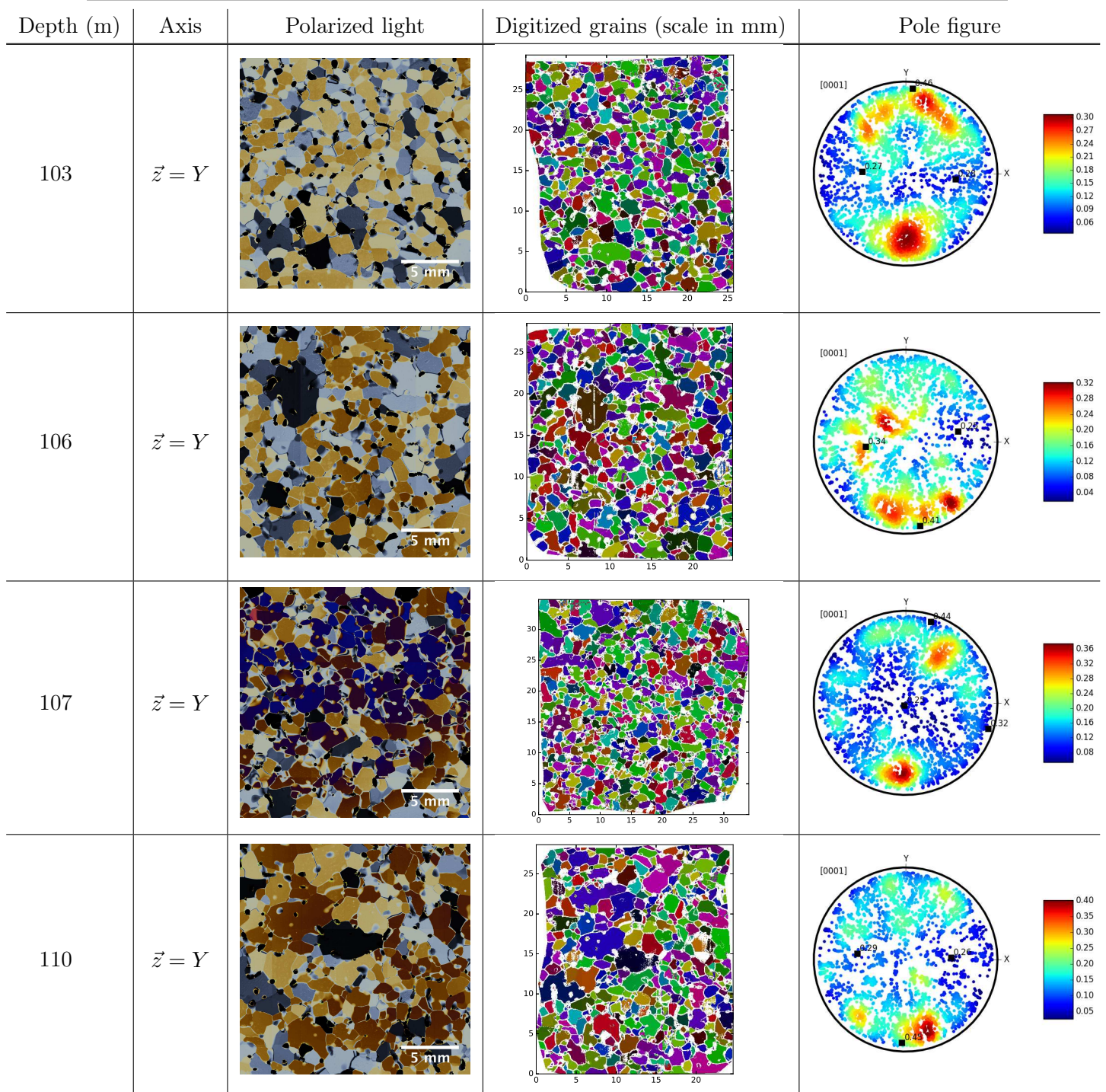
Depth (m)	Axis	Polarized light	Digitized grains (scale in mm)	Pole figure
66	$\vec{z} = Y$			
83	$\vec{z} = Y$			

Continued on next page ...



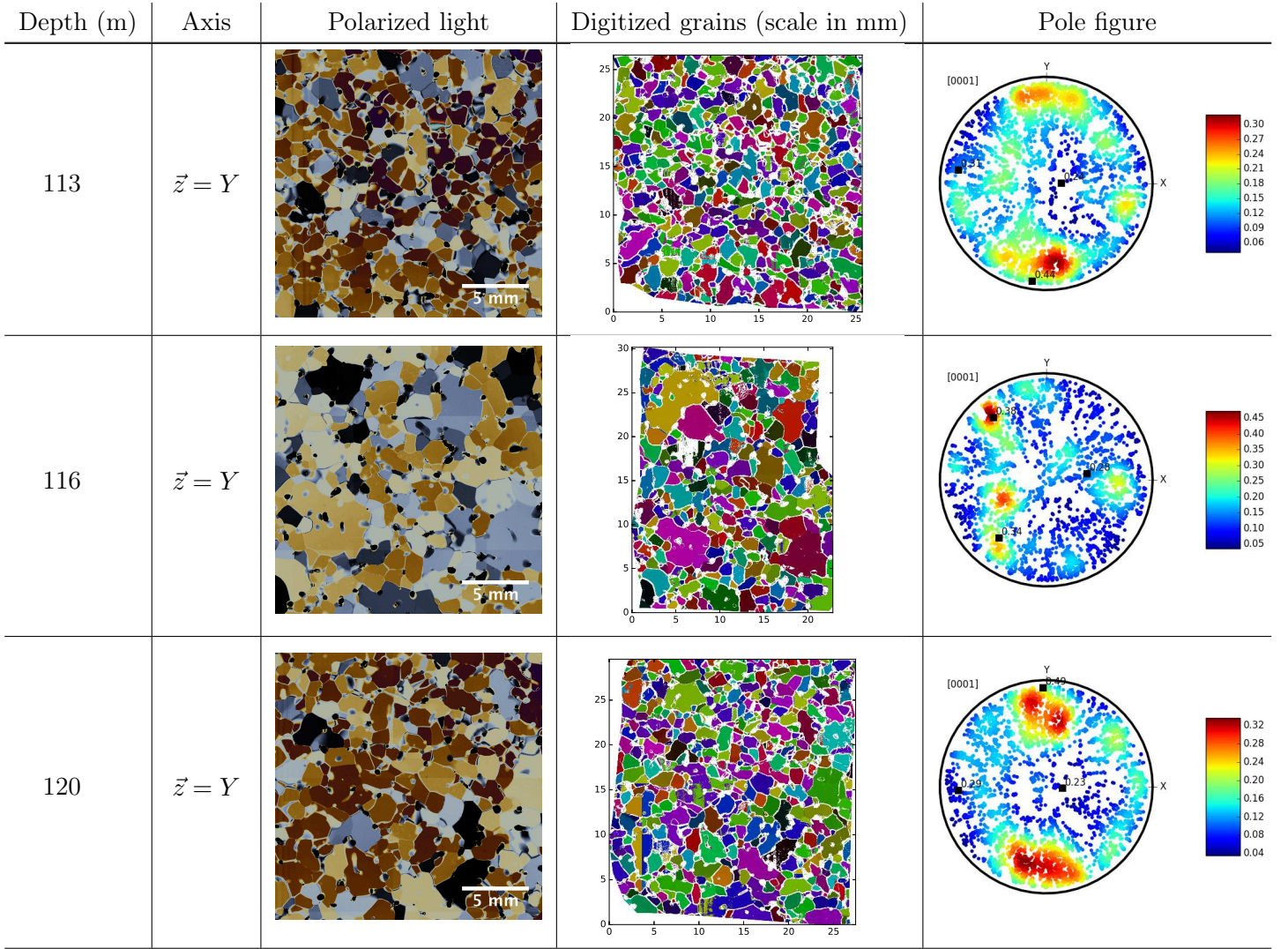
Continued on next page ...

APPENDIX D. EVOLUTION OF FIRN MICROSTRUCTURE AT DOME C AND LOCK IN



Continued on next page ...

D.4. Microstructure of in situ samples before and after the compression tests.



D.4 Microstructure of in situ samples before and after the compression tests.

The following samples are introduced in chapter 4. After X-ray scans, samples are cut in two pieces as illustrated by Fig. D.2 and are analyzed with the AITA.

APPENDIX D. EVOLUTION OF FIRN MICROSTRUCTURE AT DOME C AND LOCK IN

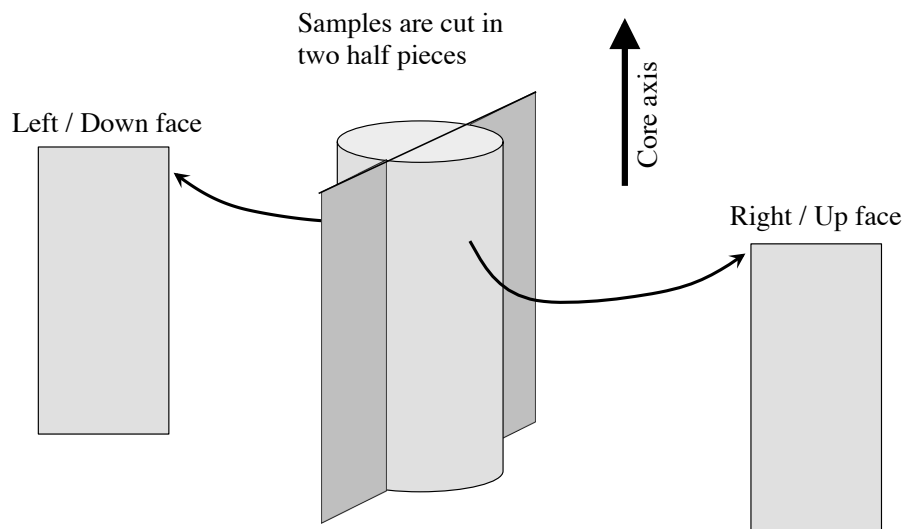
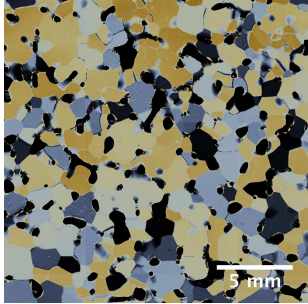
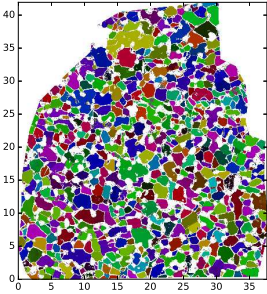
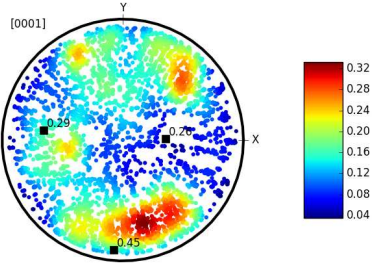
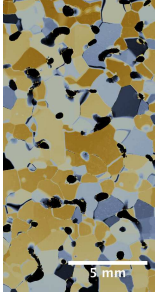
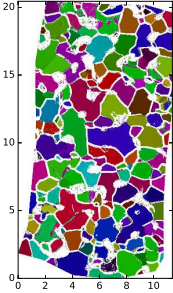
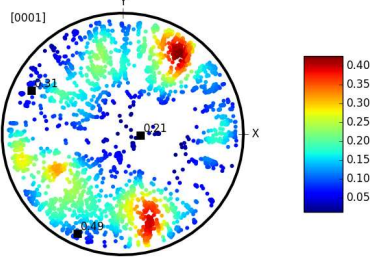


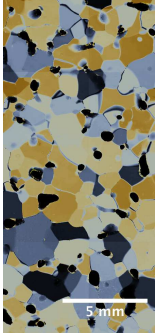
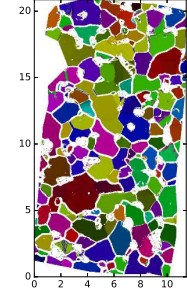
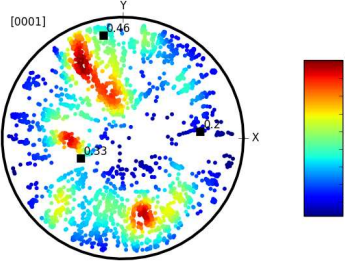
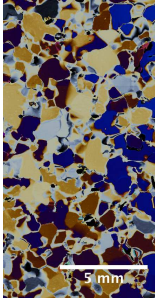
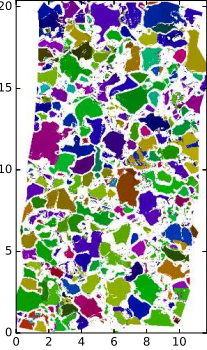
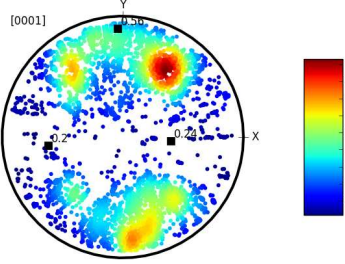
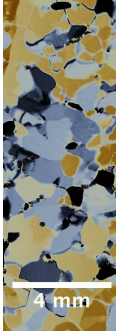
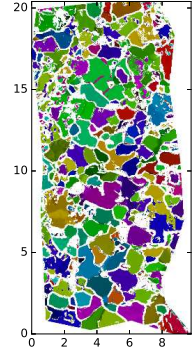
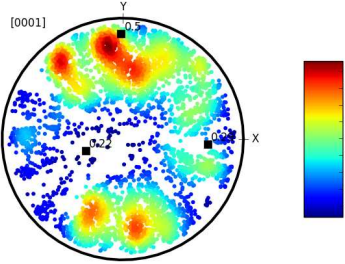
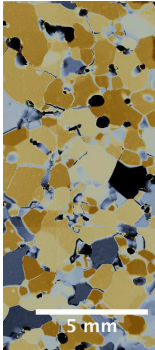
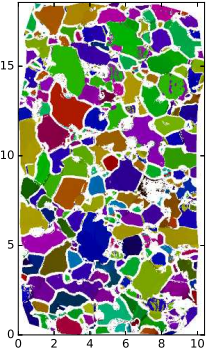
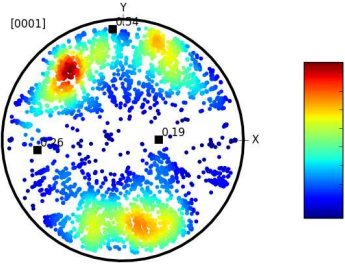
Figure D.2: Diagram of the procedure to cut the sample.

Table D.3: Microstructure after compression tests of firn samples from 80 m deep.

Depth (m)	Axis	Polarized light	Digitized grains (scale in mm)	Pole figure
80m_initial	$\vec{z} = Y$			
80m_c1_left	$\vec{z} = Y$			

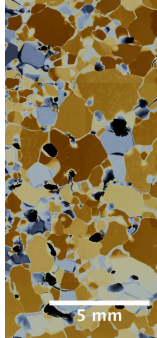
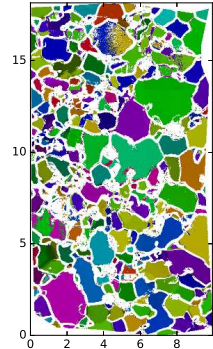
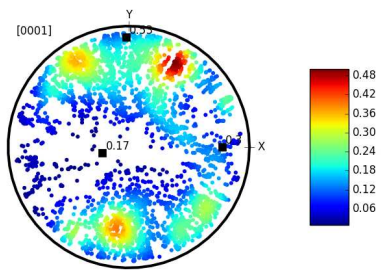
Continued on next page ...

D.4. Microstructure of in situ samples before and after the compression tests.

Depth (m)	Axis	Polarized light	Digitized grains (scale in mm)	Pole figure
80m_c1_right	$\vec{z} = Y$			
80m_c2_left	$\vec{z} = Y$			
80m_c2_right	$\vec{z} = Y$			
80m_c3_left	$\vec{z} = Y$			

Continued on next page ...

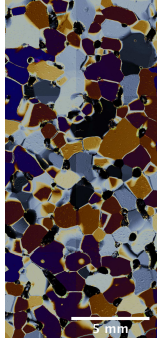
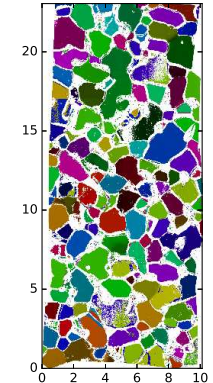
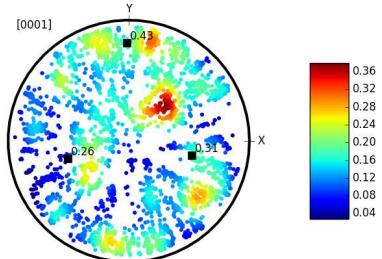
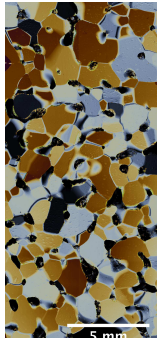
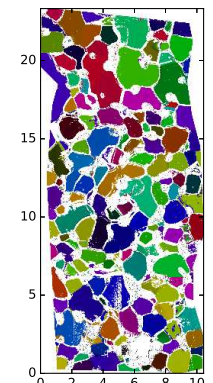
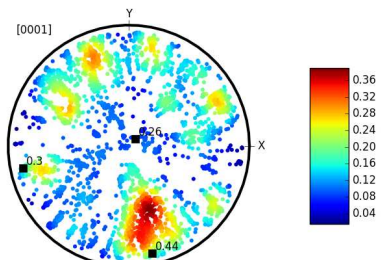
APPENDIX D. EVOLUTION OF FIRN MICROSTRUCTURE AT DOME C AND LOCK IN

Depth (m)	Axis	Polarized light	Digitized grains (scale in mm)	Pole figure
80m_c3_right	$\vec{z} = Y$			

D.5 Microstructure of in situ samples after Heat Treatment.

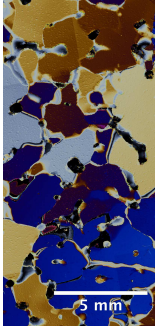
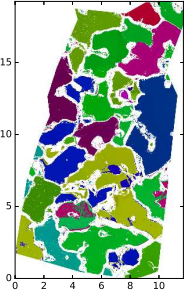
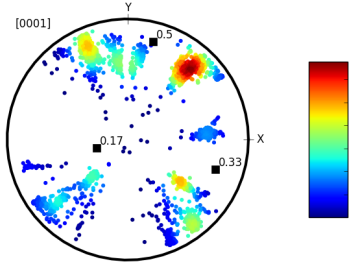
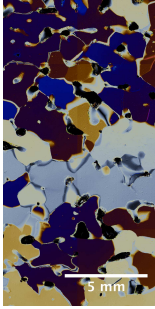
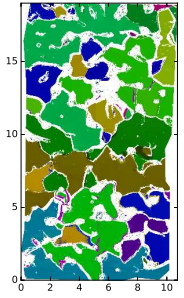
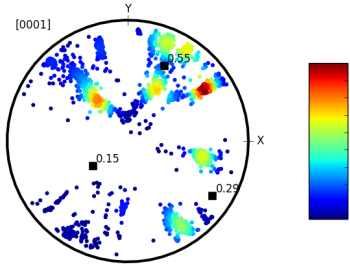
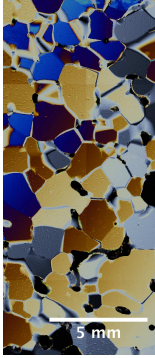
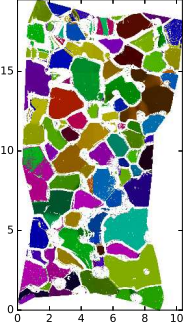
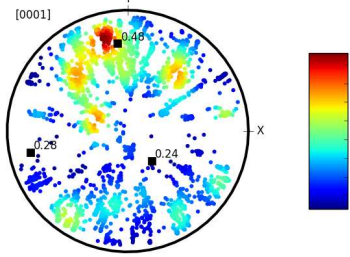
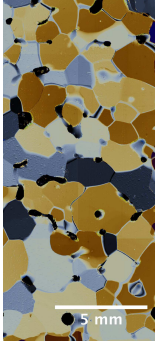
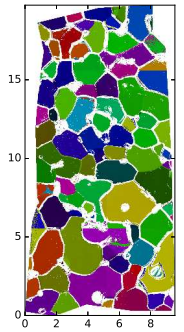
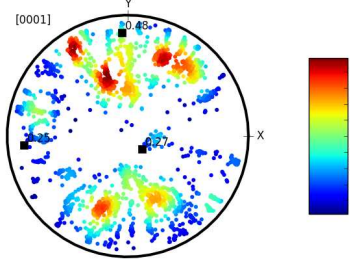
The following samples are introduced in Table 4.2 from section 4.5.

Table D.4: Microstructure after compression tests of firn samples from 80 m deep.

Depth (m)	Axis	Polarized light	Digitized grains (scale in mm)	Pole figure
80m_ref_left (A2)	$\vec{z} = Y$			
80m_ref_right (A2)	$\vec{z} = Y$			

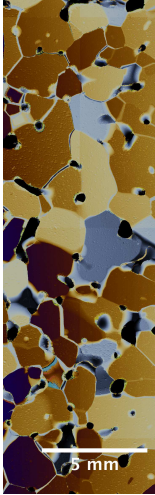
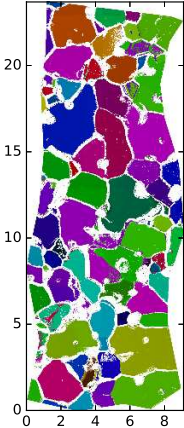
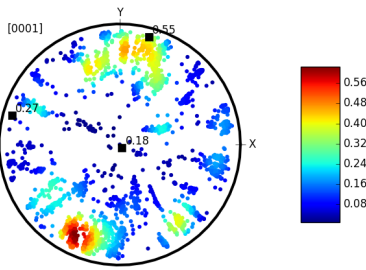
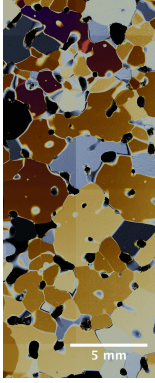
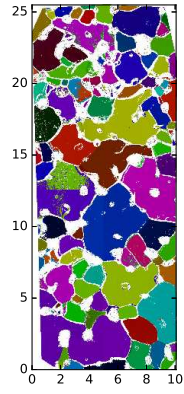
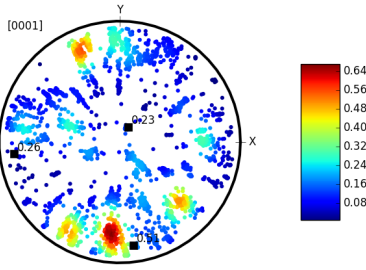
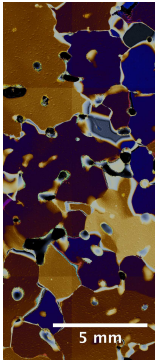
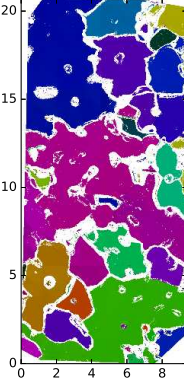
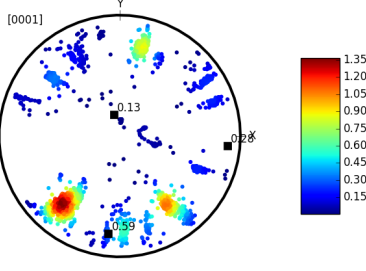
Continued on next page ...

D.5. Microstructure of in situ samples after Heat Treatment.

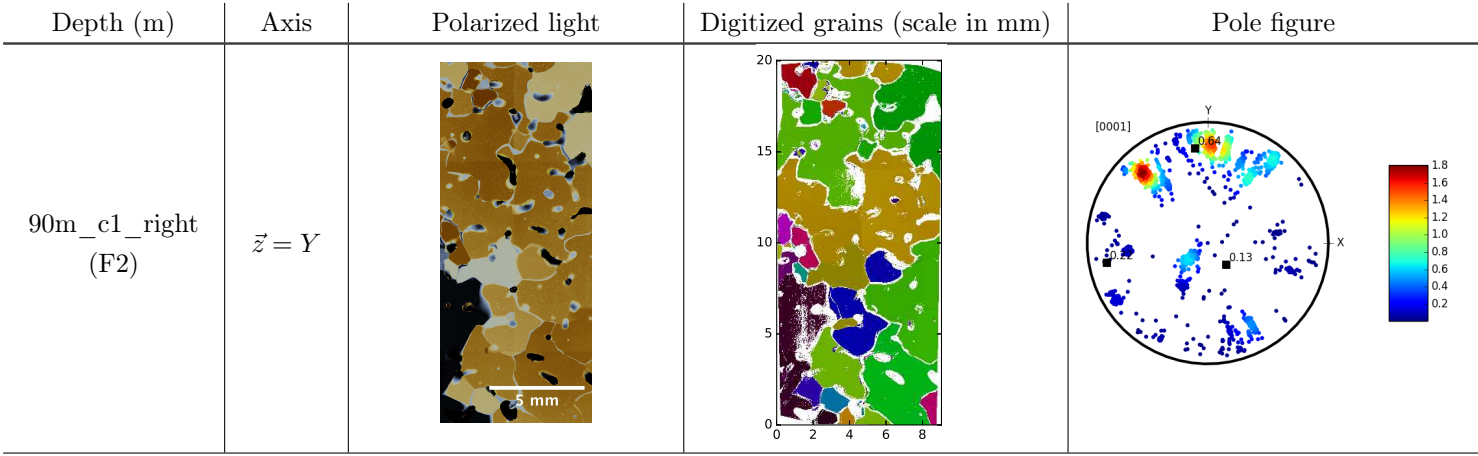
Depth (m)	Axis	Polarized light	Digitized grains (scale in mm)	Pole figure
80m_c4_left (B2)	$\vec{z} = Y$			
80m_c4_right (B2)	$\vec{z} = Y$			
80m_c5_left (D3)	$\vec{z} = Y$			
80m_c5_right (D3)	$\vec{z} = Y$			

Continued on next page ...

APPENDIX D. EVOLUTION OF FIRN MICROSTRUCTURE AT DOME C AND LOCK IN

Depth (m)	Axis	Polarized light	Digitized grains (scale in mm)	Pole figure
90m_old_left (E2)	$\vec{z} = Y$			
90m_old_right (E2)	$\vec{z} = Y$			
90m_c1_left (F2)	$\vec{z} = Y$			

Continued on next page ...



D.6 Evolution of eigenvalues and vectors with depth

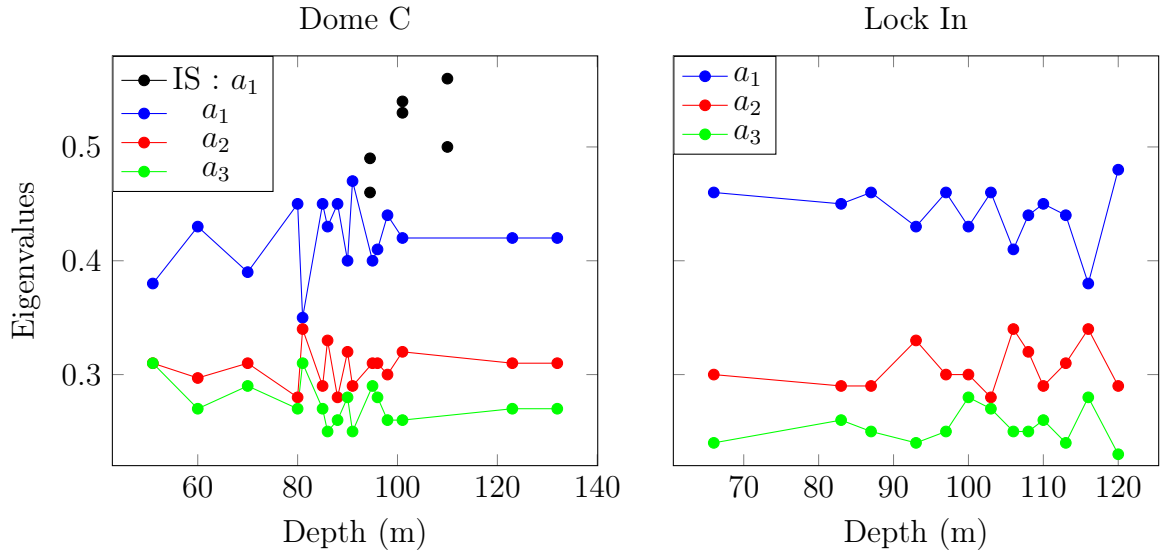


Figure D.3: Evolution of eigenvalues with depth for Dome C and Lock In, with comparison with the in situ compression tests.

APPENDIX D. EVOLUTION OF FIRN MICROSTRUCTURE AT DOME C AND LOCK IN

Dome C	Eigenvalues / eigenvectors		
Depth (m)	$a_3 \cdot \vec{v}_3$	$a_2 \cdot \vec{v}_2$	$a_1 \cdot \vec{v}_1$
51.00	$0.31 \begin{pmatrix} 0.921 \\ -0.290 \\ 0.259 \end{pmatrix}$	$0.31 \begin{pmatrix} -0.334 \\ -0.931 \\ 0.146 \end{pmatrix}$	$0.38 \begin{pmatrix} -0.199 \\ 0.221 \\ 0.955 \end{pmatrix}$
59.05	$0.27 \begin{pmatrix} 0.797 \\ 0.108 \\ 0.594 \end{pmatrix}$	$0.297 \begin{pmatrix} -0.602 \\ 0.056 \\ 0.797 \end{pmatrix}$	$0.43 \begin{pmatrix} 0.053 \\ -0.993 \\ 0.110 \end{pmatrix}$
69.95	$0.29 \begin{pmatrix} 0.373 \\ 0.928 \\ 0.018 \end{pmatrix}$	$0.31 \begin{pmatrix} -0.927 \\ 0.372 \\ 0.040 \end{pmatrix}$	$0.39 \begin{pmatrix} 0.031 \\ -0.032 \\ 0.999 \end{pmatrix}$
79.87	$0.27 \begin{pmatrix} 0.975 \\ -0.142 \\ 0.173 \end{pmatrix}$	$0.28 \begin{pmatrix} -0.169 \\ 0.043 \\ 0.985 \end{pmatrix}$	$0.45 \begin{pmatrix} -0.147 \\ -0.989 \\ 0.018 \end{pmatrix}$
80.97	$0.31 \begin{pmatrix} 0.818 \\ 0.545 \\ 0.182 \end{pmatrix}$	$0.34 \begin{pmatrix} 0.409 \\ -0.775 \\ 0.482 \end{pmatrix}$	$0.35 \begin{pmatrix} -0.404 \\ 0.320 \\ 0.857 \end{pmatrix}$
84.07	$0.27 \begin{pmatrix} 0.973 \\ 0.228 \\ 0.037 \end{pmatrix}$	$0.29 \begin{pmatrix} 0.217 \\ -0.959 \\ 0.184 \end{pmatrix}$	$0.45 \begin{pmatrix} -0.077 \\ 0.171 \\ 0.982 \end{pmatrix}$
86.00	$0.25 \begin{pmatrix} -0.267 \\ 0.962 \\ 0.056 \end{pmatrix}$	$0.33 \begin{pmatrix} -0.955 \\ -0.272 \\ 0.118 \end{pmatrix}$	$0.43 \begin{pmatrix} 0.129 \\ -0.022 \\ 0.991 \end{pmatrix}$
87.34	$0.26 \begin{pmatrix} 0.270 \\ -0.038 \\ 0.962 \end{pmatrix}$	$0.28 \begin{pmatrix} -0.942 \\ -0.219 \\ 0.255 \end{pmatrix}$	$0.45 \begin{pmatrix} -0.201 \\ 0.975 \\ 0.095 \end{pmatrix}$
89.50	$0.28 \begin{pmatrix} -0.972 \\ -0.212 \\ 0.099 \end{pmatrix}$	$0.32 \begin{pmatrix} 0.217 \\ -0.975 \\ 0.050 \end{pmatrix}$	$0.40 \begin{pmatrix} 0.086 \\ 0.070 \\ 0.994 \end{pmatrix}$
90.50	$0.25 \begin{pmatrix} 0.365 \\ 0.151 \\ 0.919 \end{pmatrix}$	$0.29 \begin{pmatrix} -0.931 \\ 0.062 \\ 0.359 \end{pmatrix}$	$0.47 \begin{pmatrix} -0.003 \\ -0.987 \\ 0.163 \end{pmatrix}$
94.50	$0.29 \begin{pmatrix} 0.777 \\ -0.584 \\ 0.235 \end{pmatrix}$	$0.31 \begin{pmatrix} -0.611 \\ -0.790 \\ 0.059 \end{pmatrix}$	$0.40 \begin{pmatrix} -0.151 \\ 0.190 \\ 0.970 \end{pmatrix}$
96.00	$0.28 \begin{pmatrix} -0.251 \\ -0.949 \\ 0.193 \end{pmatrix}$	$0.31 \begin{pmatrix} 0.941 \\ -0.192 \\ 0.280 \end{pmatrix}$	$0.41 \begin{pmatrix} -0.229 \\ 0.252 \\ 0.940 \end{pmatrix}$
97.50	$0.26 \begin{pmatrix} 0.507 \\ 0.862 \\ 0.011 \end{pmatrix}$	$0.30 \begin{pmatrix} -0.840 \\ 0.491 \\ 0.231 \end{pmatrix}$	$0.44 \begin{pmatrix} 0.194 \\ -0.126 \\ 0.973 \end{pmatrix}$
100.38	$0.26 \begin{pmatrix} 0.270 \\ 0.029 \\ 0.962 \end{pmatrix}$	$0.32 \begin{pmatrix} -0.962 \\ 0.053 \\ 0.268 \end{pmatrix}$	$0.42 \begin{pmatrix} -0.043 \\ -0.998 \\ 0.042 \end{pmatrix}$
123.34	$0.27 \begin{pmatrix} -0.991 \\ 0.131 \\ 0.021 \end{pmatrix}$	$0.31 \begin{pmatrix} 0.133 \\ 0.983 \\ 0.129 \end{pmatrix}$	$0.42 \begin{pmatrix} 0.004 \\ -0.130 \\ 0.991 \end{pmatrix}$
132.07	$0.27 \begin{pmatrix} -0.533 \\ -0.844 \\ 0.053 \end{pmatrix}$	$0.31 \begin{pmatrix} 0.827 \\ -0.507 \\ 0.244 \end{pmatrix}$	$0.42 \begin{pmatrix} -0.179 \\ 0.173 \\ 0.968 \end{pmatrix}$

Table D.5: Eigenvalues and eigenvectors of crystal orientations at Dome C.

Lock In	Eigenvalues / eigenvectors		
Depth (m)	$a_3 \cdot \vec{v}_3$	$a_2 \cdot \vec{v}_2$	$a_1 \cdot \vec{v}_1$
66	$0.24 \begin{pmatrix} 0.286 \\ -0.016 \\ 0.958 \end{pmatrix}$	$0.30 \begin{pmatrix} -0.957 \\ -0.065 \\ 0.284 \end{pmatrix}$	$0.46 \begin{pmatrix} -0.058 \\ 0.998 \\ 0.033 \end{pmatrix}$
83	$0.26 \begin{pmatrix} -0.022 \\ -0.019 \\ 0.9996 \end{pmatrix}$	$0.29 \begin{pmatrix} 0.997 \\ -0.071 \\ 0.021 \end{pmatrix}$	$0.45 \begin{pmatrix} 0.070 \\ 0.997 \\ 0.021 \end{pmatrix}$
87	$0.25 \begin{pmatrix} -0.383 \\ -0.082 \\ 0.920 \end{pmatrix}$	$0.29 \begin{pmatrix} 0.919 \\ 0.066 \\ 0.388 \end{pmatrix}$	$0.46 \begin{pmatrix} -0.092 \\ 0.994 \\ 0.050 \end{pmatrix}$
93	$0.24 \begin{pmatrix} -0.188 \\ 0.128 \\ 0.974 \end{pmatrix}$	$0.33 \begin{pmatrix} 0.979 \\ 0.011 \\ 0.017 \end{pmatrix}$	$0.43 \begin{pmatrix} 0.083 \\ -0.986 \\ 0.013 \end{pmatrix}$
97	$0.25 \begin{pmatrix} 0.376 \\ -0.002 \\ 0.928 \end{pmatrix}$	$0.30 \begin{pmatrix} -0.926 \\ -0.071 \\ 0.371 \end{pmatrix}$	$0.46 \begin{pmatrix} -0.065 \\ 0.997 \\ 0.029 \end{pmatrix}$
100	$0.28 \begin{pmatrix} -0.812 \\ -0.012 \\ 0.584 \end{pmatrix}$	$0.30 \begin{pmatrix} 0.582 \\ 0.056 \\ 0.811 \end{pmatrix}$	$0.43 \begin{pmatrix} 0.043 \\ -0.998 \\ 0.038 \end{pmatrix}$
103	$0.27 \begin{pmatrix} -0.664 \\ 0.030 \\ 0.747 \end{pmatrix}$	$0.28 \begin{pmatrix} 0.743 \\ -0.084 \\ 0.664 \end{pmatrix}$	$0.46 \begin{pmatrix} -0.082 \\ 0.996 \\ 0.033 \end{pmatrix}$
106	$0.25 \begin{pmatrix} 0.768 \\ 0.154 \\ 0.621 \end{pmatrix}$	$0.34 \begin{pmatrix} -0.618 \\ -0.076 \\ 0.783 \end{pmatrix}$	$0.41 \begin{pmatrix} 0.168 \\ -0.985 \\ 0.037 \end{pmatrix}$
107	$0.25 \begin{pmatrix} -0.021 \\ -0.039 \\ 0.999 \end{pmatrix}$	$0.32 \begin{pmatrix} 0.954 \\ -0.2996 \\ 0.008 \end{pmatrix}$	$0.44 \begin{pmatrix} 0.299 \\ 0.953 \\ 0.044 \end{pmatrix}$
110	$0.26 \begin{pmatrix} 0.689 \\ 0.031 \\ 0.724 \end{pmatrix}$	$0.29 \begin{pmatrix} -0.724 \\ 0.091 \\ 0.684 \end{pmatrix}$	$0.45 \begin{pmatrix} -0.045 \\ -0.995 \\ 0.085 \end{pmatrix}$
113	$0.24 \begin{pmatrix} 0.210 \\ 0.011 \\ 0.978 \end{pmatrix}$	$0.31 \begin{pmatrix} -0.967 \\ 0.152 \\ 0.206 \end{pmatrix}$	$0.44 \begin{pmatrix} -0.147 \\ -0.988 \\ 0.043 \end{pmatrix}$
116	$0.28 \begin{pmatrix} 0.548 \\ 0.084 \\ 0.832 \end{pmatrix}$	$0.34 \begin{pmatrix} -0.568 \\ -0.693 \\ 0.444 \end{pmatrix}$	$0.38 \begin{pmatrix} -0.614 \\ 0.716 \\ 0.332 \end{pmatrix}$
120	$0.23 \begin{pmatrix} 0.224 \\ -0.0198 \\ 0.974 \end{pmatrix}$	$0.29 \begin{pmatrix} -0.974 \\ -0.038 \\ 0.223 \end{pmatrix}$	$0.48 \begin{pmatrix} -0.033 \\ 0.999 \\ 0.028 \end{pmatrix}$

Table D.6: Eigenvalues and eigenvectors of crystal orientations at Lock In.

Sample	Eigenvalues / eigenvectors		
	$a_3 \cdot \vec{v}_3$	$a_2 \cdot \vec{v}_2$	$a_1 \cdot \vec{v}_1$
80m_c1_left	$0.21 \begin{pmatrix} 0.220 \\ -0.015 \\ 0.975 \end{pmatrix}$	$0.31 \begin{pmatrix} -0.884 \\ 0.421 \\ 0.205 \end{pmatrix}$	$0.49 \begin{pmatrix} -0.413 \\ -0.907 \\ 0.079 \end{pmatrix}$
80m_c1_right	$0.20 \begin{pmatrix} 0.843 \\ 0.072 \\ 0.533 \end{pmatrix}$	$0.33 \begin{pmatrix} -0.505 \\ -0.236 \\ 0.830 \end{pmatrix}$	$0.46 \begin{pmatrix} -0.186 \\ 0.969 \\ 0.163 \end{pmatrix}$
80m_c2_up	$0.20 \begin{pmatrix} -0.819 \\ -0.092 \\ 0.567 \end{pmatrix}$	$0.24 \begin{pmatrix} 0.572 \\ -0.046 \\ 0.819 \end{pmatrix}$	$0.56 \begin{pmatrix} -0.049 \\ 0.995 \\ 0.090 \end{pmatrix}$
80m_c2_down	$0.22 \begin{pmatrix} -0.446 \\ -0.142 \\ 0.884 \end{pmatrix}$	$0.29 \begin{pmatrix} 0.895 \\ -0.053 \\ 0.443 \end{pmatrix}$	$0.50 \begin{pmatrix} -0.016 \\ 0.988 \\ 0.151 \end{pmatrix}$
80m_c3_left	$0.19 \begin{pmatrix} 0.430 \\ 0.006 \\ 0.903 \end{pmatrix}$	$0.26 \begin{pmatrix} -0.898 \\ -0.099 \\ 0.428 \end{pmatrix}$	$0.54 \begin{pmatrix} -0.092 \\ 0.995 \\ 0.038 \end{pmatrix}$
80m_c3_right	$0.17 \begin{pmatrix} -0.322 \\ -0.073 \\ 0.944 \end{pmatrix}$	$0.30 \begin{pmatrix} 0.946 \\ -0.002 \\ 0.323 \end{pmatrix}$	$0.53 \begin{pmatrix} -0.022 \\ 0.997 \\ 0.070 \end{pmatrix}$
80m_ini	$0.26 \begin{pmatrix} 0.510 \\ 0.018 \\ 0.860 \end{pmatrix}$	$0.29 \begin{pmatrix} -0.856 \\ 0.105 \\ 0.506 \end{pmatrix}$	$0.45 \begin{pmatrix} -0.081 \\ -0.994 \\ 0.069 \end{pmatrix}$

Table D.7: Eigenvalues and eigenvectors of crystal orientations after in situ compression test.

Appendix E

Correction of the closed porosity ratio at Dome C

A correction of the closed porosity ratio was proposed in Fig. 3.24 in chapter 3. This appendix sums up how this was performed.

E.1 Parameterizations of the closed porosity ratio

E.1.1 Parameterization of Schaller et al. [2017]

The closed porosity ratio as expressed by Schaller et al. [2017] is used and defined by Eq. (1.8).

Parameters of B53 from table 2 [Schaller et al., 2017] are used, i.e. $\phi_{crit} = 0.1$, $\lambda_1 = 206.36$, $\lambda_2 = 48.06$, $b = 0.7072$, as the temperature is the same than at Dome C (-55 °C).

E.1.2 Parameterization of Goujon et al. [2003]

Equations (1.1) to (1.4) are used for the blue curve on Fig. 3.24. Note that the density of pure ice used by Goujon et al. [2003] is slightly larger than what Schwander et al. [1997] proposed. The temperature of the site is chosen at -55 °C (mean temperature according to Leballeur et al. [2015]).

The close-off density for parameterization Goujon and Mitchell follows Eq. (1.2) and not Eq. (1.7).

E.1.3 Parameterization of Mitchell et al. [2015]

Equations (1.5) and (1.6) are used for the parameterization of Mitchell et al. [2015].

As prescribed by Mitchell et al. [2015], $\sigma_{Mc} = 0.007 \text{ g.cm}^{-3}$. However equations (1.2) and (1.3) are chosen for ρ_c and ρ_{ice} to be consistent with Goujon et al. [2003] (see Fig. 3.24). Equation (1.7) is however recommended by Mitchell et al. [2015] for the close-off density as Eq. (1.2) is a mean close-off density, which is slightly different. Using recommendation of Mitchell et al. [2015] (thus $\rho_{ice} = 0.917 \text{ gcm}^{-3}$) leads to small differences shown in Fig. E.1.

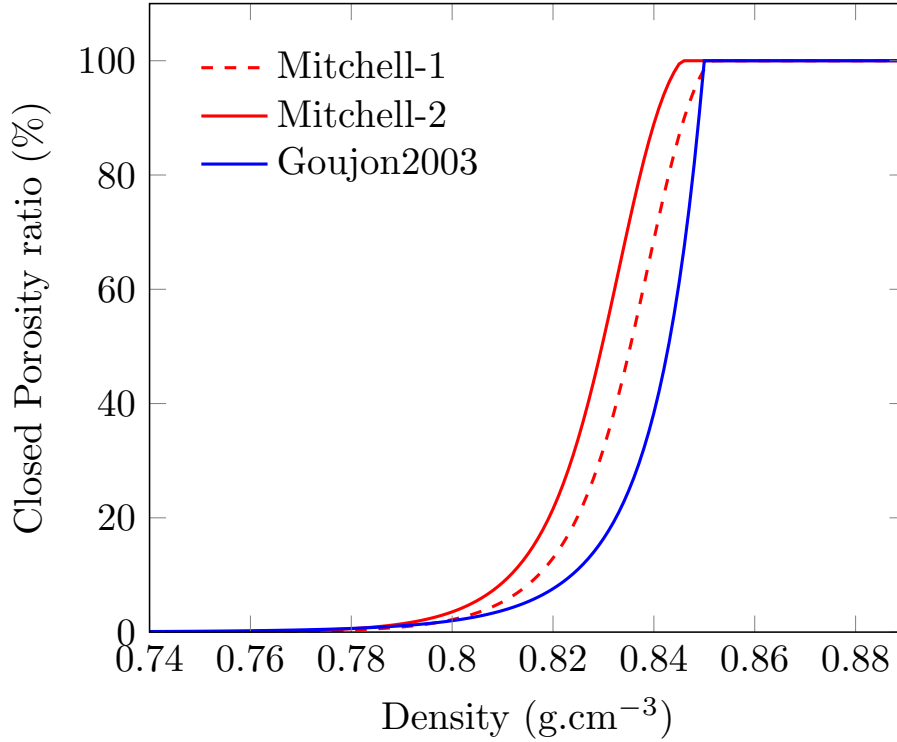


Figure E.1: Comparison between parameterizations with parameters from Mitchell et al. [2015] (Mitchell-1) and Goujon et al. [2003] (Mitchell-2), accompanied by the parameterization from Goujon et al. [2003].

E.2 Correction of closed porosities

Errors from table 3.4 are used on samples L60, in order to guess closed porosities for hypothetic L30 samples (large samples with a resolution of $30 \mu\text{m}$). The variation of density with these errors is neglected. Table E.1 gives the deduced L30 points. Making the assumption that samples below 70 m have no closed porosities, and that samples above 101 m have no open porosities (which is confirmed by measurements Landais et al. [2006]), the Fig. E.2 is obtained, linking the closed porosity values from DC-S12 and DC-S30, to the deduced corrected value.

A quintic fit is performed to scale all the data. In other words, to plot Fig. 3.24, one must multiply closed porosities from DC-S12 or DC-S30 with the correction factor

Sample	87.34 m	94.50 m	100.33 m
L60	27.05 %	82.73 %	91.45 %
L30	18.01 %	58.68 %	91.06 %

Table E.1: Closed porosity values of corrected L60 points

proposed Fig. E.2. Moreover, the density of samples is also changed with the density obtained with Eq. (1.3), i.e. $\rho_{ice} = 0.924 \text{ gcm}^{-3}$ at -55°C instead of 0.917 gcm^{-3} used in first approximation for pure ice at 0°C [Bader, 1964].

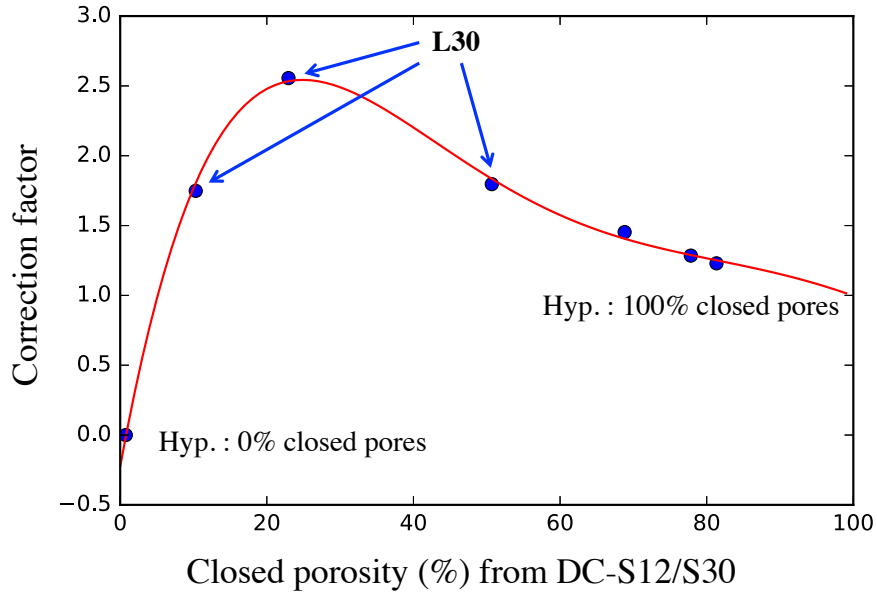


Figure E.2: Correction factor to apply to the closed-porosity of DC-S12 and DC-S30 samples to obtain the Fig. 3.24.

Appendix F

Dimension and calibration of the in situ cold cell

F.1 Micro-compression cold cell

To do mechanical tests on firn, a special cold cell was developed. It was designed to be adapted to a micro-compression device lent by Novitom, a french company based in Grenoble. Gears pulls up and down a piston thanks to a motor. A load cell is set just under the piston. From a software, one can pilot the displacement of a piston from a large range of rates (between 0.1 and $10\mu\text{m.s}^{-1}$). The top of the loading device is a second part that is fixed onto the apparatus, and that consists of an air chamber, and a hat that must bear the compression. The sample is put between the piston and the hat. The hat was designed with the help of finite element simulations (Fig. F.1). Figure F.1 shows that the maximum equivalent stress is about 11.4MPa for an applied stress of 5MPa . Both polycarbonate (PC) and polymethylmethacrylate (PMMA) exhibit yield strength superior than 55MPa with the PC being softer but more resistant to shocks. They are also good thermal insulator as they yield a thermal conductivity between 0.17 and $0.22\text{W.m}^{-1}\text{.K}^{-1}$. These plastic materials should be sufficiently strong to sustain the predicted stresses, and should limit the thermal conduction. We thus made two cover hats (one of each material) in case of the failure of one of them.

The PMMA socket was designed using the common relationship for stresses in thick-walled cylinders. After equalizing the pressure inside the tube with the internal stresses of the hollow cylinder, one obtains a hoop stress $\sigma_{\theta\theta}$ in function of the diameter d of the tube, the pressure p of the air against the tube and the thickness e of the tube. Using a yield strength σ_y equal to 55MPa , one must verify that :

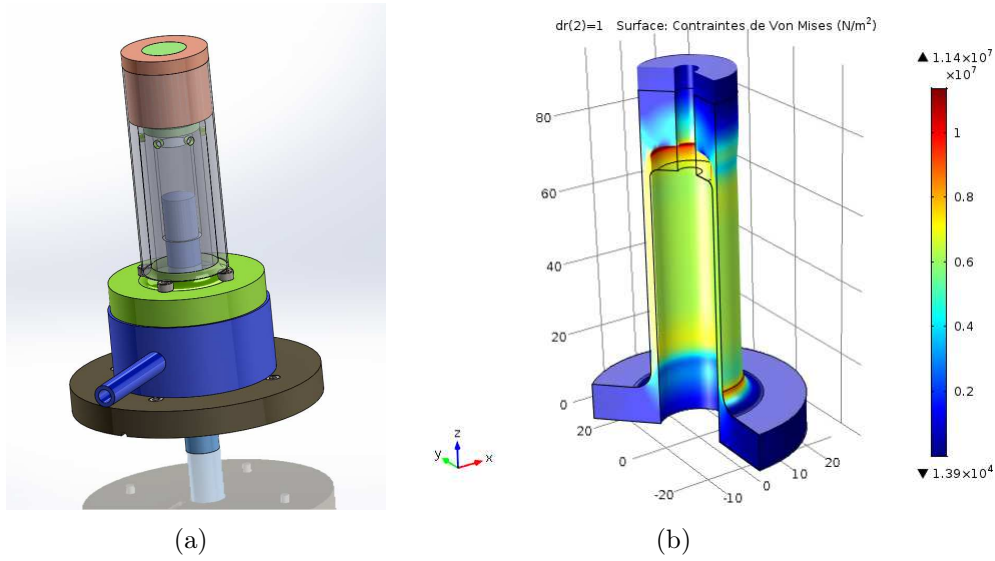


Figure F.1: (a) Compression cell designed with the CAD software SolidWorks [Solidworks, 2013]. (b) Finite element simulations with COMSOL Multiphysics [COMSOL, 2013], giving the Von Mises equivalent stress in the hat (in Pa). The simulation is axisymmetric, with an applied stress of 5 MPa on the upper inside of the hat. The bottom of the hat is locked.

$$e > \frac{pd}{2\sigma_y} \quad (\text{F.1})$$

For $p = 5$ MPa, and $d = 12$ mm, the thickness should be superior than $e > 545$ μm . Thus we chose $e = 1$ mm leading to a maximal stress of about 9 MPa, which was never reached in experiments. No fillet between the tube and the cap of the PMMA socket was made, to have a perfectly plane surface.

The load cell was first calibrated with a MTS compression device (from MTS Systems). The relation between the force given by the MTS, and the one given by the Novitom software is linear, with an offset of roughly 450 N. However, signal from the load cell is noisy, with errors about 10 N to 30 N (as depicted in section 4.3). Thus, each points on the Fig. F.2 is an average of the read signal. When using the Novitom device for firm deformation, the force can be easily smoothed by a moving average.

Moreover, the displacement of the piston was also studied, to find out if it moves as set in the software. Results show that for displacement rate above $1 \mu\text{m.s}^{-1}$, the piston seems to move accurately, however when the rate is decreased, the piston can not reach the desired speed. It does not follow linearly the set speed, and fluctuates occasionally when reaching very low speed like $0.05 \mu\text{m.s}^{-1}$ (see Fig. F.3b). Curves at $0.1 \mu\text{m.s}^{-1}$ shows that the piston moves correctly at a bit lower speed than expected. These tests were realized

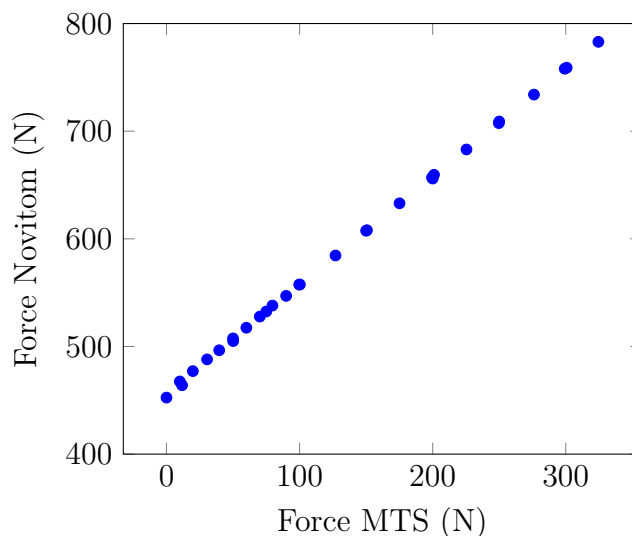


Figure F.2: Force calibration : Evolution of the average force read on the Novitom software with the force given by the MTS.

with a LVDT calibrated to the micron. Hence precisions of $0.1\ \mu\text{m}$ as given by the LVDT are full of errors. Finally, the sampling frequency is hardly above 10 Hz, limiting also the resolution. In fact figures F.3a-b are staircase functions.

Moreover these evolutions are certainly hindered when a load is applied, but this could not be measured with an LVDT. During firm deformation the evolution of the piston was followed by X-ray radiography at a resolution of $15\ \mu\text{m}.\text{pix}^{-1}$. This means that one must wait 150 s at $0.1\ \mu\text{m}.\text{s}^{-1}$ to see the piston moves one pixel, while with the LVDT, a measurement was done every 0.1 s. This leads the observer to be unable to know what happens in this 150 s and only to hope that the piston moves linearly with time. On the other hand, it was measured that every 150 s, the piston does move one pixel without loading.

When designing the loading device, thickness of PMMA or PC walls was studied, such that the detector get enough flux of photons. Using XOP software [Del Río & Dejus, 2011], the Fig. F.4a was obtained after 3.5 mm of PC, 12 mm of firm and 3.5 mm of PC. At 60 kV of acceleration, the energy transmitted ranges from 0 keV to 60 keV. The transmitted intensity is sufficient to have enough contrast. According to Fig. F.4b, the absorption of all S12 samples (see table 3.3) is not particularly pronounced, However, scanning an entire slice of ice core as the L60, and M30 samples is challenging as most of X rays are absorbed. That is why, the flux was drastically increased for these samples, as described in section 3.3.

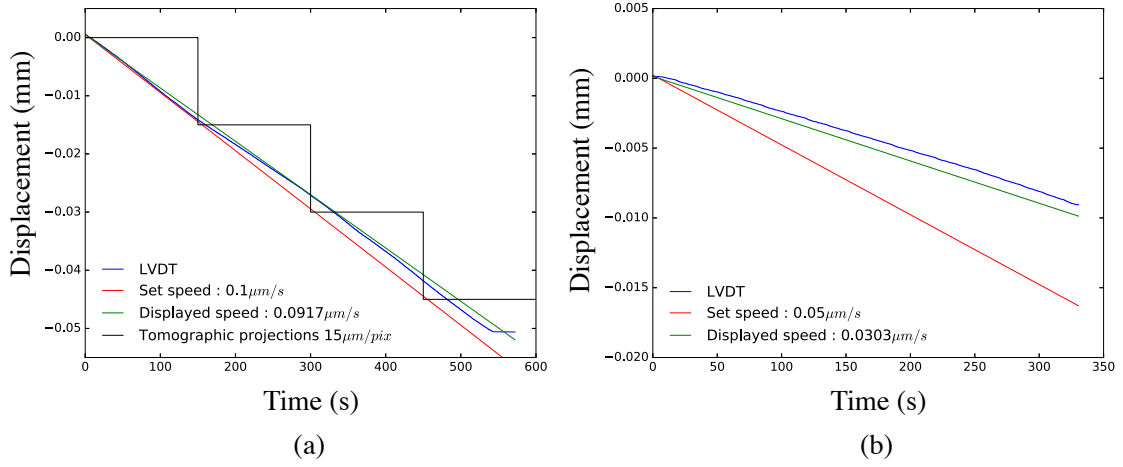


Figure F.3: Displacement of the piston without charge with time for a set speed of (a) $0.1 \mu\text{m.s}^{-1}$ and (b) $0.05 \mu\text{m.s}^{-1}$. All curves come from LVDT measurements, except for the black one that comes from the pixel displacement during X-ray scan, when the piston moves up.

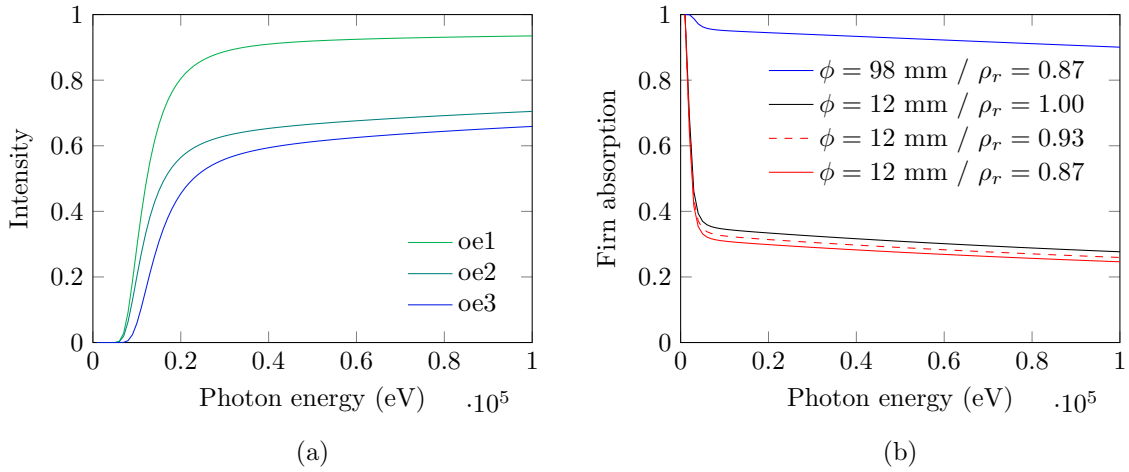


Figure F.4: From XOP software : (a) Intensity after successive optical elements (oe). The cover hat is 7 mm thick in polycarbonate. Thus the curve on top represents the transmission after 3.5 mm of PC, then the curve oe2 is the transmission after PC + 12 mm of firm, and finally oe3 is the final transmission after PC + firm + PC. (b) Absorption of the firm for different densities and diameters without PC.

F.2 Oedometric test

In the case of an oedometric test, the stress tensor is composed of non-zero diagonal terms. In the reference adopted Fig. F.5, radial stresses are equal and we define $\sigma_a = \sigma_{xx} = \sigma_{yy}$. The stress tensor writes :

$$\boldsymbol{\sigma} = \begin{pmatrix} \sigma_a & 0 & 0 \\ 0 & \sigma_a & 0 \\ 0 & 0 & \sigma_{zz} \end{pmatrix}_{(\mathbf{x}, \mathbf{y}, \mathbf{z})}$$

The deviatoric stress writes :

$$\mathbf{S} = \boldsymbol{\sigma} - \frac{\text{tr}(\boldsymbol{\sigma})}{3} \mathbf{I} = \frac{1}{3} \begin{pmatrix} \sigma_a - \sigma_{zz} & 0 & 0 \\ 0 & \sigma_a - \sigma_{zz} & 0 \\ 0 & 0 & 2(\sigma_{zz} - \sigma_a) \end{pmatrix}_{(\mathbf{x}, \mathbf{y}, \mathbf{z})}$$

In the case of a viscoplastic material, radial components of the strain rate tensor are zero, thus :

$$\dot{\boldsymbol{\epsilon}} = \begin{pmatrix} 0 & 0 & 0 \\ 0 & 0 & 0 \\ 0 & 0 & \dot{\epsilon}_{zz} \end{pmatrix}_{(\mathbf{x}, \mathbf{y}, \mathbf{z})}$$

Assuming a behavior law of the material is known, and the flow is isochoric, then $\dot{\epsilon}_{zz}$ can be related to σ_{zz} and σ_a thanks to a typical Norton-Hoff law :

$$\mathbf{S} = 2K \left(\sqrt{3} \dot{\epsilon}_{eq} \right)^{m-1} \dot{\boldsymbol{\epsilon}} \quad (\text{F.2})$$

with K and m material parameters, and $\dot{\epsilon}_{eq}$ is the equivalent strain rate. To express σ_a in function of σ_{zz} and $\dot{\epsilon}_{zz}$ which are known values from the experiment, one should use an appropriate law. For instance, a power-law creep for porous material is given by [Duva & Crow \[1994\]](#) and enable the estimation of σ_a . For instance, this type of law for porous material was successfully used in the case of modeling the flow of firn from glacier [[Gagliardini & Meyssonier, 1997](#)].

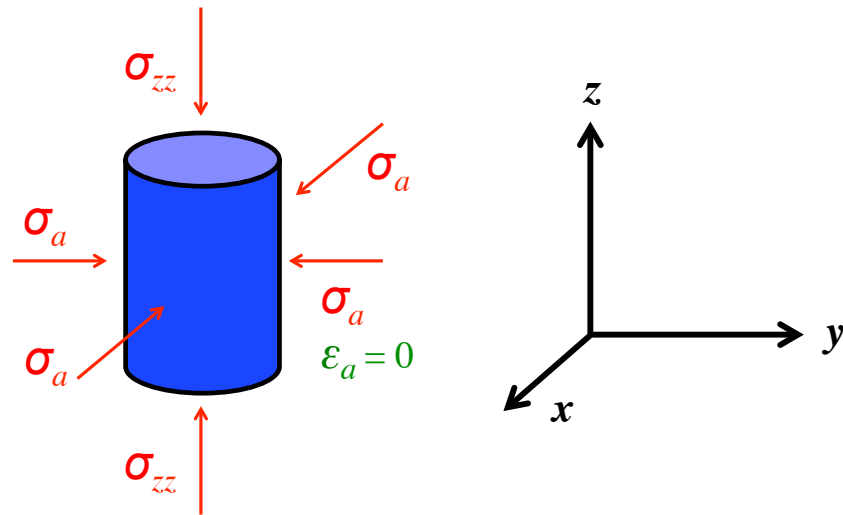


Figure F.5: Diagram of an oedometric test and the reference axes. σ_{zz} , σ_a and ε_{zz} are different from 0 but $\varepsilon_a = 0$.

